FATIGUE DAMAGE CHARACTERIZATION OF BRAIDED AND WOVEN FIBER REINFORCED POLYMER MATRIX COMPOSITES AT ROOM AND ELEVATED TEMPERATURES

by

John Montesano
Master of Applied Science, Ryerson University (2005)
Bachelor of Engineering, Ryerson University (2003)

A dissertation

presented to Ryerson University

in partial fulfillment of the

requirements for the degree of

Doctor of Philosophy

in the Program of

Aerospace Engineering

Toronto, Ontario, Canada, 2012

AUTHOR'S DECLARATION FOR ELECTRONIC SUBMISSION OF A DISSERTATION

I hereby declare that I am the sole author of this dissertation. This is a true copy of the dissertation, including any required final revisions, as accepted by my examiners.

I authorize Ryerson University to lend this dissertation to other institutions or individuals for the purpose of scholarly research.

I further authorize Ryerson University to reproduce this dissertation by photocopying or by other means, in total or in part, at the request of other institutions or individuals for the purpose of scholarly research.

I understand that my dissertation may be made electronically available to the public.

FATIGUE DAMAGE CHARACTERIZATION OF BRAIDED AND WOVEN FIBER REINFORCED POLYMER MATRIX COMPOSITES AT ROOM AND ELEVATED TEMPERATURES

John Montesano
Doctor of Philosophy, Aerospace Engineering, Ryerson University, Toronto (2012)

ABSTRACT

The use of polymer matrix composites (PMC) for manufacturing primary load-bearing structural components has significantly increased in many industrial applications. Specifically in the aerospace industry, PMCs are also being considered for elevated temperature applications. Current aerospace-grade composite components subjected to fatigue loading are over-designed due to insufficient understanding of the material failure processes, and due to the lack of available generic fatigue prediction models. A comprehensive literature survey reveals that there are few fatigue studies conducted on woven and braided fabric reinforced PMC materials, and even fewer at elevated temperatures. It is therefore the objective of this study to characterize and subsequently model the elevated temperature fatigue behaviour of a triaxial braided PMC, and to investigate the elevated temperature fatigue properties of two additional woven PMCs.

An extensive experimental program is conducted using a unique test protocol on the braided and woven composites, which consists of static and fatigue testing at various test temperatures. The development of mechanically-induced damage is monitored using a combination of non-destructive techniques which included infrared thermography, fiber optic sensors and edge replication. The observed microscopic damage development is quantified and correlated to the exhibited macroscopic material behaviour at all test temperatures. The fiber-dominated PMC materials considered in this study did not exhibit notable time- or temperature-dependent static properties. However, fatigue tests reveal that the local damage

development is in fact notably influenced by temperature. The elevated temperature environment increases the toughness of the thermosetting polymers, which results in consistently slower fatigue crack propagation rates for the respective composite materials. This has a direct impact on the stiffness degradation rate and the fatigue lives for the braided and woven composites under investigation. The developed analytical fatigue damage prediction model, which is based on actual observed damage mechanisms, accurately predicted the development of damage and the corresponding stiffness degradation for the braided PMC, for all test temperatures. An excellent correlation was found between the experimental and the predicted results to within a 2% accuracy. The prediction model adequately captured the local temperature-induced phenomenon exhibited by the braided PMC material. The results presented in this study are novel for a braided composite material subjected to elevated temperature fatigue.

ACKNOWLEDGEMENTS

There are numerous individuals and organizations that have provided me with great support throughout the course of my PhD studies, and the completion of this dissertation would not have been possible otherwise. I would like to start by thanking my supervisors Dr. Zouheir Fawaz, Dr. Kamran Behdinan and Dr. Cheung Poon for their continuous encouragement, guidance and support throughout the duration of my studies, including during the writing of my dissertation. I am especially grateful to my supervisors for providing me with the opportunity to study in the field of composite materials, to be involved in a collaborative industrial-based research project, and to present my work at a number of international conferences. I would like to acknowledge the Natural Sciences and Engineering Research Council (NSERC) of Canada, the Consortium for Research and Innovation in Aerospace in Quebec (CRIAQ), Pratt and Whitney Canada and Rolls Royce for financially supporting the research project. I would also like to acknowledge NSERC, Engineers Canada, Ryerson International, the Department of Aerospace Engineering (Ryerson University) and Sun Microsystems of Canada for additional funding in the form of scholarships during my studies.

I am thankful for the support of Dr. Martin Levesque, Mr. Thibaut Crochon and Mr. Amine El Mourid from École Polytechnique de Montréal for their collaboration in the research project, and specifically for their valuable feedback and for providing some of the data contained in this dissertation. I would also like to acknowledge Mr. Steven Caulfeild of Pratt and Whitney Canada for his input and valued discussions during biannual meetings related to this research project. I would like to thank Dr. Xijia Gu of the Department of Electrical Engineering at Ryerson University for supplying the fiber optic sensors required for my research. I would also like to thank Ms. Marina Selezneva for assistance during the preliminary testing phase of this research, and for many discussions regarding fiber optic sensors. I am indebted to Dr. Habiba Bougherara of the Department of Mechanical and Industrial Engineering at Ryerson University for supplying the infrared camera which was invaluable for this study. A special thanks to Dr. Lotfi Toubal from the Université du Québec à Trois-Rivières for the many discussions regarding the application of infrared thermography on composite materials. I am grateful for the support of Mr. Qiang Li, technical officer at Ryerson University, for assisting with the acquisition of the

scanning electron microscopic images. I would like to acknowledge Mr. Gopi Thamilselvan for manufacturing some of the materials tested in this study. A special thanks to Dr. Hamid Ghaemi for technical support within the structural testing facility in which the experimental research was conducted, and to Alan Machin, technical officer at Ryerson University, for his much needed assistance. I would also like to thank Kavya Roy, Shahpour Turkian and Filip Boskovic for their assistance in preparing some of the test specimens and samples for microscopic observations.

I would also like to extend a special thank you to my friends and colleagues at Ryerson University for their many insightful discussions, whether technical in nature or otherwise, and for much needed motivational support. I am grateful for the support of my family who were always encouraging and emotionally supportive throughout the duration of my studies. Finally, I would like to thank my wife Julia for being patient, understanding, encouraging and supportive in every respect - I could not have completed this journey without her.

DEDICATION

I would like to dedicate this thesis to my parents, my family and especially to my wife Julia.

TABLE OF CONTENTS

LIST OF TABLES

LIST OF FIGURES

NOMENCLATURE

Latin Symbols

$[A]$	laminate extensional matrix
A_D	effective damaged area (damage mechanics)
A_O	total area of representative element (damage mechanics)
A, b	S-N curve fitting coefficients
a_1, a_2, a_3, a_4	crack density regression coefficients
b_1, b_2	fatigue damage model parameters
D	accumulated fatigue damage
d_1, d_2	braider yarn crack and interface crack damage parameters
$E(n)$	dynamic stiffness (fatigue)
E_{11}	axial modulus (composite or bulk material)
E_{11f}	fiber axial tensile modulus
E_{11o}	lamina longitudinal modulus
E_{22}	transverse modulus (composite or bulk material)
E_{22o}	lamina transverse modulus
E_d	dissipated energy
E_f	final stiffness at fracture (fatigue)
E_m	Matrix modulus
E_o	initial dynamic stiffness (i.e., static modulus)
f	cyclic loading frequency
L	fiber Bragg grating length
N_f	fatigue life, number of cycles to failure
n	fatigue loading cycles
n_{eff}	index of refraction (fiber Bragg grating)
P_{11}, P_{12}	Pockel's coefficients (fiber Bragg grating)
Q_{ij}	lamina stiffness matrix terms
$\overline{Q}_{ij}$	transformed lamina stiffness matrix terms
R	stress ratio (fatigue)
R^2	data correlation factor for numerical regression
S_u	static ultimate tensile stress
T	ambient temperature
T_g	glass transition temperature
$T_{g,\,dry}$	polymer dry glass-transition temperature
$T_{g,\,wet}$	polymer wet glass-transition temperature
V_f	fiber volume fraction

Greek Symbols

α	glass coefficient of thermal expansion (fiber Bragg grating)
α_1, α_2	damage model scaling coefficients

β_1, β_2	damage model exponent coefficients
ΔT	temperature rise
ΔT_{stab}	temperature increase at stabilization
$\Delta\varepsilon$	strain range (fatigue)
ε_1, ε_2	lamina strain in material direction
ε_{max}	maximum strain (fatigue)
ε_{mean}	mean strain (fatigue)
ε_{min}	minimum strain (fatigue)
ε_r	ratcheting strain (fatigue)
ε_x, ε_y	lamina strain in laminate direction
ε_λ	fiber Bragg grating strain
Λ	fiber Bragg grating pitch
λ	fiber Bragg grating wavelength
ν_λ	Poisson's ratio for glass (fiber Bragg grating)
ν_{12}	major Poisson's ratio
ξ, η	Halpin-Tsai parameters
ρ	material density
ρ_{by}	braider yarn crack density
ρ_{int}	interface crack density
σ_1, σ_2	lamina stress in material direction
σ_a	stress amplitude (fatigue)
σ_{max}	maximum applied stress (fatigue)
σ_{mean}	mean stress (fatigue)
σ_{min}	minimum applied stress (fatigue)
σ_r	stress range (fatigue)
σ_x, σ_y	lamina stress in laminate direction

1 INTRODUCTION

1.1 Motivation

In recent years, the application of advanced polymer matrix composites (PMC) has notably increased in many industries due to their superior strength-to-weight and stiffness-to-weight ratios compared to traditional monolithic metallic alloys. The significant advancement in PMC technology has led to practical applications in aerospace, automotive, marine and civil structures. Particularly in the aerospace industry, PMC materials have become the material of choice for primary load bearing components, which is exemplified by considering modern commercial transport aircraft such as the Airbus A380 and the Boeing 787. An overview of the usage of composite materials in the Boeing 787 commercial aircraft is shown in Figure 1, which consists of an airframe structure that is comprised of 50% composite materials by weight and 80% composite by volume [1]. The obvious benefit in using composite materials for aircraft structures is the significant reduction in fuel consumption due to the decrease in aircraft structural weight. The established acceptance of these materials in the aerospace industry and their importance for future development of more efficient aircraft is apparent. Currently, fiber reinforced polymeric composite components are over-designed due to the many uncertainties associated with these advanced materials and due to their complex microscopic behaviour. A better understanding of composite material mechanical behaviour is consequently necessary to optimize the material in order to ensure sustained widespread usage.

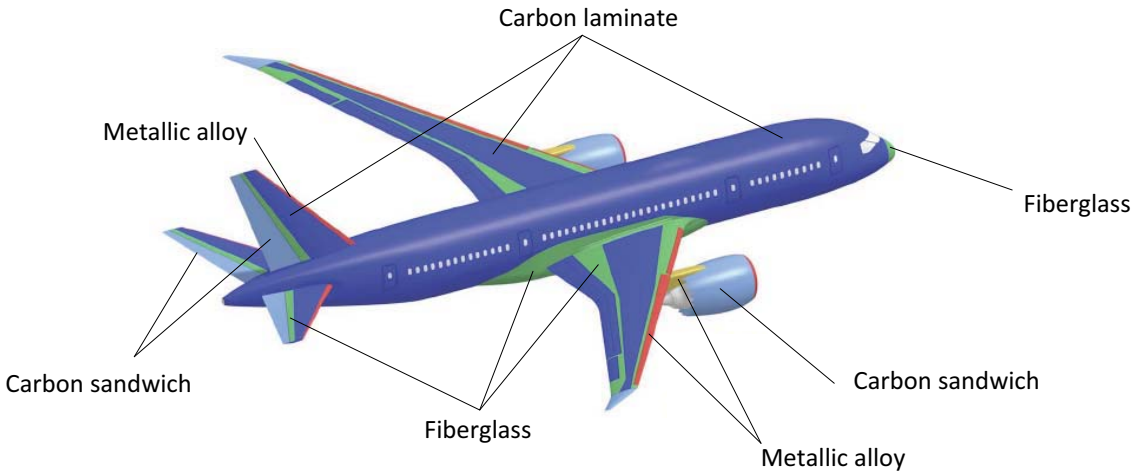

Figure 1. Boeing 787 airframe structure material usage by volume [1].

Polymeric composites are typically comprised of a reinforcing constituent material embedded in a polymer matrix constituent material, which combine to form a heterogeneous and anisotropic material. The polymer matrix can be either thermosetting or a thermoplastic, which influences not only the mechanical properties but also the material manufacturing process. The reinforcing material can be in the form of particles, short fibers or continuous fibers. Some types of commonly used continuous fibers include carbon, glass, Kevlar and boron. Composites consisting of layered unidirectional continuous carbon fiber reinforced polymer plies have been largely employed for primary load bearing applications in the aerospace industry. Despite their substantial use, a number of manufacturing and performance disadvantages have been identified with unidirectional-ply PMC laminates. This has consequently prompted the recent development of textile PMC materials, including woven, stitched, knitted and braided fabric reinforcements. Compared to conventional laminates, fabric reinforced PMC materials present a number of clear advantages [2, 3]. Some of these advantages include having better overall through-the-thickness strength properties including superior impact damage resistance and delamination resistance, balanced in-plane performance, improved fatigue performance and lower notch sensitivity. In addition, producing complex shaped parts can be easier to manufacture and generally have a much lower

manufacturing cost due to the conformability of textile fabrics coupled with the use of an out-of-autoclave manufacturing technique such as resin transfer moulding (RTM). The automation of the textile fabrics may further reduce manufacturing costs, eliminating tedious manual lay-up which renders textile composites as cost-competitive alternatives for component manufacturing. In spite of the indicated advantages, the use of some textile composites such as braided PMC materials is only limited to a few applications in the aerospace industry to date. One of the issues restricting their wider use is that there have been few studies conducted which characterize the material behaviour, thus limiting the available mechanical performance data of braided PMC materials. It is therefore imperative to better understand the mechanical behaviour of braided composite materials that results from their complex microstructure.

Furthermore, continuous carbon fiber reinforced polymeric composite materials are gaining substantial consideration in the aerospace industry for elevated temperature applications such as supersonic vehicle airframe and propulsion system components. A schematic of the components of a turbofan jet engine is shown in Figure 2, with the indicated zones for potential application of composite material components. This class of materials may be adequate replacements for their metallic counterparts for manufacturing aircraft components exposed to long-term temperatures in the 150 - 350°C range. A new generation of high glass-transition temperature (T_g) polymers has enabled this early stage development. Commercially available polymers such as PMR-15 [4], bismaleimide (BMI) [5] and a number of additional high temperature polyimide resins have been used or are being considered for fiber-reinforced composite materials to manufacture jet engine components or supersonic vehicle airframe components. The integration of composite materials into the propulsion systems of modern commercial and military aircraft has not experienced a great deal of advancement. This is mainly due to the demanding temperature regime that engine components must withstand during standard operation. Clearly, there is a requirement to better understand the mechanical behaviour of this class of PMC material at elevated temperatures.

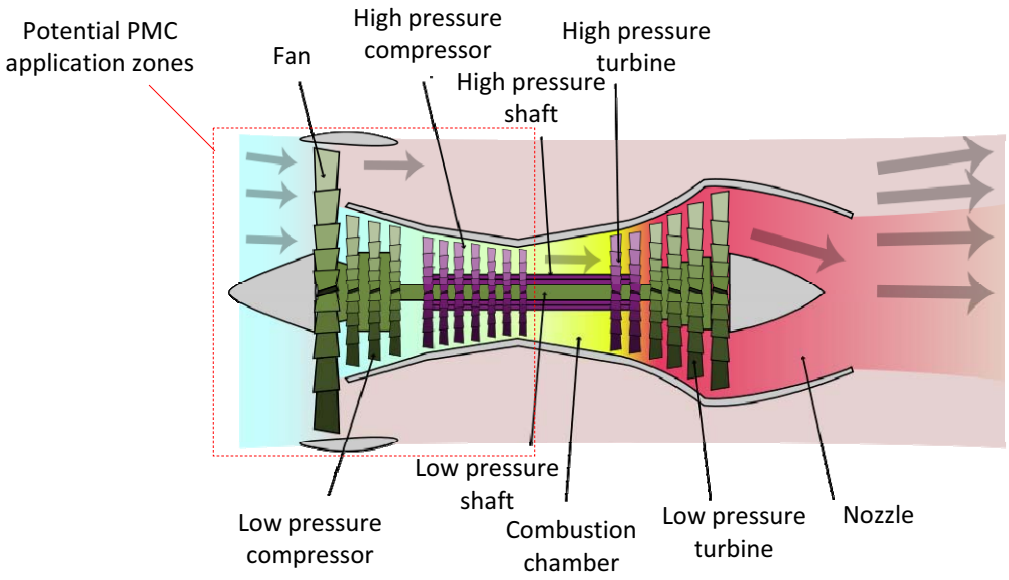

Figure 2. Turbofan jet engine schematic (source wikipedia.com).

In addition, the concept of a structural material failing in service when subjected to a repeating or cyclic stress with a magnitude much lower than its fracture stress is a phenomenon that has been on the agendas of many researchers for well over 100 years. Failure in materials such as metals or composites that occurs under dynamic loading conditions over a substantial period of time is called a fatigue failure. In the aerospace industry, there are many examples of structures subjected to cyclic loads such as the repeated pressurization and depressurization loading on the skin of an aircraft fuselage, the vibration of an aircraft component due to dynamic flight loading, the rotation of engine turbine blades and the rotation of compressor components. In fact, fatigue loading accounts for a large percentage of service failures due to mechanical causes. With respect to polymeric composite materials, understanding the microscopic damage development caused by cyclic loading is of paramount importance for developing damage tolerant materials, or for predicting the fatigue life of a structural component. For braided PMC materials, there is a requirement to better understand the influence of fatigue loading, the effects of elevated temperatures, and the influence of the associated damage development on the exhibited material behaviour. Currently, clear design criteria similar to those that are employed for fatigue of metallic alloys have not been well established for composites in general.

1.2 Objectives

The main objective of the study is to investigate the fatigue behaviour of a braided carbon fiber reinforced resin at elevated temperatures, and to provide a better understanding of the effects of both temperature and cyclic loading on the material behaviour. The characterization of damage development and the corresponding material behaviour during both static and fatigue loading, at both room temperature and elevated temperatures, is considered in detail. The critical microscopic damage modes and the development of damage are considered and correlated to the exhibited material behaviour. A corresponding fatigue damage model is also developed for the braided material, and used to predict the degradation of the material properties during cyclic loading. The predicted results of the fatigue damage model are then compared to the observed experimental damage development. The analytical damage model is based in part on the obtained quantitative damage observations, and thus developed accordingly. In addition, consideration for the effects of cyclic loading of other woven composites at elevated temperatures is investigated to provide a basis for discussion and comparison to the aforementioned braided composite material.

1.3 Scope

Polymeric composite material behaviour is a function of not only the type and size of the reinforcing fibers, but also their geometry. As a result, material properties of unidirectional-ply, woven-ply and braided composites will significantly differ. Consequently, various techniques are required to analytically determine the material properties of the different types of fiber reinforced composites. The direction of loading relative to the local material coordinates will also greatly influence the material behaviour. Chapter 2 contains an overview of the typical conventions associated with the various types of fiber reinforced composites, as well as a review of equations necessary to predict the material properties.

Although a number of fatigue studies have been conducted on PMC materials, few studies have been conducted on braided composites, and fewer studies have been conducted at elevated temperatures. Braided composite materials exhibit complex microscopic deformation and damage development due to cyclic loading. An elevated temperature

environment will undoubtedly influence the development of microscopic damage development. Also, damage development in braided and woven composites are distinct from that observed in conventional unidirectional laminates, which requires new fatigue damage models to be developed. A comprehensive literature survey of existing PMC material fatigue studies, elevated temperature studies, damage characterization studies, and developed fatigue damage models is presented in Chapter 3.

Fatigue testing that includes damage characterization generally requires a highly accurate and calibrated experimental setup, and a well planned test procedure. Non-destructive techniques are typically employed to monitor damage development throughout testing. In addition, testing at elevated temperatures introduces difficulties which often requires a slightly modified test protocol. The experimental testing details for the static and fatigue tests conducted on the braided PMC material will be discussed in Chapter 4, while the detailed test results will be presented in Chapter 5 for both room temperature and elevated temperature.

Development of the fatigue damage model, as pertaining to the braided composite material, will be presented and compared to the experimental data in Chapter 6. Additional results for other woven laminates will also be discussed in Chapter 6. An overall discussion of the experimental characterization and damage modeling results will be presented in Chapter 7. Finally, concluding remarks and a list of the contributions of this study will be presented in Chapter 8, which will also outline areas for future work.

2 COMPOSITE MATERIALS

Continuous fiber reinforced polymeric composite materials may consist of various forms of fiber geometries which influence both the microscopic and macroscopic behaviour of the material. The following sections present the conventions used for various types of continuous fiber reinforcements, the relevant methods required to determine the respective material properties, and a considerations for fiber-dominated and matrix-dominated material behaviour of continuous fiber reinforced PMC materials.

2.1 Fiber Geometric Conventions

Polymeric composite materials reinforced with continuous fibers can be classified either as laminates consisting of individual two-dimensional layers of fibers (or fabrics), or as three-dimensional composites consisting of a single reinforcing fabric layer with fibers in the through-thickness direction. Common examples of polymeric laminate two-dimensional fiber arrangements and polymeric composite three-dimensional fabrics are shown in Figure 3 and Figure 4, respectively. The corresponding warp direction is indicated in all figures, as well as the material coordinates in the longitudinal, transverse and through-thickness directions labelled 1, 2, and 3 respectively. Note that the yarns labelled in many of the images in the figures consist of a bundle of many fibers.

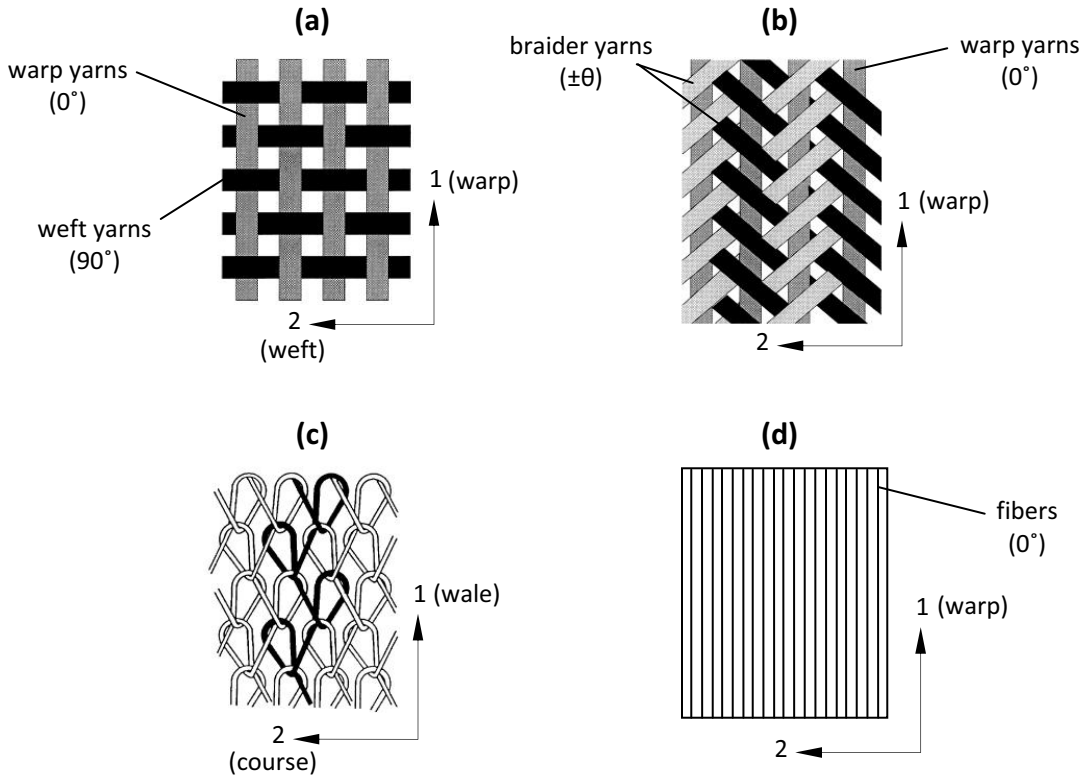

Figure 3. PMC laminate ply schematic of (a) plain woven, (b) triaxial braided, (c) knitted, (d) unidirectional.

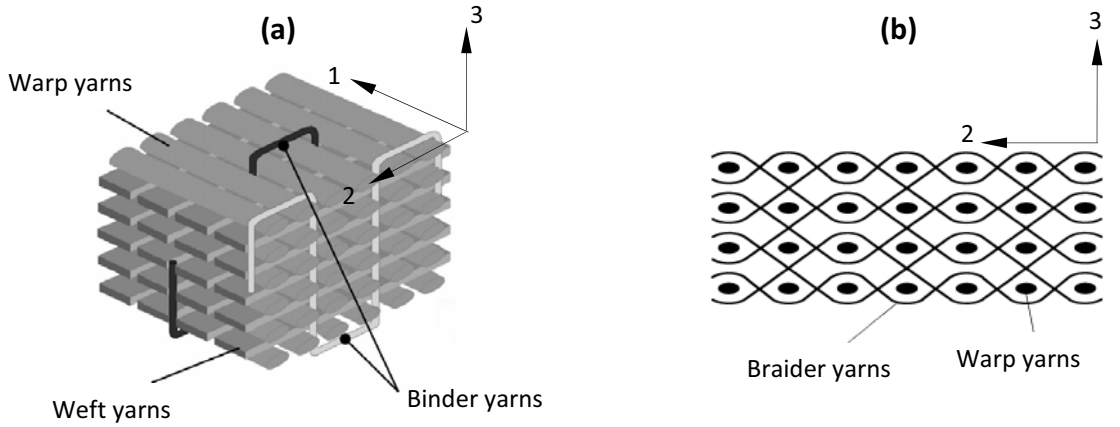

Figure 4. PMC three-dimensional fabric schematic of (a) orthogonal woven, (b) multi-layer interlock braided [2].

Conventional laminates employed in aerospace applications typically consist of stacking unidirectional plies, such as that shown in Figure 3 (d), with each ply oriented at a particular angle, θ, with respect to the x-direction of the laminate. Figure 5 shows a schematic of a four-

ply unidirectional laminate with the in-ply angles indicated (i.e., the angle between longitudinal material direction, 1, and the laminate x-direction). Unidirectional-ply laminates are typically manufactured from unidirectional layers that are pre-impregnated with the polymer matrix in an autoclave or by compression moulding. More recently, two-dimensional fabric layers such as those shown in Figure 3 (a)-(c) have also been utilized to manufacture multi-ply laminates. The fabric layers are typically all oriented in the same orientation with the material longitudinal direction, 1, parallel to the laminate x-direction, although the plies may be oriented with an angle θ relative to the laminate x-direction. These fabric-ply laminates are often manufactured by placing the dry fabric layers into a mould and using a RTM technique. They can also be manufactured from pre-impregnated layers in an autoclave. Finally, three-dimensional fabric composites such as those shown in Figure 4 (a) and (b) have also been utilized for some applications. These dry fabrics are typically placed in a mould and a RTM technique is used for manufacturing the components. These types of composites are typically employed in applications requiring very high out-of-plane strength, such as components subjected to impact loading.

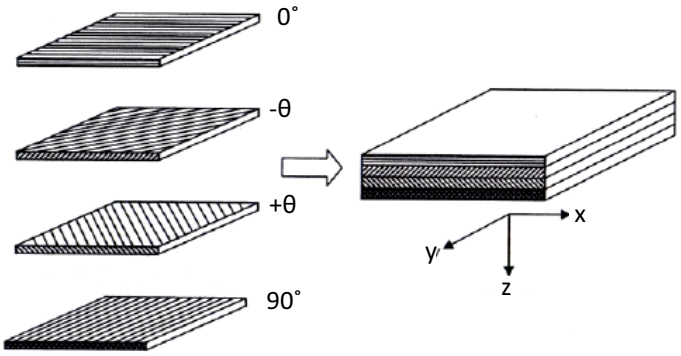

Figure 5. Four-ply unidirectional laminate schematic [6].

The fabric-ply laminates shown in Figure 3 (a) and (b) will be the focus of discussion in many chapters within this study. The fabric shown in Figure 3 (a) is a woven fabric with a plain weave, while the fabric shown in Figure 3 (b) is a triaxial braided fabric with a 2x2 braid pattern. The triaxial braided composite fiber geometry consists of fiber yarns oriented along the warp directions which are ideally straight, and braider yarns oriented in the ±θ directions which are

formed around the warp yarns and the adjacent braider yarns. A woven composite fiber geometry consists of fiber yarns in both the 0˚ and 90˚ directions that are formed around each other.

2.2 Material Properties

In order to determine material properties for fiber reinforced PMC materials, the material properties of the constituents, fiber geometry, fiber (or ply) orientation, and fiber volume fraction of the composite must be known and considered. This requires a study of the constituent materials and their geometric arrangement, which is known as micromechanics. Mechanical tensile properties of some common reinforcing fibers and some conventional metallic alloys are listed in Table 1, while typical tensile properties of polymers are listed in Table 2 as reference.

Table 1. Room temperature properties of fibers and conventional metallic alloys [6, 7].

Material	E_{11} **(GPa)**	S_u **(GPa)**	ρ **(g/cm^3)**
Fibers			
E-glass	72.4	3.5	2.54
S-glass	85.5	4.6	2.48
IM8 graphite	310	5.2	1.80
AS4 carbon	235	3.6	1.80
T650-35 carbon	255	4.3	1.77
Kevlar 49	130	2.8	1.50
Boron	385	2.8	2.63
Conventional alloys			
Aluminum	70.0	0.14 - 0.62	2.70
Steel	210	0.34 - 2.10	7.80

Table 2. Room temperature properties of polymers [6, 7].

Polymer Material	E_{11} (GPa)	S_u (MPa)	ρ (g/cm^3)
Thermosetting			
Epoxy	4.6	58.6	1.38
BMI	4.6	103	1.25
Polyimide	3.5	103	1.46
Thermoplastic			
PEEK	3.2	92	1.30
Polypropylene	1.2	30	0.90

For unidirectional-ply laminates, the properties of the individual plies or lamina are first considered. The laminae are typically assumed to be orthotropic due to the unidirectional orientation of the fibers. Mechanical properties such as the longitudinal modulus, transverse modulus, shear modulus and Poisson's ratio can be found using a well established homogenization technique such as the rule of mixtures or the Halpin-Tsai equations. For the approximation of the lamina longitudinal modulus (E_{11o}), it is assumed that the fibers and matrix undergo the same strain magnitude during loading [6]. For a fiber volume fraction denoted as V_f, the modulus is defined as:

$$E_{11o} = E_{11f}V_f + E_m\left(1 - V_f\right) \tag{1}$$

The fiber axial tensile modulus is defined as E_{11f}, while the matrix modulus is defined as E_m. The lamina transverse modulus (E_{22o}) can be found using the Halpin-Tsai equations.

$$E_{22o} = \left(\frac{1 + \xi\eta V_f}{1 - \eta V_f}\right)E_m \tag{2}$$

The term ξ is dependent on the fiber geometry and arrangement, while the parameter η is defined as [6]:

$$\eta = \frac{\left(E_{11f} / E_m\right) - 1}{\left(E_{11f} / E_m\right) + \xi} \tag{3}$$

Once all the lamina properties are known, the equivalent laminate properties can then be determined based on the orientation and stacking sequence of the individual plies. The individual orthotropic plies are typically assumed to be in a state of plane stress. If the plies deform in a linearly elastic manner, the relevant stress-strain relations are given as [6]:

$$\begin{Bmatrix} \sigma_1 \\ \sigma_2 \\ \tau_{12} \end{Bmatrix} = \begin{bmatrix} Q_{11} & Q_{12} & 0 \\ Q_{12} & Q_{22} & 0 \\ 0 & 0 & Q_{66} \end{bmatrix} \begin{Bmatrix} \varepsilon_1 \\ \varepsilon_2 \\ \gamma_{12} \end{Bmatrix} \tag{4}$$

The stress and strain terms in Equation (4) are written in terms of the material coordinate system shown in Figure 3 (d). The stiffness matrix terms Q_{ij} are functions of the engineering constants for the lamina. Equation (4) can be transformed to account for the orientation of the individual plies with respect to the laminate warp direction using the orientation angle θ. Equation (4) can then be written in terms of the laminate (or global) coordinate system (see Figure 5), as is defined by Equation (5). The transformed stiffness matrix terms $\overline{Q}_{ij}$ are functions of Q_{ij} [6].

$$\begin{Bmatrix} \sigma_x \\ \sigma_y \\ \tau_{xy} \end{Bmatrix} = \begin{bmatrix} \overline{Q}_{11} & \overline{Q}_{12} & \overline{Q}_{16} \\ \overline{Q}_{12} & \overline{Q}_{22} & \overline{Q}_{26} \\ \overline{Q}_{16} & \overline{Q}_{26} & \overline{Q}_{66} \end{bmatrix} \begin{Bmatrix} \varepsilon_x \\ \varepsilon_y \\ \gamma_{xy} \end{Bmatrix} \tag{5}$$

Classical laminate theory (CLT) can then be employed to define the stress-strain relations for a general laminate using the transformed stiffness matrices, $\left[\overline{Q}\right]^k$, of the *k*-th plies. The laminate stress-strain relation in vector and matrix notation is defined by:

$$\left\{\sigma\right\}^k = \left[\overline{Q}\right]^k \left\{\varepsilon^o\right\} + \left[\overline{Q}\right]^k z \left\{\kappa\right\} \tag{6}$$

The superscript *k* denotes the *k*-th ply, *z* is the lamina distance from the laminate mid-plane, $\left\{\varepsilon^o\right\}$ are the mid-plane strains, and $\left\{\kappa\right\}$ are the curvatures [7]. The equivalent laminate engineering constants (i.e., E_{11}, E_{22}, etc.) can then be determined for a symmetric laminate by defining the effective laminate stresses $\left[\overline{\sigma}\right]$, defined by Equation (7). The term 2*H* is the total

laminate thickness, and [*A*] is the laminate extensional matrix. A detailed overview of the development of the CLT equations and the definition of laminate engineering constants for specific types of symmetric laminates can be found in [7].

$$\{\bar{\sigma}\} = \frac{1}{2H}[A]\{\varepsilon^o\} \tag{7}$$

For two-dimensional fabric laminates, the equivalent lamina properties are often difficult to determine using a simple homogenization technique, such as the rule of mixtures, due to the complex geometry of the reinforcing fabric. As a result, more advanced analytical techniques are often employed to determine the equivalent lamina and laminate properties. If the fabric layers do not all have the same orientation, the homogenization technique can then be combined with CLT to determine the equivalent laminate engineering constants. Similar homogenization techniques are typically adopted for approximating the mechanical properties of three-dimensional fabric reinforced composites. These techniques are based on a continuum approach and they assume that the material exhibits statistical homogeneity at the macroscopic scale. A representative volume element (RVE) of the composite microstructure is typically defined in order to perform the homogenization. The review of continuum homogenization approaches conducted by Herakovich [7] discusses many commonly employed homogenization techniques such as Voigt approximation, Reuss approximation, the method of cells, the self-consistent method, the Mori-Tanaka method and the micromechanical approach using finite element analysis.

One commonly employed analytical homogenization technique is the method originally developed by Mori-Tanaka [8], which was subsequently adapted for application to composite materials [9, 10]. More recently, this technique was applied to textile composites [11]. The fiber yarns in textile composites are effectively represented by a series of inclusions within the matrix. The geometry and size of the fictitious inclusions are defined based on the actual textile fabric geometry, and a series of geometrical tensors are defined. These tensors are used along with the fiber and matrix material properties to define the composite mechanical properties, such as the tensile modulus. Full details of the technique as applicable to textile composite

materials can be found in [12]. It is also common to employ numerical homogenization techniques which are based on the finite element method (FEM). These techniques explicitly model the micromechanical RVE and use the constituent material properties with appropriate boundary conditions to approximate the composite mechanical properties [7, 12].

2.3 Fiber- and Matrix-Dominated Behaviour

The mechanical behaviour of composite materials is not only a function of the constituents and their arrangements, but also of the type and direction of loading. In this study, the type of loading considered is in-plane tensile loading, thus the discussion will be limited accordingly. The direction of applied loading relative to the orientation of the fibers will determine whether the composite exhibits fiber-dominated behaviour or matrix-dominated behaviour. Fiber-dominated behaviour suggests that the fibers have a greater influence on the polymeric composite stress-strain response, while the opposite is true for matrix-dominated composite behaviour. For example, a unidirectional PMC laminate with all plies oriented in the same direction, which is parallel to the loading direction as shown in Figure 6 (a), will clearly exhibit fiber-dominated behaviour. The same would be the case for a PMC woven-ply laminate with the loading condition shown in Figure 6 (b). Fiber-dominated materials typically exhibit linear stress-strain behaviour [13]. Conversely, the same woven-ply laminate with the warp fiber direction, 1, oriented at an angle θ to the applied load as shown in Figure 6 (c) will likely exhibit matrix-dominated behaviour. In this case, the properties of the matrix and perhaps the strength of the fiber-matrix interface cohesion will dictate the stress-strain behaviour (which would typically be nonlinear), the development of damage and the fracture behaviour of the material [14].

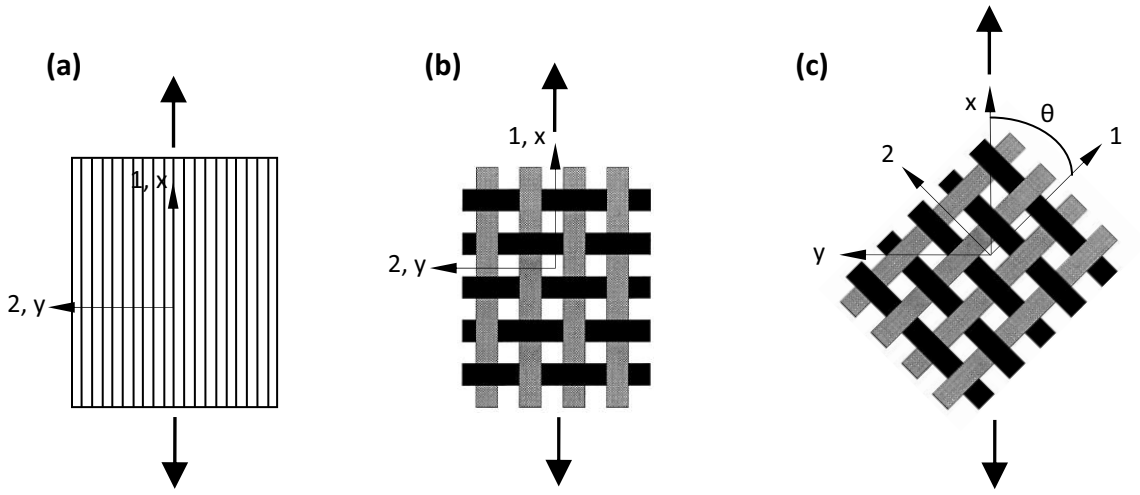

Figure 6. (a) Unidirectional laminate loaded in the fiber direction, (b) woven-ply laminate loaded in the warp direction, (c) woven-ply laminate loaded at angle θ biased from the warp direction.

Carbon fiber reinforced PMC materials that exhibit fiber-dominated mechanical behaviour are less susceptible to the effects of an elevated temperature environment. This is due to the fact that the carbon fibers are fairly stable at elevated temperatures. Note that the degradation of the matrix constituent will likely cause changes in its localized deformation behaviour, which may result in slightly altered macroscopic mechanical properties for fiber-dominated composites. Conversely, the mechanical response of matrix-dominated carbon fiber reinforced PMC materials is more vulnerable to environmental effects due to the deterioration or reduction of the matrix material properties [15]. The degradation of the matrix constituent will directly influence the composite mechanical behaviour, the degree of which depends on the specific matrix material and the actual testing temperature.

3 LITERATURE SURVEY AND BACKGROUND

The following sections present an in-depth literature survey and the applicable technical background regarding a number of aspects relevant to this study. First, a review of general fatigue theory will be introduced, followed by a literature survey of fatigue studies conducted on PMC materials. Next, a review on the influence of elevated temperature on polymer materials will be presented, followed by a literature survey of elevated temperature fatigue studies conducted on PMC materials. Since damage characterization is a central topic in this study, a discussion on fatigue damage characterization of various PMC materials will be presented, with a subsequent review of various damage monitoring techniques employed for PMC materials. Finally, a detailed literature survey on various types of fatigue models developed for PMC materials will be presented.

3.1 General Fatigue

As indicated in Chapter 1, structural components may fail when subjected to repeated loading well below the material ultimate strength, which is an important phenomenon for aerospace applications. This is true for almost all existing materials including metallic alloys, polymers and continuous fiber reinforced composite materials. Failure due to fatigue loading is caused by progressive localized damage which is induced by the fluctuating stresses (or strains). Fatigue loading in terms of fluctuating stresses will be considered in this discussion and within this study. Fatigue failure is typically initiated at a high stress concentration location caused by

a discontinuity, or, on the microscopic scale, at a location of a material defect. There are three main components of the applied load that will determine the extent of fatigue damage in materials. The first is the magnitude of the maximum applied stress that the material is subjected to, which may include stress concentrations due to notches or singularities in the material. This is typically measured in terms of a stress ratio R (= σ_{min} / σ_{max}). The second is the magnitude of the fluctuation in the applied stress or the stress range, and the third is the total number of repeated cycles, n. Note that other factors such as ambient temperature and moisture can also influence the material fatigue damage characteristics. Also note that for composite materials, the fiber type and geometric arrangement of the fibers will also influence the fatigue behaviour [16]. Typical repeated stress cycles have a fluctuation with a magnitude of σ_r, a stress amplitude of σ_a, and a mean stress of σ_{mean}. An ideal repeated stress cycle for tension-tension fatigue is shown in Figure 7. If the mean stress is equal to zero, the cycle is deemed completely reversed. The repeated stress cycle illustrated in Figure 7 is for an ideal case, where in some practical applications the stress cycles are typically random. However, for most fatigue studies including this study, this is the repeated stress cycle that is considered.

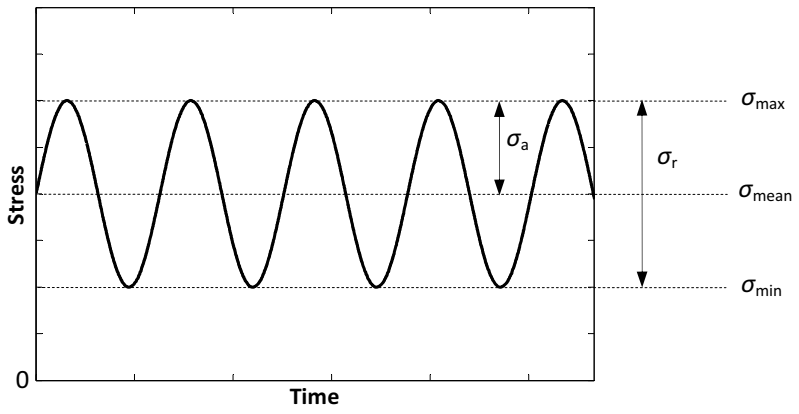

Figure 7. Ideal sinusoidal repeated stress cycle (tension-tension fatigue).

The stress-life or S-N curve is the most basic way to represent the fatigue data in terms of stress as a function of the number of cycles to failure (N_f). Maximum stress, σ_{max}, is typically plotted, however minimum stress or stress amplitude are occasionally plotted as functions of the log(N_f). Typical S-N curves are shown in Figure 8, where the various curves represent

different values of mean stress. An increasing mean stress has the effect of lowering the number of cycles to failure for a constant σ_{max} as shown. It is also clear that with a higher applied repeated stress, the number of cycles to failure will be much lower which represents the high-strain low-cycle fatigue (LCF) region on the S-N curve. Fatigue loading with a lower applied repeated stress will require more cycles before failure occurs which represents the low-strain high-cycle fatigue (HCF) region as indicated in Figure 8. Most materials exhibit different damage development and damage mechanisms in the HCF and LCF regimes, which ultimately controls failure for cyclic loading. The review by Harris [16] discusses these mechanisms for fiber reinforced PMC materials. For some metallic alloys, the S-N curve becomes horizontal at a certain limiting stress, which is deemed as the material endurance limit or fatigue limit. Below this limiting stress, the material can theoretically endure an infinite number of cycles without failure. This of course is an ideal situation, where even materials with fatigue limits can fail under cyclic loading with a stress below the limit if the material is also subjected to a high temperature or humid environment. Figure 9 depicts the S-N curves for common steel and aluminum alloys. As shown, steel typically has an endurance limit, while most non-ferrous alloys like aluminum do not have this limit [17]. Composite materials are typically not found to have a fatigue limit, however most fatigue studies are discontinued without cycling at lower stress levels, thus it is uncertain whether a true fatigue limit actually exists for many composites [16].

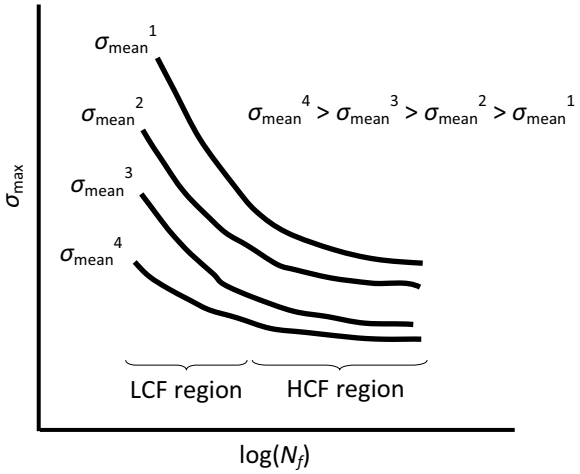

Figure 8. Schematic of typical S-N curves for different applied mean stresses.

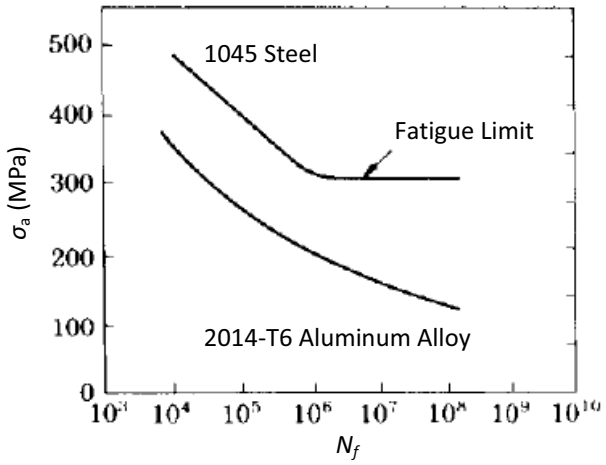

Figure 9. Common metallic alloy S-N curves [17].

For metallic alloys, determining the fatigue response and fatigue life for a component from available S-N curves has become common practice in many industries, including the aerospace industry. An S-N curve is often represented by an empirical logarithmic or power law relationship between the applied stress and the number of cycles to failure [18]. In addition, linear elastic fracture mechanics (LEFM) is often employed for metallic components to perform damage tolerance analysis in the aerospace industry. At the outset, researchers that studied the fatigue behaviour of non-metallic materials such as polymeric composites employed the same methods to predict fatigue life [19]. Although for some polymeric composites the same empirical methods used for metallic components may be satisfactory (i.e., analyses based on experimental S-N curves or LEFM), the fact is that damage mechanisms are significantly different for composite materials [16]. Therefore, there was (and still is) a requirement for developing common practice procedures for reliably predicting the fatigue behaviour and the fatigue life for PMC materials. As a result, other mechanical parameters such as the evolving material stiffness became indicators of fatigue damage development and criterion for fatigue failure prediction [20, 21]. A literature survey with focus on a number of studies conducted on fatigue of fiber-reinforced PMC materials will be presented in the subsequent section.

3.2 Literature Survey on PMC Fatigue

Conventional composites consist of two (or more) distinct constituent materials or phases at the macroscopic level, which are combined to form an inhomogeneous and anisotropic material. As a result, continuous fiber reinforced polymeric composites exhibit markedly different material behaviour relative to homogeneous and isotropic materials such as metallic alloys. This in turn makes it difficult to determine the fatigue properties and predict fatigue failure of continuous fiber reinforced PMC materials. Early research showed that fiber reinforced PMC laminates were superior to metals based on a fatigue life comparison [16]. In fact many researchers falsely believed that these composite materials did not suffer from fatigue failure, which initiated the use of composite materials for many industrial applications. After appreciable in-service use of composite structural components, it eventually became common knowledge that composite materials do not have the same fatigue failure mechanisms as metals. As a result, over the past four decades a number of studies have investigated the uniaxial in-plane fatigue behaviour of various un-notched unidirectional-ply continuous fiber PMC laminates, including unidirectional, cross-ply, angle-ply and quasi-isotropic lay-ups [20 - 50]. Most of these studies focussed on glass fiber or carbon fiber reinforced thermosetting epoxies. In recent years, a number of studies have focussed on the fatigue behaviour and characterization of continuous fiber reinforced woven-ply laminates [51 - 58], as well as other fabric reinforced laminates [59 - 63]. It should be noted however that there are few studies currently available in the open literature that have focussed on the fatigue behaviour and damage characterization of braided fabric composites [13, 64-68]. The following paragraphs will discuss the details of a number of the aforementioned fatigue studies.

Some of the initial fatigue studies on unidirectional-ply PMC laminates focussed on developing S-N curves and strength criteria for specific composites. Hashin and Rotem [22] developed macroscopic fatigue failure criteria for an elementary lamina, while Reifsnider and Gao [35] developed more general fatigue failure criteria. These and similar studies did not focus on the developing damage during cyclic loading, which is important to understanding and predicting fatigue behaviour of PMC laminates. It is well established that the complex damage patterns observed in unidirectional-ply laminates consist of matrix cracks, fiber fractures, fiber-

matrix interface debonding, inter-ply delamination cracks and their respective interactions. As a result, a number of researchers focussed on relating the observed damage or a damage parameter to the mechanical properties of the laminates. One of the initial approaches was to relate the strength of the material, or the residual strength, to the evolving damage state. Studies by Broutman and Sahu [23], Hahn and Kim [24], Rotem [27] and more recently Whitworth [44] investigated the residual strength of glass or carbon reinforced polymers. Since it was observed that fatigue induced damage progressively increased as the number of load cycles increased, the strength of the laminate would naturally decrease with increasing damage. A schematic of the strength degradation, or residual strength, for a laminate is shown in Figure 10. The hypothesis is that once the residual strength decreases to the magnitude of the maximum applied stress, failure occurs. The schematic process depicted in Figure 10 may be a realistic representation of the composite residual strength. Although the residual strength is a meaningful indicator for determining the extent of fatigue damage in composites, determining its magnitude requires destructive evaluation of test specimens which is not a practical approach.

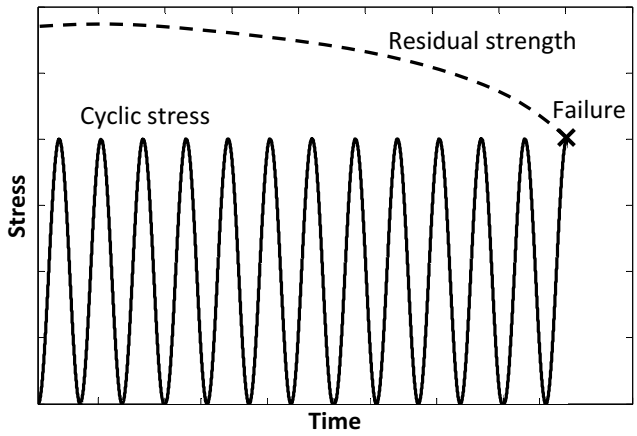

Figure 10. Schematic of strength degradation and applied stress leading to failure.

Another approach adopted by many researchers is to relate the residual stiffness of composite laminates to the evolving damage states. As PMC laminates accumulate fatigue induced damage, the stiffness typically decreases due to the added compliance in the laminate caused by the opening of the internal crack faces. Since Salkind [69] originally suggested that

changes in stiffness may be an appropriate measure of fatigue damage in composites, numerous researchers have investigated the effectiveness of residual stiffness as a measure of fatigue damage. Studies by Hahn and Kim [20] and O'Brien and Reifsnider [25] investigated the usefulness of the secant or dynamic modulus as an indicator of fatigue damage. Additional studies by Hashin [29], Hwang and Han [31], Whitworth [32, 33, 43], and Yang *et al*. [34] among others have considered the degradation of the fatigue or dynamic modulus as indicators of fatigue damage. Unlike the residual strength, the residual stiffness is a parameter that can be monitored non-destructively and thus be used to continuously track fatigue damage development. The residual stiffness can in fact be related to the residual strength as was investigated by Whitworth [32], which renders the residual stiffness as a practical indicator of fatigue damage.

In more recent years, other mechanical properties of cyclically loaded PMC laminates that can be monitored non-destructively have been investigated to determine whether they are appropriate indicators of fatigue damage development. Ellyin and El-Kadi [36] investigated the mechanical energy input during fatigue loading of glass/epoxy laminates. More recently, a similar study was conducted by Shokrieh and Taheri-Behrooz [48] on both glass/epoxy and carbon/epoxy laminates. Giancane *et al*. [50] monitored the energy dissipated on a cycle-by-cycle basis for cross-ply laminates, and correlated that with the development of fatigue damage. Petermann and Schulte [47] studied the evolution of the mean strain for angle-ply laminates and concluded that the mean strain was a more meaningful indicator of fatigue damage development. VanPaepegem *et al*. [70] investigated the effectiveness of the Poisson ratio as an indicator of fatigue damage development in unidirectional and cross-ply laminates.

In these studies, as well as the presented studies that considered the residual stiffness, an attempt was made to non-destructively monitor a particular material property and correlate that with the fatigue damage development. The material properties such as the residual stiffness are effective indicators of the evolving hysteretic material behaviour. A schematic of the typical evolution of a composite material stress-strain curve during stress-controlled tensile cyclic loading is shown in Figure 11. As shown, the slope of the stress-strain curve (i.e., dynamic stiffness) decreases from the initial cycle with a value of $E(1)$ to a value of $E(m)$ during cycle m,

which is a schematic of stiffness degradation. Note that the fatigue modulus of cycle k, $E_{\text{fatigue}}(k)$, is also shown for reference as this was considered by some researchers [31]. Shifting of the stress-strain curve (i.e., ratcheting deformation) has also been observed to occur in PMC materials during stress-controlled cyclic loading under a positive mean stress [49]. It is evident that the mean strain continuously increases during cycling, as is indicated by the mean strain for cycle m, $\varepsilon_{mean}(m)$. The increasing mean strain is not only a consequence of the stiffness degradation, but also in part due to stress-strain ratcheting. In fact, the evolution of the fatigue modulus also accounts for both stiffness degradation and ratcheting in its definition. Stiffness degradation is typically a result of damage accumulation. Ratcheting can be caused by damage accumulation resulting from crack faces not closing perfectly upon unloading [71], and potentially creep deformation [47]. Therefore, monitoring the fatigue modulus or the mean strain includes combined effects of fatigue damage and potential creep deformation. Also, the area enclosed by the stress-strain ellipses (i.e., energy dissipated) tends to change during cyclic loading [50]. Energy dissipated during cyclic loading also may be a result of both the damage development and local viscous deformation behaviour of the polymer matrix [72]. It should be noted that the evolving material hysteretic behaviour not only depends on the type of reinforcing fibers and their arrangement, but also on the loading parameters and the environmental conditions (e.g., ambient temperature or humidity).

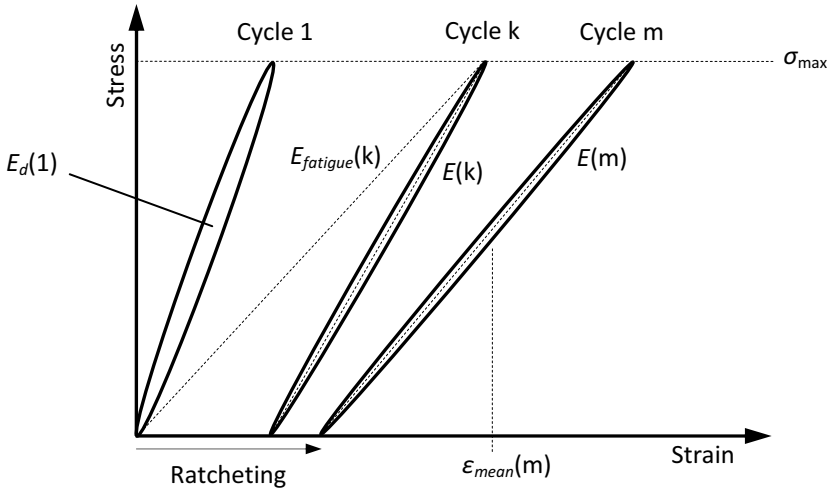

Figure 11. Schematic of evolving material hysteretic behaviour due to cyclic loading.

For the studies conducted on woven-ply and other textile fabric reinforced PMC materials, the dynamic stiffness is often considered as an indicator of fatigue damage accumulation [57, 59]. Studies by Pandita *et al*. [51] on plain woven-ply glass/epoxy laminates, and by Quaresimin [52] on 2x2 twill woven-ply carbon/epoxy laminates investigated the stiffness degradation during cyclic loading which was qualitatively correlated to the damage development. Tate and Kelkar [13] and Kelkar and Whitcomb [66] investigated the stiffness degradation and damage development in biaxial braided carbon/epoxy composites. Few similar studies on any other types of braided composites are available in the open literature. In fact, a comprehensive fatigue study on triaxial braided carbon reinforced PMC materials has not been published in the open literature.

3.3 Elevated Temperature Behaviour of Polymers

The use of composite materials for elevated temperature applications has considerably increased in recent years. Metal-matrix composites (MMC) and ceramic-matrix composites (CMC) have been successfully used for supersonic aircraft and space vehicle airframes, and for propulsion system components due to their excellent resistance to the effects of heat. As indicated however, the integration of polymeric composite materials into the propulsion systems of modern commercial and military aircraft has not experienced a great deal of advancement. A new generation of high glass transition temperature (T_g) polymers have been developed since the 1980's, which have been recently considered for jet engine composite component design. These elevated temperature PMC materials are candidates to replace MMC or CMC for components with service operating temperatures in the 150°C - 350°C range. Elevated temperature exposure of these PMC materials will undoubtedly add additional material property degradation effects, as well as the potential influence of local creep deformation on the fatigue damage mechanisms for long-term exposure. Understanding the behaviour of the polymer matrix at elevated temperatures is crucial for understanding the fiber reinforced composite behaviour at elevated temperatures, which is important for investigating the stiffness degradation (among other material properties) and its relationship to damage development during cyclic loading.

According to their molecular structure and behaviour, polymers are typically classified as being either thermosetting or thermoplastic. The main difference between these types of polymers is that thermosetting polymers have cross-linked molecular structures that contain strong covalent bonds, whereas thermoplastics consist of branched-chain molecules with weak intermolecular bonds [6]. Thermosetting polymers are created by an elevated temperature chemical reaction (i.e., curing or cross-linking) that is irreversible. Thermosetting polymers are more often used to manufacture composites in the aerospace industry, thus the following discussion will focus on thermosetting polymers. Some examples of conventional thermosetting polymers often used for manufacturing fiber reinforced composites are epoxies, polyesters, phenolics and silicone. At room temperature, thermosetting polymers typically exhibit glassy (brittle) behaviour, whereas at elevated temperatures near their T_g they typically begin to exhibit rubbery (viscoelastic) behaviour. This is exemplified through a schematic plot of the logarithm of the modulus as a function of temperature as shown in Figure 12. At temperatures well below the T_g, thermosetting polymers have an almost constant modulus. The modulus begins to notably decrease as the glass-transition temperature is approached. Note, however, that there is typically a small reduction in the modulus due to the highly cross-linked molecular structure of thermosetting polymers. The time-dependent or rate-dependent behaviour of thermosetting polymers is schematically illustrated in the stress-strain plots of Figure 13 (a). Some thermosetting polymers can also exhibit the time-dependent or viscoelastic stress-strain behaviour depicted in Figure 13(a) at temperatures well below their T_g [73]. Typical creep behaviour of polymers is illustrated in Figure 13(b), which is the strain response over time of a polymer with a constant applied tensile stress.

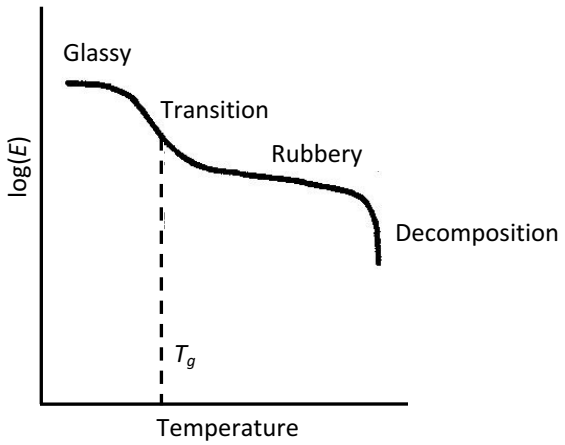

Figure 12. Schematic of thermosetting polymer modulus variation with temperature.

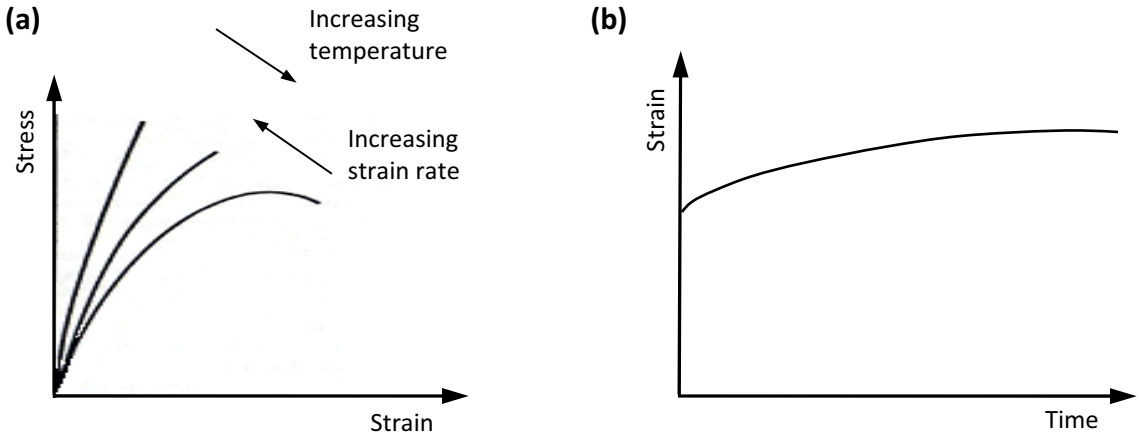

Figure 13. Schematic of thermosetting polymer (a) stress-strain variation with temperature and strain rate, (b) constant tensile stress creep response.

In order to improve the elevated temperature capabilities and increase the service temperature limits of thermosetting polymers, the T_g can effectively be increased. As indicated, a number of high T_g thermosetting polymers have been developed in recent years. One of the commercially available polyimide resins that was initially developed by NASA is PMR-15 [74], which has been employed in some aerospace structural applications. Due to the successful development and wide regard of PMR-15, additional polyimide resins were subsequently developed for high temperature composite applications. NASA also developed AMB-21 [75], DMBZ-15 [76] and RP46 high temperature resins. These thermosetting polyimide resins have

similar properties and temperature capabilities as PMR-15, but without the hazardous carcinogenic compounds. Dupont developed a thermoplastic polyimide Avimid K3B, which has been considered for supersonic transport aircraft [77]. A number of additional polyimide resins such as R1-16, PETI-5 and PIXA have also been considered for PMC components on supersonic aircraft [5]. Finally, a number of high temperature BMI resins have also been developed and used in the industry. Common BMI resins include 5250 and 5260 developed by Cytec Engineered Materials, as well as F655-2 developed by Hexcel Corporation. These BMI resins were designed for high temperature applications, as well as for processing using RTM [78] which is an advantage over many polyimide resins. A list of the glass transition temperature ranges for conventional epoxies, BMI and polyimide thermosetting polymers is shown in Table 3, which also includes the T_g for some specific resins. As shown, the glass transition temperature range, and thus the service temperature range, is significantly higher for BMI and polyimide resins relative to conventional epoxies. Although a number of high temperature polymers and their respective fiber-reinforced composites have been developed, there has been little use of these materials in high temperature primary load bearing aerospace applications. The subsequent section outlines some noteworthy studies focussed on elevated temperature fatigue of fiber reinforced PMC materials.

Table 3. Typical thermosetting polymer glass transition temperatures.

Thermosetting Polymer	T_g (˚C)
Epoxy	100 - 200
BMI	230 - 290
5250	270
Polyimide	300 - 450
PMR-15	370
RP46	310

3.4 Literature Survey on PMC Elevated Temperature Fatigue

Most PMC elevated temperature studies available in the open literature focus on temperature-dependent material property degradation during static or isothermal aging

conditions. There are few studies that consider fatigue loading at elevated temperatures, as is indicated in the review by Montesano *et al*. [79]. High temperature exposure during cyclic mechanical loading undoubtedly augments the matrix material behaviour and the development of damage mechanisms due to the potentially complex thermo-mechanical interactions. Additional property degradation mechanisms such as physical and chemical aging may also continuously alter the composite properties with time, specifically impacting the polymer matrix behaviour. The influence of the time-dependent material behaviour on the fatigue damage mechanisms will be more significant at severe operating temperatures. This may in fact also be the case at temperatures well below the T_g of the polymer matrix for particular composites [80]. Although the temperature sensitivity of the polymer matrix ultimately governs the microscopic behaviour of a fiber reinforced PMC material, the macroscopic cyclic behaviour at elevated temperatures is still primarily dictated by the arrangement of the reinforcing fibers relative to the loading direction. Therefore, the degree of influence that an elevated temperature environment has on the composite behaviour is strongly, but not entirely, dependent on whether the material exhibits fiber-dominated or matrix-dominated behaviour (see Figure 6). This will be further discussed in the following paragraph.

Some studies that focussed on the elevated temperature tensile fatigue behaviour of unidirectional-ply PMC materials have been reported during the last two decades [5, 81-90]. Most of these studies consider carbon/polymer laminates with various lay-ups such as unidirectional, cross-ply, quasi-isotropic and angle-ply. Studies by Uematsu *et al.* [83] and Sjogren and Asp [86] correlated the growth of delamination cracking with temperature for unidirectional composites subjected to cyclic loading. Both studies concluded that elevated temperatures accelerated delamination crack growth rates, and that the influence of temperature was mainly manifested through localized viscoelasticity at the crack tips. A similar study by Gregory and Spearing [88] also reported that fatigue delamination crack propagation rates were higher at elevated temperatures, but the quasi-static fracture toughness was in fact higher for the laminate at elevated temperatures. A similar study by Uematsu *et al.* [90] was later conducted with a PMR-15 unidirectional composite. They found that there was absolutely no creep or time-dependent effects on the composite behaviour during fatigue at 300°C. It

should be noted that in all four studies, double cantilever beam and/or flexure test specimens were used to propagate delamination cracks. It is therefore unclear from the literature whether or not delamination cracks will have the same influence during uniaxial cyclic loading. A study by Shimokawa *et al.* [5] on quasi-isotropic BMI laminates and by Sun *et al.* [87] on unidirectional and cross-ply epoxy laminates showed that fatigue tests at elevated temperatures had minimal effects on the resulting S-N curves when compared to the S-N curves obtained for the same laminates at room temperature. The specimens in these studies exhibited fiber-dominated behaviour. A similar study by Branco *et al.* [82] on glass/phenolic unidirectional composites reported that an elevated temperature environment had a slight influence on the exhibited stiffness degradation. A study by Kawai *et al.* [85] on a series of unidirectional (on-axis) and angle-ply (off-axis) polyimide and epoxy laminates revealed that temperature notably influenced the S-N curves for the off-axis tests, but did not notably affect the S-N curves for the on-axis tests. It was also reported that matrix ductility was enhanced at elevated temperatures, but fiber-matrix bonding was weaker. Clearly, the fiber-dominated composites are not nearly as influenced by the elevated temperature relative to the matrix-dominated or off-axis composites.

Few elevated temperature fatigue studies on woven-ply laminates have been reported in the literature [15, 72, 91-93]. Gyekenyesi *et al.* [91] studied the elevated temperature fatigue behaviour of a satin woven carbon/polyimide laminate, while Shimokawa *et al.* [93] studied a plain woven carbon/epoxy laminate. Both studies concluded that the elevated temperature environment had minimal influence on the fiber-dominated laminate fatigue behaviour. A similar study by Kawai and Taniguchi [15] on on-axis and off-axis plain-woven carbon/epoxy laminates reported that the off-axis specimens were significantly influenced by elevated temperatures, while the influence was notably less for the on-axis specimens. A study by Montesano *et al.* [72] on off-axis satin woven carbon/BMI laminates also reported a strong influence of temperature on the stiffness degradation, ratcheting and energy dissipation behaviour during cyclic loading. Similar to the unidirectional-ply laminates, the off-axis woven-ply laminates are notably influenced by elevated temperatures due to their matrix-dominated configurations. Note that until the present date, there are no studies in the open literature that

focus on elevated temperature fatigue of any type of braided PMC material. Since the general material behaviour and microscopic damage development will vary for a braided composite compared to either unidirectional-ply or woven-ply laminates, a study on braided composites is consequently required. Details of the development of fatigue damage for various types of PMC materials will be discussed in the following section.

3.5 Fatigue Damage Characterization Theory

For many homogeneous and isotropic materials such as metallic alloys, the damage processes that lead to fatigue failure are well established and understood. For metallic alloys, it has been commonly observed that fatigue damage occurs in four main stages: crack initiation, stage I crack growth, stage II crack growth, and rapid crack growth leading to ultimate ductile failure [17]. Crack initiation in a metallic alloy can be caused by the existence of second-phase particles or micro-voids. Although the macroscopically applied stress may be elastic, local plastic deformation will cause dislocations to slip. Dislocation pile-ups can occur at the location of these second-phase particles or micro-voids, which causes high localized stresses and the formation of micro-cracks. Stage I crack growth or slip-band crack growth involves the deepening of the initial crack on planes of high shear stress (i.e., inter-granular crack propagation). Stage II crack growth involves the growth of a well defined crack in the direction normal to the loading axis (i.e., trans-granular crack propagation). The final stage involves the propagating crack reaching a critical length so that the remaining section cannot support the load, which leads to rapid crack propagation and ultimately component failure. Although micro-cracks initiate in metallic alloys subjected to cyclic loading, one main crack eventually forms and propagates which leads to failure. Methods based on LEFM are typically employed to predict the crack propagation rates during cyclic loading [17].

For inhomogeneous and anisotropic materials like continuous fiber reinforced polymeric composite materials, the fatigue damage processes are much more complex. Microscopic damage is observed to be widespread or diffused throughout the materials [16], and not only locally in the eventual fracture region as is observed in metallic alloys. Damage commences after only a few load cycles, thus there is gradual stiffness loss in the damaged areas of the

material which leads to a continuous redistribution of localized stress during cyclic loading. The accurate prediction of the fatigue behaviour, and thus the fatigue life, is consequently a difficult task. Moreover, many different damage mechanisms are observed in PMC materials which are strongly dependent on the type of fiber arrangement and the particular lay-up for laminated composites. The interaction of damage modes can also significantly influence the crack development states and ultimately the fatigue performance. In addition, the reinforcing fibers may act to mitigate cracking in the matrix material, which will also directly influence the fatigue behaviour. For this reason, fracture mechanics-based methods are typically not applicable to fiber reinforced PMC materials. Since fatigue damage is cumulative in PMC materials, damage mechanics-based methods are typically employed. Schematic plots of the quantitative damage development as a function of the number of loading cycles for monolithic and composites materials are shown in Figure 14. As indicated, cracking during the early part of cycling for metallic alloys occurs with a very low growth rate, after which a single dominant crack begins to propagate. In composite materials, damage begins to accumulate extensively early on during cycling and continues through until specimen failure occurs. This is a direct consequence of the local heterogeneity of composite materials and the mismatch between the fiber and matrix constituent material properties. The matrix constituent typically has a much lower strength compared to the reinforcing fibers. Thus, upon the initial application of a cyclic load local cracking in the matrix occurs throughout the composite. Local stress concentrations at the fiber-matrix interfaces also cause interface crack initiation upon the application of loading.

The mechanisms of fatigue crack growth and initiation are quite complex in composite materials. In order to understand why fiber reinforced polymeric composite materials fail when subjected to cyclic loads below their ultimate strengths, an in depth characterization of their physical microscopic damage development processes is imperative. Regardless of the reinforcing fiber arrangement, all fiber reinforced PMC materials will exhibit three basic modes of localized damage: cracking in the matrix constituent, fracture of the fibers and fiber-matrix interfacial debonding [16]. A schematic of these common localized damage modes is shown in Figure 15 (a)-(c). Fracture of individual fibers can typically be characterized as non-progressive due to their sudden fracture behaviour. This is due to the brittle nature of many conventional

fibers such as carbon or glass which deform elastically until they reach their respective failure strains. Matrix cracks and interfacial debonding cracks are progressive in nature, and their propagating length depends on the number of applied loading cycles. As indicated, polymer matrix materials are much weaker than their reinforcing fibers, thus local stress concentrations which cause high local strains in the matrix during cyclic loading initiate cracking. Interfacial debonding cracks are a result of high shear stresses at the fiber-matrix interfaces due to the mismatch of the fiber and matrix material properties. Additional damage modes and the interaction of these damage modes will depend on the specific fiber arrangement, as will be discussed in the following paragraphs.

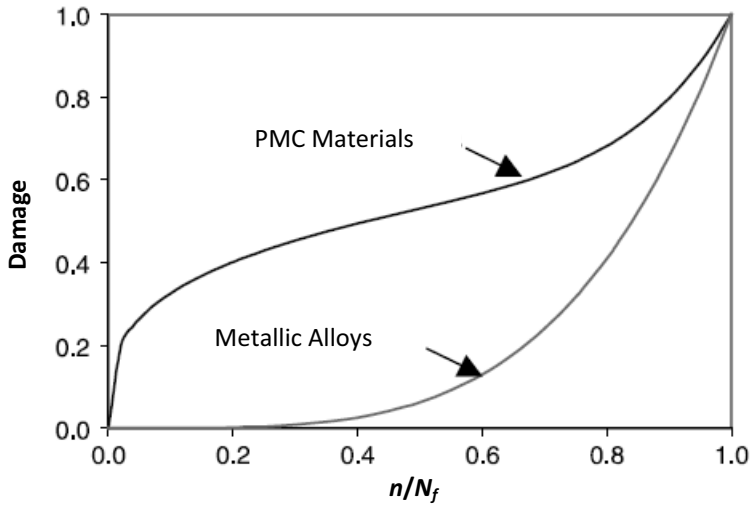

Figure 14. Schematic of damage parameter development for PMC and metallic alloys.

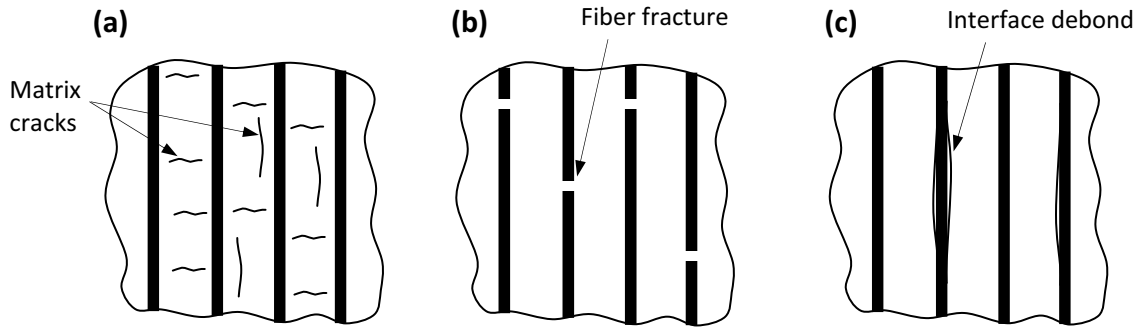

Figure 15. Localized damage schematics of (a) matrix cracking, (b) fiber fracture, (c) fiber-matrix debonding.

Damage characterization of unidirectional-ply PMC laminates has been somewhat well established over the past few decades. The study by Salkind [69] was one of the first reported studies which characterized fatigue damage in fiber reinforced PMC laminates. In addition to the localized modes of damage such as matrix cracking, fiber fracture, and interfacial debonding (see Figure 15), additional damage modes include inter-ply cracking (i.e., delamination) between adjacent plies caused by shear stresses at the ply interfaces. The orientation of the matrix cracks within the laminate plies depends upon the orientation of the ply with respect to the loading direction. Plies oriented along the loading direction tend to develop matrix cracks normal to the fibers in the transverse direction, as well as splitting type cracks along the fiber direction (often at the fiber-matrix interfaces). Plies oriented transverse to the loading direction develop matrix cracks in the transverse direction along the direction of the fibers (often at the fiber-matrix interfaces), while off-axis plies also typically develop matrix cracks that initially propagate perpendicular to the applied load and then along the fiber directions. Matrix cracks within all the plies of laminates typically develop during the early stages of cycling, often after the very first loading cycle [94], and are generally the first form of damage observed in a laminate along with fiber-matrix interfacial debonding. In a multi-orientation laminate, the transverse and off-axis plies will typically exhibit significantly more cracking relative to the on-axis plies. Matrix cracks will often propagate until they reach a fiber-matrix interface and either cause the failure of the fiber for a weak fiber [95], or continue to propagate along the fiber-matrix interface as an interfacial debond due to high shear stresses. Matrix cracks typically extend through the entire thickness of a ply and are generally unable to propagate into the adjacent ply, particularly if that ply orientation is different. These arrested cracks generate high localized stresses at their tips, which provide favourable conditions for initiating inter-ply delamination cracks [6]. An image of extensive matrix cracking in the transverse plies of a cross-ply laminate are shown in Figure 16 (a), while Figure 16 (b) shows the propagation of a delamination crack initiated at the tip of a matrix crack in a transverse ply.

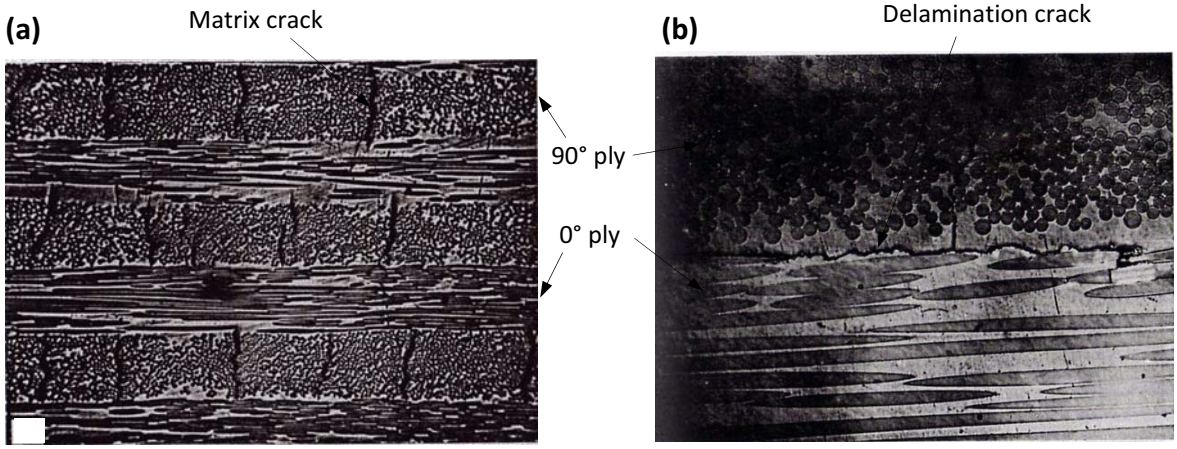

Figure 16. Cross-ply laminate (a) transverse ply matrix cracks, (b) delamination and matrix crack interaction [6].

The progression of fatigue damage in unidirectional-ply laminates typically begins with extensive matrix cracking in off-axis and/or transverse plies during the initial stage of cycling, which is accompanied by the growth of interfacial debonding cracks. Additional fiber-matrix debonding cracks will then form, as well as inter-ply delamination cracks, which initiate and propagate during the second stage of cycling which is a long portion of the laminate fatigue life. Splitting type cracks will also form during the latter part of the second stage of cyclic loading, weakening the on-axis plies. This eventually leads to a localized region of high crack accumulation which induces local fiber fracture, which ultimately causes the final failure event during the third stage of cycling. It was in fact reported by Highsmith and Reifsnider [26] that many laminates, including cross-ply laminates, reach a state of damage saturation by the end of the first stage of cyclic loading, which was deemed a characteristic damage state (CDS). Matrix cracks within the transverse plies gradually propagate and eventually arrest at the ply interfaces and at fiber locations. When these transverse cracks reach a state in which the crack spacing is consistent, the CDS has been achieved. Thereafter, the existing cracks within a transverse ply act to reduce the stress locally which inhibits any further crack development within the ply. As a result, delamination cracks between adjacent plies begin to propagate after the CDS is attained. A schematic of the discussed development of fatigue damage for cross-ply laminates is shown in Figure 17. The events corresponding to the aforementioned three stages of cyclic loading and to the damage parameter profile are indicated. Note that the laminate

sketches shown in Figure 17 are of a plane perpendicular to the transverse plies. The study by Cain [96] discussed damage scenarios for particular unidirectional-ply laminate lay-ups. Also, the study by Hahn and Kim [20] discussed the overview of damage development in quasi-isotropic laminates and the first-ply failure phenomenon. In both studies, the damage mechanisms discussed in the previous paragraph contribute to the overall laminate damage development and failure events.

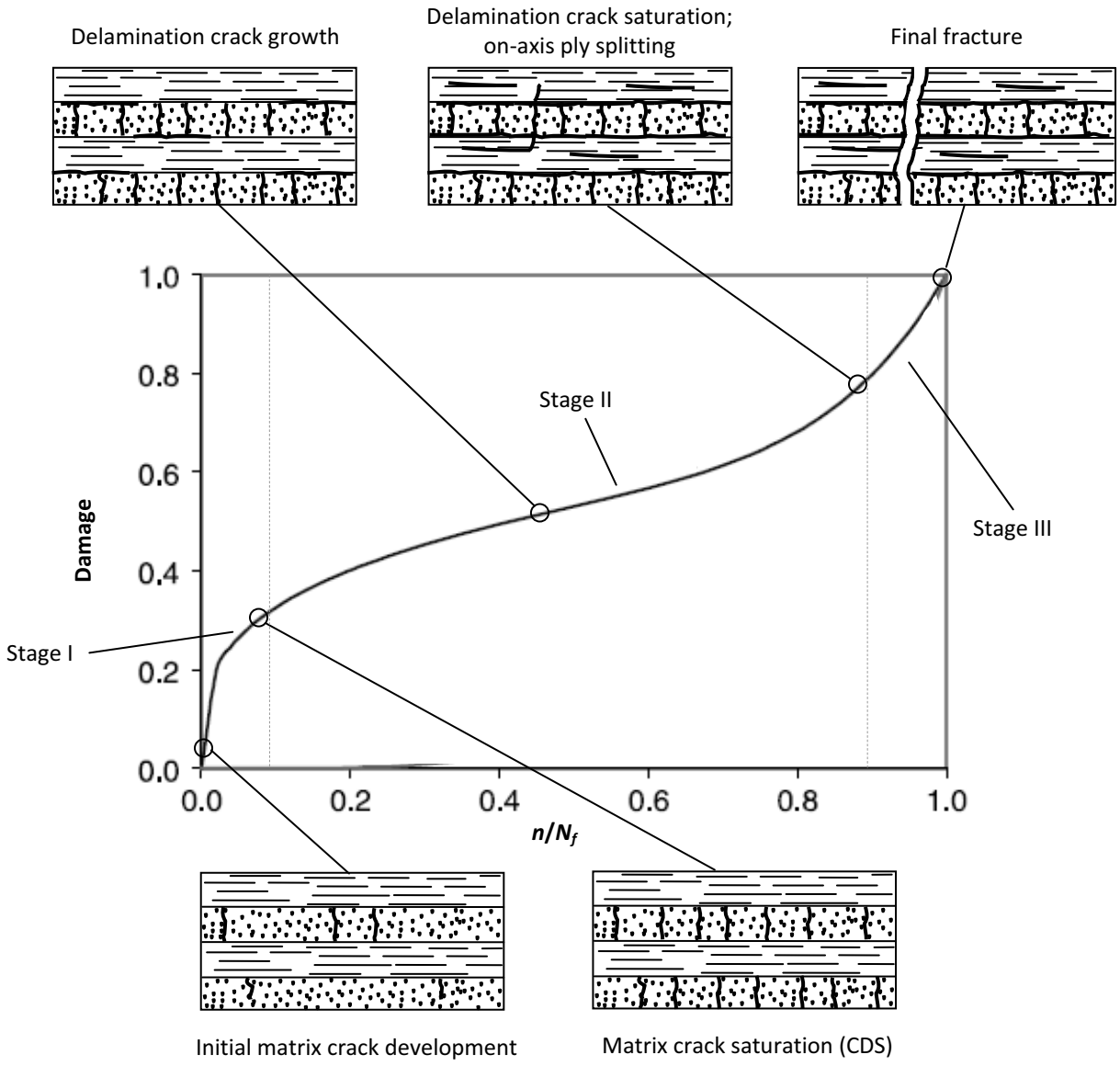

Figure 17. Schematic of fatigue damage development for a cross-ply laminate.

Fatigue damage characterization of woven-ply laminates has not been as widely studied as for unidirectional-ply laminates. The orientation of the crimped woven fiber yarns in the warp and weft directions undoubtedly influences the development of fatigue damage and the type of damage mechanisms observed. The specific type of weave pattern (i.e., plain weave, 2x2 twill weave, satin weave) will also influence the progression of fatigue damage. As with unidirectional-ply laminates, localized matrix cracking, fiber fracture and interfacial debonding are also observed in woven-ply laminates (see Figure 15). However, the development of these localized cracks does significantly change for woven laminates. Some studies that focussed on the on-axis tensile fatigue behaviour of woven laminates have shown that extensive cracking in the weft (or transverse) yarns and notable intra-ply debonding (or meta-delamination) between adjacent fiber yarns are commonly observed damage mechanisms [51, 52]. Cracks in the weft yarns are observed to be a combination of series of local matrix cracks and fiber-matrix interfacial debonds, which have formed into a continuous crack propagating along the fiber yarn axis and through the thickness of the yarn [51, 97]. The initiation of cracks within the weft yarns are due to the high localized stresses at the fiber-matrix interfaces and the stress concentrations within the matrix. Since the weft fiber yarns are normal to the applied load, weft yarn cracks tend to propagate as mode I cracks (i.e., opening mode). Weft yarn cracks were also observed to propagate into adjacent matrix-rich zones, and also combine with weft yarn cracks in adjacent weft yarns [97]. The intra-ply debonding cracks are mainly observed to initiate at the tip of weft yarn cracks, and are due to the high stress concentrations at the crack tips. These cracks propagate as mode II cracks due to the shear stresses generated between the warp and weft yarns at the yarn crossover locations. Few inter-ply delamination cracks and warp yarn cracks were observed for on-axis woven laminates, while fiber fractures only occurred prior to failure [52]. A study by Montesano *et al.* [14] also found that there were few delamination cracks throughout the duration of cyclic loading for a satin woven laminate, but reported notable cracking in the warp yarns propagating like splitting type cracks. A schematic of the expected development of fatigue damage based on the discussed damage mechanisms for on-axis plain woven laminates is shown in Figure 18. Note that the crack scenarios shown in Figure 18 are with respect to a plane perpendicular to the weft yarns (i.e., parallel to the

applied tensile load). Studies on tensile fatigue of off-axis woven laminates [51, 52, 97] have reported that cracking occurs in the off-axis warp and weft yarns, while fiber yarn reorientation leads to localized delamination and ultimately fiber fracture.

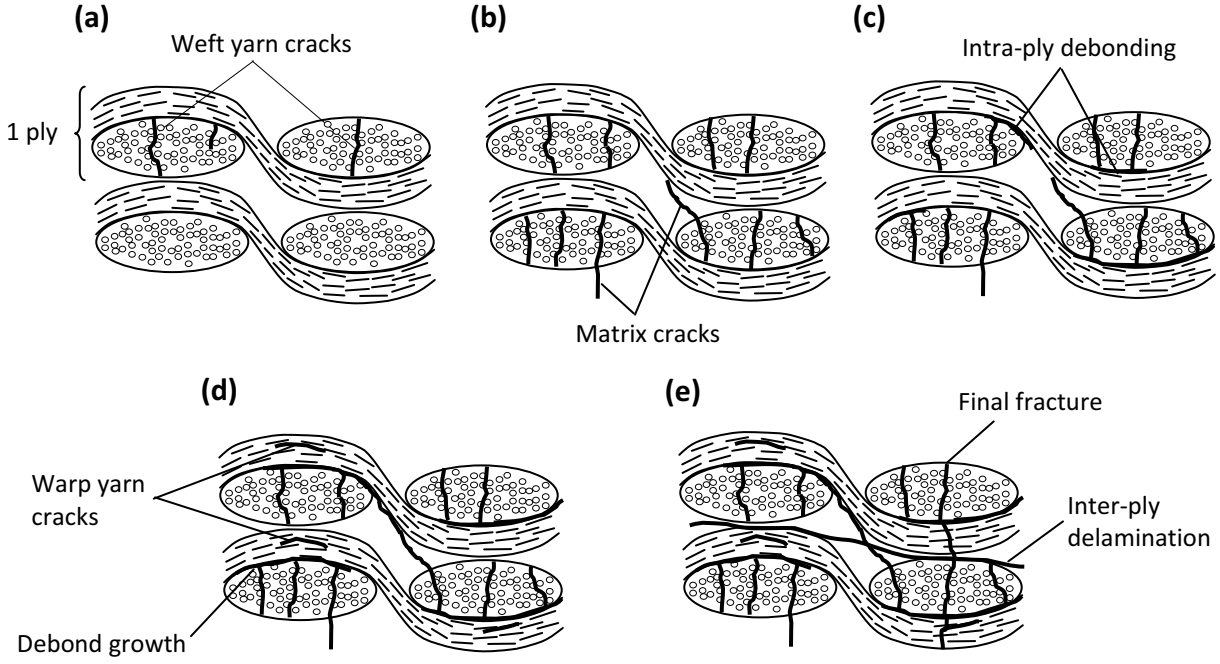

Figure 18. Schematic of fatigue damage development for an on-axis plain woven laminate from weft yarn crack initiation (a) to final fracture (e).

Although braided fabric resembles woven fabric, the damage mechanics concepts of woven composites cannot be directly applied to braided composites. This is due to the fact that woven fabrics contain fiber yarns in only the warp and weft directions (i.e., 0˚ and 90˚ directions), whereas braided fabrics contain yarns that are oriented in the +θ/-θ directions, as shown in Figure 3 (a) and (b) respectively. For the case of braided composites, very little work has been reported on fatigue damage characterization and the correlation between the evolving microscopic damage and macroscopic properties such as stiffness. Studies by Tate, Kelkar and Whitcomb [67] and Kelkar and Whitcomb [66] characterized the fatigue behaviour of biaxially braided carbon/epoxy composites. The studies reported that notable stiffness degradation was exhibited by the biaxial braided composites; however, the studies did not report any details of the observed microscopic damage mechanisms. A similar study by Huang *et al.* [68] on biaxial braided carbon/epoxy composites reported that splitting in the braider

yarns and delamination was found at the fracture surface when the biaxial braided composites were subjected to certain maximum stresses. However, the study only reported observations made at the fracture surface and did not attempt to characterize the progression of damage during the tension-tension fatigue tests. A study by Burr and Morris [64] on two-dimensional triaxial braided graphite/epoxy composites reported that during tension-tension fatigue testing in the warp direction, cracks within the braider yarns and cracking in the matrix rich-regions were the first visible damage mechanisms. At latter stages in cycling, the axial yarns began to disbond from the surrounding constituents, which occurred until specimen failure which involved rapid fracture of the axial fiber yarns. There was however no direct correlation between the observed damage development and the exhibited stiffness loss. Clearly, additional research is required for characterizing tension-tension fatigue damage development in triaxial braided composites.

A depiction of the observed or expected damage modes in triaxial braided composites loaded in the warp direction can still be made at this stage based on the limited observations reported in the literature. Since braider yarns are oriented in an off-axis direction, damage within these yarns during tensile fatigue loading will include cracking in the matrix-rich zones and fiber-matrix interface debonding within the yarns. This is due to the high stress concentrations in the matrix and at the fiber-matrix interfaces within the fiber yarns. These type of cracks have been extensively observed in braided composites subjected to tensile static loading [98, 99], and are schematically shown in Figure 19 for a 2x2 triaxial braided composite. The braider yarn cracks would tend to propagate as mixed mode I and mode II cracks along the braider yarn axis, due to the local perpendicular tensile loading and shear loading on the crack faces. Cracks in the braider yarns are in fact a combination of a series of local matrix cracks and fiber-matrix interfacial debonds, which have formed into a continuous crack propagating along the fiber yarn axis and through the thickness of the yarn [99] as shown in the figure. Cracking in the warp yarns may also occur, which is analogous to splitting type cracks in unidirectional laminates. Note however that due to crimping of the warp yarns caused by the braiding process, cracking in the warp yarns may be limited in appearance. This in fact was observed by Masters and Ifju [99]. Local cracking at the braider yarn and warp yarn interfaces (i.e.,

debonding) have also been reported in the study by Burr and Morris [64], and are shown schematically in Figure 19. These may in fact be initiated at the locations of the braider yarn cracks due to the high stresses at the crack tips [100]. Interfacial debonding cracks will propagate as mixed mode II and mode III cracks due to the high shear stresses at the warp yarn and braider yarn crossover locations. The development of large delamination cracks, or large-scale debonding, between the braided layers is another potential damage mechanism. The study by Ivanov *et al.* [100] reported that there was no preferential role of the edges in inducing damage and there were no large-scale delaminations observed during tensile static loading. This in fact was also reported in the study by Masters and Ifju [99]. Cracks may also develop in the resin-rich zones between fiber yarns, which is shown in the figure. The main damage modes identified in triaxial braided composites are: (i) cracks propagating within the braider yarns in the matrix and at the fiber-matrix interfaces, (ii) matrix cracks propagating within the resin-rich zones between fiber yarns, (iii) cracks propagating at the interfaces between adjacent fiber yarns, and (iv) cracks propagating within the warp yarns. These damage modes will hereafter be referred to as braider yarn cracks, matrix cracks, interface cracks, and warp yarn cracks, respectively. Since fatigue damage characterization for a triaxial braided composite is one of the main focuses in this study, additional discussions will be presented in Chapter 5.

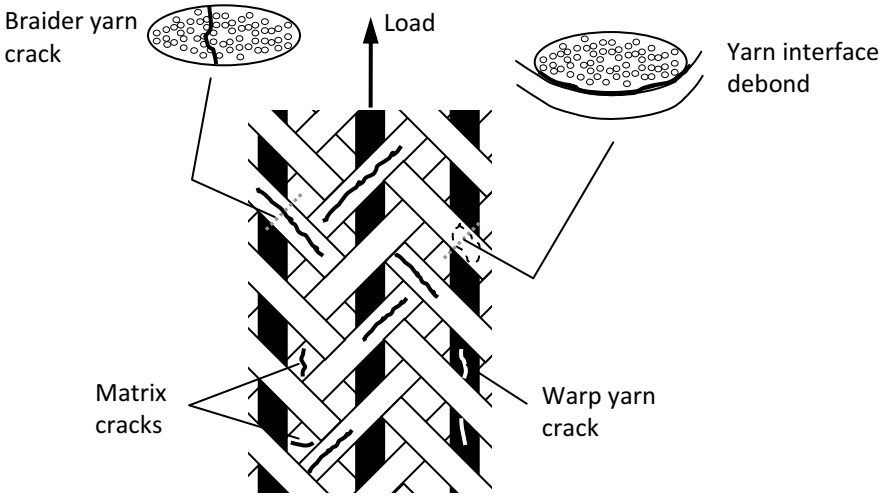

Figure 19. Schematic of fatigue damage mechanisms for a 2x2 triaxial braided composite.

The evolution of damage in textile fabric reinforced composites is notably more complex compared with unidirectional-ply laminates as was shown in Figure 18 and Figure 19. The influence of the observed damage mechanisms on the textile composite material properties (such as stiffness) during cyclic loading is an area of research that requires much needed attention. In order to investigate the damage development during cyclic loading, non-destructive techniques must be employed. The following chapter presents a number of non-destructive evaluation (NDE) techniques that have been adopted by many researchers, with an emphasis on the techniques to be used in this study.

3.6 Literature Survey on Damage Monitoring Techniques

Damage monitoring or damage detection is one of the biggest challenges in determining the damage events that lead to failure in composite materials. There have been numerous destructive and non-destructive techniques applied for detecting damage in PMC materials. Applying these techniques during fatigue loading presents additional difficulties, while fatigue testing at elevated temperatures poses even more complications. The subsequent paragraphs provide a literature survey on NDE damage monitoring techniques that have been employed for PMC materials, and their relevance for fatigue testing at elevated temperatures. Extensive detail will be provided for the particular NDE techniques used in this study.

Many techniques exist that can detect actual damage in PMC materials such as matrix cracks, while other techniques simply monitor material properties in order to follow the evolution of damage. As discussed in Section 3.2, residual strength measurements and monitoring of the residual stiffness can be used as indicators of damage during cyclic loading. Also, monitoring the electrical resistance of components can yield insight on the evolving damage state of a material. For detecting the actual damage mechanisms, various optical, acoustic, radiographic, thermographic, and local strain-based methods have been successfully employed for PMC materials. One of the first established techniques for monitoring damage development in PMC materials was x-ray radiography, which has been adopted in many fatigue studies [101-105]. To employ x-ray radiography, a liquid penetrate such as iodine must be injected into the sample every time an x-ray image is obtained. This requires damage

propagation from a surface or an edge, which is why this technique is often employed for notched test specimens. This is however limiting because if the liquid penetrate does not reach the damage 'cavities' or if the damage zone is not known *a priori*, damage may go undetected. There are also obvious health risks if using a toxic penetrate, and through x-ray exposure. In spite of its limitations, x-ray radiography has been employed to successfully detect matrix cracking and delamination in cross-ply and quasi-isotropic laminates [103, 104]. Another well established NDE technique is ultrasonic scanning, including c-scanning and a-scanning, which have also been extensively employed for many fatigue studies [106-109]. These techniques require either pulse-echo or through-transmission coupled transmitter/receiver sensors to be placed on the specimen surface(s). The transmitted or reflected acoustic waves will undergo a change in amplitude if damage is present in the material. These ultrasonic techniques were successfully employed for detecting matrix cracking and delamination in laminates, but the poor resolution of the obtained images makes it difficult to distinguish certain damage modes which limits the usefulness of this technique.

One of the main drawbacks with radiographic and ultrasonic NDE techniques is that they cannot be employed in-situ since the test specimen must be removed from the test apparatus for the methods to be used. As a result, additional NDE techniques were developed for PMC materials with in-situ capabilities such as light microscopy (LM), acoustic emission (AE), infrared thermography (IRT), and edge replication (ER). Light microscopy has been effectively used to visualize matrix cracks and delamination zones in a number of studies [59, 60, 110-113]. The technique effectively involves illuminating the sample on one surface which allows light to penetrate through it, while using a high resolution microscope and camera to capture images of the opposite surface. Although light microscopy can be very effective in visualizing actual cracks, its application is limited to glass fiber reinforced PMC materials with a relatively transparent matrix. It has not been used for detecting damage in carbon fiber reinforced PMC materials, and may be difficult to apply in a high temperature environment without pausing the test. AE has also become an established NDE technique for PMC materials, being successfully employed for detecting fatigue damage in PMC materials [58, 113-115]. Sensors are coupled to the specimen surfaces in order to detect acoustic noise emitted during the development of

damage processes. Although all forms of damage have been reported to be detected using AE, the sensitivity of the sensors to ambient noise (including the loading machine) make characterization of the unfiltered signals very difficult. Also, distinguishing the different forms of damage from the varying acoustic intensity levels is very difficult. Equally difficult is the task of coupling the sensors to the specimen surface in a high temperature environment.

Another technique that can be employed to continuously monitor fatigue damage development in-situ for any type of material in a non-contact manner is IRT. A number of studies have successfully employed IRT techniques to monitor damage development in PMC materials [56, 60, 113, 116-118]. IRT is a measurement technique that relies on the use of an infrared (IR) camera to provide a time-dependent contour map of the surface temperature (i.e., thermographs) of the material under investigation. This technique involves decoding temperature information which results from the IR radiation emitted by an object. Post-processing software is typically employed to process the captured images. There are two main types of IRT techniques regularly employed for composite materials: active thermography and passive thermography. Active thermography involves actively heating the specimen to monitor the temperature gradients during heating or cooling using an IR camera. Since damage initiation and propagation events during both static and cyclic loading are associated with the release of energy in the form of heat, passive thermography is an alternate approach that has gained considerable attention for damage detection of composites subjected to cyclic loading [56, 60, 113, 118]. Passive IRT is an effective tool for indirectly monitoring damage development in real-time over a large surface area. One of the main drawbacks with passive IRT is that small-scale damage cannot always be detected, which is limited by the pixel resolution of the IR camera. The passive approach is ideal for cyclic loading because the resulting hysteretic heating allows for a time-dependent temperature variation which can be monitored with the IR camera. The recorded images can then be analyzed to determine the material fatigue strength or to understand damage initiation and development. Analyzing thermographic images can however be a challenge since the detected temperature rise may be due to a number of different factors. For composite materials subjected to cyclic loading, intrinsic energy dissipation caused by internal irreversible mechanisms such as damage development and local

viscous heating of the matrix will be detected as heat dissipation by the IR camera. A passive IRT technique is employed in this study, and will be further discussed in Chapter 4.

An additional well established NDE technique for detecting damage development in composite materials is ER. Replication techniques have been successfully employed in-situ to monitor fatigue damage developed for PMC materials in many studies [96, 119]. ER provides a local imprint of the actual damage state from the specimen edge, and a chronology of damage throughout the loading process. A major drawback is that the test must be paused in order to apply the technique. A second drawback is that damage in the specimen interior cannot be detected using ER. The method involves the use of a thin transparent film covered by acetone which is applied to the polished edge of a test specimen. The material microstructure and associated damage is then imprinted on the film (or replica), which can be subsequently inspected using an optical microscope or a scanning electron microscope (SEM). This technique was also employed in this study, thus further details will be presented in Chapter 4.

In order to monitor the local strains associated with microscopic cracking, in-situ micro-scale strain measurements have been employed as an indirect gage of damage development in composites. One commonly employed technique is digital image correlation (DIC) which is a non-contact technique, while a second technique that has been extensively employed for PMC materials is the use of surface-bonded or embedded fiber optic sensors (FOS). Since in the present study FOS were used, the subsequent discussion will focus on their theory and application. Numerous studies have reported successful detection of various modes of damage in PMC materials such as matrix cracking, delamination and fiber fracture using FOS [120-123]. The main drawback with FOS is that they detect local damage only and do not provide an overall map of damage. This can however be remedied by using a network of FOS on or within the test specimen. An optical sensor that is often employed for damage detection in composites is the fiber Bragg grating (FBG) sensor. A comprehensive overview of the theory of FBG sensors and their application to PMC materials was reported by Selezneva [124], thus only the relevant details will be presented here.

The fundamental principle for a uniform optical FBG sensor located in a single mode coated glass optical fiber is illustrated schematically in Figure 20 (a). The gratings used in this

study have a constant or uniform pitch (Λ) and length (L), and an index of refraction denoted by n_{eff}. When a broadband light source is transmitted through the core of the fiber towards the grating with a certain wavelength denoted by λ_{in}, light of a certain wavelength is transmitted (λ_{tr}), while light with a different wavelength is reflected (λ_{ref}). The reflected light will have the spectrum shown in Figure 20 (b), with a central or Bragg wavelength denoted by λ_B. The Bragg wavelength for the reflected spectrum is defined by:

$$\lambda_B = 2n_{eff}\Lambda \tag{8}$$

Any change in either n_{eff} or Λ will cause the Bragg wavelength to shift, which will facilitate in determining the strain and temperature environment to which the optical fiber is subjected to. The shift in the Bragg wavelength ($\Delta\lambda_B$) due to both strain (ε_λ) and temperature (T) is obtained by [124]:

$$\Delta\lambda_B = 2n_{eff}\Lambda\left(\left\{1-\left(\frac{n_{eff}^{\,2}}{2}\right)\left[P_{12}-\nu_\lambda\left(P_{11}+P_{12}\right)\right]\right\}\varepsilon_\lambda+\left[\alpha+\frac{dn_{eff}/dT}{n_{eff}}\right]\Delta T\right) \tag{9}$$

The terms P_{11} and P_{12} are Pockel's coefficients of the stress-optic tensor, ν and α are the glass fiber Poisson's ratio and coefficient of thermal expansion respectively. For an isothermal environment (i.e., $\Delta T = 0$), the strain acting along the grating can be determined for a glass fiber using Equation (10) [124].

$$0.7981\,\varepsilon_\lambda = \frac{\Delta\lambda_B}{2n_{eff}\Lambda} = \frac{\Delta\lambda_B}{\lambda_B} \tag{10}$$

Uniform FBG sensors were successfully employed by Montesano *et al.* [72, 125] for both room temperature and elevated temperature cyclic loading of PMCs, and were shown to sustain the high cyclic loading and the elevated temperature environment without degradation.

In terms of their damage monitoring capabilities, FBG sensors offer the option of not only monitoring the local strain variation, but also to monitor the variation of the reflected light spectrum. When an FBG sensor is subjected to a non-uniform strain field, its wavelength spectrum becomes distorted. Since local cracking in the vicinity of an FBG sensor can cause

localized non-uniform strain fields, FBG sensors can in fact be used to detect damage [120]. An example of a distorted wavelength spectrum is shown in Figure 20 (c), which is referred to as chirping. Additional details of damage detection capabilities of FBG sensors, with a review of additional studies employing FBG sensors for damage detection in PMC materials can be found in [124].

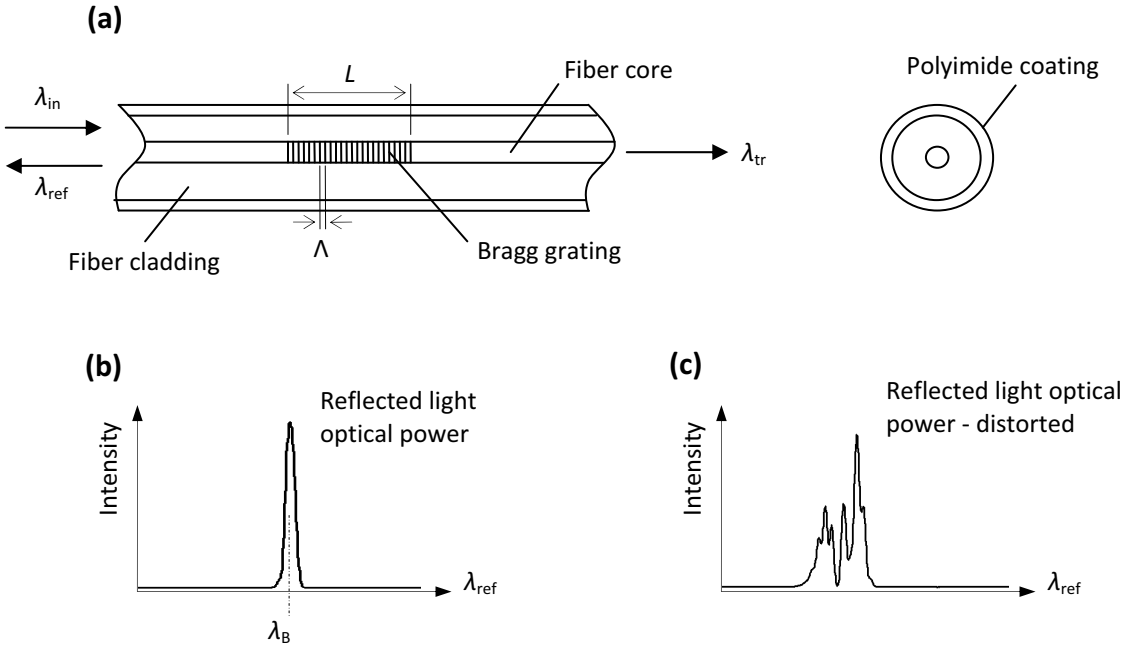

Figure 20. Fundamental principle of uniform FBG sensors (a) geometry, (b) reflected spectrum, (c) distorted spectrum.

Post-test destructive inspection of specimens is done for verification of the damage modes observed using a NDE technique, and for further characterization of the specimen material damage. This allows for a detailed look at the extent of damage and the type of damage in the specimen, but obviously does not provide insight on the progression of damage. A destructive technique such as sectioning of the specimen or de-plying of the specimen is typically employed prior to inspection allowing for explicit visual access of the damage zones or the failure surfaces within the specimens. Use of SEM or an optical microscope is commonly employed for PMC materials. Post-test inspection often allows for detection of smaller-scale damage such as fiber fracture and fiber-matrix debonding, which are not detectable by most of the NDE methods presented.

Although all NDE methods presented have their advantages, the drawbacks for each method were also discussed. This is summarized in Table 4, which indicates the applicability of each method for the listed categories. As is evident in the table, in order to fully characterize the damage development for a material subjected to cyclic loading, a combination of techniques is required. In an ideal case, the combination of 'local' and 'global' NDE techniques will be sufficient. The local technique will assist with identifying particular damage modes and counting cracks to quantify the crack density development, while a global technique can yield an overall map of damage throughout the component continuously. If these techniques are coupled with post *mortem* SEM observations to verify damage modes, a complete picture of the damage development progression during a fatigue test will be attained. For this study, the local NDE techniques employed include ER and the application of surface-mounted FBG sensors. The global NDE technique used is IRT, and for post *mortem* damage verification SEM was used. This is a unique combination of techniques for fatigue damage monitoring of PMC materials. Once the damage development is understood and quantified with the use of the aforementioned techniques, the empirical data can be used to either define or validate a damage prediction model. The following section provides a detailed literature survey of existing fatigue damage prediction models for PMC materials.

Table 4. Summary of NDE techniques.

Technique	In-Situ	Pause Test to Use	Know Damage Location	Small-Scale Damage	Large-Scale Damage	Large Area Capability	Material Limitations
X-ray		●	●	●	●	●	
Ultrasonic		●			●	●	
LM	●	●		●	●	●	●
AE	●			●	●		
IRT	●				●	●	
ER	●	●		●	●		
FOS	●	●		●	●		
DIC	●			●	●	●	

3.7 Literature Survey on Fatigue Models

As was shown in Sections 3.2 and 3.5, the fatigue behaviour of fiber-reinforced PMC materials is a complex phenomenon. The added complexities due to an elevated temperature environment were discussed in Sections 3.3 and 3.4. As a result, there has been great effort by researchers in the past few decades to develop methods for modeling the development of fatigue damage, predicting failure, and predicting the fatigue life of PMC materials. In the aerospace industry, however, issues concerning the durability and fatigue behaviour of composites still remain. This is mainly due to the lack in understanding of the importance of different damage mechanisms involved, and the lack of widely accepted generic models. As a result, many of these research efforts are being continued to date. A classification of existing fatigue models can be made based on the classification of fatigue criteria made by Sendeckyj [126]. According to Sendeckyj, fatigue criteria can be classified into four main categories: macroscopic strength fatigue criteria, criteria based on residual strength, criteria based on residual stiffness and criteria based on actual damage mechanisms. Existing fatigue models for fiber reinforced PMCs can therefore be classified into three main general categories, which include: (a) macroscopic strength models based on experimental S-N curves and not actual damage mechanisms or damage accumulation, (b) residual strength/stiffness models based on damage accumulation, and (c) progressive damage models which are based on specific measurable or observed damage mechanisms. These fatigue models can be either empirical, semi-empirical, phenomenological, statistical, mechanistic or deterministic in nature regardless of their classification. The following paragraphs provide a review of existing fatigue models which is separated into the three aforementioned categories. Although the following review is not completely exhaustive, fatigue models that are deemed noteworthy are presented. A complimentary review conducted by Degrieck and VanPaepegem can be found in [127]. Note that the notation of the original study was maintained for the presented equations in this section, thus the parameters in these equations are not included in the nomenclature or in any other section of this report.

3.7.1 Macroscopic Strength Models

Macroscopic strength models do not account for damage accumulation and do not consider specific damage mechanisms in their formulation (e.g., matrix cracking and fiber fracture). Rather, these models quantify failure based on specific macroscopic failure criteria, or determine the composite fatigue life based solely on a fixed loading condition. In either case, these models use corresponding experimental testing data in the form of S-N curves.

Hashin and Rotem [22] developed one of the first macroscopic fatigue failure criterion for fiber reinforced composites. The fiber and matrix constituents each have a separate failure mode, with each failure criteria based on a fixed stress state in the material. They postulate that failure of one constituent implies failure of the composite material. The failure criteria are defined as follows:

$$\begin{aligned} \sigma_A &= \sigma_A^u \\ \left(\frac{\sigma_T}{\sigma_T^u}\right)^2 + \left(\frac{\tau}{\tau^u}\right)^2 &= 1 \end{aligned} \tag{11}$$

The terms with superscripts are ultimate allowable stresses, and are determined from experimental testing of off-axis unidirectional specimens. These terms are based on maximum or minimum cyclic stress levels, the number of loading cycles, and number of cycles to failure (N_f). The model is however only valid for laminates with unidirectional plies.

Reifsnider and Gao [35] proposed a similar model based on the average stress formulation of unidirectional composites (derived from the Mori-Tanaka method), which accounted specifically for the constituent material properties and the bonding nature between the fibers and matrix. The failure criteria are given by:

$$\begin{aligned} \langle \sigma_f \rangle &= \sigma_f^u \\ \left(\frac{\langle \sigma_m \rangle}{\sigma_m^u}\right)^2 + \left(\frac{\langle \tau_m \rangle}{\tau_m^u}\right)^2 &= 1 \end{aligned} \tag{12}$$

The terms in the brackets $\langle\ \rangle$ denote average stress values, while the ultimate allowable stresses depend on the stress ratio, *R*, and number of cycles which must be determined experimentally. The model is valid for unidirectional-ply laminates of various ply orientations.

Ellyin and El-Kadi [36] developed a fatigue criterion for unidirectional laminates which relates the total mechanical energy input and the 'damage' due to cyclic loading. The prediction of fatigue life is based on an assumed fixed stress state and corresponding material constants (κ and α) which are found experimentally. The fatigue life is found using the expression in Equation (13), where the term on the left-side is the total energy input due to mechanical loading (i.e., the stress state).

$$\Delta W = \kappa N_f^{\alpha} \tag{13}$$

Fawaz and Ellyin [128] proposed a semi-log linear relationship between the applied cyclic stress (S) and the number of cycles (logN) for unidirectional laminates:

$$\begin{aligned} S &= m\log N + b \\ S_r &= m_r \log N + b_r \end{aligned} \tag{14}$$

The subscript r denotes a chosen reference line, where the relation between the parameters m, b, and m_r, b_r are based on ply orientation, stress ratio *R* and the state of stress. The objective is to determine m and b for a given cyclic loading state and material, where the S-N curve can then be determined using Equation (14).

Jen and Lee [129] proposed a modified version of the well known Tsai-Hill failure criterion for plane stress multi-axial fatigue loading of unidirectional fiber reinforced laminates. The failure criterion is expressed as:

$$M_{11}^2\left(\frac{\sigma_{xx}}{\bar{\sigma}_{11}}\right)^2 + M_{22}^2\left(\frac{\sigma_{xx}}{\bar{\sigma}_{22}}\right)^2 - M_{11}M_{22}\left(\frac{\sigma_{xx}}{\bar{\sigma}_{11}}\right)^2 + M_{12}^2\left(\frac{\sigma_{xx}}{\bar{\sigma}_{12}}\right)^2 = 1 \tag{15}$$

The coefficients M_{ij} are based on the stress state and the fiber orientation, while the experimentally determined fatigue strengths, $\bar{\sigma}_{ij}$, are based on the number of load cycles and the stress ratio, *R*.

Philippidis and Vassilopoulos [130] also proposed a multi-axial fatigue failure criterion for unidirectional and woven laminates, which is similar to the quadratic Tsai-Wu failure criterion for static loading. The failure expression is given by:

$$F_{ij}\sigma_i\sigma_j + F_i\sigma_i - 1 \leq 0 \tag{16}$$

The components of the failure tensors F_{ij} and F_i are functions of the failure stresses (i.e., functions of the number of cycles, the stress ratio, *R*, and the loading frequency). Thus, the failure stresses are found based on the S-N curves of the corresponding material and loading condition. The criterion is general enough to consider a laminate with an arbitrary stacking sequence, however experimental testing is required for all stacking sequences.

Bond [42] developed a semi-empirical model to predict fatigue life of unidirectional and woven fiber reinforced laminates subject to variable amplitude loading. The fatigue life can be calculated based on the applied cyclic stress, and the model has the form:

$$\sigma_{max} = b\log N + c \tag{17}$$

This relation represents the S-N curve for the composite, where b and c are functions of the stress ratio, *R*. Bond found that there was a satisfactory correlation between the predicted and experimental data.

Recently, Sarfaraz *et al.* [131] developed a semi-empirical hybrid S-N curve formulation for constant amplitude fatigue of composite materials. It is stated that the common semi-logarithmic and power law fatigue S-N models have drawbacks, whereas the presented model combines both inefficient models to improve modeling accuracy in both LCF and HCF regimes. The model which is a hybrid semi-logarithmic and power law fitting function is defined by:

$$\sigma = CN_f^D + \left[\frac{1}{1+\left(N_f / N_{trans}\right)^2}\right]\left[A + B\log(N_f) - CN_f^D\right] \tag{18}$$

The parameters A, B, C and D are regression parameters for the individual semi-logarithmic and power law fitting functions, while N_{trans} is the transition number of cycles which is defined as the shortest lifetime among the examined sample of fatigue data.

3.7.2 Residual Strength/Stiffness Models

Residual strength or stiffness models are based on the concept of cumulative damage or damage accumulation. These models do not account for specific damage mechanisms in their formulations, but rather define an analytical damage parameter based on the deterioration of observable macroscopic material properties (i.e., strength or stiffness). The early concept of damage accumulation was introduced by Miner [132] for metallic alloys, where the damage accumulation parameter, *D*, was defined as a function of the life fraction for multi-stage fatigue loading. The formulation, often referred to as Miner's rule, is given as:

$$D = \sum_i \frac{n_i}{N_i} \tag{19}$$

A number of similar cumulative damage models were subsequently developed for metals and composites by Marco and Starkey [133], Henry [134], Howe and Owen [135] and Hashin and Rotem [136]. The developed residual strength and residual stiffness models are based on the same concepts.

3.7.2.1 Residual stiffness models

Residual stiffness cumulative damage models use the degradation of the material stiffness to determine the cumulative damage and/or the fatigue life of a composite. Since stiffness is used as the damage metric, this allows for non-destructive testing of specimens [20, 25]. One of the early residual stiffness models for unidirectional composites was proposed by Hwang and Han [30, 31]. A fatigue modulus concept was introduced, where the fatigue modulus is determined based on a power function of the number of loading cycles (n) and the applied stress (r). The degradation rate of the fatigue modulus (F) and the cumulative damage (D) are determined from the following expressions:

$$dF/dn = -Acn^{c-1}$$
$$D = \frac{r}{1-r}\left[\frac{F_o}{F(n)} - 1\right] \tag{20}$$

The parameters A and c are material functions, F_o is the initial fatigue modulus, and failure occurs when the damage parameter is unity.

Whitworth [32, 33] proposed a residual stiffness model for unidirectional-ply laminates in which the degradation of the material stiffness is based on the number of cycles (n), the applied stress level (B) and material parameters a and H. The expressions for the evolving stiffness and the corresponding damage parameter are defined in Equation (21), where D=1 denotes failure.

$$E(n)^a = E(0)^a - H[E(0) - B]^a \frac{n}{N}$$
$$D = \left[\frac{H(1-S)^a}{1-S^a}\right]\frac{n}{N} \tag{21}$$

Yang *et al.* [34] proposed a residual stiffness model for unidirectional laminates. The model assumes that the residual stiffness degradation rate is a power function of the number of loading cycles (n):

$$\frac{dE(n)}{dn} = -E(0)Qvn^{v-1} \tag{22}$$

The variables Q and v depend on the applied stress, load frequency, stress ratio and ambient temperature. Yang *et al.* [137] later employed this model with the concept of the fatigue modulus to develop a similar model for prediction of fatigue modulus degradation. These models were used within a statistically-based model for predicting specimen stiffness loss undergoing both low-cycle and high-cycle fatigue loading.

Hansen [117] proposed a fatigue model for impact-damaged woven fiber-reinforced composite laminates. A damage parameter (β) is introduced and based on the number of cycles (N), the effective strain (ε_e) and constants (A and n):

$$\beta = A\int_{0}^{N}\left(\frac{\varepsilon_e}{\varepsilon_o}\right)^n dN \tag{23}$$

The effective strain is based on the cyclic loading stress level. The damage parameter is used to scale down the material modulus using the expression $E = E_o(1 - \beta)$. This fatigue model was implemented into a finite element (FE) analysis model to predict the stiffness reduction of the corresponding test specimen.

VanPaepegem and Degrieck [138] employed a stiffness degradation model for woven composites, while also implementing the model into a FE algorithm. The rate of the damage parameter (D) is defined as:

$$\frac{dD}{dN} = \begin{cases} \dfrac{A(\Delta\sigma)^c}{(1-D)^b} & \text{tension} \\ 0 & \text{compression} \end{cases} \tag{24}$$

The parameters A, b and c are material constants, and $\Delta\sigma$ is the cyclic stress amplitude. The material modulus is reduced by the commonly adopted expression $E = E_o(1 - D)$.

Tate and Kelkar [13] developed a residual stiffness model to predict the fatigue life and residual stiffness of a biaxial braided composite subjected to tension-tension fatigue. The expression relating the fatigue modulus (E(n)) to the number of cycles (n) is:

$$E(n) = E(N)\left\{-a\left[\ln\left(\ln\left(\frac{n}{N}\right)\right)\right]\right\} + c \tag{25}$$

The fatigue life is denoted by N, while E(N) is the fatigue modulus at failure, which are both determined from experimental testing data (i.e., S-N curves). The empirical parameters a and c are assumed to be independent of stress ratio and loading frequency.

Over the past decade, a number of additional nonlinear cumulative damage models have been developed to predict fatigue damage accumulation of PMC laminates [61, 139-141]. The definition of the cumulative damage parameter fitting function in each study is found through the correlation of the evolving parameter (D) with an experimentally obtained damage index

(D_{exp}), which was defined by measured stiffness values. As a result, these models are deemed stiffness degradation models. One noteworthy example is the model developed by Mao and Mahadevan [139]. An experimentally obtained damage index based on the initial stiffness (E_o) and the stiffness at failure (E_f) was used, which is defined in Equation (26). The cumulative damage model also defined in Equation (26) was equated to the experimental damage index, and the material parameters q, m_1 and m_2 were found for a particular maximum applied stress level.

$$D_{exp} = \frac{E_o - E}{E_o - E_f}$$
$$D = q\left(\frac{n}{N}\right)^{m_1} + (1-q)\left(\frac{n}{N}\right)^{m_2} \tag{26}$$

3.7.2.2 Residual strength models

Residual strength models use the degradation of the initial material strength to determine failure or the fatigue life of a composite. These models have a natural failure criterion, in which failure occurs when the residual stress reduces to the level of the applied cyclic stress. Unlike the residual stiffness models, tracking the residual strength of a composite must be done via destructive testing. For this reason, many of these models are incorporated within statistical models to predict the probability of fatigue failure or strength degradation. Residual strength models are either based on the sudden death approach or the wear-out approach, used for LCF and HCF respectively.

One of the earliest residual strength models was developed by Broutman and Sahu [23] for unidirectional composites. They found that the residual strength is a linear function of the number of cycles spent at a particular stress level. The expression used to correlate residual strength and the cumulative fatigue damage for two-stage loading is given by Equation (27), where failure occurs when the damage parameter is unity.

$$D = \left(\frac{\sigma_{uts} - \sigma_1}{\sigma_{uts} - \sigma_2}\right)\frac{n_1}{N_1} + \frac{n_2}{N_2} \tag{27}$$

Hahn and Kim [24] also developed a linear model relating residual strength and the number of load cycles. The model predicts failure when the residual strength reduces to the level of the maximum applied load (i.e., D=1). The expression describing the rate of change of residual strength (F) is defined in Equation (28). The parameter A is based on the applied stress, while m is a material constant. This expression is used in a cumulative damage model which incorporates the life (L) and the applied rupture stress (σ_a).

$$\frac{dF}{dt} = -AF^{-m}$$
$$D = \frac{\left(F_s^{m+1} - \sigma_a^{m+1}\right)}{(m+1)L(\sigma_a)} \tag{28}$$

Yang and Jones [142] proposed a nonlinear residual strength model for two-stage loading in unidirectional laminates. The expression for residual strength (R) is:

$$R(n_B)^v = R(n_A)^v - \left[\left(\frac{n_B}{N}\right)^\gamma - \left(\frac{n_A}{N}\right)^\gamma\right]\frac{R(0)^v - \sigma^v}{\left[R(0)^c - \sigma^c\right]^\gamma} \tag{29}$$

The parameters v, c and γ are material constants and based on the applied stress (σ).

Caprino and D'Amore [143] proposed a fatigue model for random fiber-reinforced thermoplastic composites. A power law is proposed for continuous decay of the residual strength (σ_n) during cyclic loading, and is defined in Equation (30). The stress amplitude is $\Delta\sigma = \sigma_{max} - \sigma_{min}$, and the constants a_o and b are based on the loading conditions and the material. With the initial static strength (σ_o) and stress ratio (R), the model for strength degradation is also defined in Equation (30). Fatigue failure occurs when $\sigma_n = \sigma_{max}$, which allows for estimation of the fatigue life. This model was implemented into a statistical model for strength degradation prediction.

$$\frac{d\sigma_n}{dn} = -a_0 \Delta\sigma n^{-b}$$
$$\sigma_o - \sigma_n = \frac{a_o}{1-b}\sigma_{max}(1-R)(n^{1-b} - 1) \tag{30}$$

Whitworth [44] developed a residual strength model for unidirectional laminates based on a previously developed residual stiffness model [43]. The residual strength (S_R) is related to the fatigue life (n) by the expression in Equation (31).The maximum cyclic stress is S, the ultimate tensile stress is denoted by S_U, and γ, h, m, c_1 and c_2 are constants. Equation (31) is used to determine the residual strength during fatigue loading, and can be used to determine the fatigue life (i.e., if S_R = S). This model was then implemented into a statistical residual strength model.

$$S_R^\gamma = S_U^\gamma - \left[\frac{S_U^\gamma - S^\gamma}{\exp\left\{ \frac{1}{h} \left[\left(\frac{c_1 S_U}{S} \right)^{m/c_2} - 1 \right] \right\} - 1} \right] n \tag{31}$$

Post *et al.* [54] developed a residual strength model for fiber-dominated woven-ply laminates which is applicable for composites subjected to variable amplitude fatigue loading. The postulate of the model is that the residual strength in the critical plies of the laminate dictates failure of the material. The normalized remaining strength (Fr) in the critical plies is given by:

$$Fr(n) = 1 - \left[\int_0^n \left\{ \left(1 - Fa(n)\right)^{1/j} \frac{1}{N(Fa)} \right\} dn \right]^j \tag{32}$$

The term Fa is the normalized maximum applied stress on the critical plies, N(Fa) is the fatigue life, and j is a fitting parameter. Failure occurs when Fa > Fr. The normalized maximum applied stress is determined using an empirically-determined stiffness, E(n), while the fatigue life is found using an experimental S-N curve. This model is incorporated into a statistically-based simulation model to predict residual strength degradation.

3.7.3 Progressive Damage Models

Progressive damage models introduce specific damage mechanisms (e.g., matrix cracking, fiber-matrix debonding, delamination, fiber fracture, yarn cracking) in order to simulate the

development of damage in order to describe the deterioration of the composite component. These models are based on a physical interpretation of the actual underlying damage mechanisms, which cause macroscopically observable degradation of the material properties. The damage criterion is often based on micromechanical formulations, and are often used in the context of the FEM. These models can be classified into two sub-categories: (i) models that predict damage growth, and (ii) models that correlate damage growth with material property degradation.

3.7.3.1 Models that predict damage growth

Models that predict actual damage growth consider one (or more) specific damage mechanism, and determine the physical change in that damage mechanism with increasing loading cycles. These models are typically of the form of the well-known fracture mechanics-based Paris Law for crack propagation in homogeneous materials (i.e., d*a*/d*n*). Notched laminates are typically employed to initiate the specific damage type required, allowing for clear observation of the damage growth area for comparison with predicted results. More recently, explicit micromechanical models have also been developed to explicitly predict damage development using the FEM.

Bergmann and Prinz [144] developed a model for predicting the growth of delamination area in unidirectional laminates. The equation representing the growth of the inter-ply delamination area (A_i) subjected to N loading cycles is:

$$\frac{dA_i}{dN} = c \cdot f(G_{it})^n \tag{33}$$

The energy release rate due to delamination growth is denoted by G_{it}, where c and n are empirical factors determined from corresponding tests.

Feng *et al.* [145] developed a model for predicting matrix crack growth in unidirectional laminates, using maximum strain-energy release rate (G_{max}) along with empirical material constants in the model formulation. The modified Paris law has the form:

$$\frac{dA}{dN} = DG_{max}^n \tag{34}$$

The damage area (A) is caused by matrix cracking, while N is the number of loading cycles. A FE model was used to determine G_{max}, and the fatigue life (N_f) was approximated based on a critical damage area at failure (A_f).

A similar model was proposed by Hernaff-Gardin *et al.* [39], where the progression of damage due to matrix cracking in cross-ply laminates was predicted. The propagation expression for crack surface area (S) during fatigue cycling (N) is denoted by Equation (35). The strain energy release rate due to cracking is denoted by G, while A and n are empirical constants.

$$\frac{dS}{dN} = A\left(\frac{G_I}{G_{max}}\right)^n \tag{35}$$

Shivakumar *et al.* [55] proposed a delamination growth model to predict the fatigue life for fiber-reinforced woven-ply laminates. Their expression for determining the delamination area growth rate (da/dn) is also analogous to a fracture mechanics approach, and is given by:

$$\frac{da}{dn} = A\left(\frac{G_{Imax}}{G_{IR}}\right)^m \frac{\left(1-\left(\frac{G_{Ith}}{G_{Imax}}\right)^{D_1}\right)}{\left(1-\left(\frac{G_{Imax}}{G_{Ith}}\right)^{D_2}\right)} \tag{36}$$

The empirical parameters A, m, D_1 and D_2 are determined from various fracture tests and tension-tension fatigue tests. The maximum energy release rate is expressed as G_{Imax}, while G_{IR} is the inter-laminar fracture resistance which causes the growth rate of the delamination area to decrease; this is caused by for example matrix cracking and fiber bridging for unidirectional composites. The threshold energy release rate G_{Ith} is a minimum value below which da/dn is nearly zero. Note that G_{Imax}, G_{Ith}, and G_{IR} are all determined from experimental test data and empirically-based equations.

In addition, many micromechanical models (i.e., explicit model of fibers and matrix) have been developed within the framework of FE simulation models to explicitly simulate the

progression of specific damage mechanisms in PMC materials [146-149]. These models employ the concept of a repeated unit cell (RUC), in which a small representative volume of the bulk material is included in the three-dimensional simulation model. These models tend to drastically oversimplify the geometry of the RUC and the locations of the damage initiation zones. In addition, most of these models only consider static loading; however, a recent study by Shi and Zhang [150] successfully simulated the development of a single matrix crack near and a single interface crack at the location of a reinforcing fiber.

3.7.3.2 Models that correlate damage growth with residual mechanical properties

Models that correlate damage growth with material property degradation often employ numerical simulation models (e.g., FE analysis) to simulate damage progression, predict material property degradation and to predict the fatigue life of a component. The composite material is typically treated as a homogenous material for the analysis, where the degraded material properties are introduced into the constitutive equations via any number of numerical or phenomenological methods. Some studies considered analytical micromechanical representations of the stress fields in the vicinity of cracks, and incorporated the modified stresses into the constitutive equations to reduce the mechanical material properties. Other studies incorporate the effects of certain damage mechanisms directly into the formulation of the global constitutive equations.

One of the first fatigue models that correlated matrix cracking with stiffness loss in fiber-reinforced laminates was the one-dimensional shear-lag model developed by Highsmith and Reifsnider [26]. The saturation of transverse matrix cracking in the off-axis plies yielded near-uniform crack spacing after a certain number of loading cycles, and was experimentally observed and correlated to the specimen stiffness reduction. These observations were then implemented into the analytical constitutive equations to model material stiffness loss via the stiffness tensor. This model effectively considers the local state of stress caused by damage and uses this to predict the global behaviour of the composite. A number of similar local stress state based models were developed in many additional studies, which are known as variational approaches [29, 40, 151, 152]. Variational methods consider certain damage mechanisms, often only matrix cracking, and their effects on the local stress fields. The local stress fields are then

used to reduce the material properties such as stiffness. The influence of local cracking is introduced indirectly into the governing equations by stress perturbation functions.

Wang *et al.* [153] developed a fatigue damage model for a short-fiber PMC. Randomly oriented matrix cracking was considered as the primary damage mechanism. An analytical damage model was developed, based on statistical probability crack density functions for damage progression. A crack density function that was based on the crack lengths, orientations and densities was incorporated into the composite constitutive equations in the form of an effective damage-induced compliance tensor in order to degrade the stiffness of the material during numerical simulations of cyclic loading conditions. The influence of the local damage state was introduced directly into the global constitutive equations to model stiffness degradation, which is notably different than the presented models that consider the local stress state. A similar study by El-Mahi *et al.* [38] proposed a similar model in which matrix cracking in PMC laminates was correlated to the stiffness through a crack density function, which was employed to directly reduce the material axial stiffness component and used in a FE analysis. An earlier study by Poursartip *et al.* [154] defined a damage parameter (*D*) which was based on the delamination area observed in PMC laminates. The parameter was then correlated to the stiffness of the laminate using a semi-empirical expression.

Bartley-Cho *et al.* [155] investigated ply cracking in quasi-isotropic laminates under constant amplitude fatigue and block loading, and subsequently developed a model to predict the development of ply cracking. The ply level stresses were determined from the applied laminate stress, and a ply-level empirical failure function was assumed which was a function of the number of loading cycles. The crack density development (ρ_{crack}) in plies with different orientations was derived from an empirical fitting function, which is defined in Equation (37). The parameters b and ρ_{∞} are material parameters which are found from fitting of the experimental data. The corresponding reduced ply-level stiffness parameters (C_{ij}) are then found from the crack densities, as is shown in Equation (37). The updated ply-level stresses, which are based on the current crack densities, were then used to evaluate the failure function.

$$\rho_{crack} = \rho_{\infty}\left(1 - \exp\left(-b\log\frac{N}{N_i}\right)\right)$$
$$C_{ij} = C_{ij}^{o}\exp\left(-\alpha_{ij}\rho_{crack}t_{ply}\right) \quad (37)$$

A similar study by Gagel *et al.* [59] investigated ply cracking in non-crimp laminates subjected to tension-tension fatigue loading, and developed a similar model to predict the degradation of axial stiffness based on observed crack densities. The crack densities in the different plies were defined from empirical data as functions of the number of loading cycles. The definition of the crack density (ρ) for an arbitrary ply is presented in Equation (38), where the parameters m_p and n_p are linear functions of the maximum applied stress. The crack densities were then used to define a cumulative damage parameter, and the axial stiffness was consequently determined from that damage parameter. An analytical expression for the normalized axial stiffness reported in the study is shown in Equation (38), which is a function of the crack density for a 45˚ ply.

$$\rho = m_p\log\left(\frac{n}{N_f}\right) + n_p$$
$$\frac{E}{E_o} = -2.9853\text{x}10^{-5}\rho_{45} + 1 \quad (38)$$

Many similar studies focussed on directly introducing the effects of local damage mechanisms into the global constitutive equations to degrade the mechanical properties. One model that was developed by Reifsnider [156, 157] correlated stiffness degradation and strength degradation to particular damage mechanisms in unidirectional-ply laminates. The so-called critical element method effectively divides the material into critical and sub-critical elements. The critical elements are for example 0˚ plies at the ply level or the fibers at the micromechanical level, and the subcritical elements can be the off-axis or transverse plies at the ply level and the matrix at the micromechanical level. The model assumes that the mechanical properties of the sub-critical elements degrade due to the evolution of damage, which is represented through analytical expressions and/or empirical parameters within the

constitutive equations. This consequently reduces the strength of the critical elements. The critical elements will fail if local strength criteria are met, while failure of the critical elements is assumed to cause complete failure of the laminate. Sendeckyj [126] reported that the critical element method is inconsistent with the experimental observations of many PMC laminates.

Other methods that include the effects of damage directly into the global constitutive equations are based on self-consistent schemes, such as the model proposed by Laws *et al.* [158]. A scalar damage parameter based on matrix crack density was formulated and implemented into the homogenized composite material linear elastic constitutive equations to reduce the material stiffness. The scalar crack density damage parameter (β) that was used in the study is defined in Equation (39). The parameter defines the average number of cracks with length 2a in a square section with side length of 2a. The parameter has a value between 0 and 1 as was observed experimentally. The cracked stiffness tensor (L) is also defined in Equation (39), and is a function of the un-cracked material stiffness tensor (L_2) and the damage parameter (β).

$$\beta = 4\eta a^2$$
$$L = L_2 + c_1(L_1 - L_2)[I + P_1(L_1 - L)]^{-1} - \frac{1}{4}\pi\beta L_2\Lambda \tag{39}$$

Additional models that incorporate the effects of damage directly into the global constitutive equations are based on the pioneering work of Kachanov [159], which is referred to as damage mechanics or continuum damage mechanics (CDM). Models based on CDM consider the effects of particular damage mechanisms, which are represented by scalars, vectors or tensors within the constitutive equations. Damage is homogenized within the bulk material and is considered as a set of internal variables. This concept is contrary to fracture mechanics which treats damage as a set of internal surfaces within the material; however, damage mechanics is more suitable for composite materials based on the discussion presented in Section 3.5. The formulation of the 'damaged' constitutive equations is based on the concepts of irreversible thermodynamics in that damage events are irreversible microscopic processes within the bulk material. The damage parameters are typically incorporated within the material stiffness tensor, and thus the degradation of the mechanical properties are directly modeled. The

damage parameters are typically determined from experimental data, but can also be defined by analytical expressions or from micromechanical analysis. Some of the notable studies that developed fatigue prediction models based on CDM are those by Talreja [160-162], Allen et al. [163, 164], Coats and Harris [165, 105], and Ladeveze et al. [166-169].

Another fatigue prediction model for notched PMC laminates was the so-called generalized residual material property degradation model developed by Shokrieh and Lessard [170-173]. The model did not consider specific damage modes, but did employ specific 'failure modes' within the fatigue simulation. Hashin-type polynomial fatigue failure criteria were employed in the model to check for sudden material property degradation, and are based on specific failure modes within the plies and the number of loading cycles. The failure modes considered were fiber tension, fiber compression, fiber-matrix shearing, matrix tension, matrix compression, normal tension and normal compression. The gradual degradation of the residual strengths and stiffness properties during cycling (prior to sudden failure) was approximated using corresponding semi-empirical expressions. These expressions are functions of the number of loading cycles, empirical fitting parameters, the loading conditions and the number of cycles to failure which is determined from S-N data. The generalized residual material property degradation model was implemented within the context of a three-dimensional FE model which assumes an orthotropic material. An algorithm was developed to simulate cycle-by-cycle fatigue damage development.

3.7.4 General Discussion

A number of fatigue prediction models have been presented in the preceding sections, the summary of which is included in Table 5. It can be argued as to which model, or which category of models, are the most applicable for a certain type of composite. The development of the varying types of fatigue prediction models does however illustrate an important point: one common fatigue modeling approach has not yet been established or accepted. While each category of models have their own advantages and disadvantages, it is in the opinion of the author that a fatigue prediction model should incorporate the underlying damage mechanisms within its definition. Accounting for specific damage mechanisms in a prediction model allows for a quantitative representation of the progressive damage in a composite structure, which is

important not only for fatigue prediction but for damage tolerance analysis in aerospace structures. Specifically, the models based on damage mechanics are attractive because they are more applicable to composites compared to models that are based on the principles of fracture mechanics (see Section 3.5). Cumulative damage models may be effective if they can be based, to some degree, on the observed damage mechanisms for a particular material.

Table 5. Summary of fatigue prediction models.

Macroscopic Strength Models	**Residual Models**		**Progressive Damage Models**	
	Stiffness	**Strength**	**Actual Growth Prediction**	**Correlated to Material Properties**
Hashin & Rotem [22]	Hwang & Han [30, 31]	Broutman & Sahu [23]	Bergmann & Prinz [144]	Highsmith & Reifsnider [26]
Reifsnider & Gao [35]	Whitworth [32, 33]	Hahn & Kim [24]	Feng *et al*. [145]	Hashin [29]
Ellyin & El-Kadi [36]	Yang *et al*. [34, 137]	Yang & Jones [142]	Hernaff-Gardin *et al*. [39]	Akshantala & Talreja [40]
Fawaz & Ellyin [128]	Hansen [117]	Caprino & D'Amore [143]	Shivakumar *et al*. [55]	Hashin [151]
Jen & Lee [129]	VanPaepegem & Degrieck [138]	Whitworth [44]	Shi & Zhang [150]	Nairn [152]
Philippidis & Vassilopoulos [130]	Tate & Kelkar [13]	Post *et al*. [54]		Wang *et al*. [153]
Bond [42]	Plumtree & Melo [61]			El-Mahi *et al*. [38]
Sarfaraz *et al*. [131]	Mao & Mahadevan [139]			Poursartip *et al*. [154]
Miyano *et al*. [92]	Wu & Yao [140]			Bartley-Cho *et al*. [155]
	Mivehchi & Varvani-Farahani [141]			Gagel *at al*. [59]
	Kawai & Taniguchi [15]			Reifsnider *et al.* [156, 157]
				Laws *et al*. [158]
				Talreja [160-162]
				Allen *et al*. [163, 164]
				Coats & Harris [105, 165]
				Ladeveze *et al*. [166-169]
				Shokrieh & Lessard [170-173]

It can be gleaned from the review that few models have been developed or have been employed for prediction of elevated temperature fatigue of PMC materials. One of the notable models is the macroscopic strength model developed by Miyano *et al.* [92] that considers the influence of creep on fatigue. Another is described in the work by Case *et al.* [84], which employed the aforementioned critical element method to predict fatigue damage development for a PMC laminate at elevated temperatures. The final notable model was that employed by Kawai and Taniguchi [15] to predict the cumulative damage in on-axis and off-axis laminates at both room temperatures and elevated temperatures. In addition, few of these models have been developed for braided composites. Since the evolution of damage in braided composites is very complex and not fully understood, the corresponding prediction of the effective material properties for braided materials containing damage is not well established, especially at elevated temperatures. The complex geometry of braided fabric reinforcements and the number of geometric variables makes the use of certain presented models even more difficult.

4 MATERIAL AND EXPERIMENTAL DETAILS

This chapter presents the relevant details of the experimental portion of this study. The first section presents a description of the composite materials under investigation, with specific overview of the micro-structural arrangement of the constituents. The second section describes the preparation of the braided composite material test specimens, while the third section presents an overview of the experimental protocol. The fourth section includes a discussion on the damage monitoring methods used in this study, while the fifth section describes the test procedures employed. The final section presents the relevant data analysis used in this study.

4.1 Material Details

The main focus of this research is to investigate a specific braided composite material, thus the details of this section will have that focus. An alternate objective of this study is to analyze two additional woven-ply laminates, which will also be described in brief in Section 4.1.2.

4.1.1 Triaxial Braided Composite

The composite material under investigation is a triaxial braided fabric reinforced thermosetting polymer resin, which was shown schematically in Figure 3 (b). The braided fabric is manufactured using fiber yarns that each consist of 6,000 carbon fibers (6K). The T650/35 carbon fibers used to manufacture the braided fabric are commercially available from Cytec

Industries. The braided fiber yarns are oriented in the 0˚/+60˚/-60˚ directions, as shown by the image of the dry braided fabric in Figure 21. The braid pattern is a regular 2x2 braid, which consists of each +60˚ braided yarn alternating over two -60˚ braider yarns and under two -60˚ braider yarns (and vice versa) as shown. The 0˚ or warp yarns are aligned in the regions between the interlacing braider yarn crossover locations and are ideally non-crimped. The percentage of fiber yarns in the warp direction is 20%, while the percentage in each of the -60˚ and +60˚ directions is 40%. Note that the name and specific details of the thermosetting polymer resin are proprietary and cannot be disclosed as requested by the industry partner Pratt and Whitney Canada. The mechanical properties of the constituent materials are summarized in Table 6.

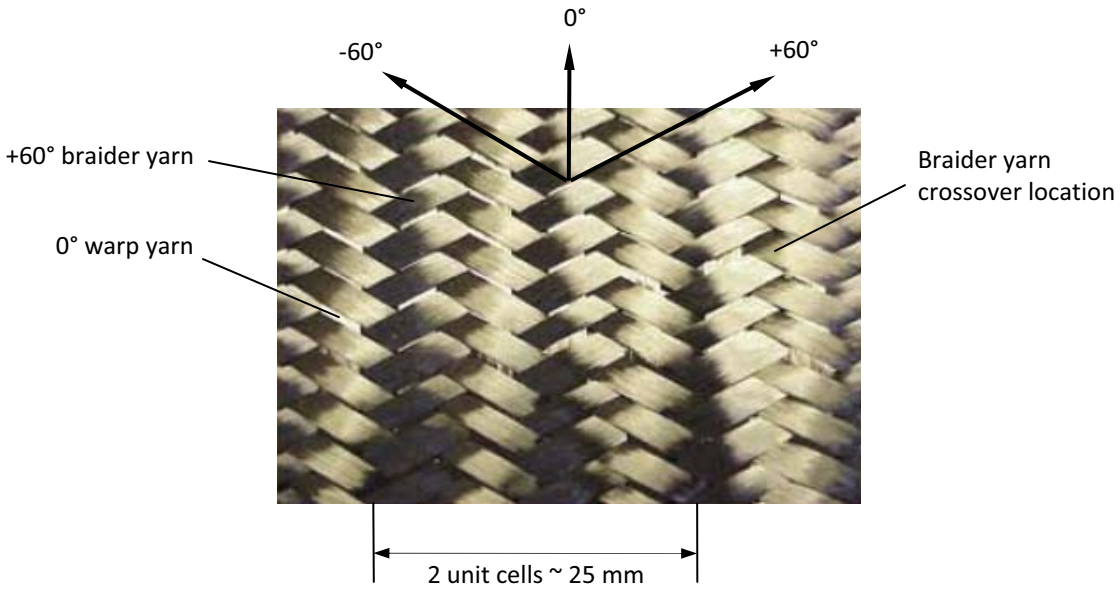

Figure 21. Photograph of dry 2x2 triaxial braided fabric.

Table 6. Mechanical properties of triaxial braided constituent materials.

Material	E_{11} (GPa)	S_u (MPa)	ρ (g/cm^3)
T650/35-6K	255	4295	1.772
Thermosetting Resin	3.5	44	1.082

The flat composite panels were manufactured by EDO Fiber Innovations Inc. by stacking dry layers of the braided fabric in a mould after stitching the periphery of the stacked braided layers. A RTM technique was used to inject the resin into the mould. Note that the

manufacturing parameters are also proprietary and cannot be disclosed as requested by the industry partner. The composite panels had final dimensions of approximately 360 mm in the warp direction and 350 mm in the transverse direction. All panels were subsequently inspected for manufacturing defects by Hansen Aerospace Laboratory Inc. using a thru-transmission immersion ultrasonic c-scan method. For all the manufactured panels, no visible defects were reported. In addition, untested or virgin samples of the material were also inspected by SEM to confirm that there were no manufacturing defects. SEM images of the virgin samples illustrating details of the composite microstructure are shown in Figure 22. As is seen in the photomicrographs, there are no voids in the resin and the fibers are entirely consolidated. Note that the localized dark regions in the photomicrographs are the sectioned ends of the carbon fibers and not resin voids. In total five panels were manufactured, where the fiber volume fraction (V_f) and thickness for each panel are listed in Table 7 (as provided by the manufacturer). It should be noted that the slight variation in the panel thickness, and thus V_f, was due to the variation in the RTM manufacturing process. Although the braided fabric was consistent for each manufactured panel, the amount of resin squeezed out of the mould during curing differed slightly for each panel which caused the variation in the cure thickness. This is demonstrated schematically in Figure 23, albeit exaggerated. This has been commonly observed for many panels manufactured using RTM, and may result in slight scatter in the mechanical testing data [66].

Table 7. Manufactured braided composite panel thickness and fiber volume fraction.

Panel Number	Avg. Thickness (mm)	V_f (%)
001	3.150	53.7
002	3.048	54.5
003	2.997	55.3
004	2.972	56.1
005	2.896	57.8

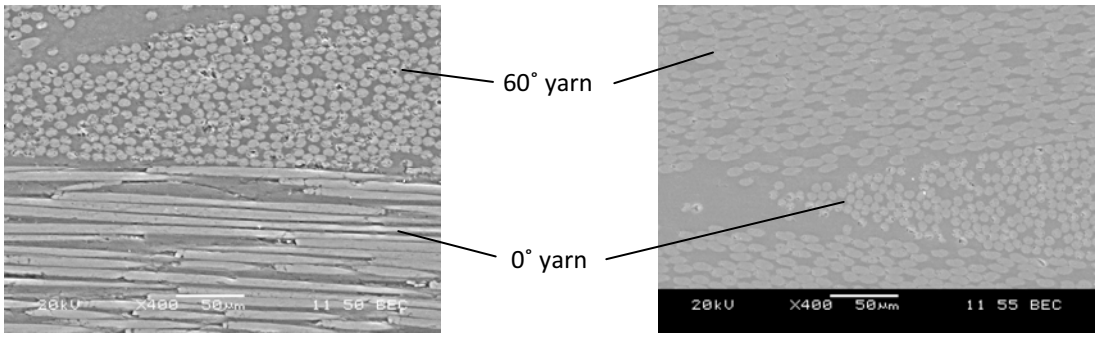

Figure 22. SEM photomicrographs of virgin braided composites samples (400x magnification).

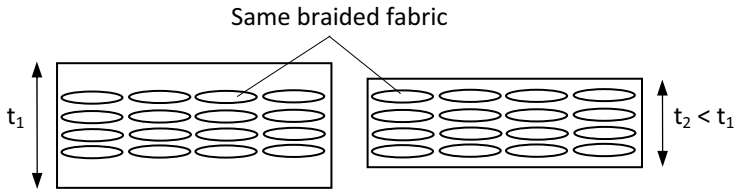

Figure 23. Schematic of manufactured braided composite panel thickness variation.

4.1.2 Woven-Ply Laminates

Two types of woven composites were investigated in this study. The first is an eight-harness satin (8HS) woven fabric reinforced BMI laminate. A schematic of the 8HS weave pattern is shown in Figure 24 (a), with the warp yarns in darker contrast and the weft yarns in lighter contrast. The fiber yarns each consisted of 3,000 (3K) T650/35 carbon fibers, with an equivalent number of ends and fills in the warp and weft directions, respectively. The flat composite panels consisted of 7 layers of the 8HS woven fabric, all oriented along the warp direction. The panels were manufactured using a RTM technique. The second composite is a four-harness satin (4HS) woven fabric reinforced polyimide laminate. A schematic of the 4HS weave pattern is shown in Figure 24 (b), with the warp yarns in darker contrast and the weft yarns in lighter contrast. The fiber yarns each consisted of 6,000 (6K) IM7 carbon fibers, with an equivalent number of ends and fills in the warp and weft directions, respectively. The polyimide resin used was RP46. The flat composite panels consisted of 10 layers of the 4HS woven fabric, all oriented along the warp direction. The panels were manufactured using a compression

moulding technique, as described in [174]. The fiber volume fraction for the satin woven laminates investigated in this study were approximately 54-56%.

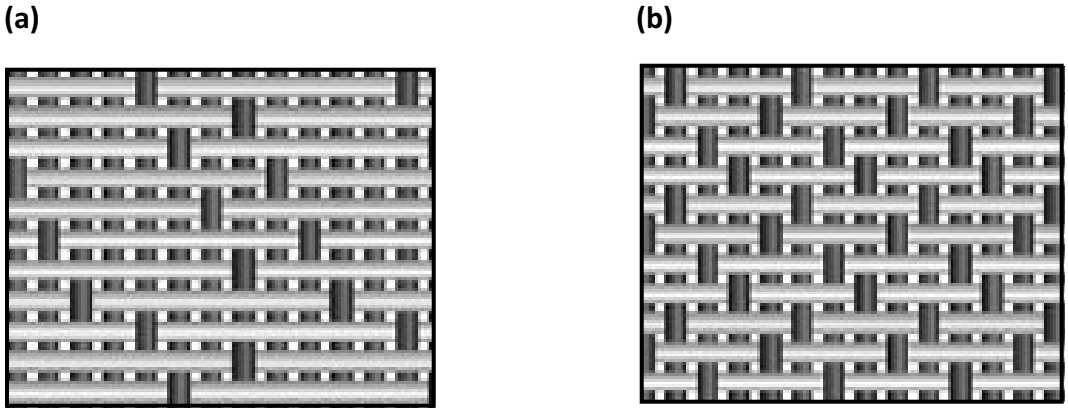

Figure 24. Satin woven fabric geometry for (a) 8HS, (b) 4HS.

4.2 Specimen Preparation

The manufactured triaxial braided composite panels were manufactured into 12 specimens each (i.e., total of 60 specimens) by cutting the panels along their warp direction using an abrasive waterjet cutting technique. A schematic of the cutting pattern for a braided panel along with the panel and specimen dimensions is shown in Figure 25 (a), where each specimen has nominal dimensions of 355 x 25 mm as shown. The specimens were each numbered according to the panel they were cut from and their sequence along the panel; e.g., specimen B1-11 was cut from panel 1, and was from the location on the panel shown in Figure 25 (a). The edges of all the cut braided specimens were subsequently wet sanded with 180-grit and then 320-grit paper for improved edge quality. The specimen width of 25 mm ensured that the ratio of specimen width to the braided fabric unit cell width was at least 2:1 (see Figure 21), as is recommended in ASTM standard D6856 [175].

All braided test specimens were subsequently equipped with tapered aluminum end tabs to eliminate potential issues with gripping induced failure. The end tabs were manufactured from 3 mm (1/8”) thick by 25 mm (1.0”) wide 6061-T6 aluminum alloy bar. The static test specimens were equipped with 76 mm long tabs with a 10° taper, while the fatigue test specimens were equipped with 57 mm long tabs also with a 10° taper. All manufactured end tabs were lightly filed after machining to remove any burs, and the end tab mating surfaces

(i.e., to the specimen) were sanded with 320-grit paper. The geometry of the end tabs for the fatigue test specimens is shown in Figure 25 (b). The end tab and specimen geometry are in accordance with ASTM Standard D3039 [176]. For the room temperature tests, the end tabs were bonded to the composite specimens using a room temperature curable adhesive, Loctite 496. For the elevated temperature tests, the end tabs were not bonded to the specimens due to exposure to the elevated temperature environment. Friction due to gripping forces were sufficient to ensure that there was no relative slippage between the end tabs and the elevated temperature test specimens.

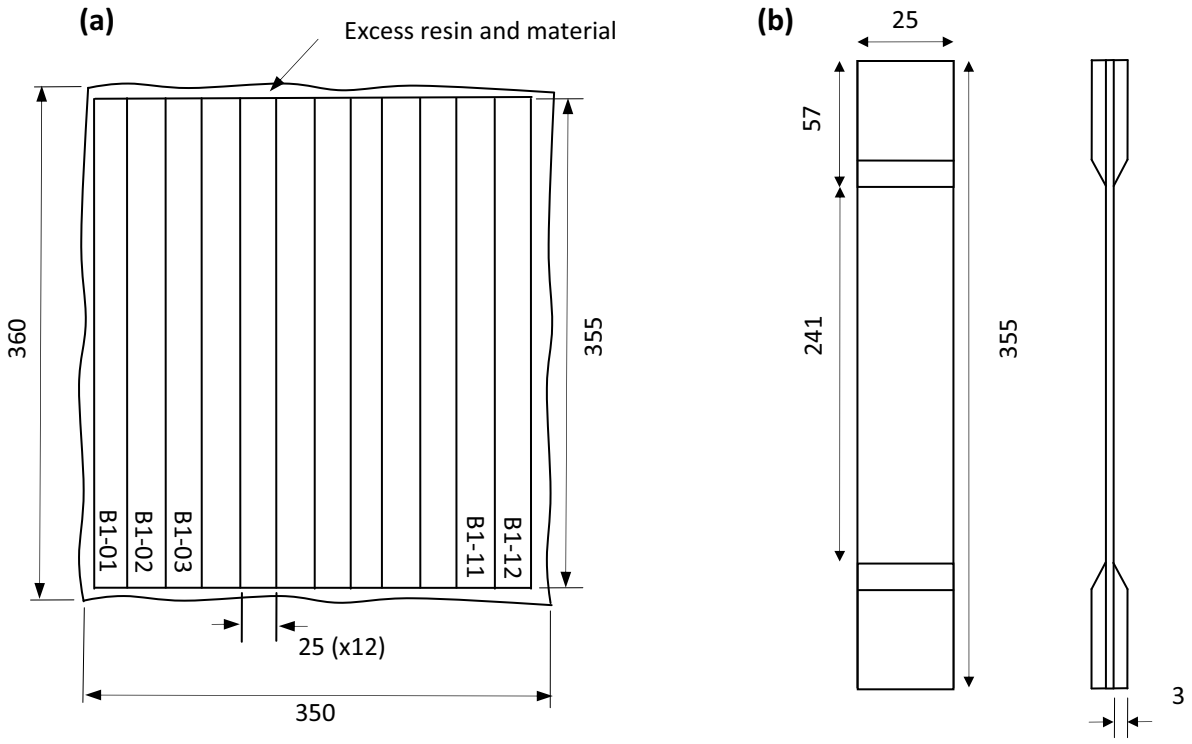

Figure 25. Sketch of braided composite (a) panel cutting pattern, (b) specimen and end tab geometry (all dimensions shown are in mm).

The 8HS woven BMI test specimens were also cut from flat panels, along the warp direction, using an abrasive waterjet cutting technique. The resulting test specimen nominal dimensions were 300 mm by 25 mm. Analogous to the braided specimens, the 8HS woven BMI specimen edges were sanded subsequent to cutting and similar aluminum end tabs were also employed. The 4HS woven RP46 test specimens were cut from flat panels, along the warp direction, using a wet diamond blade. The resulting specimen nominal dimensions were 280

mm by 25 mm. The 4HS woven RP46 specimen edges were also sanded subsequent to cutting and similar aluminum end tabs were employed for all tests. Both woven laminate specimen geometries were also in accordance with ASTM standard D3039 [176].

4.3 Experimental Setup

All mechanical tests were conducted in the Facility for Research on Aerospace Materials and Engineered Structures (FRAMES) at Ryerson University using an MTS 322 test frame. A calibrated MTS 244.31 hydraulic linear actuator provided the uniaxial stroke, a calibrated MTS 661.22C-01 force transducer with a 250 kN capacity provided the force feedback, and a calibrated MTS linear variable displacement transducer (LVDT) provided the displacement feedback. An MTS TestStar IIm digital controller/data acquisition unit connected to a Windows-operated PC was used for controlling the tests and acquiring all relevant data. Additional equipment and sensors employed for mechanical testing were dependent on whether the tests were conducted at room temperature or an elevated temperature environment. Section 4.3.1 discusses further details for the room temperature test apparatus, while Section 4.3.2 presents a description of the elevated temperature test apparatus. Although the discussion in the subsequent sections refers to the braided composite specimens, the experimental setup was the same for the 8HS woven BMI and 4HS woven RP46 laminate specimens.

4.3.1 Room Temperature Setup

For the room temperature tests, the MTS 322 test frame was equipped with MTS 647.25A-01 hydraulically operated wedge grips (force capacity: 250 kN dynamic, 333 kN static). A photograph of the typical room temperature experimental setup is shown in Figure 26. Alignment of the test frame grips was verified by using a steel sample that consisted of three bonded strain gages. Minimal out-of-plane and in-plain bending was observed (<2%), which was in accordance with ASTM standard D3039 [176]. For the room temperature tests, a number of techniques were used to measure strain during both static and fatigue tests. For all the static tests, axial and transverse surface bonded resistance strain gages, a clip-on extensometer and FBG optical sensors were used to monitor strain. Although this was redundant, the objective was to calibrate the three types of strain sensors with one another, as was similarly done by

Montesano *et al.* [125]. For the fatigue specimens, a clip-on extensometer was used for all tests, and FBG optical sensors were used for a number of these tests. Vishay EA-06-250AE-350 strain gages were used to measure axial strain and longer CEA-06-500UW-350 strain gages were used to measure the transverse strain, both of which were bonded to the specimen surface with M-Bond 200 adhesive. As specified in ASTM Standard D6856 [175], the strain gages were chosen to have a gage length greater than the length of one unit cell of the braided geometry. A photograph of one of the static test specimens showing the bonded strain gages is shown in Figure 27 (a). Polyimide coated FBG sensors with grating lengths between 5 mm and 10 mm, and Bragg wavelengths in the range of 1530 - 1580 nm were employed in this study. The FBG sensor gage lengths were smaller than one unit cell of the braided geometry, and were intentionally chosen as such in order to detect micro-scale strains. The FBG sensors were also bonded to the specimen surfaces using M-Bond 200. An MTS 634.12F-24 extensometer with a 25 mm gage length and supplied mounting clips was used for the tests. A photograph of a gripped test specimen equipped with the MTS extensometer and a surface bonded FBG sensor is shown in Figure 27 (b). The strain gages were each connected to separate P3 strain gage indicators (see Figure 26), which were both connected to the MTS TestStar IIm through an analog input. The extensometer was connected directly to the MTS TestStar IIm, which was calibrated specifically for the data acquisition unit. This ensures the strain gage and extensometer data is synchronized with the force and displacement data through the data acquisition unit with a consistent time-stamp. The FBG sensors were connected to a Micron Optics si425 interrogation device (connected to a separate PC), which provides the light source and records the reflected light wavelength. The si425 was independent of the MTS data acquisition unit, thus post-test interpolation algorithms were utilized for synchronizing the FBG data with the remaining test data. An Ando Aq6331 optical spectrum analyzer (OSA) was also employed for a number of tests to capture the entire FBG sensor wavelength spectrum. For the fatigue tests that employed FBG sensors, a k-type thermocouple adhered to the specimen surface was used to monitor the specimen surface temperature rise due to self-generated heating. The slight change in the surface temperature was used to correct the FBG signals in order to extract the actual mechanical strains.

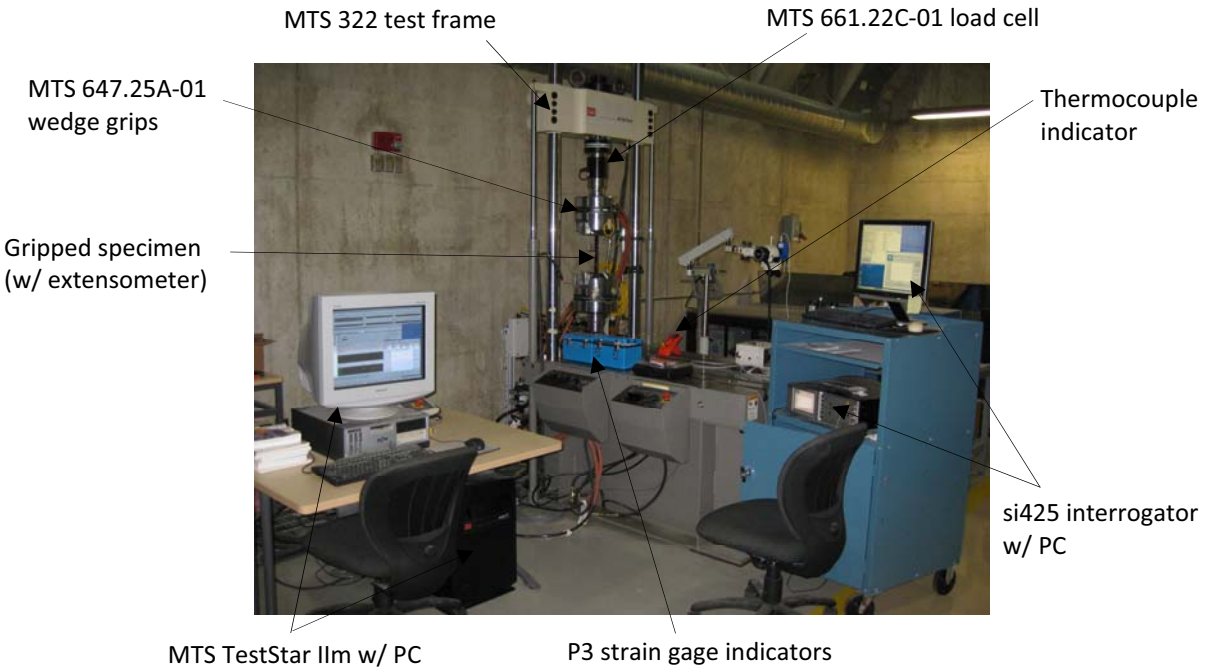

Figure 26. Typical room temperature experimental setup.

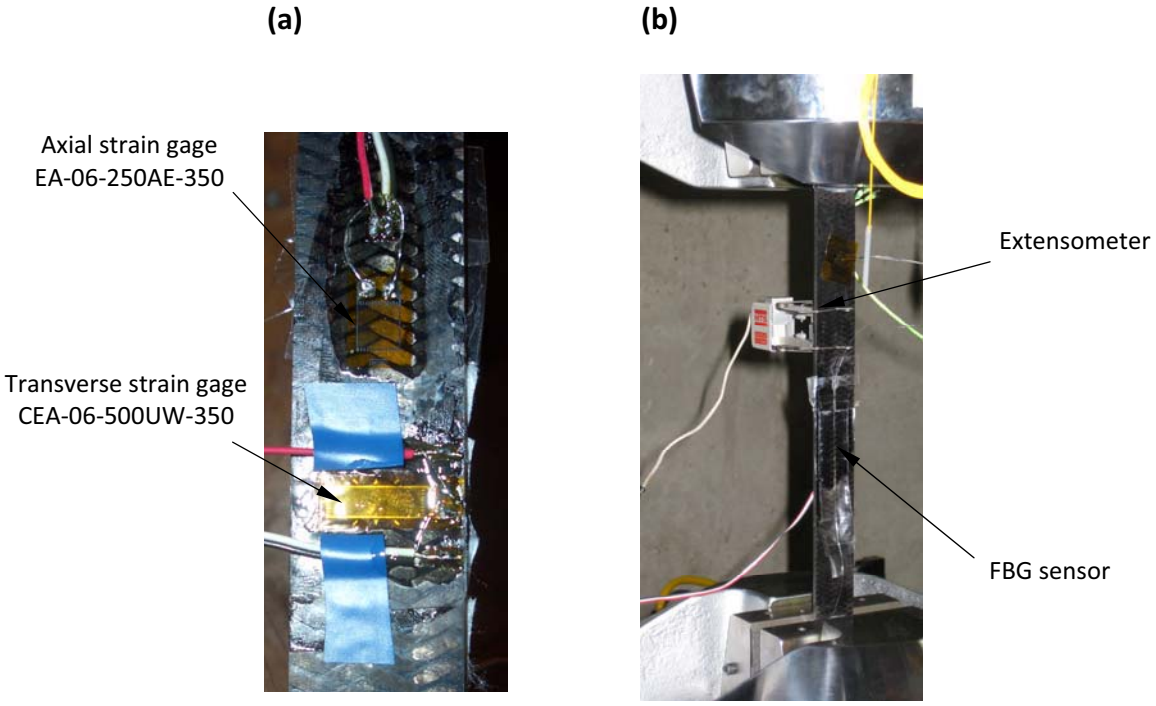

Figure 27. Strain monitoring sensors (a) axial and transverse strain gages, (b) MTS extensometer and FBG sensor.

4.3.2 Elevated Temperature Setup

For the elevated temperature tests, the MTS 322 test frame was equipped with custom clamp-type mechanical grips. Alignment of the test frame mechanical grips was verified by using the same steel sample as was used for the hydraulic grips, again with minimal out-of-plane and in-plane bending (<2%). An ATS 3610 environmental chamber with an integrated Watlow EZ-Zone controller was used to maintain the elevated temperature environment. The mechanical grips protruded into the chamber to ensure that the entire test specimen was subjected to the heated environment. The dual-thermocouple chamber provided convective heating to efficiently mix the air, which ensured the temperature along the length of the specimen was consistent within ±1˚C and that the temperature in the chamber was consistent for the duration of the test within ±0.5˚C. Prior to testing, the temperature was ramped-up at a rate of 5˚C/minute from room temperature to the target test temperature. Once the target test temperature was reached, the specimen was allowed to condition for at least 60 minutes to ensure thermal stability before beginning each test. For a number of tests, a K-type thermocouple was adhered to the specimen surface using Kapton tape to ensure the specimen temperature was in fact the same as the ambient air within the chamber. A photograph of a gripped test specimen within the environmental chamber is shown in Figure 28 (a), and a photograph of the operating environmental chamber is shown in Figure 28 (b).

To monitor the axial strain, an Epsilon 3555-0100-020 HT un-cooled capacitive-type high temperature extensometer with a 25 mm gage length was used. The extensometer was surface mounted on the specimen and operated within the high temperature environment (see Figure 28 (a)). The Epsilon extensometer was connected to a calibrated 3603 signal conditioner, which was connected through an analog input on the MTS TestStar IIm to ensure synchronization with the force and displacement data. For some tests, Vishay WK-06-250BG-350 strain gages were used to measure axial strain, and were bonded to the specimen surfaces using M-Bond 610 high temperature adhesive. These strain gages were connected to the same P3 strain indicators shown in Figure 26. In addition, similar polyimide coated FBG sensors used for the room temperature tests were employed for some elevated temperature static and fatigue tests, where the same aforementioned interrogator and OSA were also employed. For the fatigue

tests that employed FBG sensors, the aforementioned surface adhered k-type thermocouple was also used to monitor the specimen surface temperature rise due to self-generated heating. The slight change in the surface temperature was used to correct the FBG signals in order to extract the actual mechanical strains. Note that for all elevated temperature tests, once the specimen was conditioned at the test temperature for the required time, the strain was zeroed to ensure only mechanical strains were measured.

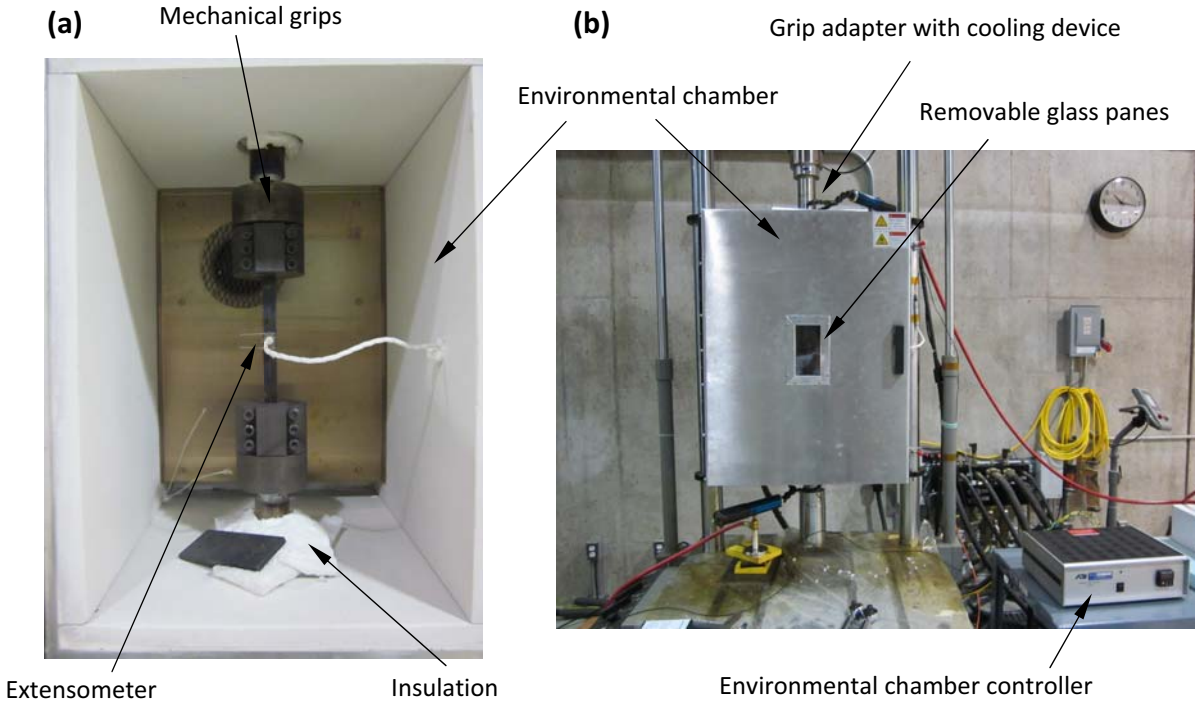

Figure 28. Elevated temperature experimental setup (a) gripped specimen in open chamber, (b) operating chamber with door closed.

4.4 Details of Damage Monitoring Techniques

The fundamental details of the damage monitoring techniques employed in this study were presented in Section 3.6. As indicated, FBG sensors and ER were used to detect local damage modes, track progression of different damage modes, and count cracks. IRT was used to develop a global map of damage and to observe the general development of damage throughout the specimen. These three techniques are considered NDE techniques. Finally, post *mortem* destructive SEM analysis was used to confirm the damage modes observed using ER, to determine the extent of damage and the distribution of damage, and to inspect for additional

small-scale damage modes. These techniques were employed for both static and fatigue tests, at both room temperature and elevated temperatures. Note that these techniques were used for a number of static tests, and a number of fatigue tests at various maximum applied stresses, but were not employed for all conducted tests. The details of the equipment and the procedures for applying these techniques will be discussed in the following paragraphs.

Uniform FBG sensors were bonded on the specimen surfaces to measure local strains, where an optical interrogator and an OSA were used to facilitate their use, as described in Section 4.3. The interrogator continuously recorded wavelength data with a frequency of 50-250 Hz. The data was then used to determine the local strains, as well as the number of peaks in a chirped FBG signal. These signals could then be related to the stress-strain data at a particular strain level for a static test, or a particular loading cycle for a fatigue test and correlated to a certain damage event. On the other hand, the OSA was used to record the entire wavelength spectrum to achieve the same objectives. Due to the slow 'sweeping' capability of the OSA, tests had to be paused in order to capture the spectra. In this study, static tests were paused at particular strain levels during quasi-static loading, while fatigue were paused after a certain number of loading cycles (i.e., various predetermined cyclic intervals). The same processes were used for all test temperatures, and the elevated temperature environment was uninterrupted for those tests.

An ER technique was used to track damage development during both static and fatigue testing. The specimens used for extracting the replicas, which were originally wet sanded with 180-grit and 320-grit paper, were subsequently wet polished with 600-grit and 1200-grit paper, and finally with 1-micron diamond paste using an extender fluid on a felt polishing cloth. This ensures that the microstructure of the constituent materials on the specimen edge where the replicas were extracted is clearly visible under microscopic investigation. During the tests, the replicas were taken by generously wetting a 125 μm thick cellulose acetate film with acetone using a cotton swab. The film, which was secured to a rubber pad, was then pressed firmly against the polished edge of the specimen for approximately 60-90 seconds which allowed time for the acetone to properly dry. This process consistently resulted in clear replicas of the microstructure and the associated damage. The rubber pad was used since it readily moulds

around the specimen edge, providing a uniform pressure on the replication area for a superior edge replica. The replicas were subsequently observed using an optical microscope. Edge replicas were extracted at or near the center of the specimens. For determining crack densities, the number of cracks in an area of 10 mm^2 was considered (see Appendix A.1 for more details). Both static and fatigue tests were required to be paused in order to extract the replicas. For the room temperature static tests, the tests were paused after particular strain levels were attained and the replicas were extracted. For room temperature and elevated temperature fatigue tests, the tests were paused after a certain number of loading cycles (i.e., various predetermined cyclic intervals) to extract the replicas. Note that for the elevated temperature fatigue tests, the specimen was cooled to extract the replicas and subsequently re-heated to continue cycling. This was done at each predetermined cyclic interval. The specimens were cooled at a very slow rate (~ 2˚C/min) in order to avoid any 'thermal cyclic' effects on the test specimens, and were heated with the same rate originally used (i.e., 5˚C/min). This did not have a significant effect on the material behaviour, which was confirmed by comparing the fatigue lives and stiffness degradation profiles with the specimens that were continuously cycled without extracting the replicas.

IRT was utilized to record temperature data from the surface of static and fatigue loaded test specimens. A FLIR SC5000 IR camera with a pixel resolution of 320x240 and a temperature sensitivity of <20 mK was used in a passive approach to monitor the loaded specimen surface temperature. This enabled the detection of the thermal emissions caused by damage initiation and/or propagation within the composite during both static and fatigue loading. The commercial software Altair was used in conjunction with the IR camera to capture the specified thermographic images. For the static tests, images were captured in a real-time video with a frame rate of 50 Hz, which allowed for real-time capture of damage progression. For the fatigue tests, images were captured in a sequential video with a frame rate of one frame per cycle (or every 10th cycle for some tests). This enabled tracking the temperature profile as a function of the number of loading cycles, and to detect damage development during cyclic loading by comparing the sequence of obtained thermographic images. In order to facilitate this for the fatigue tests, the IR camera was synchronized to the MTS TestStar IIm digital controller. An

analog voltage signal was generated by the load data in the MTS controller and was sent as input for triggering the image sequences for the IR camera. These images were triggered at the same point for each particular cycle (i.e., when the maximum stress was attained). This was necessary in order to eliminate any variation in temperature due to reversible thermoelastic heating which is caused by cycling between maximum and minimum cyclic stresses [118]. A schematic of temperature variation due to thermoelastic heating and heat dissipation during cyclic loading is shown in Figure 29 (a), while a schematic of when the IR camera is triggered to extract images during each cycle is shown in Figure 29 (b). The IRT technique was utilized continuously and in-situ without interrupting the tests. In order to use IRT for the elevated temperature tests, the observation window glass of the environmental chamber was removed (see Figure 28), which was necessary to allow the emitted IR waves to reach the camera. A photograph of the room temperature setup utilizing the IR camera is shown in Figure 30.

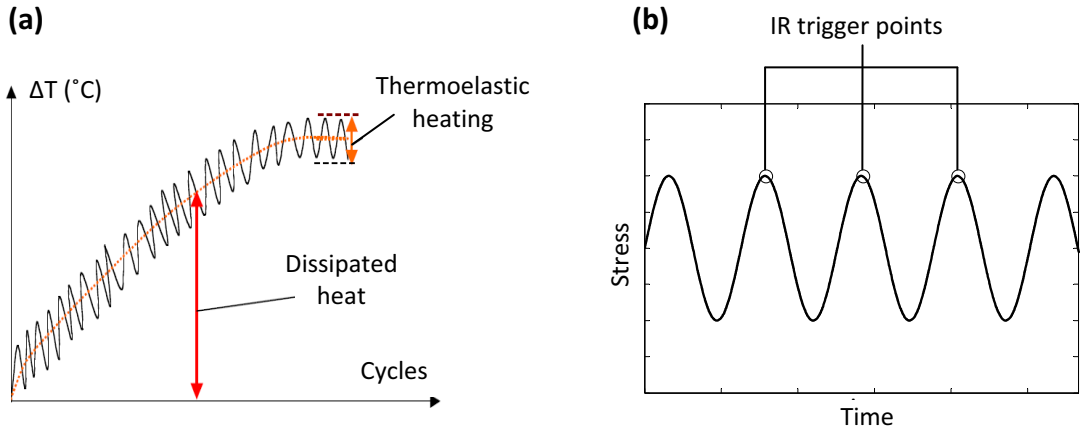

Figure 29. Fatigue loading (a) schematic of temperature variation, (b) IR camera image trigger points per cycle.

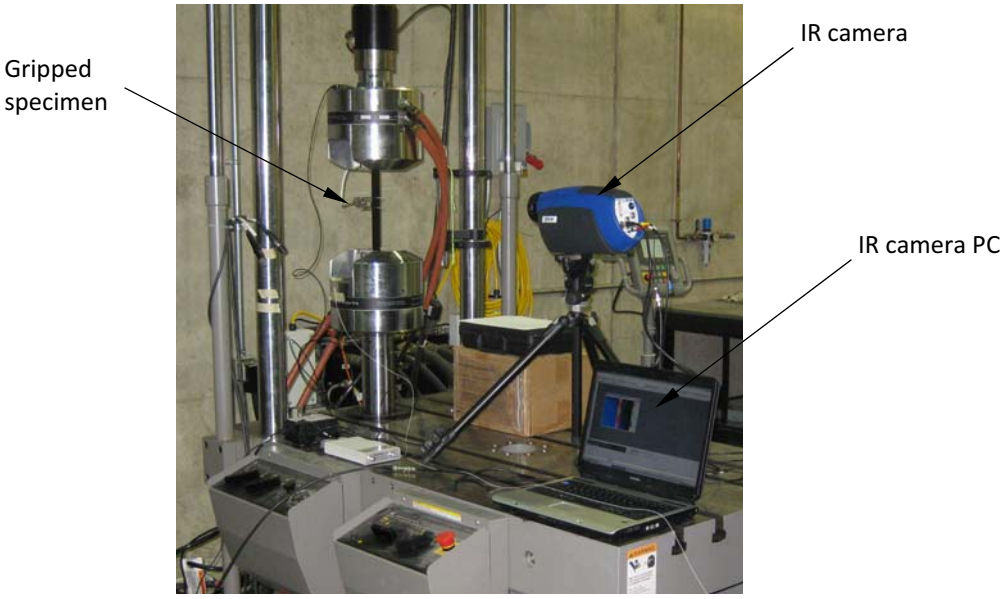

Figure 30. Room temperature experimental setup with IR camera.

Finally, the destructive technique employed in this study was microstructure characterization using a SEM. The test specimens that were inspected post *mortem* were sectioned into small samples using a wet diamond saw, mainly in the cross-sectional or axial-sectional planes of the test specimens. The cut samples were then mounted in a cylindrical mould and a cold-curing epoxy was used to create a puck with the embedded sample. The inspection edge of the sample was visible at the surface of the puck, and was subsequently wet sanded with 180-grit and 320-grit paper, followed by wet polishing with 600-grit paper, 1200-grit paper and 1-micron diamond paste using an extender fluid on a felt polishing cloth. The inspection edge was then gold-coated in a Denton Vacuum Desk IV (CTC Parker Automation). The samples were all examined under a JEOL JSM-6380LV SEM, while some samples were inspected using an optical microscope. For examining the fracture surfaces using the SEM, no preparation was required. It should be noted at this stage that for the braided composite, SEM examination was also used to confirm that damage was in fact widespread throughout the specimen width and thickness. SEM examination of all tested samples revealed that visible damage on the edges was consistent with damage in the interior of the specimens (i.e., there

was no edge-induced damage). This observation allowed for effective use of the aforementioned ER technique, the results of which will be presented in Chapter 5.

4.5 Test Procedures

Although tests were conducted at both room temperature and elevated temperatures, the tests were all conducted under isothermal conditions. The test procedures presented in the subsequent paragraphs were similar regardless of the test temperature. The room temperature recorded for those corresponding experiments was approximately 25˚C, while the elevated test temperature for the braided and woven/RP46 specimens was ($T_{g,\ wet}$ - 28)˚C. The test temperature for the woven/BMI specimens was 205˚C.

Uniaxial ultimate static tensile tests were conducted in displacement control with a constant displacement rate of 2.0 mm/minute, in accordance with ASTM Standard D3039 [176]. For static tests that were paused for edge replica extraction, once the replicas were obtained during the displacement dwell, loading was resumed under the same displacement rate. Uniaxial tension-tension fatigue tests were conducted in load control with a constant amplitude sinusoidal waveform, a stress ratio of 0.1 and a loading frequency of 5 Hz in accordance with ASTM Standard D3479 [177]. Various maximum stresses were used for the fatigue tests. The test specimens were allowed to cycle until failure occurred or until a predetermined number of cycles was reached. For fatigue tests that were paused under a zero-load dwell for extracting edge replicas, a displacement-controlled static test up to the maximum cyclic load followed by unloading down to the minimum cyclic load was conducted after the replicas were obtained. This provided another means for measuring the evolving specimen stiffness, as is suggested in ASTM Standard D3479 [177]. Cycling was resumed after the intermediate cyclic test was completed. Note, for all static and fatigue tests that employed ER, the interruption of the tests did not cause any changes in the material behaviour. This was confirmed by comparing the results of those tests with the tests that were uninterrupted.

An alternate type of test was conducted for a few specimens utilizing the IR camera in an attempt to determine the fatigue threshold of the composite. The method was originally developed by Risitano [178] for metallic materials, and will hereafter be referred to as

Risitano's method. The main points for proper application of Risitano's method are summarized in Appendix A.2. Note that only one test specimen was utilized for this test procedure. The method employed here consisted of cycling the specimen with a constant amplitude sinusoidal waveform in load control (R = 0.1, f = 10 Hz) for blocks of 7,000 loading cycles. The test begins with the first loading block subjected to the lowest peak stress level (e.g., 35% UTS - ultimate tensile stress) for 7,000 cycles. Once the 7,000 cycles are completed, the specimen is allowed to 'cool' back to ambient temperatures under a zero-load dwell (recall the surface temperature increases due to loading). The next loading block then begins under the next peak stress, and this procedure continues at incremental peak stresses (e.g., 40% UTS, 45% UTS, 50% UTS, *etc.*) until the specimen fails.

4.6 Data Analysis

The raw data acquired during both static and fatigue tests included the time, LVDT displacement values, load transducer load values, extensometer strains, and for some static tests the strain gage strains and FBG wavelengths. The axial stresses were calculated from the recorded forces and the average specimen cross-sectional area. The extensometer provided an analog signal in units of voltage, which were converted to strain values by the MTS TestStar IIm digital controller based on the manufacturer calibration data. The strain gages also provided an analog signal in units of voltage, but the P3 strain gage indicators were not initially calibrated to the MTS controller. The calibration curves for the P3 indicators were subsequently determined and coded within the MTS controller to provide strain in units of mm/mm. For the FBG sensor wavelength data, Equation (10) was used to determine the corresponding strains.

For the static tests, data was stored with a frequency of one data point every 0.1 seconds for the duration of the test. The axial modulus (E_{11}) was determined by fitting a linear regression to the axial stress-strain data within the axial strain range of 0.1% - 0.6% as specified in ASTM Standard D3039 [176]. The major Poisson's ratio (ν_{12}) was determined by fitting a linear regression to the transverse strain-axial strain data within the axial strain range of 0.1% - 0.6%, also specified by ASTM Standard D3039 [176].

For the fatigue tests, additional data output was required in order to monitor the material hysteretic behaviour during cycling, which was in the form of continuous stress-strain data and 'peak-valley' data periodically recorded at specified cycles. For the fatigue tests that were paused to extract edge replicas, the intermediate static test data was stored with a frequency of one data point every 0.1 seconds during both loading and unloading. To determine the dynamic stiffness, $E(n)$, for a particular loading cycle n, a regression on the axial stress-strain load/unload data was conducted. A schematic of the regression fit for $E(n)$ for a particular cycle, n, is shown in Figure 31. The mean strain and the strain range are determined from the maximum and minimum strains for a particular loading cycle, and defined by:

$$\varepsilon_{mean}(n) = \frac{\varepsilon_{max}(n) + \varepsilon_{min}(n)}{2} \tag{40}$$

$$\Delta\varepsilon(n) = \varepsilon_{max}(n) - \varepsilon_{min}(n) \tag{41}$$

The ratcheting strain, ε_r, can also be quantified by considering the minimum strain for a particular loading cycle, and its difference relative to the minimum strain prior to the first loading cycle.

$$\varepsilon_r = \varepsilon_{min}(n) - \varepsilon_{min}(0) \tag{42}$$

Finally, the energy dissipated per unit volume, $E_d(n)$, during one loading cycle can be determined by quantifying the area between the cyclic stress-strain curves as shown schematically in Figure 31. Although it may be difficult to directly calculate the energy dissipated on a cycle-by-cycle basis from experimental data, storing a sufficient number of data points per cycle during testing can yield fairly accurate predictions [50]. In this study, 80 data points were found to be sufficiently accurate for calculating the dissipated energy per cycle. This was done by numerically integrating the stress-strain data cycle-by-cycle to obtain the area between the corresponding curves.

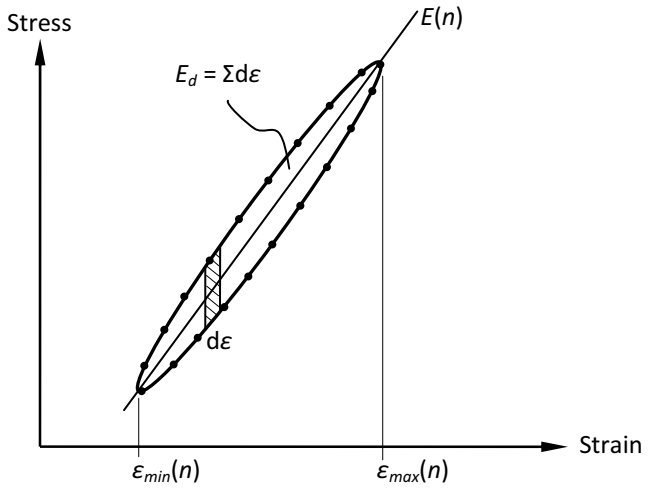

Figure 31. Schematic of dynamic stiffness and energy dissipation for cycle *n*.

5 BRAIDED MATERIAL TEST RESULTS AND ANALYSIS

The experimental results and the corresponding analysis for the triaxial braided test specimens will now be presented. Initially, the room temperature tensile static and fatigue test results will be outlined and discussed, followed by the elevated temperature test results. Additional creep test and aging results for the braided composite will then be presented in Section 5.3. Detailed discussions of the relevant experimental results will be presented within each corresponding section.

5.1 Room Temperature Results

5.1.1 Completed Test Overview

The main initiatives for the room temperature tests were to determine the material properties, develop a fatigue S-N curve, characterize the development of damage during both quasi-static and cyclic tensile loading, and to relate the observed microscopic damage mechanisms to the exhibited macroscopic material behaviour. The room temperature results and observations also provided a basis for the elevated temperature experiments. In total, four ultimate static tensile tests were conducted. Two of these tests included the use of ER while IRT was employed for one test. For the tension-tension fatigue tests, a minimum of two and a maximum of four tests were conducted at each maximum applied stress level. ER and IRT were

employed for a number of fatigue tests at each maximum applied stress level. Also, two additional tests were conducted to determine the braided composite fatigue threshold using Risitano's thermographic method [178].

5.1.2 Static Results

The results of the room temperature static tests outlined in Section 4.5 will be presented. Initially the material stress-strain behaviour and static properties will be shown, followed by a detailed characterization of damage and analysis of the fracture surface.

5.1.2.1 Material behaviour

A typical stress-strain plot for an ultimate static test is shown in Figure 32 (a). At room temperature the material exhibits a bilinear response with an average ultimate tensile stress (UTS) of 393 MPa and a transition stress of approximately 240 MPa, which corresponds to 61% UTS. The transition strain was found to be approximately 0.765%, while the failure strain was 1.38%. The presented static bilinear behaviour for the braided composite is analogous to that exhibited by some statically loaded quasi-isotropic polymeric laminates [7]. The axial modulus (E_{11}) and secondary modulus after transition of the braided composite were found to be 31.13 GPa and 25.2 GPa, respectively, which corresponds to an instantaneous drop in stiffness of approximately 20% at the transition. A plot of the transverse strain-axial strain is shown in Figure 32 (b); the axial strain was obtained using a surface-mounted extensometer while the transverse strain was obtained using a bonded resistance strain gage. The major Poisson's ratio (ν_{12}) was determined to be 0.286, which instantly reduced to 0.234 after the transition. The main material parameters for each tested specimen are summarized in Table 8, with the average values also included. As shown, the scatter in the data is negligible with less than 2% deviation from the average values.

Figure 33 illustrates the static axial stress-strain plots for test specimen B1-08 using both the measured extensometer and strain gage strain values; this particular test specimen was equipped with both a surface mounted extensometer and a bonded strain gage. The extensometer strain values produce a smooth stress-strain profile through the transition, while the strain gage strain values exhibited a slight variation in the signal during the transition. The

strain sensors both produced smooth stress-strain profiles before and after the transition 'region'. The variation in the strain profile during the transition region is due to the difference in the gage length of the strain gage and extensometer, which are 6 mm and 25 mm respectively. The strain gage has detected a variation in the local strain which is caused by a local variation in the test specimen deformation, but was not detected by the extensometer. Additional details regarding this local phenomenon will be presented in the subsequent section.

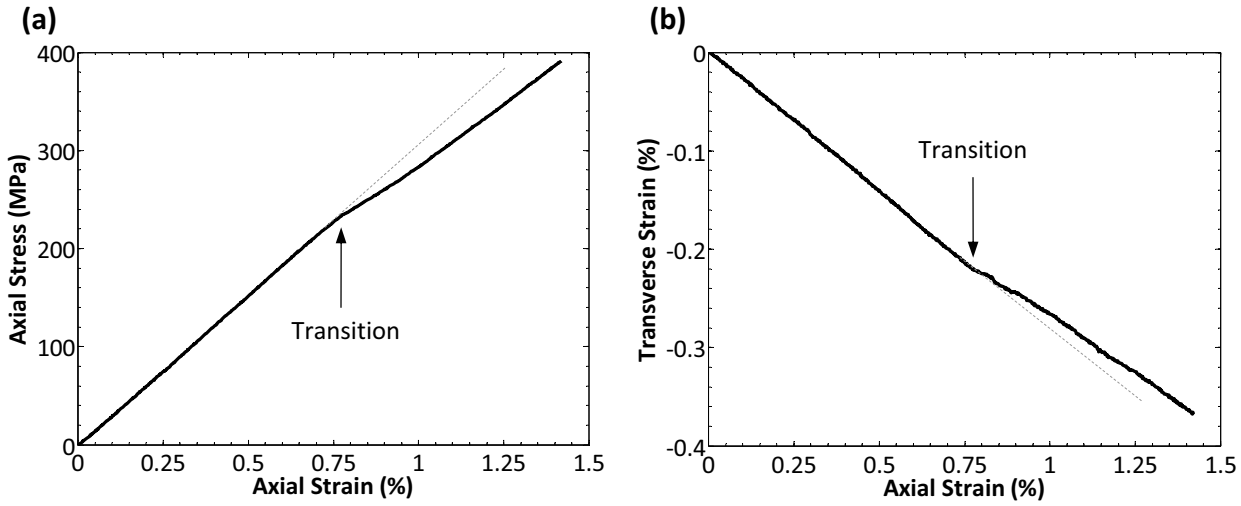

Figure 32. Braided composite (B1-08) room temperature static (a) axial stress-strain plot, (b) transverse-axial strain plot.

Table 8. Room temperature material parameters.

Specimen No.	Transition Stress (MPa)	S_u (MPa)	Failure Strain (%)	E_{11} (GPa)	ν_{12}
B1-08	235	395	1.41	30.6	0.286
B1-10	241	391	1.35	30.9	0.287
B1-11	242	397	1.37	31.9	0.288
B4-04	243	390	1.39	31.0	0.284
Average	**240**	**393**	**1.38**	**31.13**	**0.286**

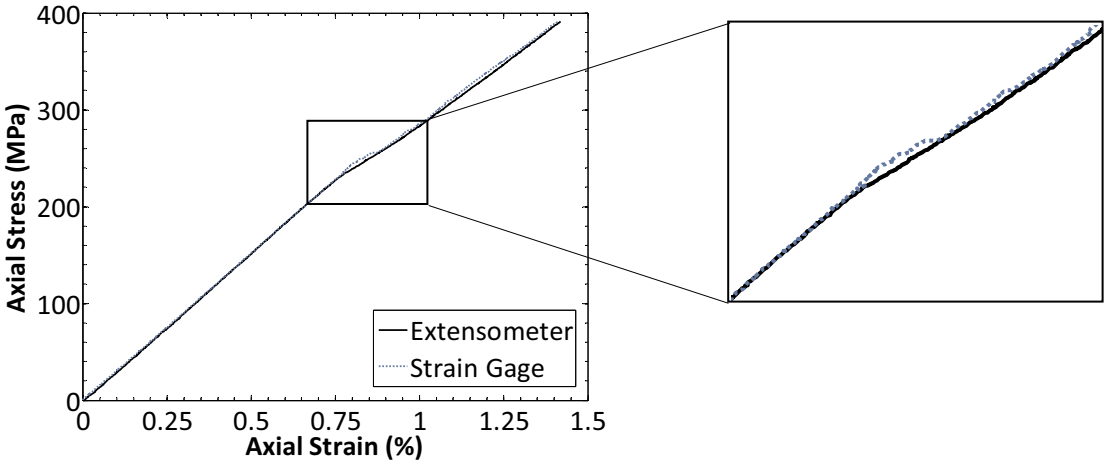

Figure 33. Braided composite (B1-08) room temperature static axial stress-strain plot - magnified.

5.1.2.2 Damage characterization

A microscopic investigation was conducted to track the development of damage from crack initiation up until final specimen failure, as well as determining the cause of the exhibited transition behaviour. To assist with the detection of damage development, FBG sensors, edge replication and IRT were all employed. In addition, post *mortem* SEM, including an analysis of the fracture surface, was utilized to determine the final failure mechanisms. Two of the tested static specimens were suited with surface bonded FBG sensors. Recall that chirping of FBG sensor wavelength spectra is a direct result of a non-uniform strain field along the grating length, which can be caused by local damage in composites. An indication of the degree of FBG sensor chirping is a measure of the total number of detected wavelength peaks, which can qualitatively be associated with local damage. Figure 34 illustrates plots of the number of wavelength peaks and the axial stress during a static test. Initially, only one wavelength peak is detected for the FBG sensor (i.e., no chirping). Once the transition stress is reached after approximately 75 seconds, the first sign of chirping is detected and subsequently followed by significant chirping for the duration of loading up until specimen failure after 132 seconds. This confirms that at the transition stress a significant amount damage suddenly initiated and/or propagated. This is in alignment with the detected strain gage signal variation when the transition stress was attained.

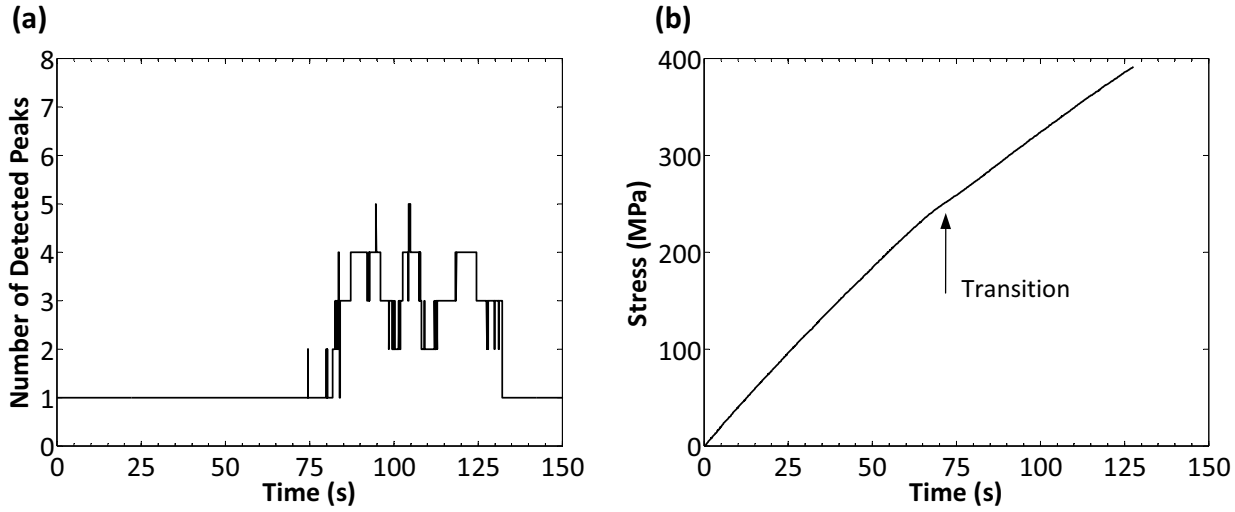

Figure 34. Specimen B1-11 (a) FBG sensor wavelength peak quantity, (b) stress-time plot.

Two of the conducted static tests involved the use of ER to monitor crack development on the specimen edge as the applied stress increased. Recall that the tests were paused at predefined stress levels to extract the edge replicas, after which the loading resumed until the subsequent stress level was attained. This process was repeated until specimen failure occurred, providing a chronology of damage events in the material from initial crack development to final specimen failure. Figure 35 shows a series of images taken of obtained edge replicas using an optical microscope with a 60X magnification. The fiber yarns oriented in the loading axis (i.e., 0˚ direction) are indicated in the image. The off-axis braider yarns are the darker regions, while the lighter regions are the resin-rich zones. The unloaded (virgin) material contained no damage as shown in Figure 35 (a). The three main observed damage modes are illustrated in the photographs of Figure 35 including braider yarn cracks, fiber yarn interface cracks and matrix cracks in the resin-rich zones. Damage initiated at lower stress levels as shown in Figure 35 (b), where the majority of visible cracks were small-scale matrix cracks at the braider yarn-matrix interfaces and cracking within the ±60˚ braider yarns. There were however few cracks at these stress levels. As loading progressed up until a load level of 225 MPa, slightly more braider yarn cracks developed as shown in Figure 35 (c). The observed damage was found to be distributed throughout the specimen, although at this stage in loading the number of cracks per braider yarn was typically limited to one. Note also that at this stage

in loading there were no cracks in the 0˚ yarns and no indication of large-scale fiber yarn debonding, which is analogous to delamination in conventional laminates and will hereafter be simply referred to as large-scale debonding. Once the loading level exceeded the transition stress, the number of observed cracks significantly increased instantaneously and they were widespread with consistent density throughout the specimen length. Again, the majority of cracks observed were through-the-yarn-thickness cracks within the braider yarns with many fiber yarns containing more than one crack. In addition, there was also evidence of some cracking in the 0˚ yarns at this stage. The number of interface cracks between adjacent braider yarns and at the braider yarn-matrix interfaces also slightly increased after the transition stress was exceeded, although these were localized cracks as shown in Figure 35 (d). There was still no indication of any large-scale debonding cracks or cracking at the braider yarn and 0˚ yarn interfaces. As the loading increased beyond the transition stress, the braider yarn crack density slightly increased until just prior to final failure.

The chronology of damage development is shown by the crack density plot (i.e., number of cracks/mm^2) in Figure 36 (a). Three equivalent size zones along the length of the specimen edge were used to determine the average crack density. The three main observed damage mechanisms including braider yarn cracks, yarn interface cracks and matrix cracks are included in the plot. Figure 36 (b) shows a schematic of these three main damage mechanisms observed during static testing. It is illustrated in the plot that the braider yarn crack density increases at a gradual rate during the initial stages of loading. When the transition stress is reached, there is a sudden increase in the braider yarn crack density. Beyond this stage, there is only a slight increase in the crack density up to final failure. The braider yarn cracks are clearly the dominant damage mechanism during tensile static loading, having a much higher density compared to the other observed damage modes. Photomicrographs of the failed specimen cross-section obtained by SEM are shown in Figure 37 (a) and (b), where the 0˚ yarns are outlined for clarity in Figure 37 (a). The damage mechanisms observed on the ER films are confirmed by the SEM photomicrographs, where damage is widespread throughout all of the braider yarns. There are no large-scale debonds or cracks in the 0˚ yarns as shown, where in fact the 0˚ yarns seem to arrest the through-the-thickness braider yarn cracks as seen in Figure 37 (b) and the optical

photograph of the specimen axial-section shown in Figure 37 (c). Although the 0˚ yarns have crimped during manufacturing, there are no indications of any fiber straightening up to specimen failure. The adjacent braider yarn interface cracks are confirmed to be localized as shown, which have resulted from localized shear strains at the crossover locations between +60˚ and -60˚ fiber yarns. This type of localized shearing mechanism between braider yarns was observed for similar geometrical triaxial braided polymeric composites [99].

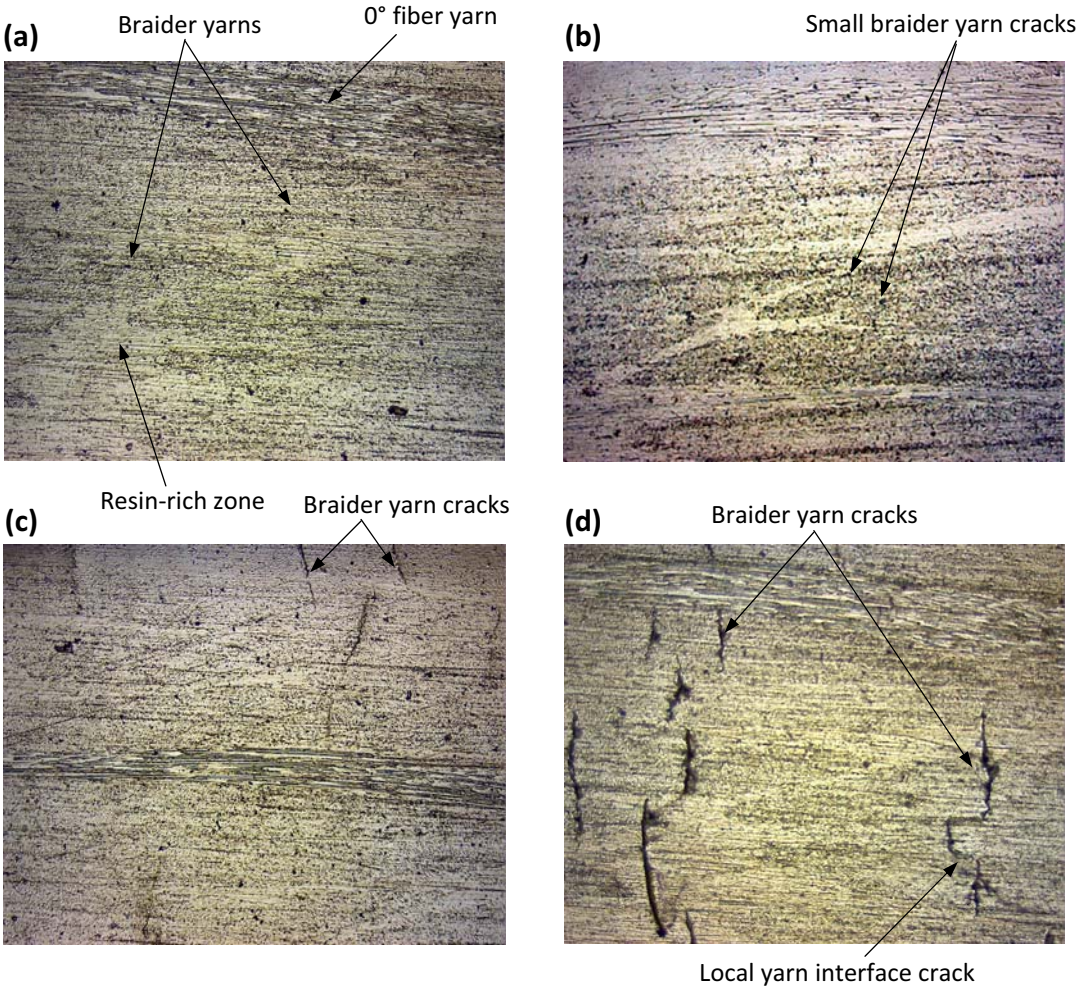

Figure 35. Photographs of braided composite (B1-10) room temperature static test edge replicas with a magnification of 60x (a) unloaded (virgin), (b) 55 MPa, (c) 225 MPa, (d) 300 MPa.

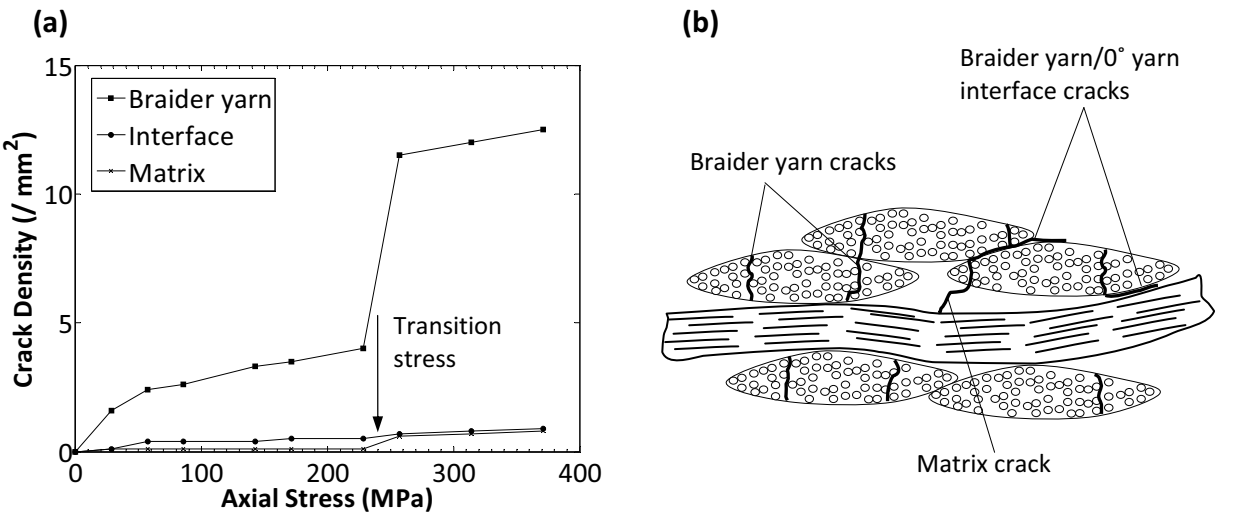

Figure 36. (a) Braided composite room temperature static crack density profiles, (b) crack schematic.

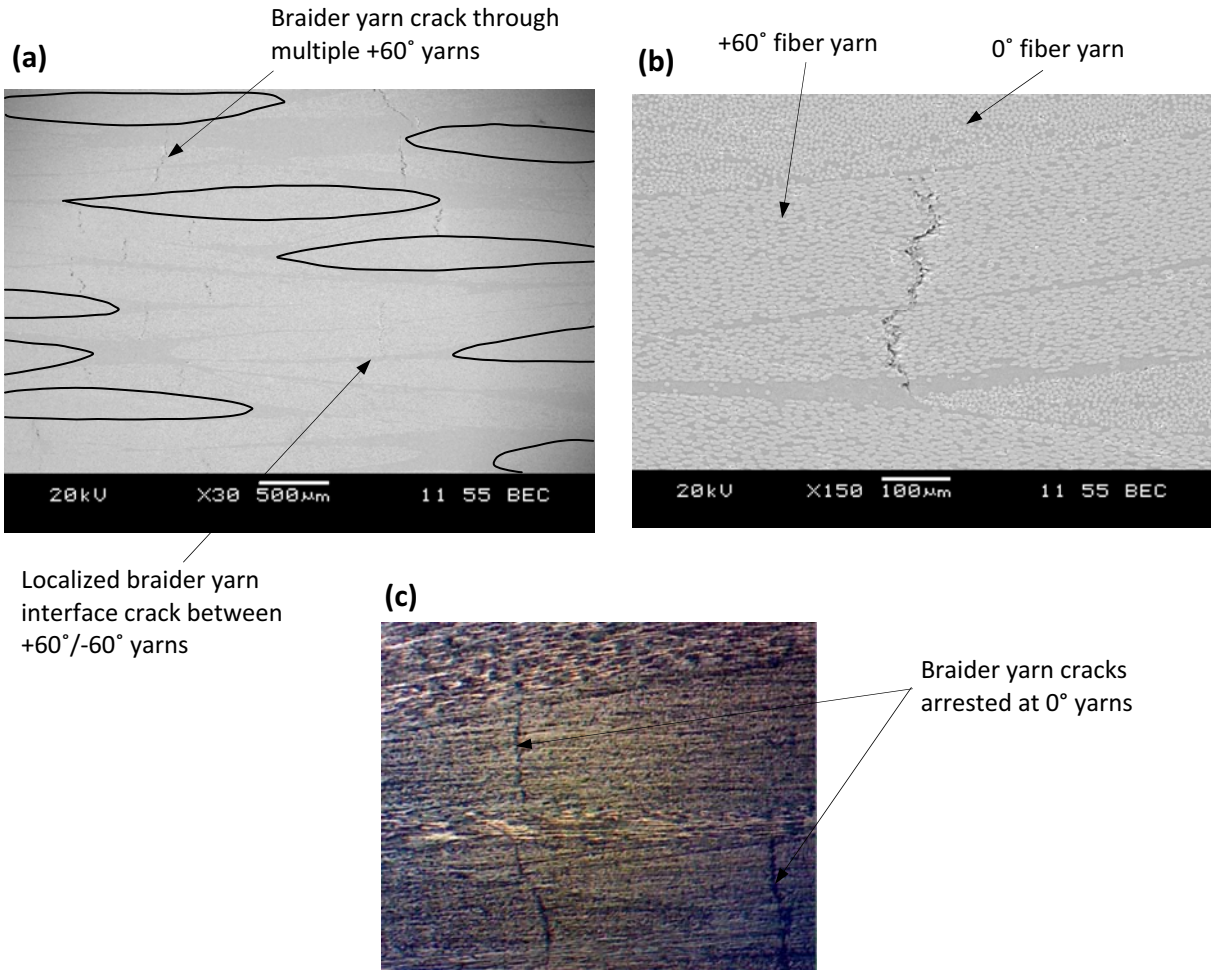

Figure 37. Braided composite (B1-08) room temperature static test (a) - (b) SEM photomicrographs of cross-section with 30x and 150x magnification, (c) optical photograph of axial-section with 60X magnification.

It is clear that the exhibited stress-strain behaviour is dominated by the observed damage development mechanism in the braider yarns. It can be gleaned that during static loading prior to the transition stress level, there are a number of smaller braider yarn cracks that are possibly not yet through the entire yarn thickness and not propagated along the entire length of the braider yarns. When the transition stress level was attained, these small braider yarn cracks instantly propagated along the braider yarn axis, and possibly many cracks within a braider yarn at different locations along its length instantly coalesced. This was the cause of severe FBG sensor chirping (see Figure 34 (a)). This ultimately caused the braider yarns to be less effective in resisting axial stresses and transverse deformation. As a result, a portion of the stress was redistributed to the 0˚ yarns and the axial material compliance instantaneously increased. This is analogous to the 'first ply failure' phenomenon exhibited by some quasi-isotropic laminates, which exhibit similar stress redistribution upon the loss of the load carrying capability of the transverse or off-axis plies [20]. The transverse compliance also instantaneously increased which was in part due to a reduction in local shear deformation resistance and slight rotation of the braider yarns. This was observed by the localized interface cracks between the +60°/-60° braider yarns. In addition, the observed cracks in the braider yarns would tend to cause the yarns to separate in the direction normal to the yarn axis which would also contribute to the increased compliance in both the axial and transverse directions.

To further confirm the discussed damage development states, IRT was employed for one static test specimen to continuously monitor the specimen surface temperature in real-time up to failure. Figure 38 (a) through (d) presents a series of thermographs extracted from a video that was captured using the IR camera at the indicated stress levels. The contours shown in the thermographs are in fact the rise in temperature (i.e., ΔT), not the absolute temperatures. The real-time thermographs confirm that the temperature peaks consistently occurred within the braider yarns, which correspond to extensive cracking in those fiber yarns. Strains are typically higher in the braider yarns in triaxial braided composites, which would result in extensive cracking in these yarns [99]. It is also confirmed that the density of braider yarn cracks was much higher during the latter stages of loading and that damage was widespread throughout the specimen length. The initiation of damage in the braider yarns is indicated by the sudden

temperature increases in the braider yarn regions (i.e., the lighter regions in the thermographs) at lower stress levels (see Figure 38 (a)). As loading progressed the initiated cracks began to propagate along the braider yarn directions and additional cracks continued to form, which maintained higher temperatures within the damaged braider yarns and/or caused more sudden temperature increases, respectively. As the transition stress was attained, the sudden onset and propagation of braider yarn cracking was captured as shown in Figure 38 (c). As the stress level approached the ultimate, the braider yarns all showed indications of cracking, which is consistent with the post *mortem* SEM observations. The IR camera has successfully captured the progressive damage states within the braider yarns during static loading. In order to more clearly illustrate the temperature variation between the braider yarns and the resin-rich zones of the test specimens, an additional test was conducted using the lock-in thermographic feature of the IR camera. Lock-in thermography is useful for establishing local stress concentrations on materials based on the principle of thermoelasticity [179]. To facilitate this, a test specimen was cycled at a low stress level of 120 MPa with a loading frequency of 5 Hz and a stress ratio of 0.1. This allowed the test specimen gage section to obtain a constant surface temperature, which was required for the lock-in feature of the IR camera to accurately perform. An obtained thermograph of the specimen is shown in Figure 38 (e). The high temperatures exhibited by the braider yarns are clearly regions subjected to higher local stresses when compared to the resin-rich zones between the braider yarns. This further supports the damage observations obtained through SEM and from the edge replicas, as well as the occurrence of instantaneous braider yarn crack development at the transition stress which caused increased material compliance.

The fracture surfaces of ultimate tensile static test specimens were also investigated to determine the final damage states which led to the observed test specimen failure event. Figure 39 (a) is an image of the fracture surface, while Figure 39 (b)-(c) are photomicrographs of the fracture surface obtained by SEM. The area affected by the fracture is very localized as shown. The fracture line has propagated along the +60˚ braider yarn axis, which resulted in fracture of the 0˚ and -60˚ fiber yarns. The material stress-strain behaviour revealed that there was no significant elongation prior to failure indicating brittle-natured fracture, which is clear in Figure 39 (a). The presence of fiber pull-out is revealed by the brushy appearance of the

fracture surface and confirmed in Figure 39 (b) by the bare fibers, which is a characteristic of brittle fracture. Furthermore, there was little indication of large-scale debonding and evidence of localized matrix fall-out in the fracture region which is also a characteristic of brittle-natured fracture. The fractured braider yarns tended to separate into smaller bundles as shown in Figure 39 (c), which is due to the existing cracks that developed in the braider yarns during loading. The separation of the 0˚ yarns due to splitting cracks reveals that cracking in these yarns occurred just prior to fracture; these type of cracks were not observed at locations in the specimens further from the fracture surface. Prior to failure, the braider yarn crack density reached a threshold after which local fiber breakage and matrix cracks significantly developed in and around these yarns at the eventual fracture location. At this stage the 0˚ yarns were supporting the entire applied load, which resulted in localized splitting and weakening of these yarns. This subsequently led to more local fiber fracture, which ultimately resulted in fracture of the 0˚ yarns at final failure instantaneously. Note that there was only evidence of slight localized fiber yarn rotation at the fracture surface as is clear in Figure 39 (a). In addition, the obtained thermographs further confirmed that the fracture zone was in fact localized, and was preceded by a high accumulation of local high temperature 'hot spots' (i.e., local damage development).

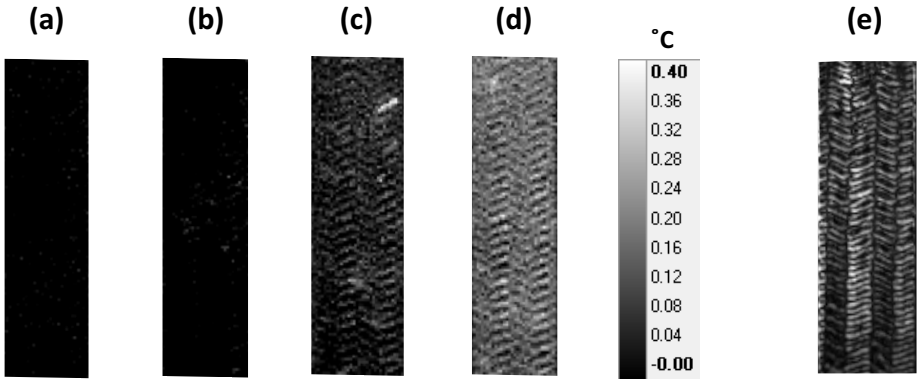

Figure 38. Captured IR thermographs for static test at (a) 98 MPa, (b) 205 MPa, (c) 248 MPa, (d) 322 MPa; (e) thermograph acquired using lock-in thermography.

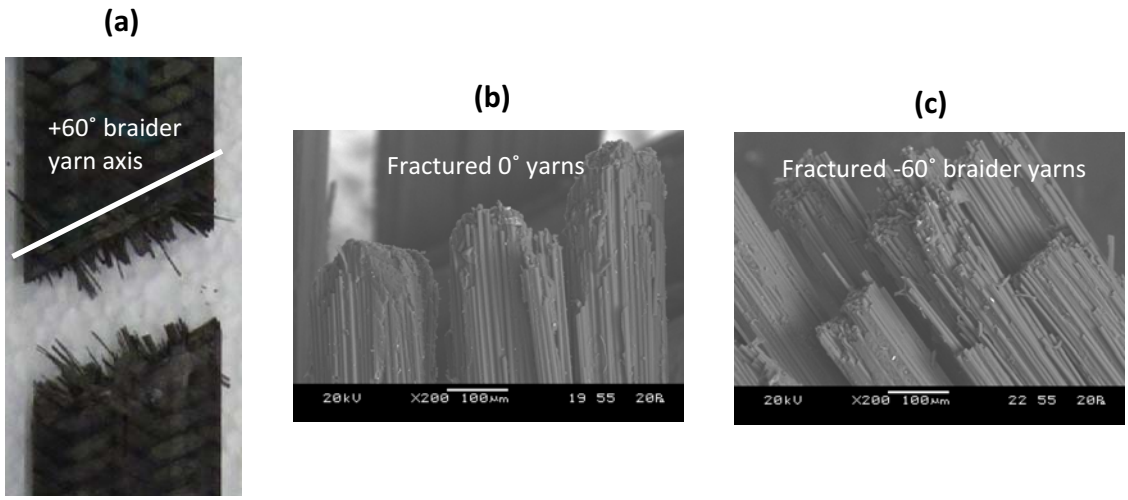

Figure 39. Static test specimen - B1-08 (a) image of fracture surface, (b)-(c) SEM photomicrographs of fracture surface with 200X magnification.

An illustration of the braided static test specimen progressive damage states is shown in Figure 40 as images superimposed on the corresponding stress-strain curve. The various damage states discussed from crack initiation to rapid braider yarn crack development and final specimen failure are illustrated. Although the stress-strain behaviour was somewhat distinct, similar damage modes were found to occur in another triaxial braided composite [98]. Complementary details can be found in Reference [180].

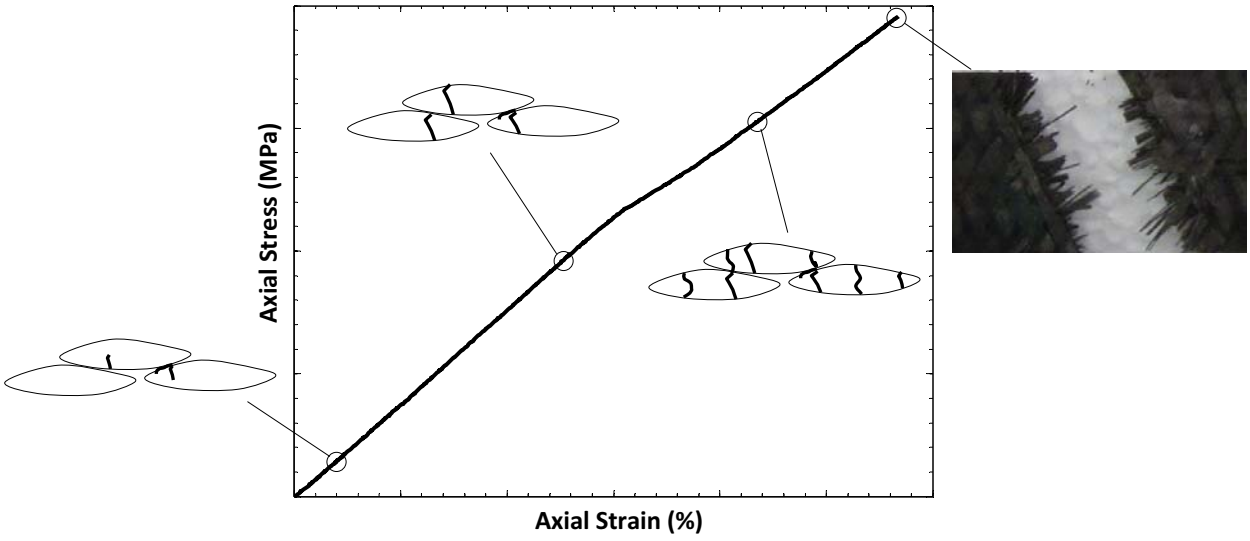

Figure 40. Progressive damage states superimposed on static stress-strain curve.

5.1.3 Fatigue Results

The results of the room temperature fatigue tests outlined in Section 4.5 will now be presented. Initially the developed S-N curve will be presented, followed by an overview of the exhibited material behaviour, a detailed characterization of damage development, and finally a discussion focussed on correlating the microscopic damage observations with the exhibited material behaviour.

5.1.3.1 S-N data

Fatigue tests were conducted for a number of maximum applied stresses within the range of 50%-85% UTS until specimen failure occurred or until a predefined run-off was reached. The corresponding stress-life (S-N) curve for the braided composite is shown in Figure 41, where the average fatigue life values for each maximum applied stress are shown in the plot. Note that due to the limited number of test specimens available, a statistical analysis of the S-N data was not conducted and therefore omitted. The ordinate of the plot is the ratio of the maximum applied stress over the static ultimate tensile stress (σ_{max}/S_u), while the abscissa is the number of cycles to failure (N_f) on a logarithmic scale. The data point on the ordinate corresponds to the static strength of the material. A run-off of 10^7 cycles was defined in this study as is indicated on the plot for stress levels of 50% and 60% UTS, which did not amount to failure for any test specimens cycled at these maximum applied stresses. For composite materials a semi-logarithmic relationship is often found to fit the S-N data, which was the case for the S-N data presented in Figure 41. The corresponding relationship determined from a numerical regression analysis is defined in Equation (43). Note that data for the test specimens cycled for 10^7 cycles without failure were not included in the regression. The data correlation factor, R^2, of 0.9930 illustrates that the S-N data has an excellent fit defined by the semi-logarithmic relationship. The numerical coefficients of Equation (43) for the braided composite at room temperature were found to be A = 0.0507 and b = 1.00.

$$\frac{\sigma_{max}}{S_u} = b - A\log\left(N_f\right) \tag{43}$$

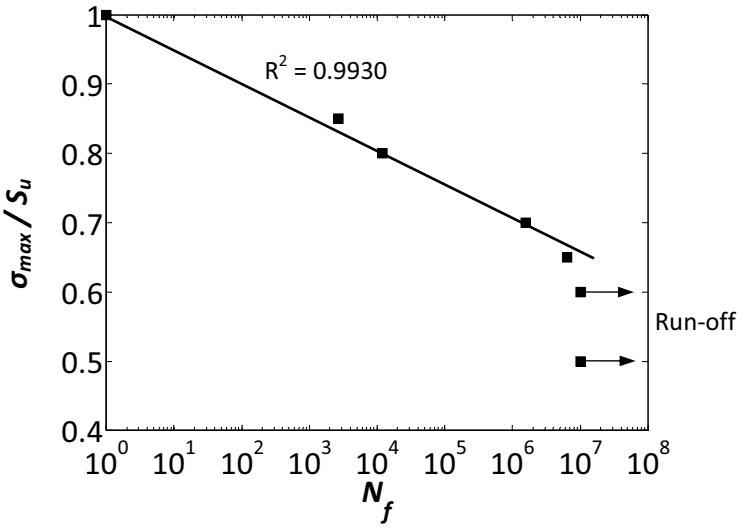

Figure 41. Room temperature S-N curve, R = 0.1, f = 5 Hz.

The S-N data suggests that there may in fact be a fatigue limit for the braided composite material, or more accurately a high cycle fatigue strength (HCFS), which may exist in the range of 60-65% UTS (235-255 MPa). From the results of many fatigue studies available in the literature it appears that conventional polymeric composites do not typically have a fatigue limit, but instead damage progresses during the entire life of the material which causes failure even at very low applied stresses [16]. This was previously discussed in Section 3.1. It has been recently shown that some polymeric composites do exhibit a fatigue threshold or HCFS, which may be due to a damage saturation state at lower applied stresses hindering the onset of failure [181]. This may not necessarily be a true fatigue limit but a new 'finite life region' that is distinct from the main slope of the S-N curve, as shown in Figure 41. This is in fact a characteristic of the triaxial braided composite material under investigation.

To confirm the existence of a HCFS, Risitano's thermographic approach for rapidly determining the fatigue limit was adopted [178]. This method was used successfully to determine the HCFS of a woven carbon fiber laminate [52], and a non-crimp glass fabric laminate [181]. The tests were conducted using a loading frequency of 10 Hz, as discussed in Section 4.5. Note that although the loading frequency is different when compared to the fatigue tests that were conducted to develop Figure 41, the resulting HCFS determined from the thermographic approach will not alter by varying the loading frequency. Figure 42 is a plot

of the absolute surface temperature as a function of the number of loading cycles for a test specimen, which was obtained using the IR camera. The maximum applied stress for each cyclic sub-test is indicated for each profile in the plot. Note that 7000 loading cycles were applied at each maximum applied stress, which was sufficient for attaining a constant temperature plateau. The temperature profile eventually stabilized which is evident for all indicated stress levels. The same location was used for each stress level to create the temperature profiles shown in Figure 42, which was at the eventual failure location of the test specimen. Figure 43 shows a sequence of surface temperature profiles, after stabilization, within the gage section for the indicated maximum applied stress levels. Up to a cyclic load of 55% UTS, there is uniform temperature across the specimen surface. As the load increases there is a clear region where the temperature is higher (i.e., a hot zone), which is where the specimen ultimately failed. Using each corresponding stabilization temperature, the temperature increase (ΔT_{stab}) is plotted as a function of the maximum applied stress in Figure 44. The maximum stress magnitude at which the dissipated heat rise becomes greater is evident in the plot, which shows the characteristic bilinear profile employed for this thermographic technique. This corresponds to an approximate HCFS of 64% UTS (252 MPa), which is within the range obtained by plotting the S-N curve of Figure 41. This confirms that a HCFS for the braided composite material exists, and has been accurately obtained using thermography.

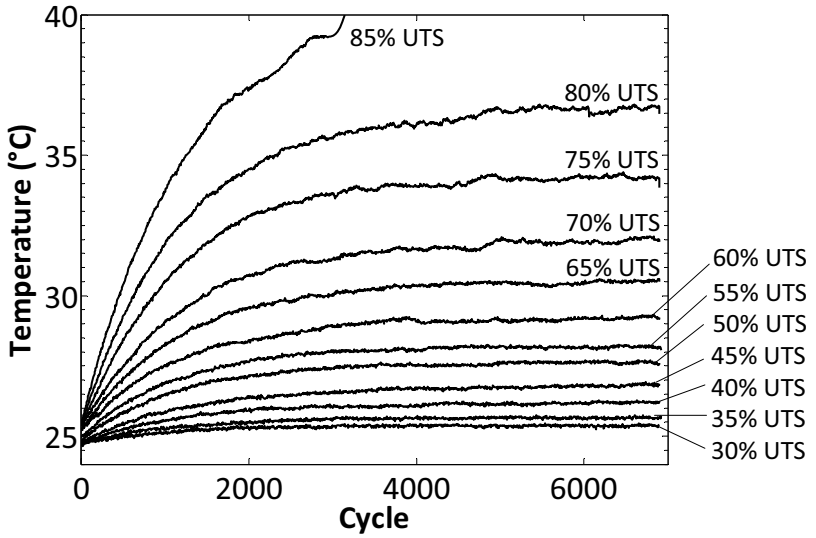

Figure 42. Surface temperature profile vs. cycle for indicated maximum stress magnitudes.

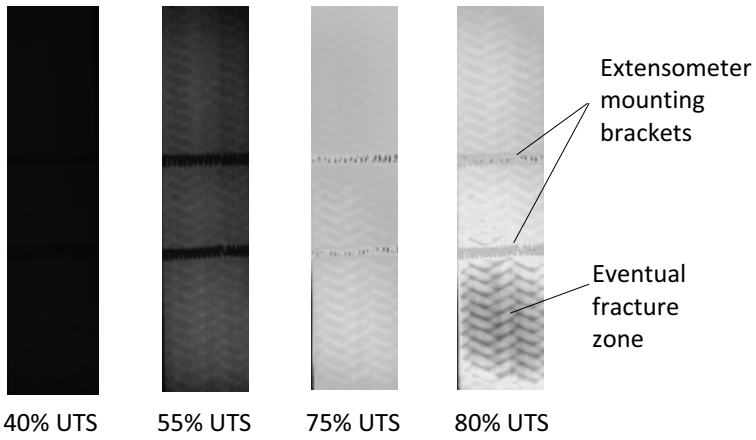

Figure 43. Captured thermographs after stabilization for indicated maximum applied cyclic stresses.

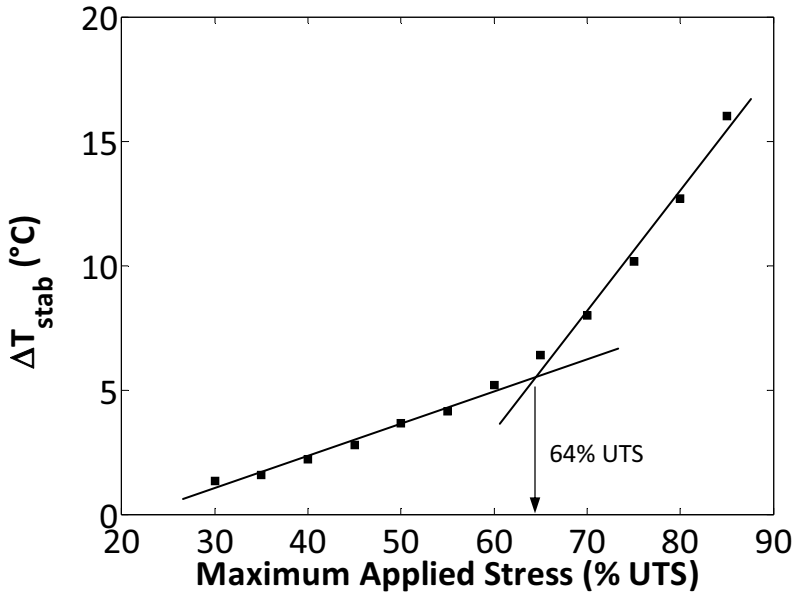

Figure 44. Surface temperature increase at stabilization vs. maximum stress magnitude.

The accuracy of the thermographic technique for determining the HCFS of the braided composite necessitates further investigation into the successful outcome of the approach. It is known that intrinsic energy dissipation in composites during cyclic loading, which may be caused by different modes of cracking or local matrix deformation, results in a corresponding dissipation of heat every cycle [56, 97]. If the energy dissipated per cycle is considered, a correlation between the temperature rise and the energy dissipation can in fact be made. The energy dissipated per unit volume of material during one loading cycle (i.e., hysteresis) can be

determined by quantifying the area between the loading and unloading stress-strain curves (see Section 4.6). By comparing the energy dissipated during a particular cycle during the temperature stabilization range (e.g., cycle 5,000) for each maximum applied stress, a correlation between the energy dissipation and the maximum applied stress was established. A plot of the energy dissipated per unit volume as a function of the maximum applied stress is shown in Figure 45 (a). A similar bilinear profile was obtained as found in Figure 44. A HCFS value of 63% UTS (248 MPa) was found for the composite material, which is similar to that obtained using the thermographic approach. A plot of the energy dissipation per unit volume versus the increase in temperature at stabilization is shown in Figure 45 (b). The relation between the temperature rise and the energy dissipated per cycle is in fact linear, with a data correlation factor, R^2, close to 1. This supports the hypothesis that the dissipated heat measured with the IR camera during cycling is in fact due to the intrinsic energy dissipation of the material, which is an important finding in this study.

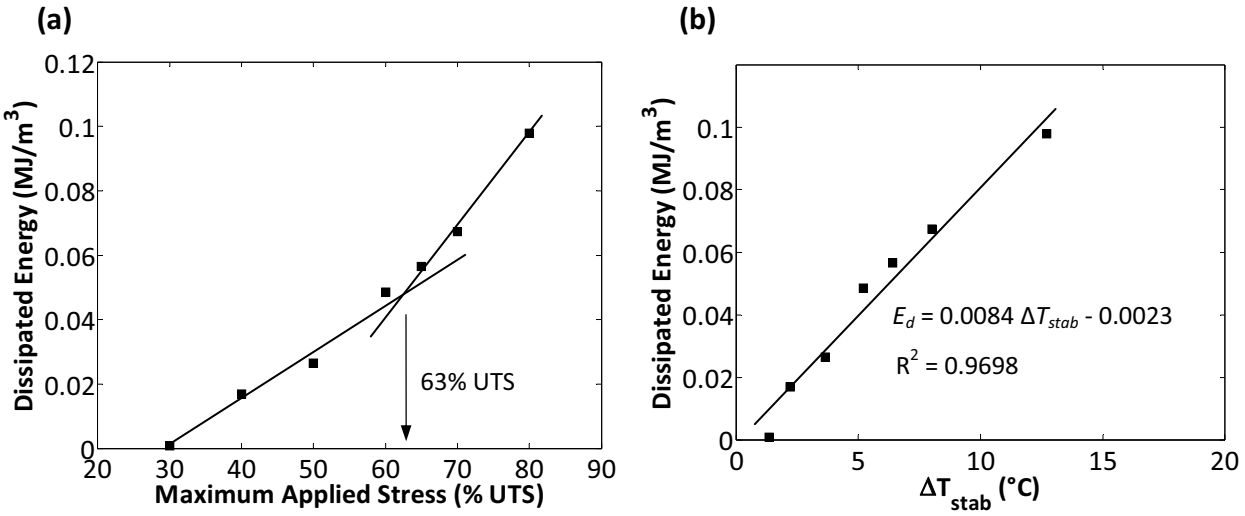

Figure 45. Dissipated energy per unit volume during cycle 5,000 plotted vs. (a) maximum applied stress, (b) ΔT_{stab}.

The established HCFS is a distinctive characteristic of the braided composite material under investigation. It should also be noted that the HCFS is also approximately equal to the exhibited static transition stress (see Figure 32). This implies that the fatigue threshold represents a transition in the damage state, or perhaps a change in damage propagation on different size scales (i.e., micro-scale to macro-scale). This is a likely scenario considering the

notable instantaneous change in braider yarn crack density during static testing when the transition stress was exceeded. Consider the cyclic stress-strain behaviour of the braided composite during the first loading cycle. Figure 46 (a) and (b) illustrate load-unload stress-strain plots for the first loading cycle of test specimens that were cyclically loading with a maximum applied stress of 70% UTS (275 MPa) and 50% UTS (195 MPa), respectively. The specimen cycled at 275 MPa (i.e., greater than the HCFS) exhibited significant ratcheting and energy dissipation in the first cycle, where the bilinear stress-strain behaviour is evident on the loading portion of the curve. This degree of ratcheting and energy dissipation was not demonstrated for any subsequent loading cycles for the duration of cycling. The specimen cycled at 195 MPa exhibited far less energy dissipation and negligible ratcheting during the first loading cycle as shown in Figure 46 (b). There is clearly a distinction in the exhibited stress-strain behaviour and thus the damage state for test specimens cycled with maximum applied stress that are greater than or less than the HCFS. Analogous behaviour was observed with quasi-isotropic laminates, where cyclic loading with a maximum applied stress greater than the static first ply failure stress resulted in off-axis plies failing during the first loading cycle due to excessive damage [20]. For the braided composite, the HCFS is a critical damage state above which significant cracking occurs after the first loading cycle which likely accelerates crack development and ultimately leads to specimen failure. When the maximum applied stress is below this critical damage state, failure does not occur. This has resulted in notably different material behaviour depending on whether the maximum applied stress is greater or less than the HCFS or critical damage state, which will be investigated further in the subsequent section.

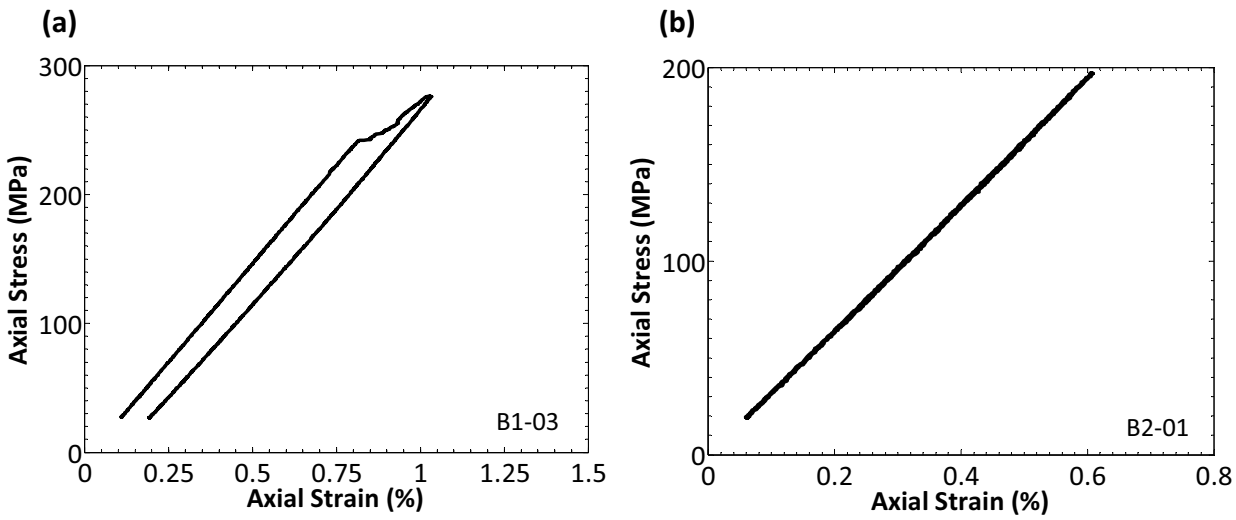

Figure 46. First cycle stress-strain curve for fatigue tests with σ_{max} of (a) 275 MPa, (b) 195 MPa.

5.1.3.2 Material behaviour

The variation in hysteretic behaviour exhibited by polymeric composite materials during cyclic loading is the product of various microscopic mechanisms, such as cracking and localized matrix deformation. The main forms of hysteresis variation typically include stiffness degradation, ratcheting, and evolving energy dissipation as outlined in Chapter 3. Plots of the normalized dynamic stiffness, $E(n)/E_o$, as a function of the number of loading cycles, n, for test specimens cycled with maximum applied stresses of 50%, 60%, 65%, 70% and 80% UTS (195, 235, 255, 275, 315 MPa) are shown collectively in Figure 47 (a). Note that the dynamic stiffness, $E(n)$, was normalized by the initial dynamic stiffness, E_o, for all plots. The same plots are included in Figure 47 (b), which only shows the initial 100,000 loading cycles. All test specimens cycled to failure demonstrated a three-stage stiffness degradation response, which is typically exhibited by many conventional cross-ply and quasi-isotropic laminates [25, 34]. This was characterized by rapid stiffness degradation during the first stage, followed by gradual stiffness degradation during the second stage, and finally rapid degradation in the third stage leading to specimen failure. For the test specimens with maximum applied stresses of 195 MPa and 235 MPa, there is a distinct difference in the stiffness degradation profile. This was characterized by initial rapid stiffness degradation, followed by a much more gradual degradation for the duration of the test. The majority of the stiffness loss occurred during the first stage for all samples tested, regardless of the maximum applied stress magnitude. For the samples cycled to

failure, the final stage of rapid stiffness degradation occurred during the last 5% of the sample life. This resulted in a relatively low magnitude stiffness drop prior to failure.

There was more stiffness degradation after a comparable number of cycles as the maximum applied stress increased as is illustrated in Figure 47 (b). This is an expected result since there would be a further advanced damage state at higher maximum applied stresses. The specimens cycled with maximum stresses greater than the HCFS also exhibited notably more stiffness degradation compared with the run-off specimens after a comparable number of cycles. For example, after 10,000 loading cycles the 195 MPa and 235 MPa specimens exhibited a residual stiffness between 94-95%, while the residual stiffness for the 255-315 MPa specimens was below 92%. There is a clear gap in the residual stiffness magnitude after a particular number of loading cycles between the specimens cycled with maximum stresses below the HCFS and those cycled above. If the specimens cycled to failure are considered, there was more stiffness degradation at failure for the specimens cycled with lower maximum applied stresses. This is illustrated in Figure 48 which shows a plot of the normalized stiffness as a function of the normalized number of cycles, n/N_f, which also illustrates the three stages of stiffness degradation. Since stiffness can be correlated to a particular damage state, it is expected that the 255 MPa test specimens will have more damage at failure compared to say the 315 MPa specimens [59, 60]. For example, the 315 MPa test specimens failed after approximately 50K cycles with a residual stiffness of 87%, presumably as the residual strength reduced to the maximum applied stress. This was a result of the critical damage state at that particular applied stress level that caused failure. The 255 MPa test specimens on the other hand failed after approximately 6.5M cycles with a residual stiffness of 81%. These specimens reached a residual stiffness of 87% (i.e., equal to the residual stiffness at failure for the 315 MPa specimens) much earlier on in cycling. This particular damage state did not cause failure for the 255 MPa test specimens because the residual strength was still higher than the maximum applied stress, thus damage continued to progress and the stiffness continued to degrade. Once the critical damage state for this particular stress level was attained, the residual strength was equal to the maximum applied stress and the specimen failed (i.e., after 6.5M cycles). This illustrates that less damage is required to cause failure at higher stresses, and therefore a

constant critical stiffness (or a critical damage state) cannot be used as an indicator of failure. If the critical stiffness is defined as a function of σ_{max}, failure may be predicted using this approach. This will be considered in the subsequent paragraph.

The stiffness degradation rate during the second stage of cycling and the total average stiffness degradation rate can yield qualitative information on the damage development rate during cyclic loading. Plots of the second-stage stiffness degradation rate ($dE(n)/dn|_2$) and the total average stiffness degradation rate ($\Delta E_{total}/N_f$) as functions of the maximum applied stress ratio (σ_{max}/S_u) are shown in Figure 49 (a) and (b), respectively. The stiffness degradation rates clearly increase with increasing maximum stress. A regression on the plotted data illustrates that a power law function is a suitable fit to the data, with R^2 values close to 1 as shown in Figure 49. This is an important finding for the braided composite material, which implies that there is a mathematical relationship between the progressive damage state and the maximum applied stress. A similar relationship between the damage rate (i.e., the stiffness degradation rate) and the maximum applied stress was found for a quasi-isotropic carbon fiber/epoxy laminate [154] and for a biaxial braided composite [66].

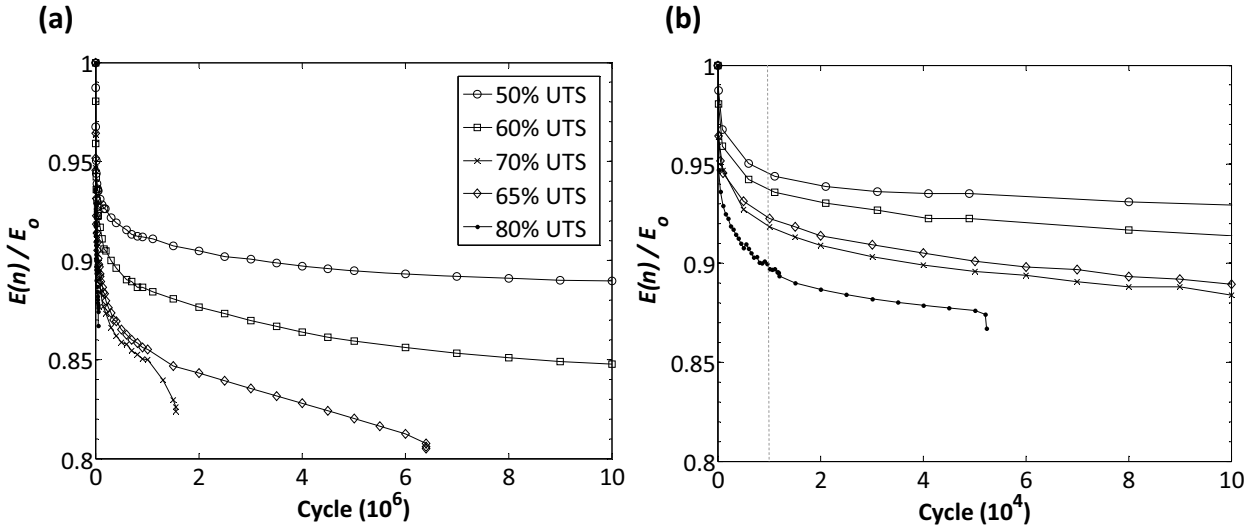

Figure 47. Room temperature fatigue normalized stiffness degradation plots.

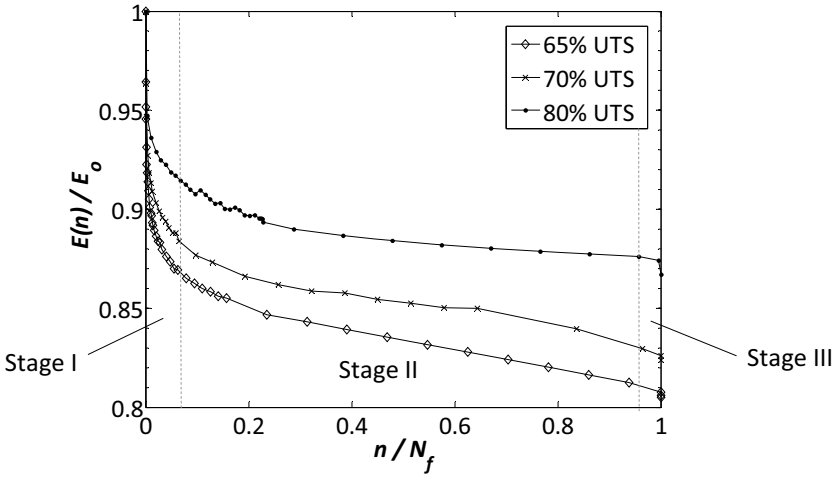

Figure 48. Room temperature fatigue normalized stiffness degradation for specimens cycled to failure.

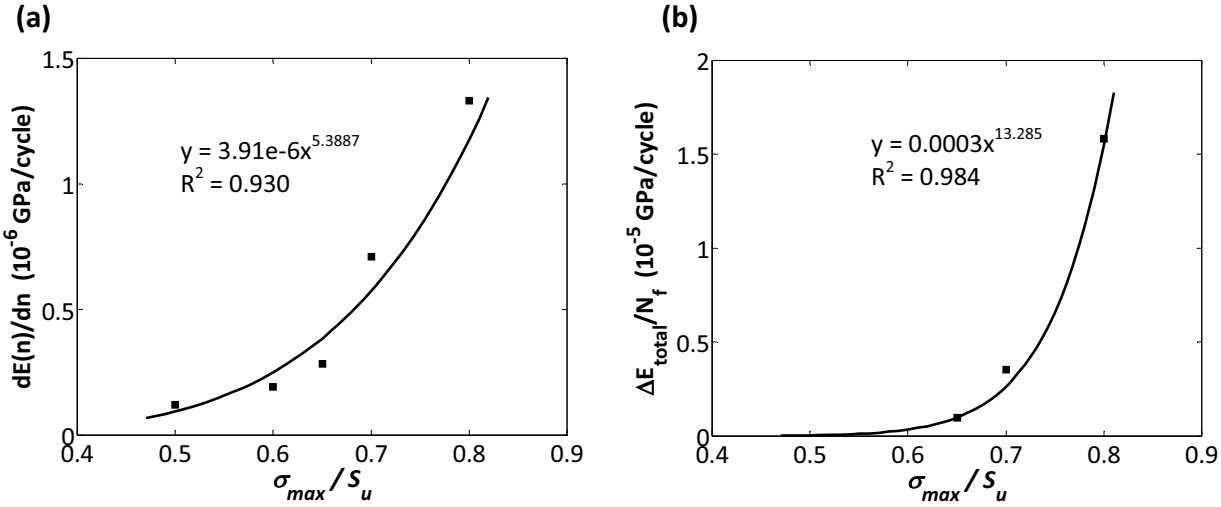

Figure 49. Room temperature fatigue (a) stage-two stiffness degradation rate, (b) average stiffness degradation rate as functions of maximum applied stress ratio.

As discussed in Chapter 3, the mean strain is an indirect measure of both stiffness degradation and strain ratcheting, and is in general another indicator of the evolving hysteretic material behaviour. A plot of the measured mean strain, ε_{mean}, as a function of the number of loading cycles, *n*, for test specimens cycled with the indicated maximum applied stresses are shown collectively in Figure 50 (a). The same plots are included in Figure 50 (b), which only shows the initial 100,000 loading cycles. Similar to the stiffness plots for the specimens that were cycled to failure, the mean strain follows a three-stage evolution consisting of rapid

increase during the early stage, followed by a gradual increase for the majority of the specimen life, and finally a rapid increase prior to failure. The mean strain rate during the second stage of cycling increased as the maximum applied stress increased, and was found to be related to σ_{max} by a power law function as shown in Figure 51. In order to isolate the degree of strain ratcheting for each applied maximum stress level, the mean strain and strain range ($\Delta\varepsilon$) can be graphically compared [57, 47]. Figure 52 (a) and (b) show combined profiles of ε_{mean} and $\Delta\varepsilon$ on a semi-logarithmic scale for test specimens cycled at 195 MPa and 275 MPa, respectively. For each maximum applied cyclic stress level, the mean strain rate was higher in magnitude compared to the strain range rate during the early stages of cycling. However, for the subsequent duration of cycling, the mean strain and strain range profiles evolved identically until specimen failure. This implies that during the early stages of cycling notable strain ratcheting occurs, however, ratcheting subsides afterwards and is negligible for the duration of cyclic loading. Recall that strain ratcheting of composite specimens subjected to stress-controlled cycling with a positive mean stress may be due to damage evolution, as well as creep deformation and fiber reorientation [47, 72]. The stiffness degradation plots of Figure 47 reveal that there is rapid stiffness degradation during the early stage of cycling, which is an indication of significant damage development. This suggests that the initially exhibited strain ratcheting is primarily due to damage accumulation and to a lesser extent creep deformation, while the negligible strain ratcheting that occurred for the duration of cycling is also due to damage. This will be discussed further in Section 5.1.3.4.

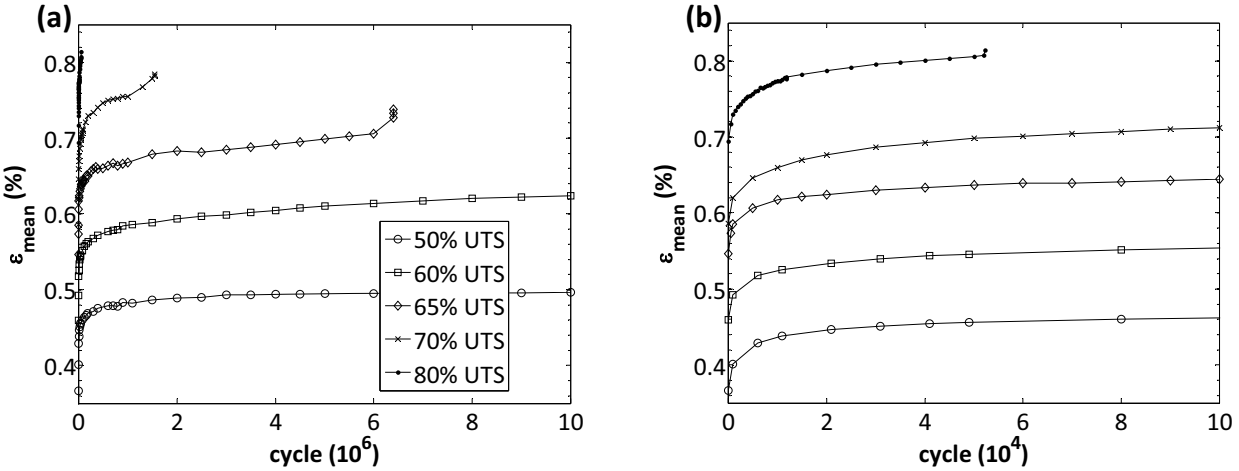

Figure 50. Room temperature fatigue mean strain plots.

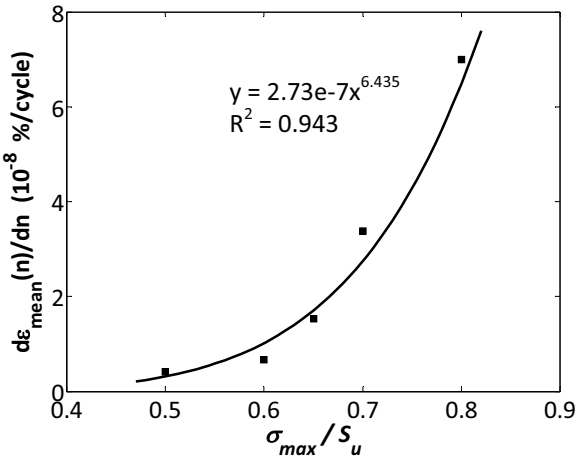

Figure 51. Room temperature fatigue stage-two mean strain rate vs. maximum applied stress ratio.

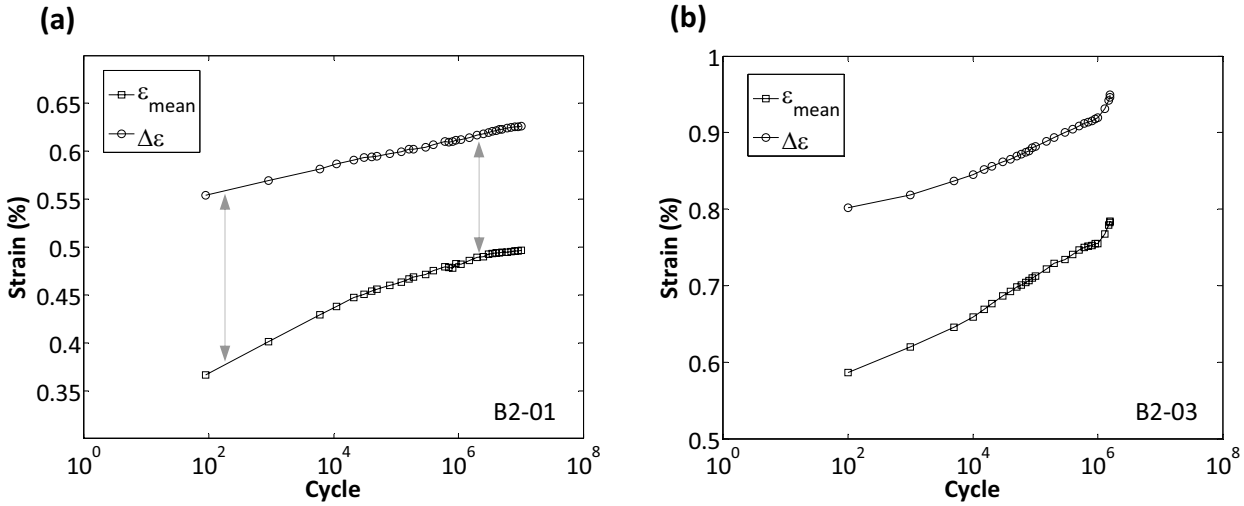

Figure 52. Strain range and mean strain profiles for specimens cycled at (a) 195 MPa, (b) 275 MPa.

The evolution of the energy dissipation (i.e., the area contained within the cyclic stress-strain ellipse) is another measure of the evolving hysteretic material behaviour during cyclic loading. Plots of the energy dissipation (E_d) for the indicated maximum stresses are shown on a semi-logarithmic scale in Figure 53 (a). For all applied cyclic stress levels, the energy dissipated during the first loading cycle was considerably high. During the subsequent loading cycles E_d rapidly decreased in magnitude until reaching a plateau, after which E_d was approximately constant or decreasing at a very gradual rate. The cyclic energy dissipation maintained this plateau for the majority of cyclic loading. Figure 53 (b) shows similar plots on a linear scale for

specimens cycled with maximum stresses of 195 MPa and 275 MPa. For the specimens cycled to failure, the dissipated energy increased slightly during the cycles prior to failure as shown in Figure 53 (b). The evolution of E_d implies that the severe onset of damage and the potential local viscous matrix behaviour during the first few loading cycles contributed to the initially high dissipated energy exhibited by the test specimens. As cycling progressed, the dissipated energy rapidly decreased since the degree of damage and local viscous matrix behaviour began to subside. For the duration of cyclic loading, E_d remained fairly constant which implies that the local viscous effects and/or evolving damage attained a constant rate. For the specimens cycled to failure, the increase in E_d prior to fracture was due to the rapid accumulation of damage leading to the final failure event. The results from Figure 52 showed that strain ratcheting occurred during the initial stages of cycling, which supports the fact that any potential viscous or creep behaviour only occurs during the initial few loading cycles. Thus, the dominant mechanism contributing to the presented energy dissipation evolution is in fact fatigue damage development. A study by Cain [96] on off-axis unidirectional carbon fiber laminates found that the energy dissipation evolution was similar to that shown for the braided composite material of this study (i.e., rapid decrease, then constant throughout the duration of cycling). It was also stated that strain ratcheting caused by creep only occurred during the first few loading cycles [96], which supports the observations of this study. Montesano *et al.* [72] also found a similar energy dissipation evolution for an off-axis woven-ply laminate. It was stated that the initial energy dissipation was due to local viscous effects and fiber reorientation, which eventually subsided for the duration of cyclic loading. This also supports the observations made in this study for the braided composite material.

An interesting observation established for the braided composite material is that there exists a correlation between the magnitude of the dissipated energy during the 'plateau' and the maximum applied stress level. A plot of the plateau energy dissipation values as a function of σ_{max} is shown in Figure 54. A power law function fits the data well as shown by the data correlation factor in the plot. This illustrates that for the majority of cyclic loading, there is a 'constant' driving force causing energy to dissipate which is a function of the maximum applied

stress level. Figure 54 is analogous to the power law relations found for the stiffness degradation rate and the mean strain rate.

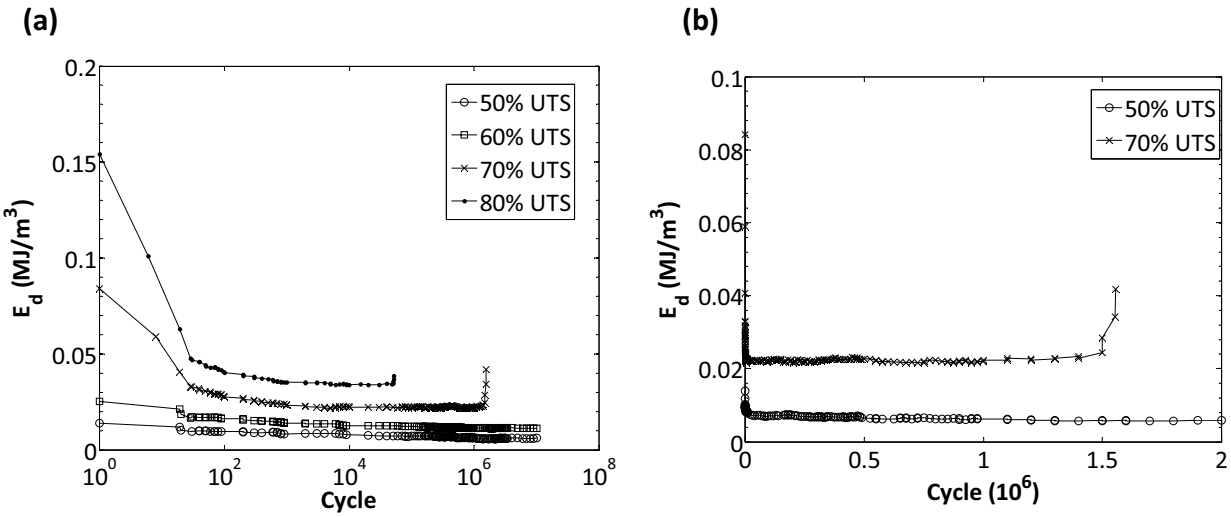

Figure 53. Plots of evolving energy dissipation (a) semi-logarithmic scale, (b) linear scale.

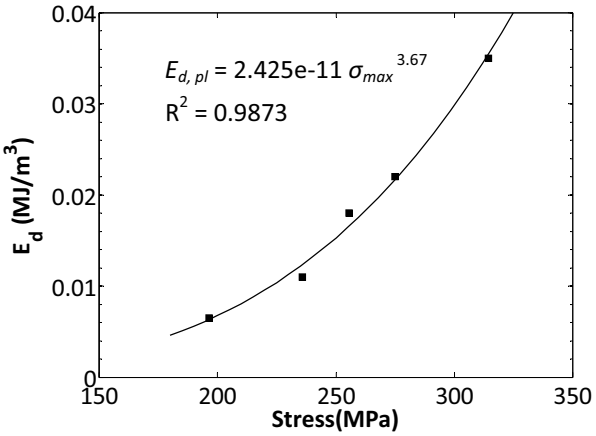

Figure 54. Plateau energy dissipation as a function of σ_{max}.

Plots of successive stress-strain curves for the indicated cycles during the early stages of cycling for specimens loaded at 235 MPa and 275 MPa maximum applied stresses are shown in Figure 55. Specimen B1-07 exhibited relatively little energy dissipation during the first cycle, with decreasing dissipation as indicated by the areas within the stress-strain ellipses. This behaviour was typical of all test specimens cycled with maximum stresses below the HCFS. Specimen B1-03 exhibited significant energy dissipation during the first cycle, with rapidly

decreasing dissipation thereafter until the plateau. This behaviour was typical for all test specimens cycled with maximum stresses above the HCFS. The small areas of stress-strain ellipses shows there is very little viscous effects or creep throughout the duration of cycling, except for the first cycle for the higher σ_{max} test specimens. There is however notable strain ratcheting as illustrated in the plots of Figure 55, which confirms that strain ratcheting is in fact mainly due to damage development. This is due to the fact that the developed crack faces do not close perfectly upon unloading, causing the apparent strain ratcheting behaviour [71, 182]. As was illustrated in Figure 52 and confirmed in the plots of Figure 55, the majority of ratcheting occurs during the initial few loading cycles.

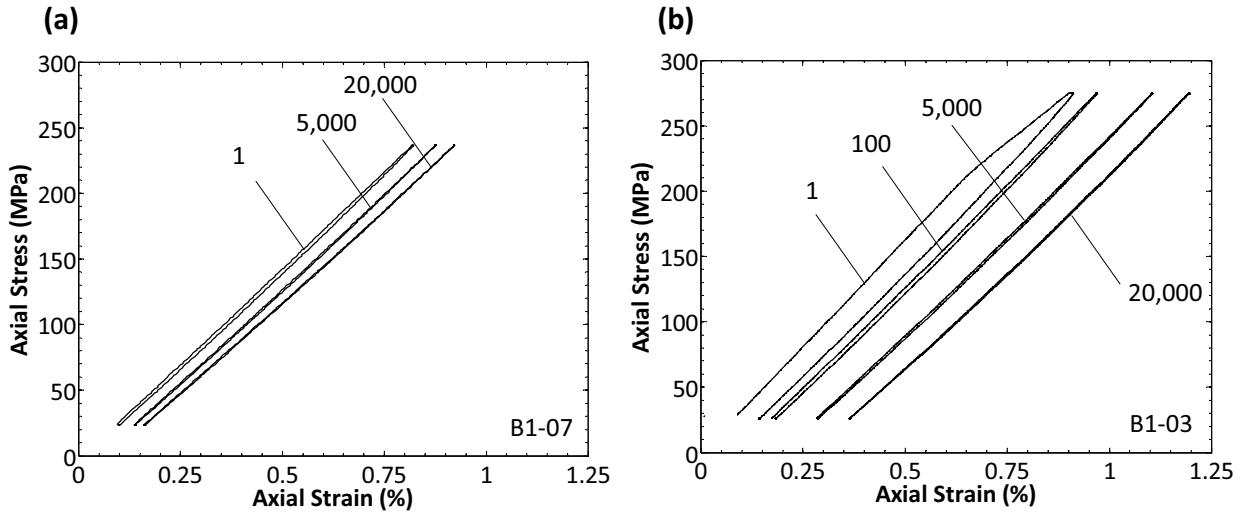

Figure 55. Successive cyclic stress-strain plots with cycle number indicated (a) 235 MPa, (b) 275 MPa.

To further confirm that there is negligible time-dependent behaviour exhibited during cyclic loading, consider the plots of stress-time and strain-time shown in Figure 56. When a material that exhibits time-dependent or viscoelastic stress-strain behaviour is cyclically loaded with a sinusoidal waveform, a phase lag occurs in time between the stress and the strain [73]. There is no such lag shown in Figure 56 after approximately 175,000 loading cycles, which was the case for all maximum applied stress levels for the duration of cycling. Thus, this further confirms that the energy dissipated by the material during cyclic loading is mainly due to the development of fatigue damage.

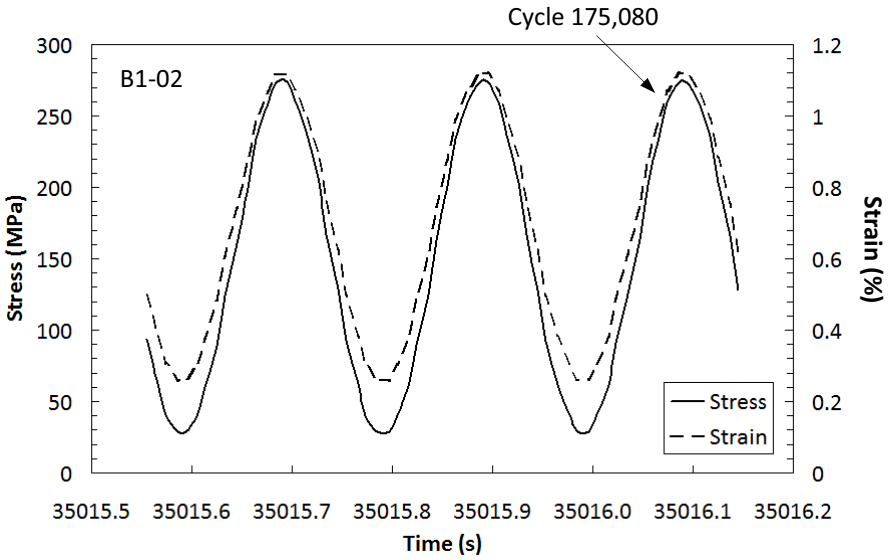

Figure 56. Combined stress-time and strain-time plots for a specimen cycled with σ_{max} = 275 MPa.

5.1.3.3 Damage characterization

A microscopic investigation was conducted to track the development of damage during cyclic loading and to investigate the mechanisms responsible for the exhibited material behaviour and ultimately failure. To this effect, a series of tests were conducted at each maximum applied stress to characterize the damage evolution in the material. This involved extracting edge replicas and IR thermographs, post *mortem* SEM observations, and analysis of the fracture surfaces for the test specimens cycled to failure. The corresponding results for the microscopic investigation will now be presented.

Figure 57 shows a series of images of the extracted edge replicas for a test specimen cycled with a maximum stress of 235 MPa, which were taken using an optical microscope with 60X magnification. These tests were paused at various predetermined cyclic intervals to extract the replicas during a zero-load dwell, after which cyclic loading resumed (see Section 4.4). During the early stages of cycling, through-the-yarn-thickness braider yarn cracks were the main modes of damage uniformly distributed throughout the specimen edge. As cyclic loading progressed, the number of braider yarn cracks continuously increased. Note that the braider yarn cracks propagated at the fiber-matrix interfaces within the braider yarns. Localized matrix cracks and localized braider yarn interface cracks were also observed, but there were few in comparison to the number of braider yarn cracks. The braider yarn crack density eventually

reached a saturation state, after which the existing and newly initiated interface cracks between adjacent braider yarns and around the 0˚ yarn peripheries grew in length. The cracks around the 0˚ yarns propagated in the loading direction along the yarn axes, while the interface cracks between adjacent braider yarns propagated in a plane in both the loading direction and the direction perpendicular to loading. The majority of the interface cracks initiated at the braider yarn crack tips due to the localized high stress field at the crack tips (e.g., see Figure 57 (c)). Few cracks developed in the 0˚ yarns throughout most of cycling. During the latter stages of cycling, the interface cracks grew significantly in length and interacted with one another and with the braider yarn cracks as shown in Figure 57 (e) - this was significant by 500,000 loading cycles. Figure 58 presents axial- and cross-sectional photomicrographs obtained using SEM for the same test specimen after cycling for 10^7 loading cycles without failure. The images confirm that the majority of damage is cracking within the braider yarns, even after 10^7 loading cycles. The propagation of the 0˚ yarn periphery cracks along the yarn axes and around the yarn cross-section is also illustrated in the photomicrographs of Figure 58. The long yarn interface cracks and the notable interactions between the various observed damage modes are confirmed by the SEM photomicrographs.

The progression of damage for all the specimens cycled with maximum stresses below the HCFS was similar to that described in the previous paragraph, however the damage progression rate increases at higher stress levels. An image of an edge replica and the sectioned cross-section for specimen B2-01 cycled at 195 MPa for 3.5M cycles without failure are shown in Figure 59. Comparison of Figure 57 (e) and Figure 59 (a) show that after a comparable number of cycles, the specimen cycled with a lower stress exhibits notably less damage. In fact, specimen B2-01 (195 MPa) does not contain very long yarn interface cracks after 3.5M cycles, which was observed for specimen B1-07 (235 MPa) after the same number of loading cycles. The growth of the interface cracks for specimen B2-01 was delayed due to the lower applied stress field. The number of braider yarn cracks is comparable for both specimens. Braider yarn cracks were evenly distributed throughout the specimen width and length, and were the main observed damage mode.

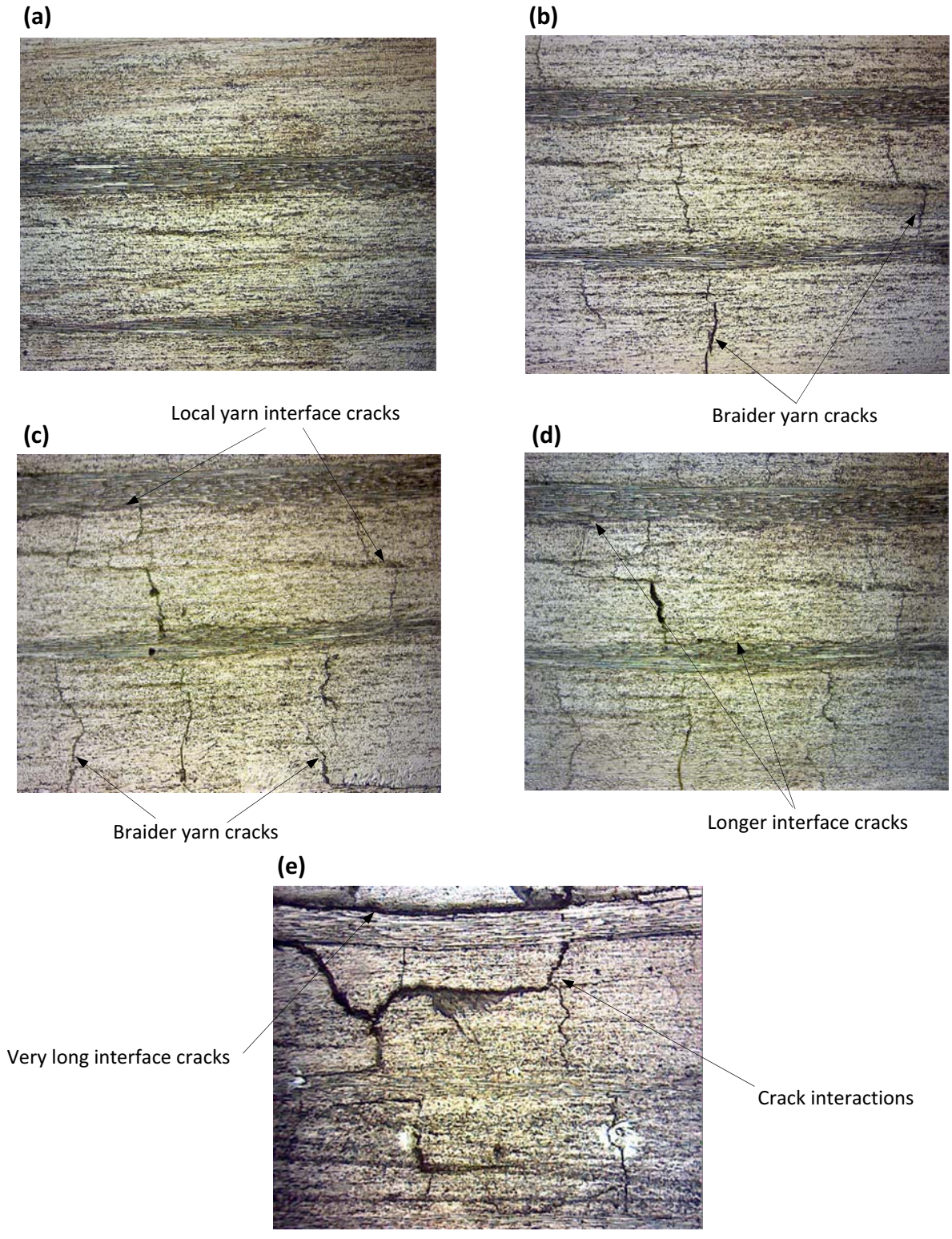

Figure 57. Images of extracted edge replicas at 60x magnification captured using an optical microscope for specimen B1-07 cycled at 235 MPa (a) virgin; after (b) 500, (c) 20,000, (d) 100,000 and (e) 3,500,000 cycles.

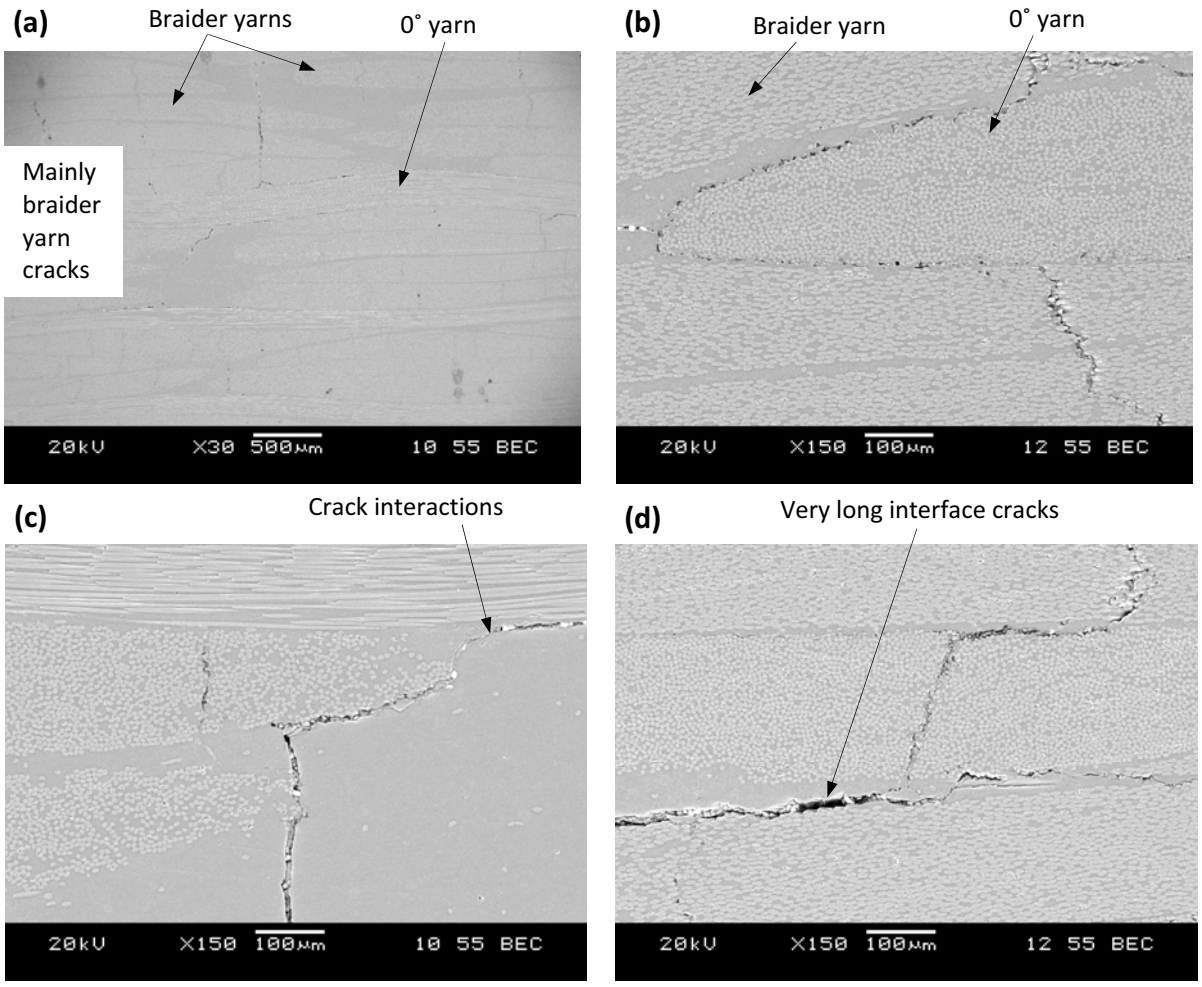

Figure 58. SEM photomicrographs for specimen B1-07 cycled at 235 MPa: (a) axial-section 30X magnification, (b) cross-section 150X magnification, (c) axial-section 150X magnification, (d) cross-section 150X magnification.

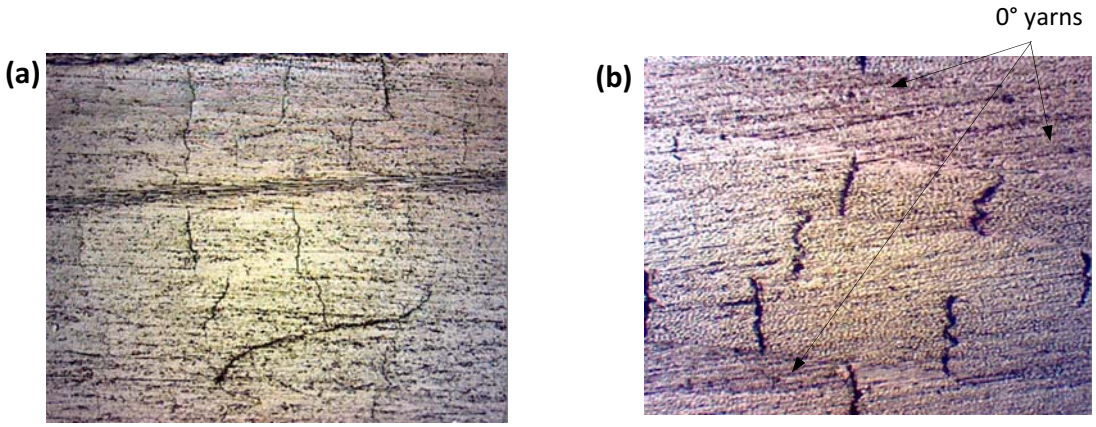

Figure 59. Specimen B2-01 cycled at 195 MPa for 3.5M cycles: (a) edge replica image at 60X magnification, (b) cross-section optical microscopic image at 60X magnification.

Figure 60 shows a series of images of the extracted edge replicas for a test specimen cycled with a maximum stress of 275 MPa, which were taken using an optical microscope with 60X magnification. During the early stages of cycling, braider yarn cracks were the main modes of damage uniformly distributed throughout the specimen edge. As cyclic loading progressed, the number of braider yarn cracks increased reaching a saturation state very early during cycling (see Figure 60 (b)). Localized braider yarn interface cracks were also observed much earlier and in greater quantity, but there were fewer in comparison to the number of braider yarn cracks as was found with the lower stress level specimens. The existing and newly initiated interface cracks between adjacent braider yarns and around the 0˚ yarn peripheries grew in length after braider yarn crack saturation. Few cracks in the 0˚ yarns developed throughout most of cycling, even up to failure. During the latter stages of cycling prior to specimen failure, the interface cracks grew to be very long and significantly interacted with one another and with the braider yarn cracks as is evident in Figure 60 (d). SEM photomicrographs of the same test specimen sectioned after failure are included in Figure 61, which confirm the observations made from the edge replicas. It should be noted that the damage state observed at the fracture surface consisted of more interface cracks. These cracks were also 'wider' in appearance which is attributed to the out-of-plane deformation of the fiber yarns at the fracture surface, and is evident in Figure 61 (c). The damage development in all specimens cycled with maximum applied stresses greater than the HCFS is analogous to this description.

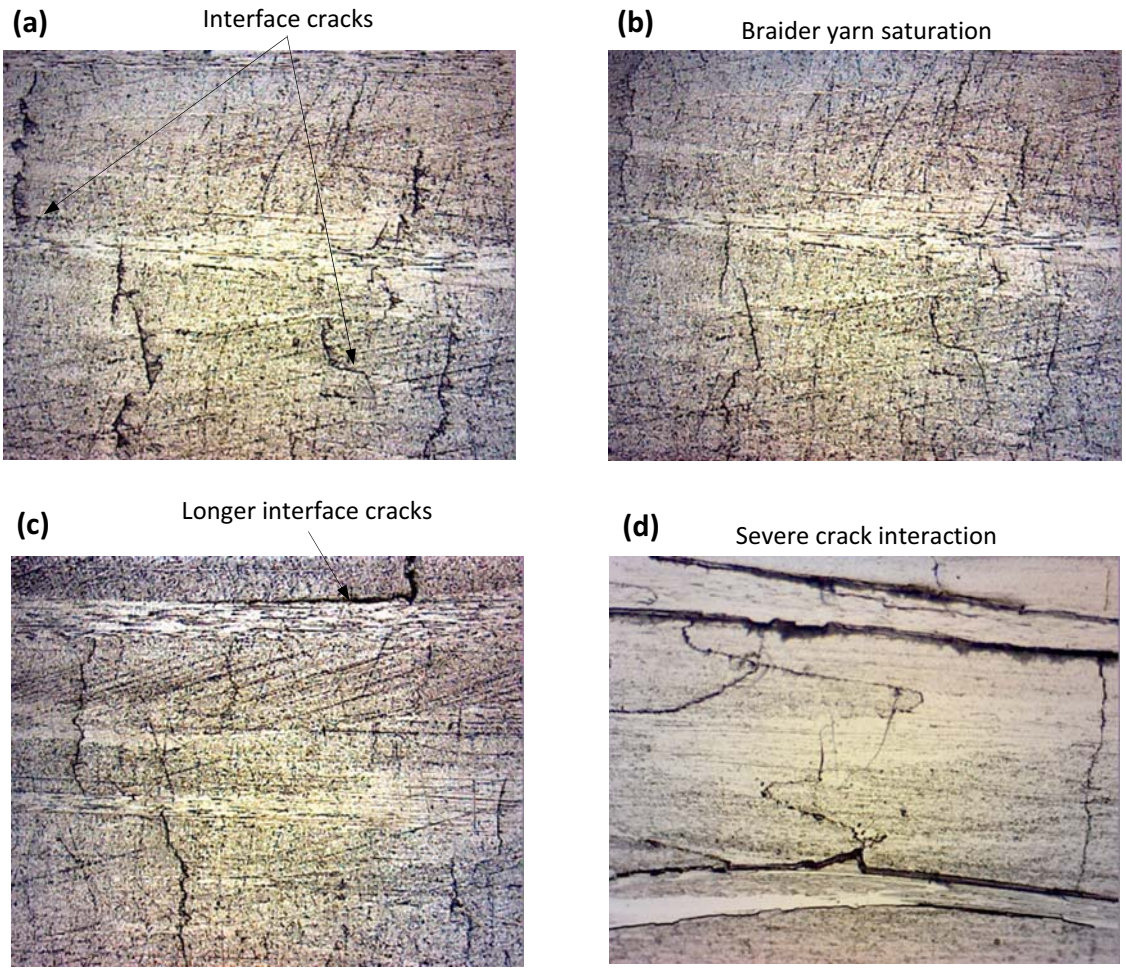

Figure 60. Images captured at 60x magnification using an optical microscope of edge replicas obtained for specimen B1-03 cycled at 275 MPa after (a) 100, (b) 1,000, (c) 10,000 and (d) after fracture (1.5M cycles).

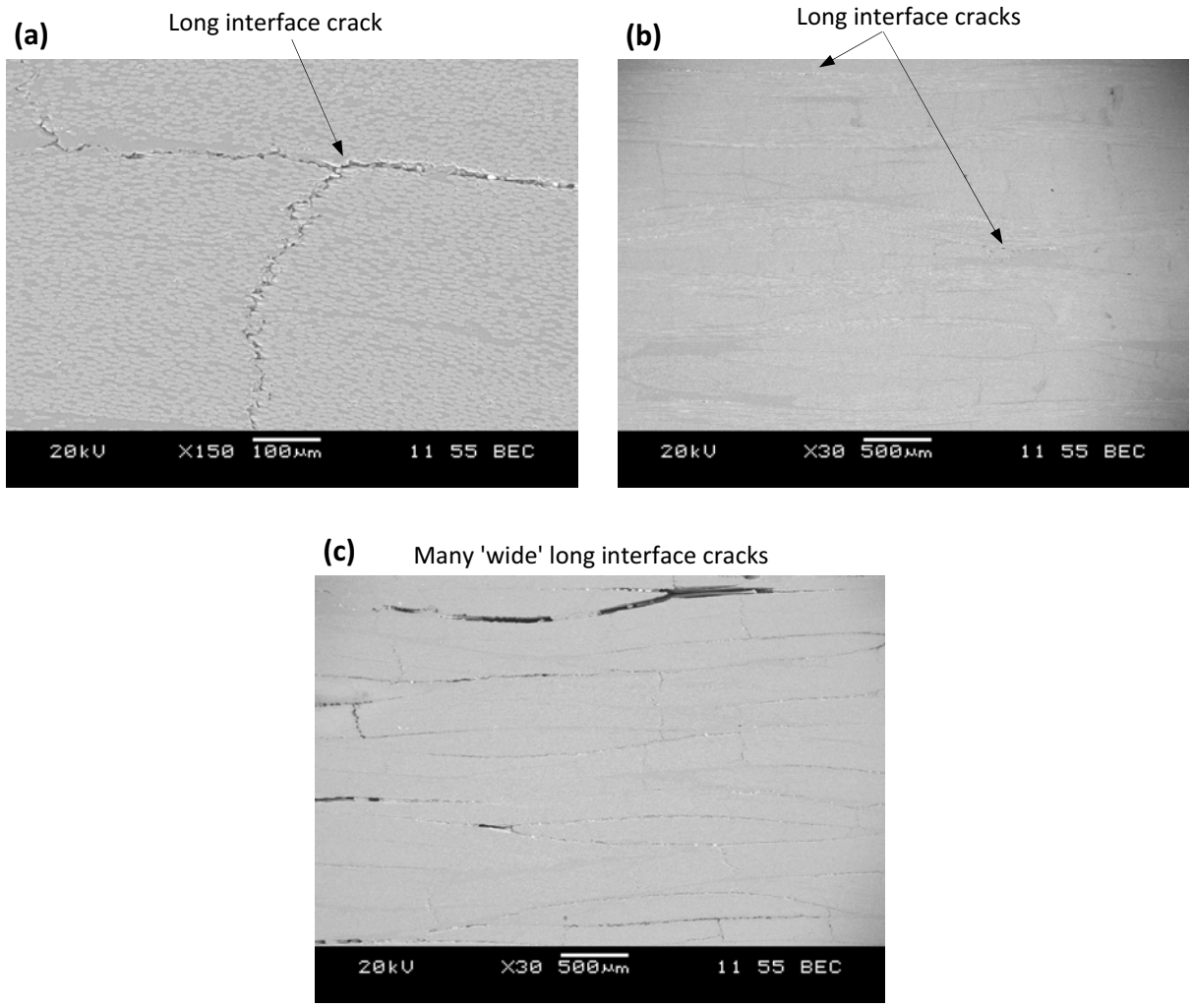

Figure 61. SEM photomicrographs for specimen B2-03 cycled at 275 MPa: (a) cross-section 150X magnification, 75 mm from fracture surface, (b) axial-section 30X magnification, 75 mm from fracture surface, (c) cross-section 30X magnification at fracture surface.

The specimens cycled with maximum applied stresses below the HCFS had braider yarn crack densities of 3 - 6 cracks per yarn after saturation, as was observed by the edge replicas and the SEM photomicrographs. The specimens cycled with maximum applied stresses above the HCFS had slightly higher braider yarn crack densities of 4-7 cracks per yarn after saturation. The obtained edge replicas were also used to plot the evolving crack density profiles for the three main observed damage modes: braider yarn cracks, interface cracks and matrix cracks. Note that all the obtained edge replicas were extracted on the specimen edges near the specimen center. For the test specimens that were cycled to failure, the replicas were taken at

a distance of 50-100 mm from the fracture surfaces. Two corresponding plots for specimens cycled with σ_{max} of 195 MPa and 275 MPa are shown in Figure 62. Three equivalent size zones along the length of the specimen edge were used to determine the average crack densities. As mentioned, the number of braider yarn cracks is notably higher than the number of interface or matrix cracks for all specimens regardless of the maximum applied stress level. The braider yarn cracks reach saturation after approximately 70,000 cycles and 5,000 cycles for the 195 MPa and 275 MPa specimens, respectively. It is clear that there are more braider yarn cracks for the 275 MPa test specimen after saturation, which is attributed to the increased damage during the initial loading cycle (see Figure 46).

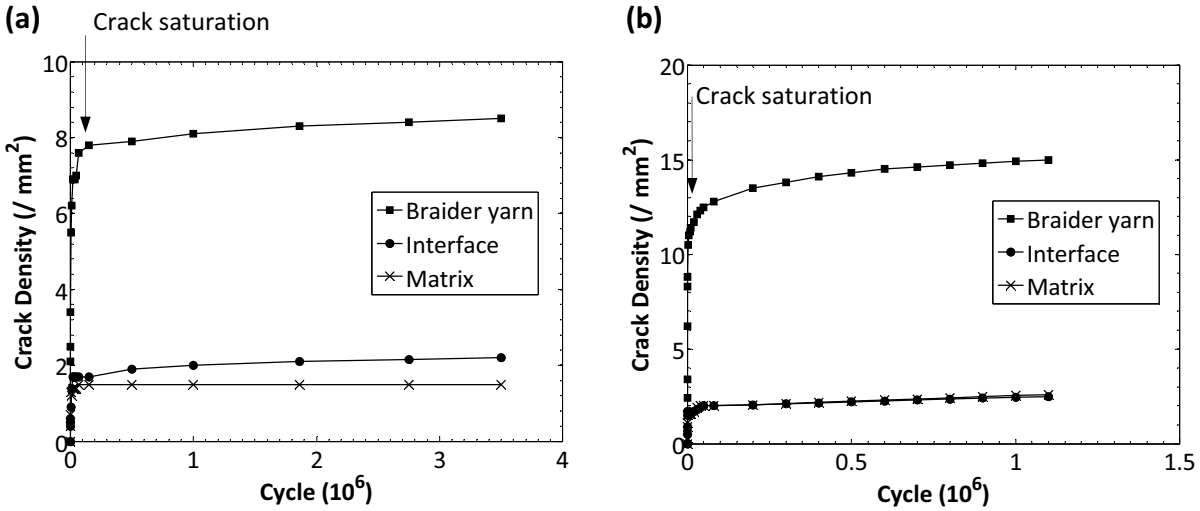

Figure 62. Crack density profiles for specimens cycled with σ_{max} of (a) 195 MPa, (b) 275 MPa.

To further confirm the occurrence of braider yarn crack saturation, IRT was employed to monitor the surface temperature of the cyclically loaded test specimens and to visually capture thermal spikes caused by braider yarn cracking. To demonstrate the observations made using thermography, the results for a test specimen cycled at 275 MPa will be presented. A plot of the temperature profile for a location on the specimen surface within the central region of the gage section is shown in Figure 63; a data point was captured every cycle to generate the plot. The temperature profile follows a similar trend as the corresponding braider yarn crack density plot in Figure 62 (b). In fact, the saturation of the braider yarn cracks corresponds approximately to the same number of cycles that temperature 'stabilization' occurs. Note that

the temperature does not actually plateau, but gradually increases for the duration of cyclic loading after stabilization. This was found for each maximum applied stress level employed in this study for the braided composite test specimens. This confirms that braider yarn crack saturation occurs, and that the initial development of braider yarn cracks is mainly responsible for the initial temperature rise (i.e., heat dissipation). Note that local viscous matrix heating due to mechanical cycling will also contribute to the initial temperature rise [56]. A series of IR thermographs obtained of the same specimen are shown in Figure 64; the images depict the temperature rise and not the absolute temperature. Beginning from the first few loading cycles, the hot spots are evident within the braider yarns whereas the surrounding matrix regions exhibited slightly lower temperatures. This was evident until approximately 1050 cycles, after which the matrix region temperatures were slightly higher than the temperatures within the braider yarns. This corresponds to the temperature stabilization point in Figure 63. After additional cycling, the braider yarns and the matrix regions had almost identical temperatures and a 'smeared' temperature hot zone existed as shown in Figure 64. This was likely due to the growth of the interface cracks and additional local viscous matrix heating. In addition, the widespread nature of damage was also confirmed by the IR thermographs for all maximum applied stresses.

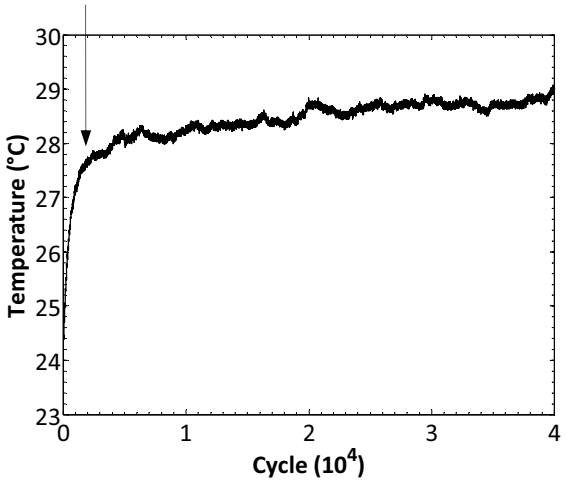

Figure 63. IRT surface temperature profile for specimen B2-03 (275 MPa).

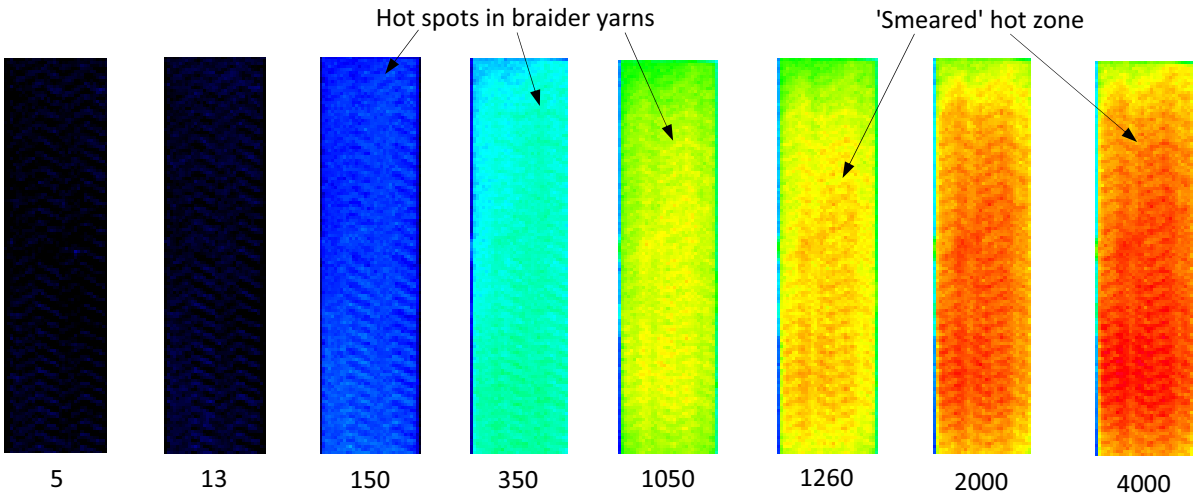

Figure 64. Captured IR thermographs during indicated cycles for specimen B2-03 (275 MPa).

The edge replicas, IR thermographs and SEM results for all maximum applied stress levels revealed that similar to the static tests, braider yarn cracking was the dominant damage mechanism during the early stages of cycling. These cracks were distributed throughout all braider yarns across the sample width and thickness, and along the length of the samples. Most braider yarns contained multiple cracks for all maximum applied stress levels. The braider yarns, analogous to off-axis plies in a conventional laminate, are subjected to higher stresses and thus exhibit cracking during the early stages of cyclic loading. In addition, significantly more braider yarn interface cracks and matrix-rich-zone cracks were observed when compared to the static test specimens, although there were few interface cracks in comparison to the number of braider yarn cracks observed. For all maximum applied stress levels, braider yarn cracks initiated and propagated along the braider yarn axes during the first stage of cycling beginning from the first cycle, eventually reaching a saturation state after which the braider yarn crack density rate was more gradual. The rate of braider yarn crack development during this early stage of cycling increased as σ_{max} increased, and saturation of the braider yarn cracks occurred after fewer cycles at higher stress levels. The vertical alignment of the braider yarn cracks (see Figure 57 and Figure 58) suggests that cracks propagate at the same rate at different locations throughout the thickness of the specimen. In addition, the rate of the braider yarn crack density during the second stage of cycling, after saturation, increased as the maximum applied stress increased. During the initial stages of cycling, a number of localized interface cracks developed

between adjacent braider yarns and at the braider yarn and 0° yarn interfaces. As indicated, these cracks typically initiated at the tip of braider yarn cracks as shown in Figure 58, which would be caused by the localized high stress fields at the braider yarn crack tips. Once braider yarn crack saturation was attained, these localized interface cracks began to propagate, becoming significantly longer and interacting with one another by the latter stages of cycling. The interface crack propagation rate was fairly gradual during the duration of cycling. This can be partially attributed to local shear deformation that occurred at the braider yarn interlace locations and at the braider yarn crack tips, and possibly due to the straightening tendency of the 0° yarns. This would cause interface cracks to propagate under higher localized shear stress fields. At lower stresses the interface cracks were allowed to grow much longer in length, while at higher stresses the interface cracks were shorter in length but reached critical lengths which caused specimen failure.

For the specimens cycled with maximum applied stresses below the high cycle fatigue strength, there were very few 0˚ yarn cracks after a run-out of 10^7 cycles, suggesting the majority of these cracks occur prior to failure. Interactions between interface cracks were minimal initially, gradually increasing as loading progressed, and more significant after millions of loading cycles. Up to a run-out of 10^7 cycles, the accumulation of interface damage and the corresponding interaction of damage modes was not sufficient to cause specimen failure.

For the specimens cycled with maximum applied stresses above the high cycle fatigue strength, a number of matrix and interface cracks developed during the very early stages of cycling due to a higher applied stress. During the latter stages of cycling, the number of interface and matrix cracks reached a high density which resulted in significant crack interactions. At this stage in cycling and at the eventual local fracture zone vicinity, the braider yarns and the matrix lost their load carrying capacity. Load was redistributed to the 0˚ yarns causing some splitting type cracks in these yarns. After only a few more loading cycles, the 0˚ yarn fibers began to break which eventually led to fracture of the fiber yarns and specimen failure. An image of the fracture surface for a 275 MPa fatigue test specimen is shown in Figure 65 (a). The fracture zone is slightly larger compared to the static test specimens, however, it is still fairly localized. The fracture line has propagated along the +60˚ and -60˚ braider yarn axes,

which resulted in fracture of the 0˚ fiber yarns, as well as some +60˚ and -60˚ fiber yarns. Although as mentioned there was slight indication of fiber rotation, there was no significant elongation prior to failure indicating brittle-natured fracture, which is clear in Figure 65 (a). The presence of some fiber pull-out is revealed by the brushy appearance of the fracture surface and confirmed in Figure 65 (b) by the bare fibers, which is also characteristic of brittle-natured fracture. The degree of fiber pull-out was however less than that observed for the static test specimens. Furthermore, there was some indication of large-scale debonding and evidence of matrix fall-out in the fracture region; however, the affected zone was very localized. Out-of-plane deformation caused by large-scale debonding occurred during final fracture causing more interface and matrix cracking with a wider appearance in the cross-sectional plane (see Figure 61 (c)). Inspection of the internal damage state at locations further from the fracture surface revealed no large-scale debonding cracks, which confirms that large-scale debonding occurred only at fracture. This suggests that the fatigued specimens developed more extensive accumulation of localized matrix-dominated failures prior to fracture, which resulted in localized large-scale debonding and slight fiber rotation during the final fracture event. Note that since the fracture surface is localized, these failure events occurred in the final few cycles instantaneously leading to failure, which explains why there was not much 0˚ yarn splitting or fiber rotation. The observed damage development occurred in three distinct stages including initial braider yarn crack growth up to saturation, gradual interface crack growth, and final rapid crack interaction and accumulation leading to fiber fracture and ultimately failure. complimentary details can be found in [180].

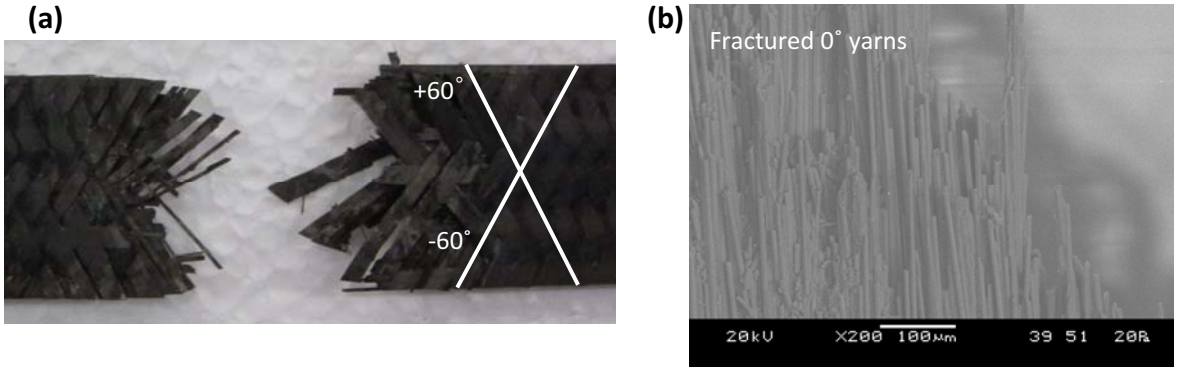

Figure 65. Failed fatigue test specimen (275 MPa): (a) image of the fracture surface, (b) SEM photomicrograph of the fracture surface with 200X magnification.

5.1.3.4 General discussion: microscopic-macroscopic correlation

The results for the room temperature fatigue tests presented in Sections 5.1.3.2 and 5.1.3.3 provided a characterization of the braided material on both macroscopic and microscopic scales, respectively. The following discussion will focus on the correlation between the microscopic damage characterization and the resulting material behaviour exhibited by the braided composite.

The plots in Figure 47 illustrated a three-stage stiffness degradation response for the test specimens cycled to failure, with an initial rapid drop in stiffness for all tested specimens regardless of the maximum applied stress. The corresponding microscopic damage characterization also revealed that damage progressed in three stages for all maximum applied stresses, where initially braider yarn cracks were the dominant damage mode, followed by growth of the fiber yarn interface cracks and gradual increase in braider yarn crack density, and finally rapid accumulation and interaction of all damage modes leading to failure. The evolving interface cracks and their interactions ultimately led to load redistribution and specimen failure during the latter stage of cycling, however the initial stage was dominated by the braider yarn crack development and partially by interface crack initiation. Braider yarn crack surfaces propagated along the braider yarns as mixed mode I and mode II cracks, while interface cracks at the braider yarn interfaces propagated along the yarn peripheries as mixed mode II and mode III cracks (See Figure 19 in Section 3.5). Figure 66 (a) and (b) show combined plots of the braider yarn crack density obtained from the edge replicas and the dynamic stiffness degradation for specimens cycled with maximum applied stresses of 195 MPa and 275 MPa, respectively. The saturation of the braider yarn cracks approximately corresponds to the initiation of the second stage of the stiffness degradation profile for all stress levels. Recall that interface cracks will also contribute to stiffness degradation. This shows that the braider yarn cracks are the main cause of rapid stiffness degradation during the initial stage of cycling, which was also confirmed by the IR thermographs and the temperature-cycle profiles. This is further demonstrated by the plots of the normalized stiffness and the braider yarn crack density shown in Figure 66 (c) and (d), which illustrate that the stiffness is directly proportional to the braider yarn crack density until braider yarn crack saturation occurs. This is a significant finding in this study. Note that each data point in the plots correspond to a specific loading cycle, whereby the

stiffness magnitude and the braider yarn crack density corresponding to the particular loading cycle are the data pairs in Figure 66 (c) and (d). Also note that the interface cracks partially contribute to the initial rapid stiffness degradation, but are not accounted for in the plots. The interface crack initiation during the early stage rapidly increases like the braider yarns, and thus the contribution of the interface cracks to the stiffness degradation is constant during this phase which is another reason why the slope is linear up until braider yarn crack saturation. Beyond braider yarn crack saturation, stiffness degradation continues, but there is a more gradual increase in the braider yarn crack density. This implies that different mechanisms (i.e., fiber yarn interface crack growth) are also responsible for the additional stiffness degradation exhibited during stage II of cycling. This may be more the case for lower stresses, but less of a factor for higher stresses. To elaborate, consider the presented plots in Figure 66 (c) and (d) for specimens B2-01 and B1-03 cycled at 195 MPa and 275 MPa, respectively. For specimen B2-01 the stiffness-crack density data points significantly deviate from the data regression line shown on the plot after braider yarn crack saturation, while for specimen B1-03 there is notably less deviation from the regression line. In fact as the maximum applied stress increases, this deviation decreases. This is due to the fact that at higher stresses the braider yarn crack density rate is higher during the second stage of cycling, thus contributing more to the stiffness degradation, while at lower stresses the interface crack growth contributes more to the stiffness degradation during the second loading stage.

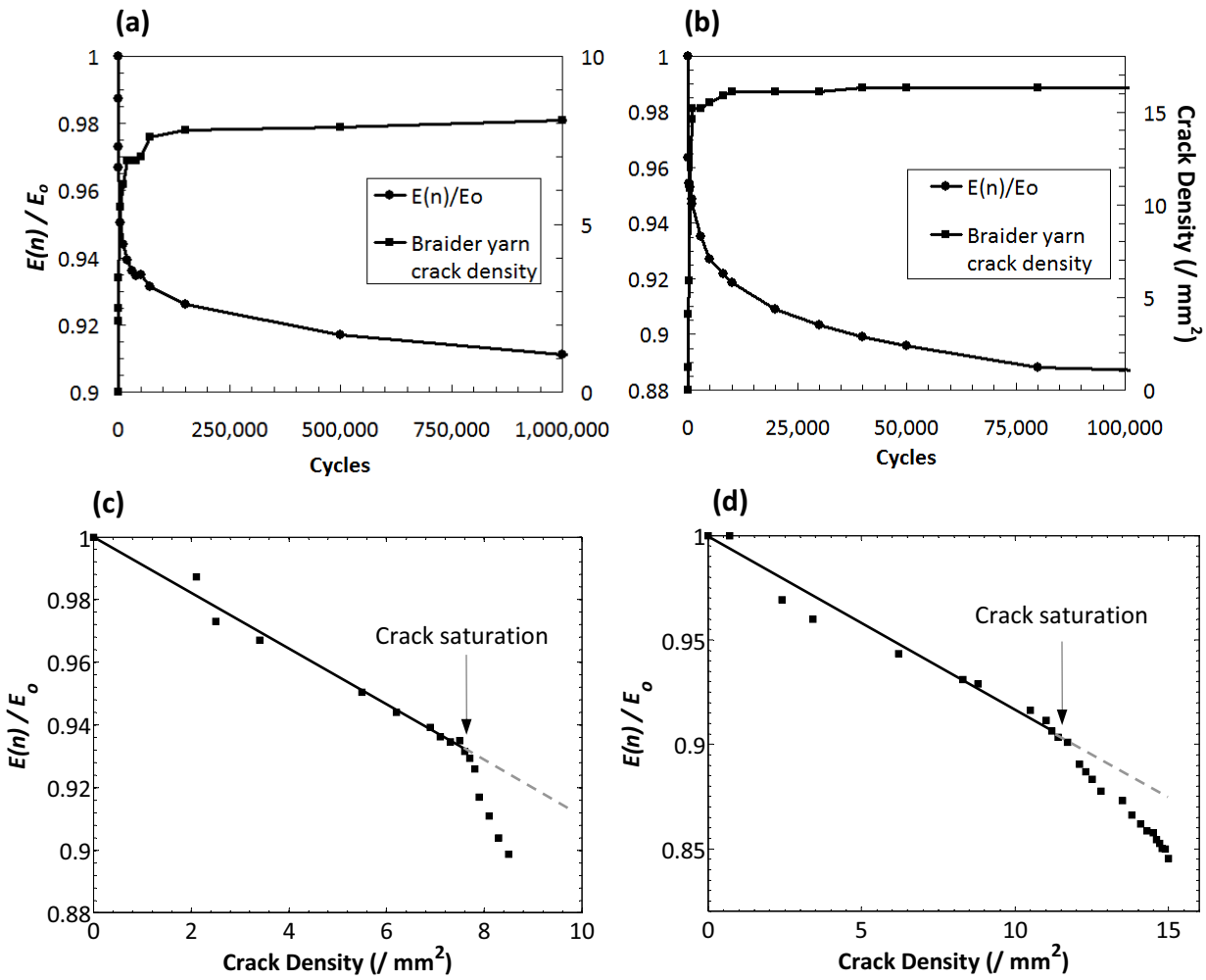

Figure 66. Combined stiffness degradation and crack density profiles for σ_{max} (a) 195 MPa and (b) 275 MPa; stiffness as a function of braider yarn crack density for σ_{max} (c) 195 MPa and (d) 275 MPa.

Consider the growth of fiber yarn interface cracks during stage I and stage II of cyclic loading. Combined plots of the normalized stiffness profiles and 0˚ yarn interface crack average length profiles for specimens cycled with maximum stresses of 195 MPa and 275 MPa are shown in Figure 67 (a) and (b), respectively. The interface crack lengths have notable growth rates during the initial stages of cycling, which confirms that the interface cracks contribute somewhat to stiffness degradation during the initial stage of cycling. Note that since the interface crack density is much lower compared to the braider yarn crack density as shown in Figure 62, the contribution of the interface cracks to stiffness degradation during the initial cycling stage is notably less compared to that of the braider yarn cracks. Plots of the normalized stiffness as functions of the 0˚ yarn interface crack average lengths are shown respectively in

Figure 67 (c) and (d) for the same test specimens. In order to determine the average crack lengths, a number of similar length 0˚ yarn interface cracks were monitored for each acquired edge replica. The length of these sets of cracks were averaged for each replica, which corresponded to a particular loading cycle. The average crack lengths were then plotted against the corresponding normalized stiffness for the specific loading cycle, which make up the data pairs in the plots of Figure 67 (c) and (d). For the specimens cycled with maximum stresses below the HCFS, during the initial stage of cycling prior to braider yarn crack saturation, the interface crack growth rate is proportional to the stiffness degradation with a much steeper slope. If the development of the braider yarn cracks during the first stage of cycling is considered, the stiffness degradation is clearly not solely due to the interface crack growth during this stage. After braider yarn crack saturation, the stiffness degradation is also directly proportional to the average crack length with a more gradual slope. This suggests that the interface crack growth causes a more gradual reduction in stiffness degradation, which is confirmed by recalling the limited braider yarn crack development during this stage in cycling for the lower stressed specimens. Also, damage development during this stage of cycling caused a gradual increase in temperature (see Figure 63), which further confirms that the propagation of the interface cracks causes gradual stiffness degradation. For the specimens cycled with maximum stresses greater than the HCFS, the stiffness degradation is directly proportional to the average crack length for the duration of cycling as shown in Figure 67 (d). The notable difference is due to the fact that the higher stressed specimens continue to exhibit significantly more braider yarn crack growth after the saturation state, which has significantly more influence on stiffness degradation compared to the interface crack growth. Therefore, interface crack growth and the corresponding crack interactions are the main causes of stiffness degradation during the second stage of cycling for the lower stress specimens, while continued braider yarn crack growth mainly contributes to stiffness degradation during the second stage of cycling for the higher stress specimens. This was also clear from the plot in Figure 66 (d).

Recall that the stiffness degradation rate during the second stage was notably higher in magnitude for the specimens cycled at stress levels greater than the HCFS, which ultimately caused these specimens to fail. There was clearly advanced damage progression during the

second stage of cycling for the specimens cycled with maximum applied stresses greater than the HCFS. Also recall that the braider yarn density was higher for the specimens cycled with maximum applied stresses greater than the HCFS (see Figure 62), and continued to increase at a higher rate after saturation. This is the main cause of the higher magnitude stiffness degradation rate during the second stage of cycling, which ultimately led to failure.

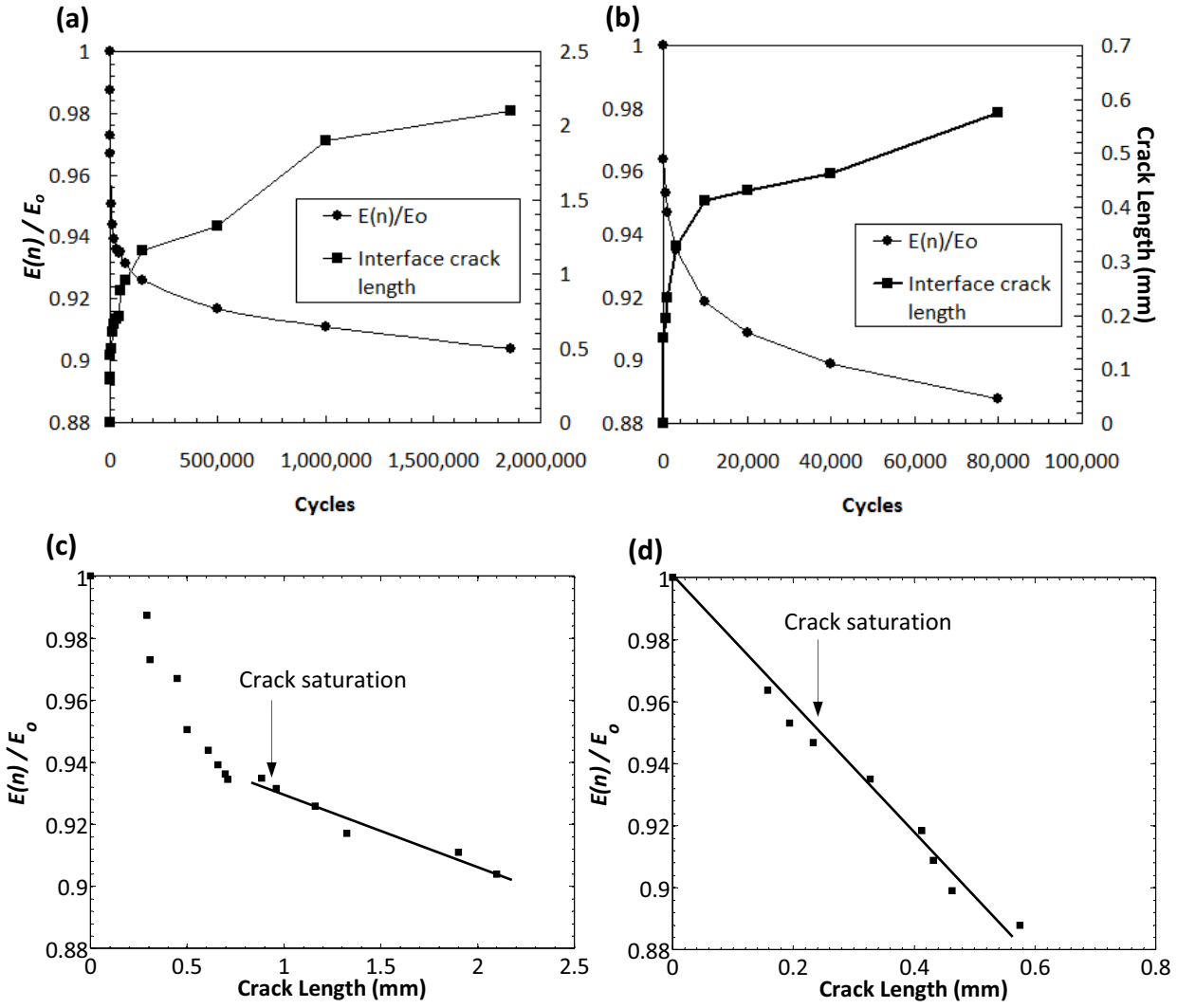

Figure 67. Combined stiffness degradation and interface crack length profiles for σ_{max} (a) 195 MPa and (b) 275 MPa; stiffness as a function of 0˚ yarn interface crack average length for σ_{max} (c) 195 MPa and (d) 275 MPa.

Regarding the exhibited energy dissipation behaviour, it was shown that regardless of the maximum applied stress level the energy dissipated per cycle (E_d) was highest during the first few loading cycles. The magnitude of E_d rapidly dropped and reached a plateau for the majority

of cyclic loading. In fact for each applied stress level, the number of cycles required to reach the energy dissipation plateau corresponds to the number of cycles in which braider yarn cracks saturation occurs. This further confirms that the initial high E_d is due mainly to braider yarn crack development. For all maximum applied stresses the braider yarn crack density rate became progressively lower as the number of cycles increases, up to the saturation state. This would result in the specimen having the highest energy dissipation during the initial few loading cycles, after which E_d rapidly drops as the braider yarn crack density rate drops approaching the saturation state. This can in fact be partially attributed to the characteristics of the matrix which exhibits high thermal stability due to a highly cross-linked molecular structure, which would therefore limit any self-generated viscous heating. IR images obtained at various cyclic intervals for all cyclic tests revealed that the temperatures in the braider yarns were consistently higher when compared to the resin-rich zones. Also, as the maximum stress increased, the energy dissipation level during the plateau increased. At higher stresses the braider yarn crack density was higher due to the higher crack driving forces, thus resulting in higher energy dissipation during the second stage of cycling. Although local viscous matrix behaviour will cause some energy dissipation during cyclic loading, it was illustrated that this was minimal in comparison to the energy dissipated due to the observed cracks development and only exhibited during the early stage of cycling. Although the evolution of E_d during cyclic loading is analogous to that exhibited by metals that strain harden during fatigue [96], the braided composite material exhibited stiffness degradation. As indicated, the initial high magnitude of energy dissipation was mainly due to crack development. The dissipated energy progressively decreased as the braider yarn crack saturation point was reached since the braider yarn crack development rate also progressively decreased, after which E_d remained constant. This is the cause of the exhibited E_d evolution shown in Figure 53.

Regarding the exhibited strain ratcheting behaviour, as was shown in Figure 52 the majority of strain ratcheting occurs during the first stage of loading for all applied stress levels. Since the rapid increase in the braider yarn crack density occurs during this cyclic loading stage, the strain ratcheting was mainly due to crack development (recall that this was due to the fact that the crack faces do not close perfectly upon unloading). In fact, during the conducted tests

that were paused to extract edge replicas for damage monitoring, there was virtually no recovery during the zero-load dwell. Even short dwells were shown to display some sort of recovery for materials that exhibit some degree of viscoelastic behaviour [20]. This further confirms that any strain ratcheting due to creep was minimal throughout cycling.

5.2 Elevated Temperature Results

5.2.1 Completed Test Overview

Similar to the room temperature tests, the main initiatives for the elevated temperature tests were to determine the material properties, develop a fatigue S-N curve, characterize the development of damage during both quasi-static and cyclic tensile loading, and to relate the observed microscopic damage mechanisms to the exhibited macroscopic material behaviour at the constant ambient test temperature of ($T_{g,\ wet}$ - 28)˚C. In total seven ultimate static tensile tests were conducted. For the tension-tension fatigue tests, a minimum of five tests were conducted at each maximum applied stress level. ER and IRT were employed for a number of fatigue tests at each maximum applied stress level, while FBG sensors were also employed for one test at each stress level. Also, two tests were conducted to determine the braided composite HCFS using Risitano's thermographic method.

5.2.2 Static Results

The results of the elevated temperature static tests conducted at a temperature of ($T_{g,\ wet}$ - 28)˚C as outlined in Section 4.5 will be presented. Initially the material stress-strain behaviour and static properties will be presented, followed by a detailed characterization of damage and analysis of the fracture surface. Comparisons to the room temperature results will be made and discussed throughout the section.

5.2.2.1 Material behaviour

A typical stress-strain plot for an ultimate static test is shown in Figure 68 (a), while in Figure 68 (b) room temperature and elevated temperature stress-strain plots are combined for comparison. Contrary to the room temperature tests, at the elevated test temperature the material exhibits a linear stress-strain response to failure. The average ultimate tensile stress

(UTS) was 369 MPa, which corresponds to 94% of the average room temperature UTS, and the average failure strain was 1.24%. The axial modulus (E_{11}) of the braided composite at the elevated temperature was found to be 30.10 GPa, which corresponds to 97% of the room temperature modulus. The main material parameters for each tested specimen are summarized in Table 9, with the average values also included. As shown, the scatter in the data is negligible with less than 2% deviation from the average values. The elevated test temperature only has a slight influence on the composite strength and modulus. Although a similar study on a triaxial braided material is not available in the open literature, the study by Shimokawa *et al*. [5] on carbon fiber/BMI quasi-isotropic laminates also revealed that the material properties were only slightly degraded at elevated temperatures.

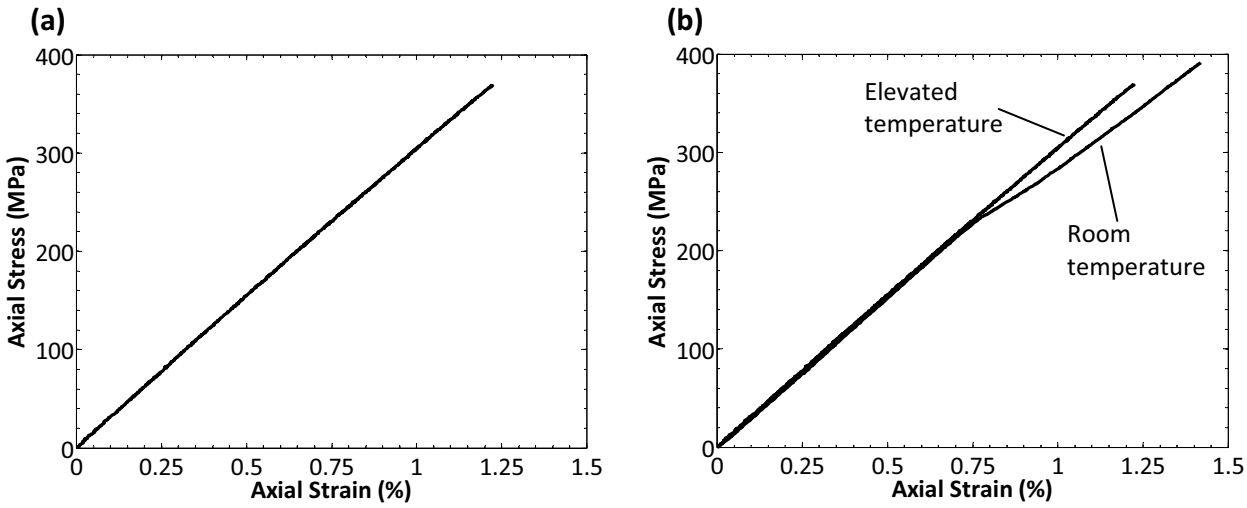

Figure 68. Braided composite (a) elevated temperature static axial stress-strain plot (B3-01), (b) combined stress-strain plots (2 mm/min).

The static tests that generated the results shown in Table 9 were conducted in displacement control with a crosshead speed of 2 mm/min. Two additional static tests were conducted at different crosshead speeds to examine the potential rate-dependent behaviour of the material. The results of these tests are summarized in Table 10, with the corresponding displacement rate indicated. Although the higher and lower displacement rates resulted in slightly higher and slightly lower modulus values, respectively, the deviation of the material properties are less than 5% and considered to be within the scatter of the data. Thus, the

braided material exhibits negligible time-dependent (or rate-dependent) behaviour at the elevated testing temperature when subjected to warp-direction static loading.

Table 9. Elevated temperature material parameters (2 mm/min).

Specimen No.	S_u (MPa)	Failure Strain (%)	E_{11} (GPa)
B3-01	369	1.22	30.2
B4-01	373	1.26	30.5
B2-07	371	1.29	30.0
B2-06 *	-	-	30.4
B3-02	362	1.17	30.2
Average	**369**	**1.24**	**30.1**

*Failed at end tab

Table 10. Elevated temperature material properties for alternate displacement rates.

Specimen No.	S_u (MPa)	Failure Strain (%)	E_{11} (GPa)	Rate (mm/min)
B2-12	389	1.27	31.0	10
B3-08	367	1.29	28.7	0.2

5.2.2.2 Damage Characterization

A microscopic investigation was conducted to track the development of damage from crack initiation up until final specimen failure, as well as to determine the cause of the exhibited stress-strain behaviour. To assist with the detection of damage development, FBG sensors and IRT were employed. In addition, post *mortem* SEM and an analysis of the fracture surface was conducted to determine the final failure mechanisms. Similar to the room temperature static tests, the specimens that were furnished with FBG sensors were analyzed to determine the degree of sensor chirping. Figure 69 illustrates a plot of the FBG sensor wavelength-time profile for the duration of the static test. The wavelength value is linearly rising as shown, without any chirping for the duration of the test until specimen failure. This indicates that there was no major damage event or critical damage state as was shown for the room temperature specimens (see Figure 32). Since the slope of the elevated temperature stress-strain curve is similar to the slope of the initial portion of the room temperature stress-strain curve (i.e., prior to transition), it can be concluded that the braider yarns are in fact fully effective until failure

for the elevated temperature tests. This suggests that the braider yarn crack density is significantly lower during the elevated temperature static tests, which will be confirmed subsequently. Analysis of the obtained IR thermographs for the elevated temperature static tests, analogous to those presented Figure 38, revealed that there was minimal braider yarn cracking for the duration of loading. Crack development, or temperature hot spots, were observed in the thermographs just prior to specimen failure and only at the fracture surface location. This further proves that braider yarn cracking was minimal and less influential for the duration of loading.

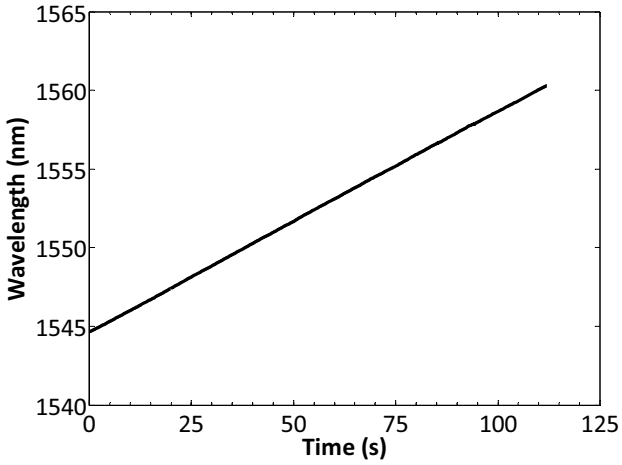

Figure 69. FBG sensor wavelength profile for elevated temperature static test (B2-07).

In order to confirm the damage state after specimen fracture, two static test specimens were sectioned both at the fracture surface and 75 mm from the fracture surface for inspection. SEM photomicrographs of the cross-sectional samples 75 mm from the fracture surface are shown in Figure 70 (a) and (b), while similar photomicrographs for the cross-sectional samples at the fracture surface are shown in Figure 70 (c) and (d). The images confirm that there is little damage throughout the specimen, at locations both near and further from the fracture surface. The damage that was observed consisted of braider yarn cracks and local braider yarn damage as shown in the photomicrographs. As was observed for the room temperature specimens, all braider yarn cracks propagated at the fiber-matrix interfaces. An image of the fracture surface for specimen B3-01 is shown in Figure 71 (a). The area affected by the fracture is very localized as shown. The fracture line has propagated along the +60˚ braider

yarn axis as was the case for the room temperature specimens, which resulted in fracture of the 0˚ and -60˚ fiber yarns. The material stress-strain behaviour revealed that there was no elongation prior to failure indicating brittle-natured fracture, which is clear in Figure 71 (a). The presence of some fiber pull-out is revealed by the slight brushy appearance of the fracture surface and confirmed in Figure 71 (c) by the bare fibers, which is a characteristic of brittle fracture. Furthermore, there was little indication of large-scale debonding and evidence of localized matrix fall-out in the fracture region which is also a characteristic of brittle-natured fracture. A closer inspection of the 0˚ yarns and the braider yarns at the fracture surface reveals that there are notably fewer braider yarn cracks and less splitting in the 0˚ yarns (see Figure 71 (b)) compared to the room temperature specimens. Prior to failure, few braider yarn cracks formed near the eventual fracture zone, however, local fiber breakage and matrix cracking developed in and around these yarns instantly. At this stage the 0˚ yarns were already loaded to their limit, which resulted in some localized splitting and further weakening of these yarns. This subsequently led to instantaneous fracture of the 0˚ yarns and ultimately specimen failure. Note that there was very little evidence of localized fiber yarn rotation at the fracture surface as is evident in Figure 71 (a). As indicated previously, the obtained IR thermographs confirmed that the fracture zone was in fact localized and was preceded by localized damage development (i.e., local high temperature hot spots).

It is clear that the exhibited stress-strain behaviour is not dominated by damage mechanisms in the braider yarns, as was demonstrated for the room temperature specimens. The elevated test temperature is mitigating the initiation and propagation of braider yarn cracks for the duration of static loading, which is the cause of the variation in the stress-strain behaviour at the different test temperatures. This may be a result of the polymer resin material fracture properties at the elevated test temperature, and the influence of the temperature-dependent resin modulus (i.e., softening) on the braided fiber local deformation behaviour. Although it was shown that the braided composite material does not exhibit any time-dependent or rate-dependent behaviour at the elevated test temperature, the polymer resin undoubtedly exhibits some degree of change in stress-strain behaviour [73]. A plot of the storage modulus for the thermosetting polymer resin as a function of temperature is shown in

Figure 72. The plotted data was obtained from various samples of the resin using dynamic mechanical analysis (DMA) [183]. It is clear from the plot that the resin undergoes notable softening at the indicated temperature of ($T_{g,\ wet}$ - 28)˚C, which is characterized by a 35% reduction of the storage modulus. Although the modulus of the braided composite material only reduced by 3% at the elevated test temperature, softening of the resin has a greater impact on the mechanically induced damage development.

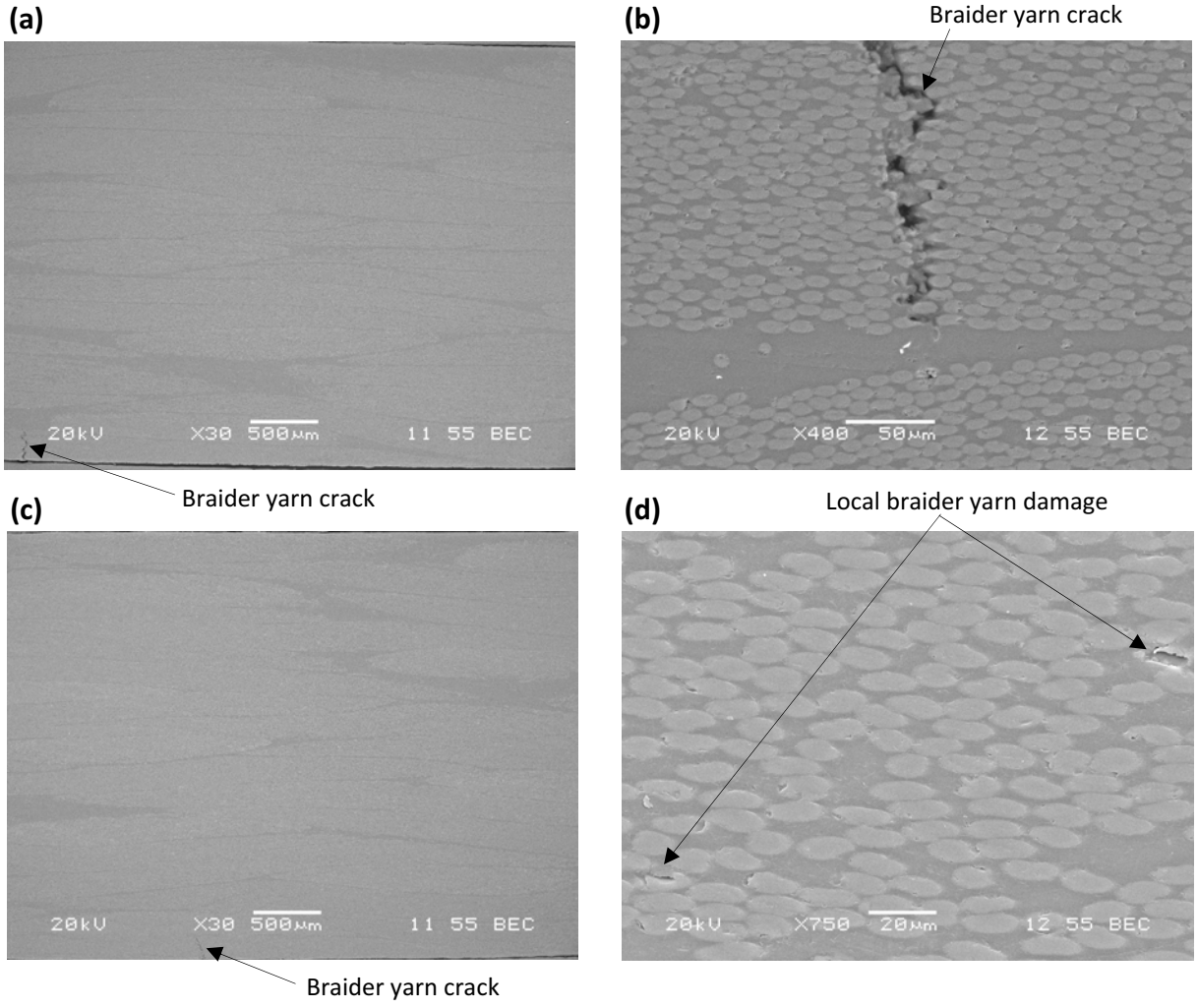

Figure 70. SEM photomicrographs of specimen cross-sections: 75 mm from fracture surface with a magnification of (a) 30X, (b) 400X; at fracture surface with a magnification of (c) 30X, (d) 750X.

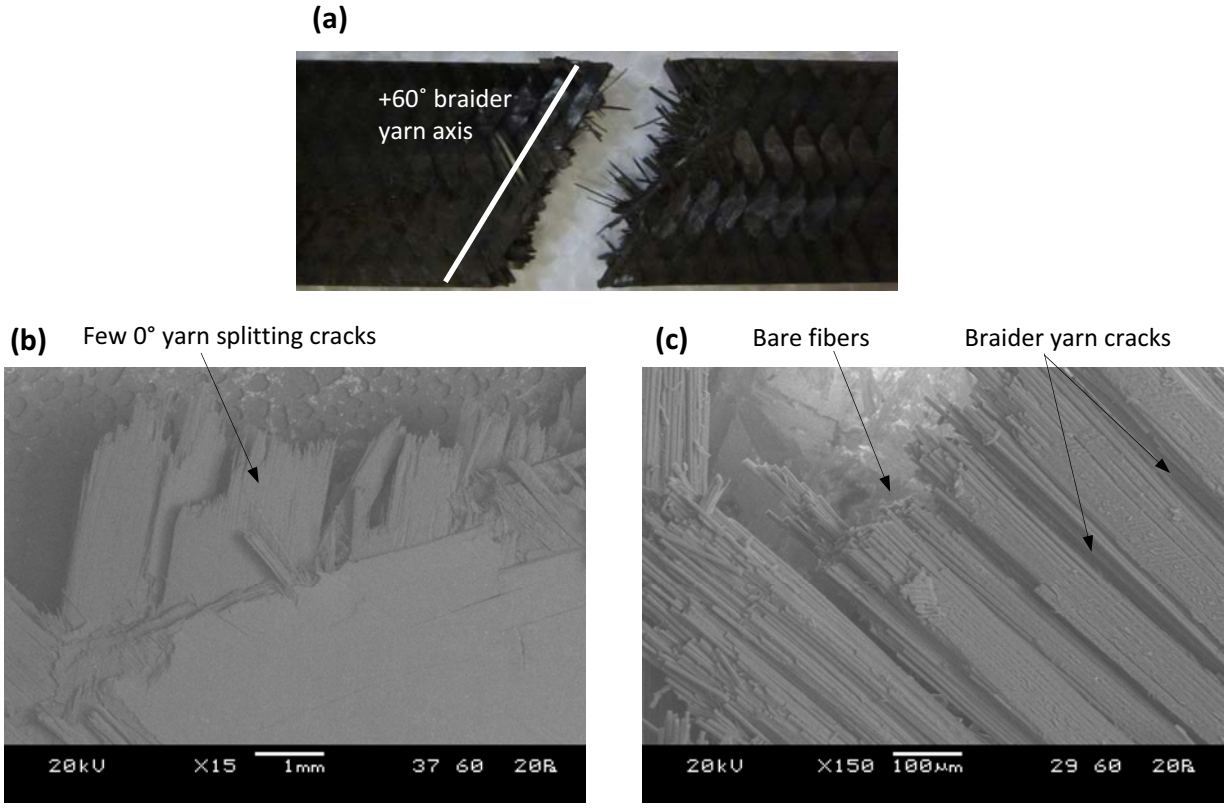

Figure 71. Elevated temperature ultimate static test specimen (B3-01): (a) fracture surface photograph; SEM fracture surface photomicrographs with magnification of (b)15X and (c)150X.

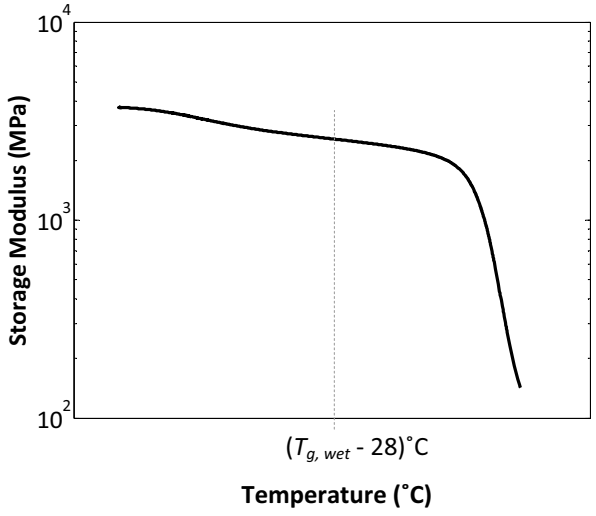

Figure 72. Thermosetting polymer resin storage modulus as a function of temperature [183].

Static testing of cross-ply and quasi-isotropic carbon fiber/BMI laminates by Kobayashi and Takeda [184] revealed that matrix crack growth rates and crack densities were significantly lower at elevated temperatures. It was also revealed that at elevated test temperatures, local matrix deformation was observed. This suggests that the braided composites may be exhibiting a similar toughening mechanism at elevated temperatures due to the softening matrix, which as a result is slowing down the crack propagation rate and limiting crack initiation. The constraint of the fibers on the resin combined with increased local matrix 'ductility' may be alleviating the local stresses in the braider yarns which consequently may also be mitigating braider yarn crack development. A similar mechanism was reported by Gregory and Spearing [88] for a graphite/epoxy composite cyclically loaded at elevated temperatures. In order to further investigate this localized phenomenon, samples of the neat resin material were statically loaded until failure at both room temperature and ($T_{g,\ wet}$ - 28)˚C. The corresponding stress-strain plots for the neat resin were developed by Crochon [183] and are reproduced collectively in Figure 73. The plots reveal that at room temperature the neat resin exhibited linear stress-strain behaviour until failure. At the elevated test temperature, the neat resin exhibited slight nonlinearity with some elongation prior to fracture. In both cases, the fracture surface was perpendicular to the loading direction. A closer inspection of the fracture surfaces of the neat resin specimens reveals that the elevated temperature specimens undergo a more ductile fracture process. This was characterized by a smoother appearance of the resin at the local fracture zones, which is an indication of increased resin toughness. This suggests that the resin fracture toughness may have increased at the elevated test temperature. It should be noted that cross-linked thermosetting resins typically exhibit brittle fracture behaviour. However, the elevated test temperature, although lower than the T_g, may be still be alleviating some of the molecular cross-linking in the resin to a certain degree. This may therefore result in localized 'crazing-type' behaviour at the crack tips, which has been observed in thermosetting resins by Sue *et al.* [185] among others. This may be the mechanism causing increased fracture toughness of the polymer matrix and slower crack propagation rates, which would otherwise require higher driving forces for crack development. Also, this type of fracture behaviour may

be accompanied by local viscoelastic effects near the crack tips which would influence the crack propagation as well.

As a result, the braided composite exhibits a greater resistance to cracking at the elevated test temperature due to the increased toughness of the resin and the potential changes in the load distribution between the fibers and the matrix caused by softening of the resin. Thus, cracks do not initiate at lower stresses during static loading, but are hindered until the stress reaches a threshold (i.e., critical crack initiation level is attained). At this threshold stress level, the cracks initiate and propagate quickly causing rapid development of local damage and instantaneous failure. This may explain the cause of the localized fracture region for the composite. An understanding of the presented matrix fracture and deformation behaviour will undoubtedly provide important microscopic information for analysis of the elevated temperature fatigue behaviour of the braided composite, which will be presented in the subsequent section.

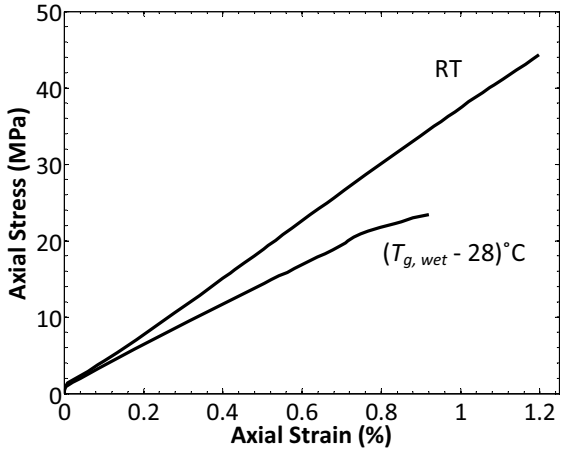

Figure 73. Neat resin stress-strain plots for indicated temperatures.

5.2.3 Fatigue Results

The results of the elevated temperature fatigue tests outlined in Chapter 4.5 will now be presented. Initially the developed S-N curve will be presented, followed by an overview of the exhibited material behaviour, a detailed characterization of damage development, and finally a discussion relating the microscopic damage observations with the exhibited material behaviour. Comparisons to the room temperature results will also be made throughout the section.

5.2.3.1 S-N data

Fatigue tests were conducted for a number of maximum applied stresses within the range of 50%-80% UTS until specimen failure occurred or until a predefined run-off was reached. The corresponding stress-life (S-N) curve for the braided composite is shown in Figure 74 (a), where the average fatigue life values for each maximum applied stress are shown in the plot. A run-off of $5x10^6$ cycles was defined for the elevated temperature tests, and is indicated on the plot for a stress level of 50% UTS, which did not amount to failure for a number of the test specimens cycled at that maximum applied stress. Note that some specimens cycled at 50% UTS failed before the run-off limit, although these were deemed grip-induced failures. A semi-logarithmic relationship was also found to fit the elevated temperature S-N data in Figure 74 (a). The corresponding relationship determined from a numerical regression analysis is also defined by Equation (43), with numerical coefficients of A = 0.1019 and b = 1.20. Data for the test samples that were cycled for $5x10^6$ cycles without failure were not included in the regression. The data correlation factor, R^2, of 0.9957 illustrates that the S-N data has an excellent fit defined by the semi-logarithmic relationship. The combined room temperature and elevated temperature S-N curves are shown in Figure 74 (b). The elevated temperature environment resulted in a notable reduction in the fatigue lives at comparable applied maximum stresses. Although the elevated temperature did not significantly alter the static material properties, the fatigue lives are notably lower in comparison.

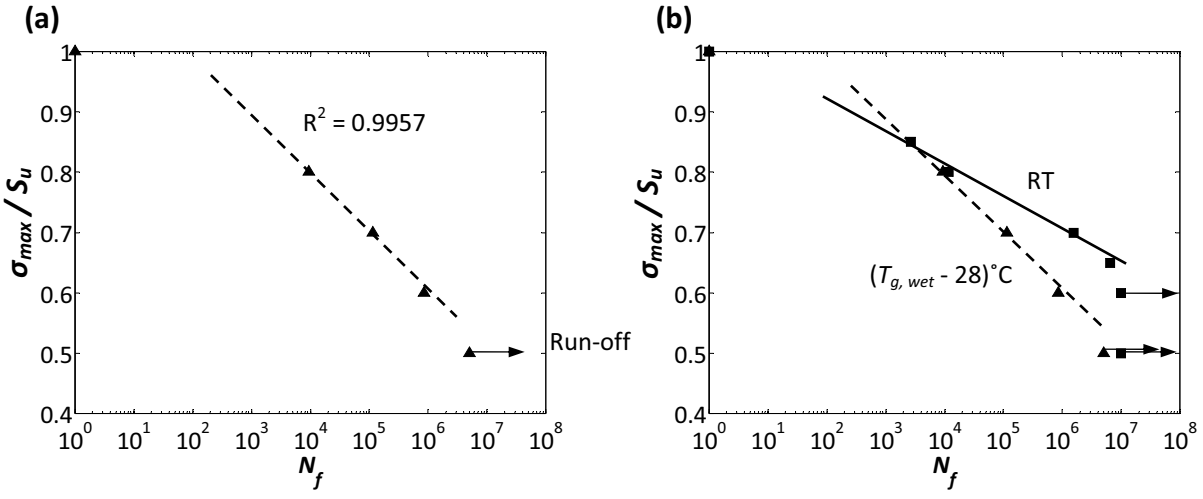

Figure 74. S-N curves (a) elevated temperature, (b) combined room and elevated temperatures.

Recall that the room temperature fatigue data revealed the existence of a HCFS that was approximately equal to the bilinear static transition stress. The damage states associated with the various stress levels were distinct and correlated to the exhibited material behaviour. For the elevated temperature static tests, it was revealed that the material stress-strain behaviour was linear until failure. Thus, the existence of a HCFS at elevated temperatures may not necessarily exist even though some specimens cycled at 50% UTS did not fail after being cycled up to the defined run-off. To confirm the existence of a HCFS, Risitano's thermographic approach for rapidly determining the fatigue limit was also employed at the elevated test temperature. The tests were conducted using a loading frequency of 10 Hz, as discussed in Section 4.5. A similar procedure that was used to determine the room temperature HCFS was employed for the elevated temperature tests. A plot of the specimen surface temperature profiles for a specimen is shown in Figure 75 (a), while a plot of the stabilization temperature rise as a function of the applied stress is shown in Figure 75 (b). The maximum stress magnitude at which the dissipated heat rise becomes greater is clear in the characteristic bilinear plot. This corresponds to an approximate HCFS of 58% UTS (214 MPa), which is greater than the applied stress that resulted in no failure after a run-off as shown on the S-N curve of Figure 74 (a). This confirms that a HCFS exists for the braided composite material at elevated temperature.

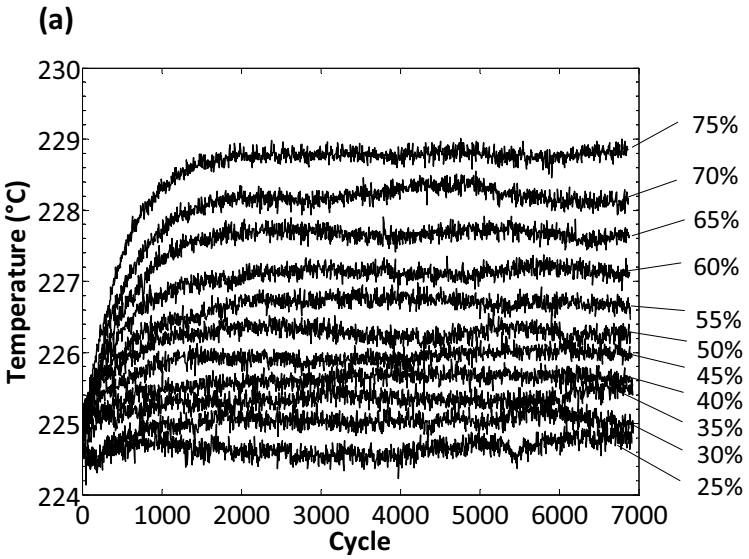

Figure 75. (a) Surface temperature vs. cycle for indicated maximum stress (%UTS), (b) surface temperature increase at stabilization vs. maximum stress.

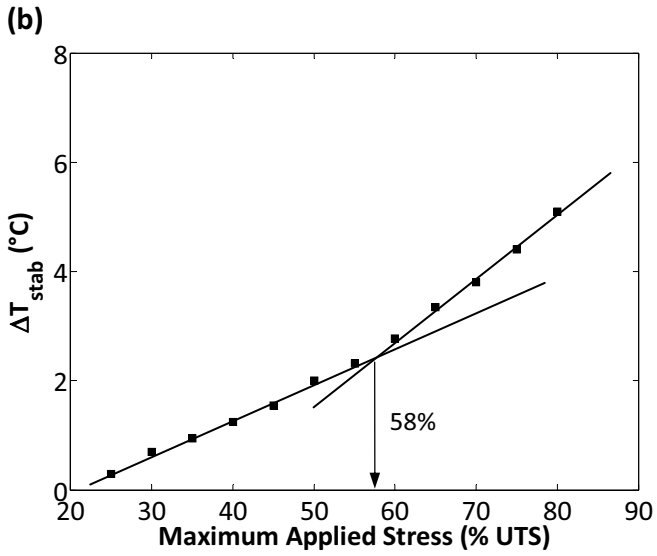

Figure 75. Continued.

Once again, the established HCFS is a distinctive characteristic of the braided composite material under investigation. This is another significant contribution in terms of the application of the thermographic technique for determining the HCFS. Although the elevated temperature static tests did not reveal a transition to a more advanced damage state, the existence of a HCFS suggests that during cyclic loading the maximum applied stress level dictates whether or not failure will occur. An important observation was made by comparing the temperature profiles for the room temperature specimens (Figure 42) and the elevated temperature specimens (Figure 75) - the temperature rise for the elevated temperature tests is significantly lower. Consider for example the ΔT_{stab} of the room temperature and elevated temperature specimens subjected to a maximum applied stress of 80% UTS, which were 12.7˚C and 5.1˚C respectively. The temperature rise for the room temperature specimens was approximately 2.5X greater than the elevated temperature specimens. This implies that the amount of dissipated energy is significantly lower at elevated temperatures, which is a result of reduced damage development. The softening of the polymer matrix at the elevated test temperature would cause additional local viscous energy dissipation, however the temperature rise is significantly lower. This proves that the energy dissipation, measured as dissipated heat by the IR camera, during the early stages of cycling for the elevated temperature specimens is mainly due to local viscous heating of the resin and partially due to damage initiation and propagation.

An investigation of the developing damage state for the elevated temperature specimens will be presented in Section 5.2.3.3. To further elaborate this point, consider the load-unload stress-strain curves of the first loading cycle for specimens cycled at 258 MPa (70% UTS) and 185 MPa (50% UTS), as shown in Figure 76 (a) and (b) respectively. There is much less energy dissipation compared to the first loading cycle of the room temperature specimens (see Figure 46). If the damage state was similar at the two test temperatures, then the energy dissipation should be higher for the elevated temperature tests, which is clearly not the case. Thus, there must be less damage development at the elevated test temperature. In addition, there is notably less dissipation and strain ratcheting for the specimens cycled with a maximum applied stress of 185 MPa compared to the specimen cycled at 258 MPa. This suggests that there is an advanced damage state at the higher stress levels (i.e., σ_{max} > HCFS) for the elevated temperature tests. This provides further support for the existence of a fatigue limit.

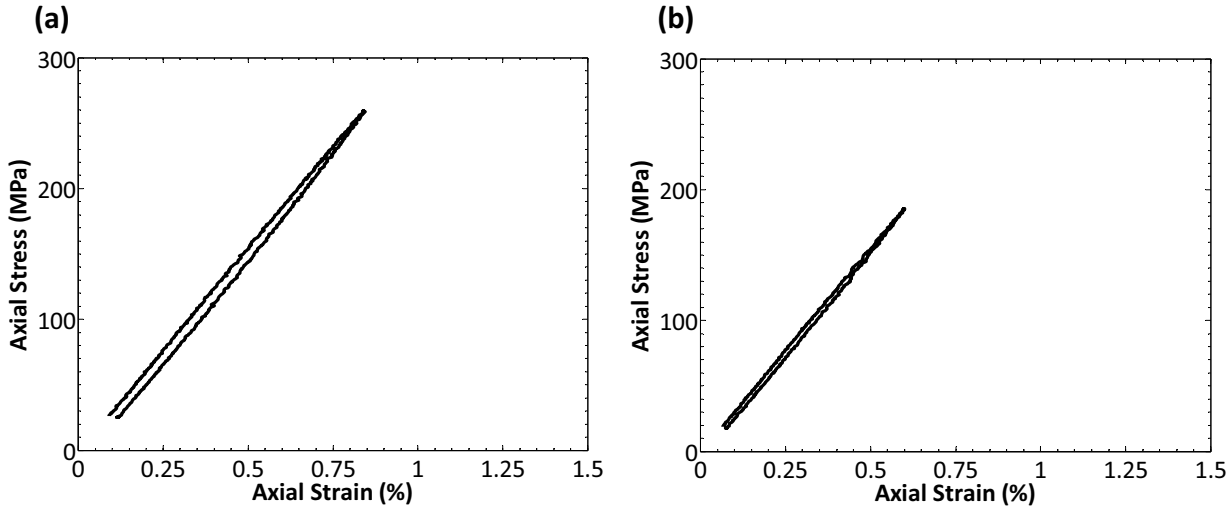

Figure 76. Elevated temperature first loading cycle stress-strain curve with σ_{max} of (a) 258 MPa, (b) 185 MPa.

5.2.3.2 Material behaviour

Plots of the normalized dynamic stiffness, $E(n)/E_o$, as a function of the number of loading cycles, n, for test specimens cycled with maximum applied stresses of 50%, 60%, 70% and 80% UTS (185, 221, 258, 295 MPa) are shown collectively in Figure 77 (a). Note that the dynamic stiffness, $E(n)$, was normalized by the initial dynamic stiffness, E_o, for all plots. The same plots are included in Figure 77 (b), which only shows the initial 100,000 loading cycles. The elevated temperature specimens also exhibit a three-stage stiffness degradation which is distinct from

the room temperature specimens. This is characterized by a gradual stiffness degradation during the first stage of cycling which is a linear function of the number of loading cycles, followed by a second stage in which the stiffness degradation becomes increasingly more gradual, and finally rapid stiffness degradation during the few cycles prior to failure (if applicable). For the specimens cycled to failure, the final rapid stiffness degradation occurs during the final few loading cycles as shown in the plot of Figure 78. There was also more stiffness degradation after a comparable number of cycles as the maximum applied stress increased, while for the specimens cycled to failure there was more stiffness degradation after failure as the maximum stress decreased. This is evident in Figure 78, and was also observed with the room temperature specimens. As shown in Figure 77, the stiffness for the 50% UTS specimens is constant during the initial stages of cycling prior to degradation initiation (in fact the stiffness appears to rise slightly). On the contrary, for all other specimens cycled with higher maximum stresses the stiffness began to reduce much earlier during cycling (instantly for the 80% UTS specimen). This further supports the fact that the specimens cycled with σ_{max} > HCFS exhibit an advanced damage state.

The stiffness degradation for the elevated temperature specimens is notably dissimilar from that exhibited by the room temperature specimens. Combined plots of stiffness degradation at both room and elevated temperatures for maximum applied stresses of 50% and 70% UTS are shown in Figure 79 (a) and (b), respectively. The relatively gradual stiffness degradation rate during the initial stage of cycling for the elevated temperature specimens is evident in the plots. Also, the stiffness degradation rate for the elevated temperature specimens eventually becomes steeper relative to the room temperature specimens as is shown in the plots, which is a result of the evolving fatigue damage development. The room temperature specimens experienced greater stiffness degradation after a comparable number of loading cycles, although the fatigue lives were notably higher. This will be discussed in greater detail in Section 5.2.3.3.

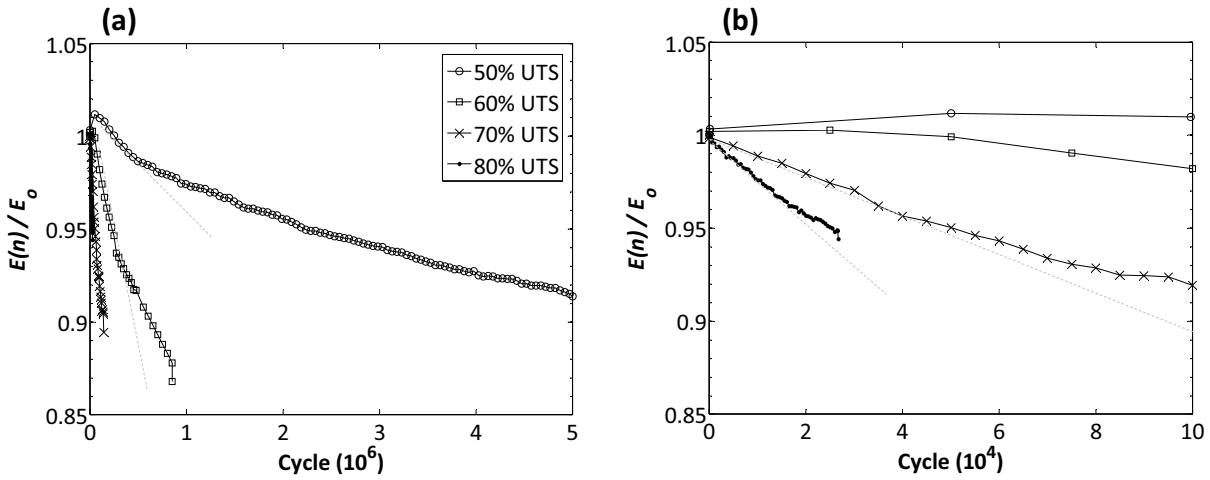

Figure 77. Elevated temperature fatigue normalized stiffness degradation.

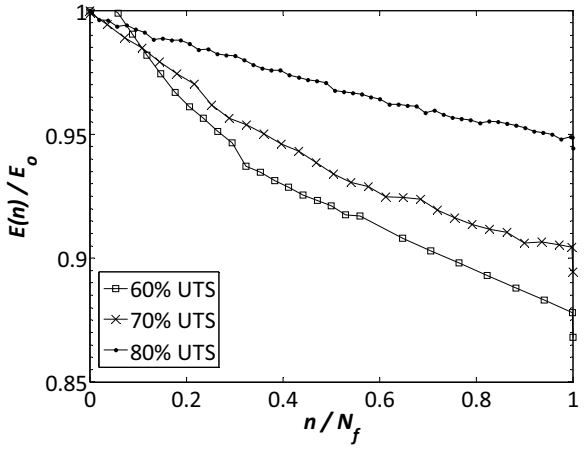

Figure 78. Elevated temperature fatigue stiffness degradation for specimens cycled to failure.

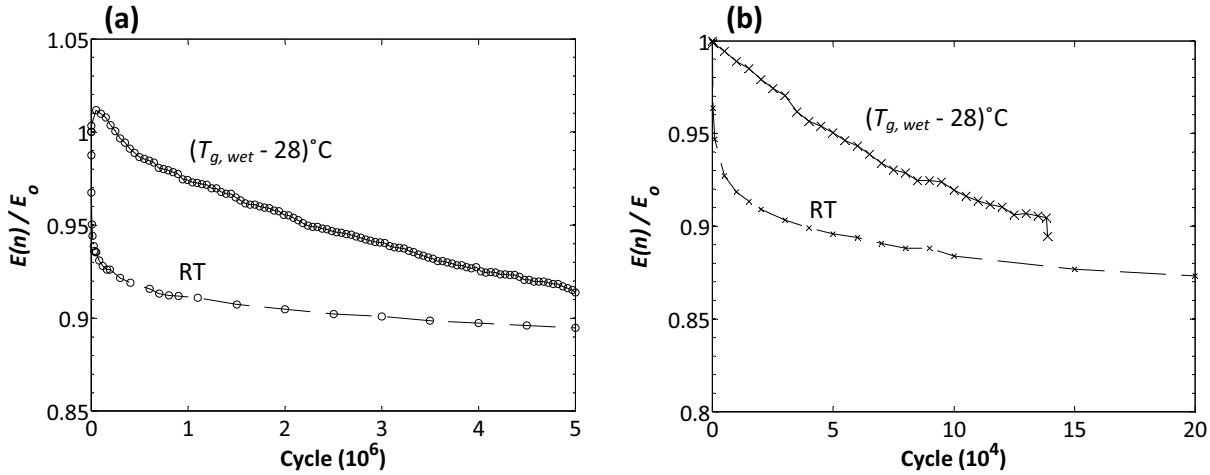

Figure 79. Combined normalized stiffness degradation plots for σ_{max} of (a) 50% UTS, (b) 70% UTS.

The stiffness degradation rate during the initial stage of cycling and the total average stiffness degradation rate also yielded qualitative information on the damage development rate during cyclic loading at the elevated test temperature. Plots of the first-stage stiffness degradation rate ($dE(n)/dn|_1$) and the total average stiffness degradation rate ($\Delta E_{total}/N_f$) as functions of the maximum applied stress ratio (σ_{max}/S_u) are shown in Figure 80 (a) and (b), respectively. The stiffness degradation rates clearly increase with increasing maximum stress. A regression on the plotted data illustrates that a power law function is a suitable fit to the data, with R^2 values close to 1 as shown in Figure 80. This is an important finding for the braided composite material, which implies that there is a mathematical relationship between the progressive damage state and the maximum applied stress at the elevated test temperature. A similar power law relationship was found for the room temperature specimens. Note that although the initial stiffness degradation rate for the room temperature specimens was significantly higher, the total average stiffness degradation rate for the elevated temperature specimens was notably higher which was a result of increased damage development during the second stage of cycling and the shorter fatigue lives. The result of Figure 80 (a) further suggests that knowledge of the stiffness degradation rate during the initial stage of cycling can be used to predict the fatigue life of the material, which is another important finding.

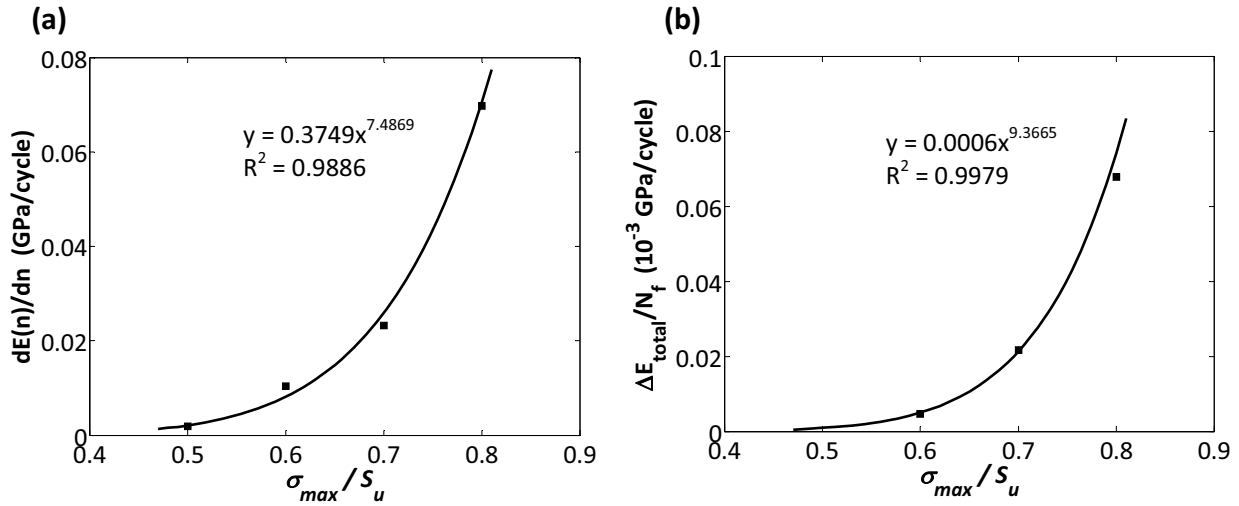

Figure 80. Elevated temperature fatigue (a) first stage stiffness degradation rate, (b) average stiffness degradation rate as functions of σ_{max} / S_u.

A plot of the measured mean strain, ε_{mean}, as a function of the number of loading cycles, *n*, for test specimens cycled with the indicated maximum applied stresses are shown collectively in Figure 81 (a). The same plots are included in Figure 81 (b), which only shows the initial 100,000 loading cycles. The mean strain follows a three-stage progression, characterized by a slight but rapid increase during the first stage, a gradual increase during the second stage which is for the majority of cycling, and a rapid increase prior to failure. The initial rise in the mean strain is significantly lower compared to the room temperature specimens for all stress levels, which suggests that there is little damage or strain ratcheting during the early stage of cycling at the elevated test temperature. Recall that for the room temperature tests there was significant damage and corresponding strain ratcheting during the early stages of cycling. It was also observed that the mean strain rate during the second stage of cycling increased as the maximum applied stress increased. A plot of the stage II mean strain rate as a function of the maximum stress is shown in Figure 82. Similar to the room temperature test specimens, a power law function was found to fit the data through a numerical regression with excellent correlation, as shown by the data correlation factor in Figure 82. The mean strain rate during the second stage of cycling is notably higher than the mean strain rate for the room temperature test specimens for all applied stresses. This implies that the elevated temperature specimens exhibit more damage development during the second stage of cycling, which is expected when observing the stiffness degradation plots in Figure 79. Another important observation is that the overall mean strain increases by a larger magnitude for the room temperature specimens, which corresponds to the larger exhibited stiffness degradation relative to the elevated temperature specimens.

Figure 83 (a) and (b) show combined profiles of ε_{mean} and $\Delta\varepsilon$ for test specimens cycled at 185 MPa and 258 MPa, respectively. For each maximum applied cyclic stress level, the mean strain rate was higher in magnitude than the strain range rate during the early stages of cycling, while for the duration of cycling the mean strain and strain range profiles evolved identically until specimen failure. This implies that during the early stages of cycling strain ratcheting occurs, however, ratcheting subsides afterwards and is negligible for the duration of cyclic loading. Recall similar strain ratcheting behaviour for the room temperature specimens. For

higher applied stress levels, the magnitude of initial strain ratcheting reduces to a negligible amount as shown in Figure 83 (b). The stiffness degradation plots of Figure 77 reveal that there is gradual stiffness degradation during the early stage of cycling for lower applied stresses. This suggests that the initially exhibited strain ratcheting is partially due to creep deformation (albeit minimal) for specimens with lower applied stress, while strain ratcheting that occurred for the duration of cycling is due mainly to damage development. This will be discussed further in Section 5.2.3.4.

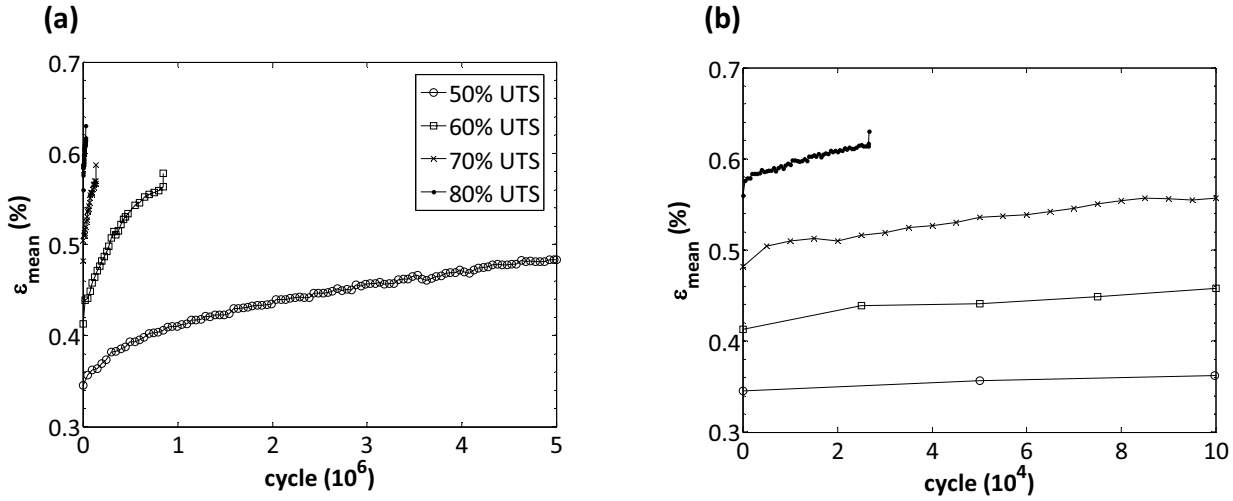

Figure 81. Elevated temperature fatigue mean strain plots.

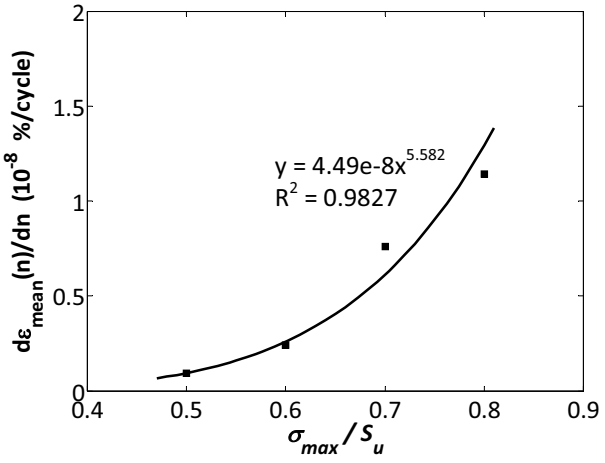

Figure 82. Elevated temperature fatigue second stage mean strain rate as a function of σ_{max} / S_u.

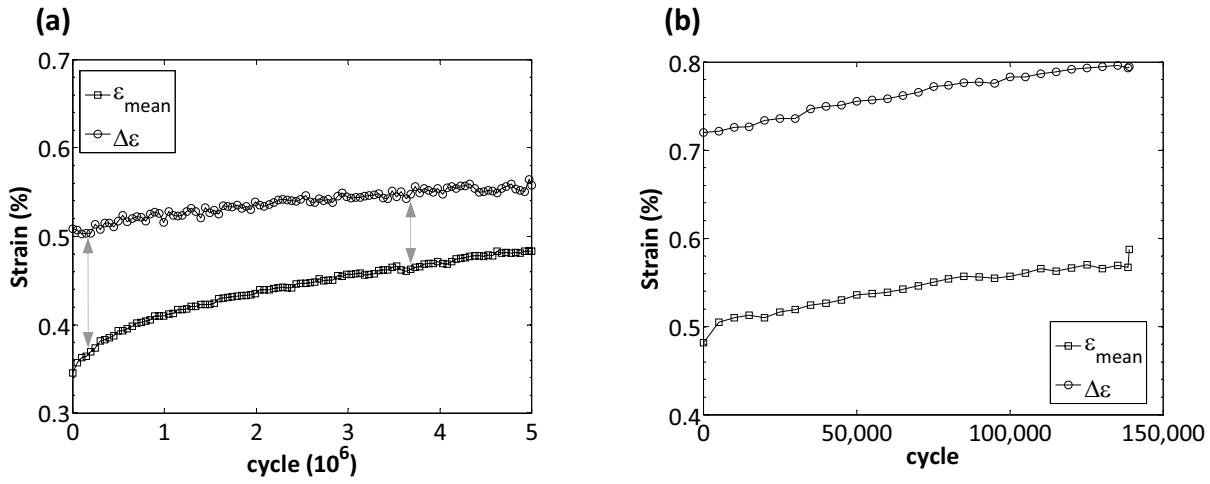

Figure 83. Strain range and mean strain profiles for σ_{max} of (a) 185 MPa, (b) 258 MPa.

A plot of the energy dissipation (E_d) for the indicated maximum stresses is shown on a semi-logarithmic scale in Figure 84 (a). For all applied cyclic stress levels, the energy dissipated during the first loading cycle was slightly higher. During the subsequent loading cycles E_d rapidly decreased in magnitude until reaching a plateau, after which E_d was approximately constant or decreasing at a very gradual rate. The cyclic energy dissipation maintained this magnitude for the majority of cyclic loading as shown. Figure 84 (b) shows similar plots on a linear scale for specimens cycled with maximum stresses of 185 MPa and 258 MPa. For the specimens cycled to failure, the dissipated energy increased slightly during the cycles prior to failure. The evolution of E_d implies that the onset of damage and/or the potential local viscous matrix behaviour during the first few loading cycles contributed to the initially higher dissipated energy exhibited by the test specimens. Recall that there was no stiffness degradation during the first stage of cycling for the 50% UTS specimens, while for the higher stress specimens the stiffness degradation was gradual. Also recall that strain ratcheting only occurred during the initial stage of cycling, the degree of which subsided as the maximum applied stress decreased. This suggests that the initial drop in E_d is due to in part by the slight creep deformation exhibited by the composite. The initial drop in energy dissipation for the 50% UTS specimens is significantly lower than the other specimens, which confirms that the degree of creep strain evolution is minimal. The initial drop in energy dissipation for the higher stress specimens is slightly higher, and can be attributed to crack initiation during the early stages of cycling for

these specimens. The E_d plateau was reached after comparable number of cycles for each stress levels, which further confirms that the energy dissipated during the initial few loading cycles was in part a result of minor creep behaviour. As cycling progressed, the dissipated energy reached a plateau since the degree of local viscous matrix behaviour began to subside. For the duration of cyclic loading, E_d remained fairly constant which implies that the local viscous effects and/or evolving damage attained a constant rate. For the specimens cycled to failure, the increase in E_d prior to fracture was due to the rapid accumulation of damage leading to the final failure event. Thus, the dominant mechanism contributing to the presented energy dissipation evolution is in fact fatigue damage development, as was the case for the room temperature specimens. The energy dissipation profiles are in fact analogous to those exhibited by the room temperature specimens. The main difference is that the initial rapid drop in E_d is significantly lower for all specimens cycled at elevated temperature, which is due to the more gradual damage progression during the initial stages of cycling. The magnitude of E_d during the second stage of cycling for each applied stress for the elevated temperature specimens is higher in magnitude compared to the room temperature specimens. This was a result of increased damage development during the second stage of cycling.

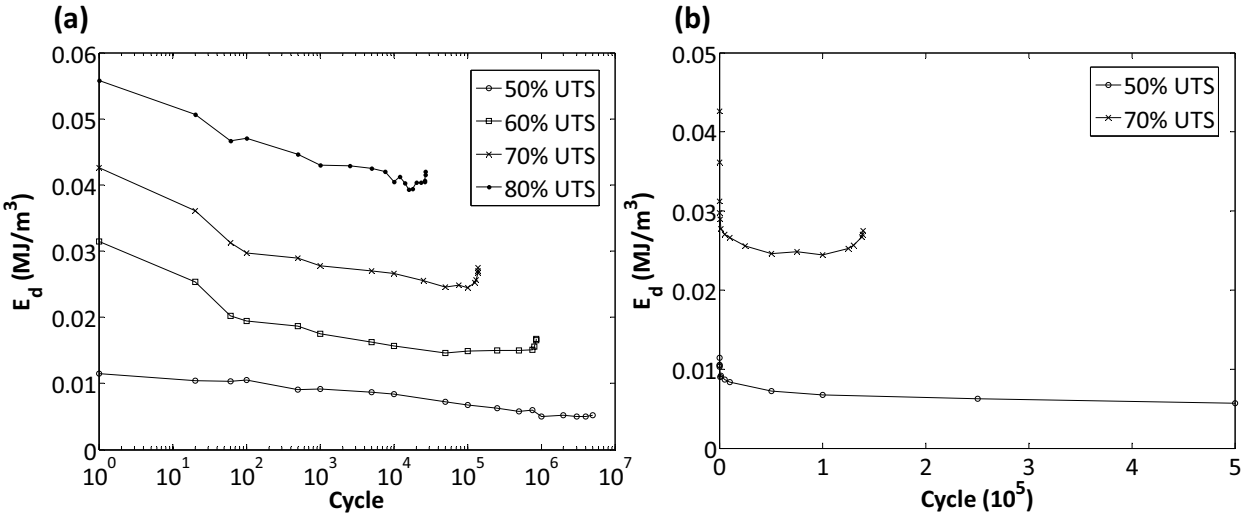

Figure 84. Plots of evolving energy dissipation (a) semi-logarithmic scale, (b) linear scale.

Similar to the room temperature specimens, there was a relationship between the magnitude of E_d and σ_{max}. A plot of the plateau energy dissipation values as a function of the

maximum applied stress is shown in Figure 85. A similar power law function fits the data well as shown by the data correlation factor in the plot.

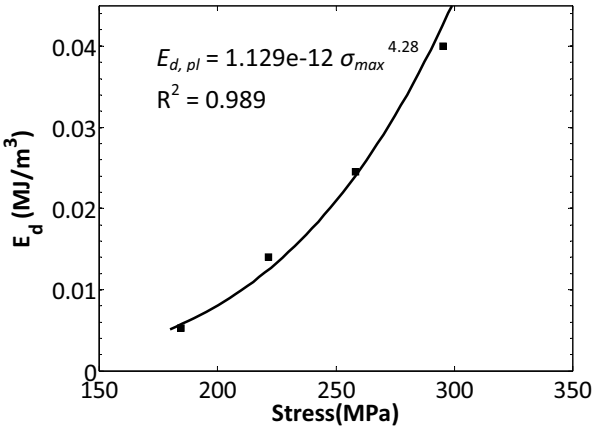

Figure 85. Plateau energy dissipation as a function of σ_{max}, elevated temperature.

Plots of successive stress-strain curves for the indicated cycles during the early stages of cycling for specimens loaded at 185 MPa and 258 MPa maximum applied stresses are shown in Figure 86. Specimen B4-02 exhibited little energy dissipation during the first cycle, with slightly decreasing dissipation as indicated by the areas within the stress-strain ellipses. This behaviour was typical of all test specimens cycled with σ_{max} < HCFS. Specimen B4-12 exhibited more energy dissipation during the first cycle, with rapidly decreasing dissipation thereafter until the plateau. This behaviour was typical for all test specimens cycled with σ_{max} > HCFS. In general, the small areas of stress-strain ellipses shows there is very little viscous effects or creep throughout the duration of cycling, even for the first cycle. There in fact was no lag between the stress and strain, as was similarly shown for the room temperature specimens (see Figure 56). There is little strain ratcheting for all maximum stress levels as illustrated in the plots of Figure 86, which confirms that strain ratcheting is in fact mainly due to the gradual damage development. As was illustrated in Figure 83 and confirmed in the plots of Figure 86, the majority of ratcheting occurs during the initial few loading cycles. The degree of ratcheting is notably less relative to the room temperature specimens, which again is due to the more gradual damage development during cycling.

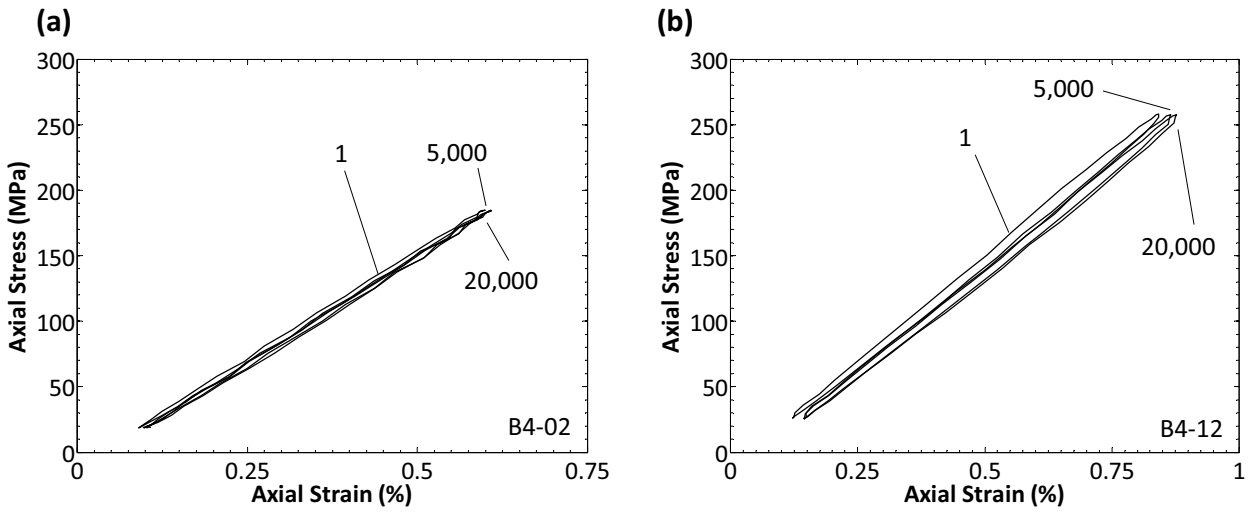

Figure 86. Successive cyclic stress-strain plots with cycle number indicated (a) 185 MPa, (b) 258 MPa.

5.2.3.3 Damage characterization

A microscopic investigation was conducted to track the development of damage during cyclic loading and to investigate the mechanisms responsible for the exhibited material behaviour and ultimately failure. To this effect, a series of tests were conducted at each maximum applied stress to characterize the damage evolution in the material. This involved extracting edge replicas and IR thermographs, post *mortem* SEM observations, and analysis of the fracture surfaces for the test specimens cycled to failure. The corresponding results for the microscopic investigation will now be presented.

In order to use the same edge replication technique for extracting the edge replicas, the elevated temperature test specimens were gradually cooled to room temperature over a three hour period while the test frame was in a load-controlled zero-load dwell. Once the replicas were extracted, the environmental chamber was gradually reheated and the test specimen was allowed to condition at the test temperature as discussed in Section 4.4. A sequence of images of edge replicas extracted from a specimen cycled with a maximum stress of 185 MPa are shown in Figure 87. During the early stages of cycling, the only damage mode observed was braider yarn cracking as shown in Figure 87 (a). At this stage, the braider yarn crack density was relatively low and there were no yarn interface cracks observed. As cyclic loading progressed the number of braider yarn cracks increased at a consistent rate, while localized matrix cracks and braider yarn interface cracks were also observed as shown in Figure 87 (b). There were few

interface and matrix cracks in comparison to the number of braider yarn cracks observed at this stage. Unlike the room temperature specimens, the braider yarn crack density did not reach a saturation state, but continued to increase throughout cycling with a relatively gradual rate. The interface cracks eventually began to increase in length after 10^6 loading cycles, while the braider yarn crack density continued to increase as shown in Figure 87 (c). Much later during cycling, the interface cracks around the 0˚ and braider yarns were notably longer and crack interaction was significantly higher as shown in Figure 87 (d). The cracks around the 0˚ yarns propagated in the loading direction along the yarn axes. The interface cracks between adjacent braider yarns propagated in a plane in both the loading direction and the direction perpendicular to loading. The majority of the interface cracks initiated at the braider yarn crack tips due to the localized high stress field at the crack tips (e.g., see Figure 87 (c) and (d)). Few cracks developed in the 0˚ yarns throughout most of cycling.

Figure 88 presents cross-sectional photomicrographs obtained using SEM for the same test specimen after cycling for $5x10^6$ loading cycles without failure. The images confirm that the majority of damage is cracking in the braider yarns, even after $5x10^6$ loading cycles. The propagation of the 0˚ yarn periphery cracks around the yarn cross-section is also illustrated in the photomicrographs of Figure 88 (a) and (b). The long yarn interface cracks and the notable interactions between the various observed damage modes are confirmed by the SEM photomicrographs. Note that the braider yarn cracks within the braider yarns and the yarn interface cracks propagated at the fiber-matrix interfaces, as highlighted in Figure 88 (c). There was also evidence of matrix fall-out near the crack faces as shown in Figure 88 (d). Although this was caused by post test sectioning of the specimens, this did not occur for any of the room temperature specimen SEM samples, which proves that there was deterioration of the fiber-matrix interface strength and/or the local matrix properties due to the high temperature environment. A study by Cain *et al*. [186] illustrated that during room temperature fatigue testing of off-axis unidirectional laminates, cracking in the off-axis plies occurred at the fiber-matrix interfaces. This was confirmed in another study on unidirectional-ply laminates by Koyanagi *et al*. [187], which also illustrated that for elevated temperature fatigue tests cracking at the fiber-matrix interface was accompanied by local matrix damage. It was however stated

that fiber-matrix interface strength was not temperature-dependent in that study. A study by Montesano *et al*. [72] also found analogous differences in the fiber-matrix interface crack behaviour in off-axis woven laminates cycled at room and elevated temperatures. For the braided composites it appears that a similar mechanism occurred, which has undoubtedly influenced the propagation rate of braider yarn cracking at the fiber-matrix interfaces. This is in-line with the observations of increased fracture surface ductility for the neat resin presented in Section 5.2.2.2.

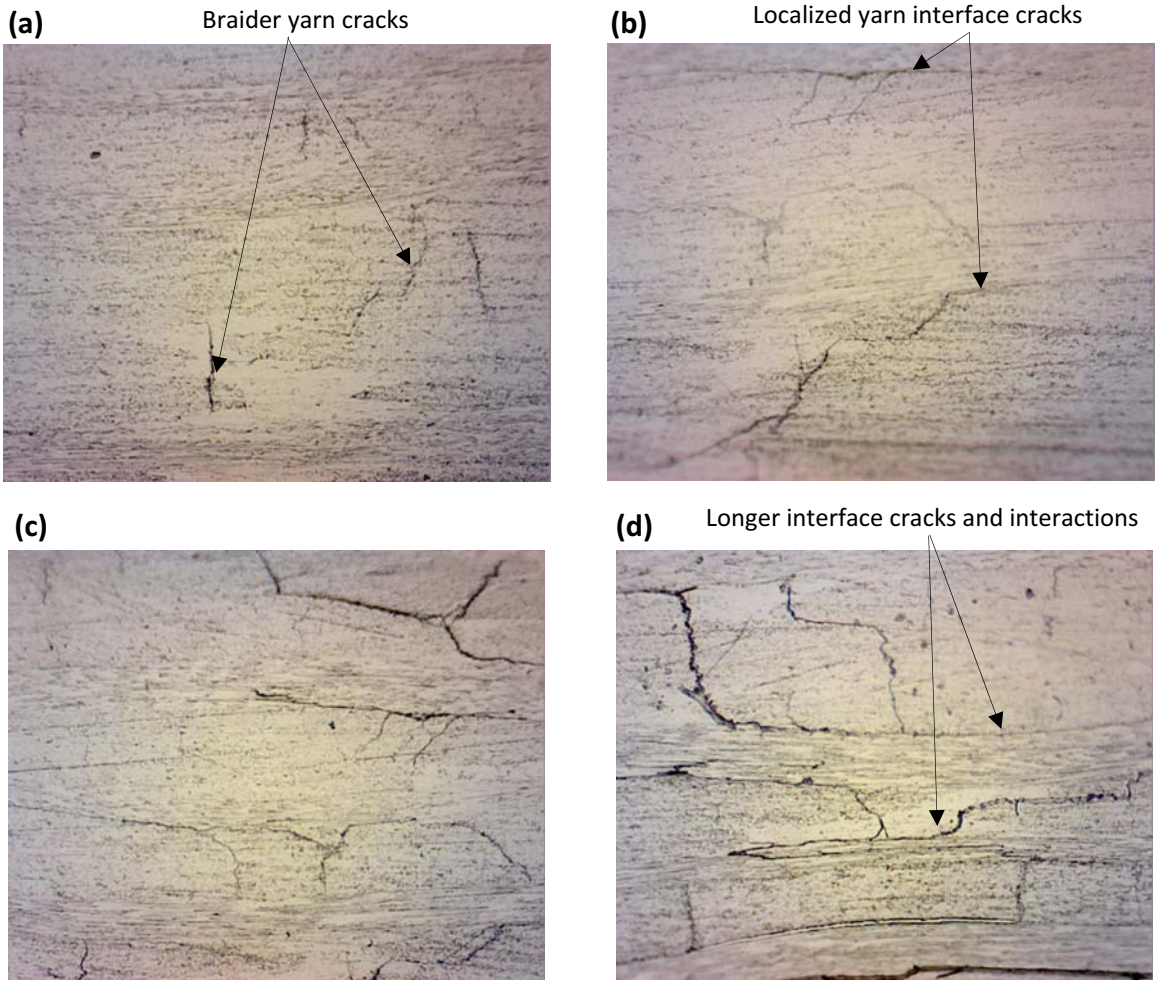

Figure 87. Images captured at 60x magnification using an optical microscope of edge replicas obtained for specimen B4-07 cycled at 185 MPa after (a) 10,000, (b) 100,000, (c) 1,130,000 and (d) 2,500,000 cycles.

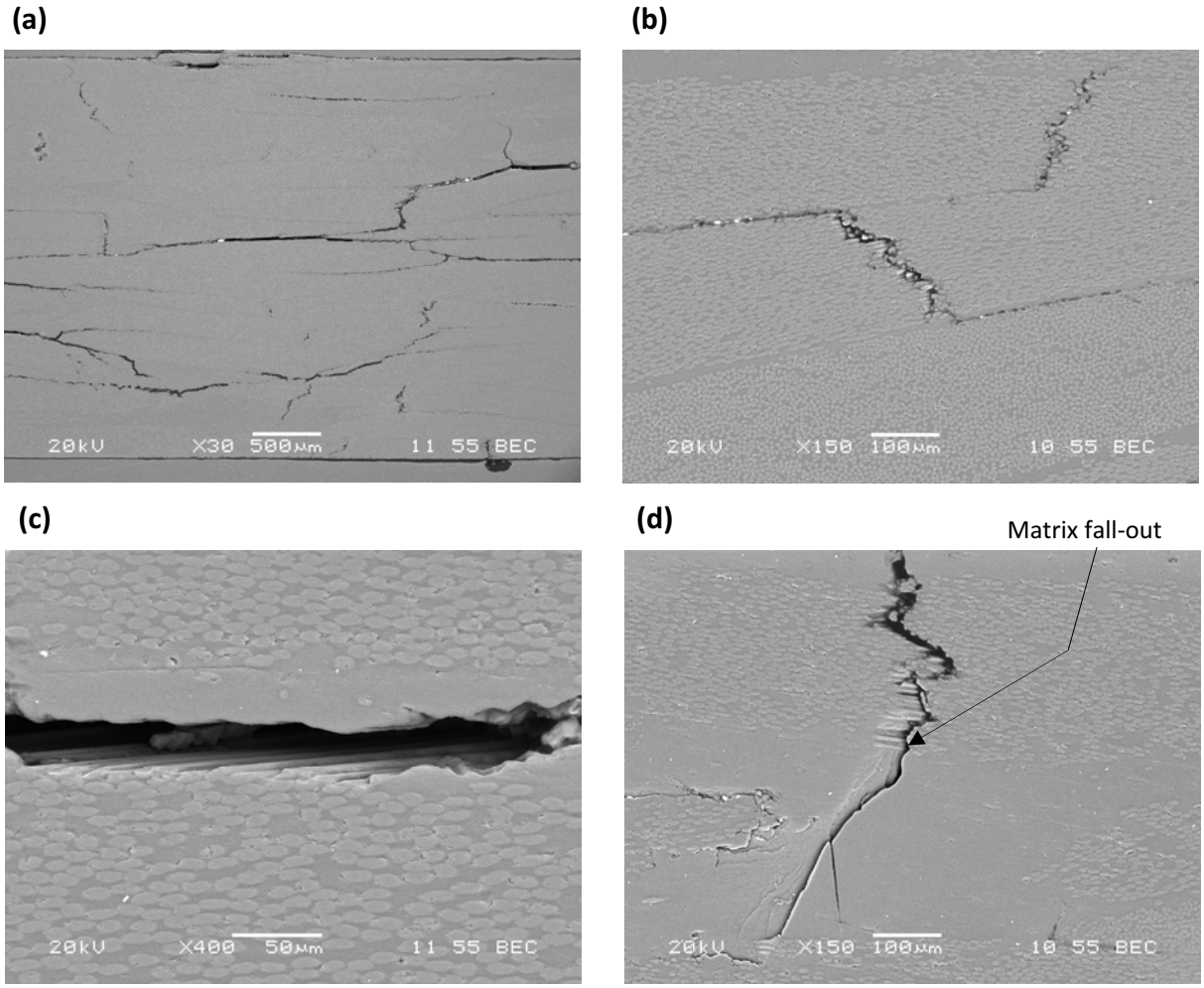

Figure 88. SEM cross-sectional photomicrographs for specimen cycled with 185 MPa for $5x10^6$ cycles at magnifications of (a) 30X, (b) 150X, (c) 400X and (d) 150X.

A sequence of edge replicas extracted from a specimen cycled with a maximum stress of 258 MPa are shown in Figure 89. A notable increase in the braider yarn crack density occurs much earlier during the early stages of cycling as shown in Figure 89 (a). The braider yarn cracks are still the main damage mode observed, which was the case for all maximum applied stress levels. The braider yarn crack density increases at a faster rate consistently for the duration of cycling, while the yarn interface cracks begin to grow after fewer loading cycles. As the maximum stress increases, the interface crack lengths become longer much earlier in cycling. Interactions between braider yarn and yarn interface cracks also occurred much sooner. Figure 90 presents cross-sectional photomicrographs obtained using SEM for the same test specimen

after cycling to failure. The observed damage modes were confirmed, as well as the observation that all cracks propagated at the fiber-matrix interfaces (see Figure 90 (b)). At a cross-section near the fracture surface, the number of interface cracks and their respective lengths has increased and the interactions between cracks has also increased. The interface crack 'widening' effect due to out-of-plane fiber yarn deformation at the fracture surface is evident in Figure 90 (c), which was also observed with the room temperature fatigue test specimens. In comparison to the specimens cycled at lower maximum applied stresses, the braider yarn crack density was lower and the number of interface cracks and their respective interaction was also lower after specimen failure. A similar observation was found for the room temperature specimens. This is attributed to the fact that at higher σ_{max}, fewer cycles are required to reduce the residual strength to the level of the applied stress.

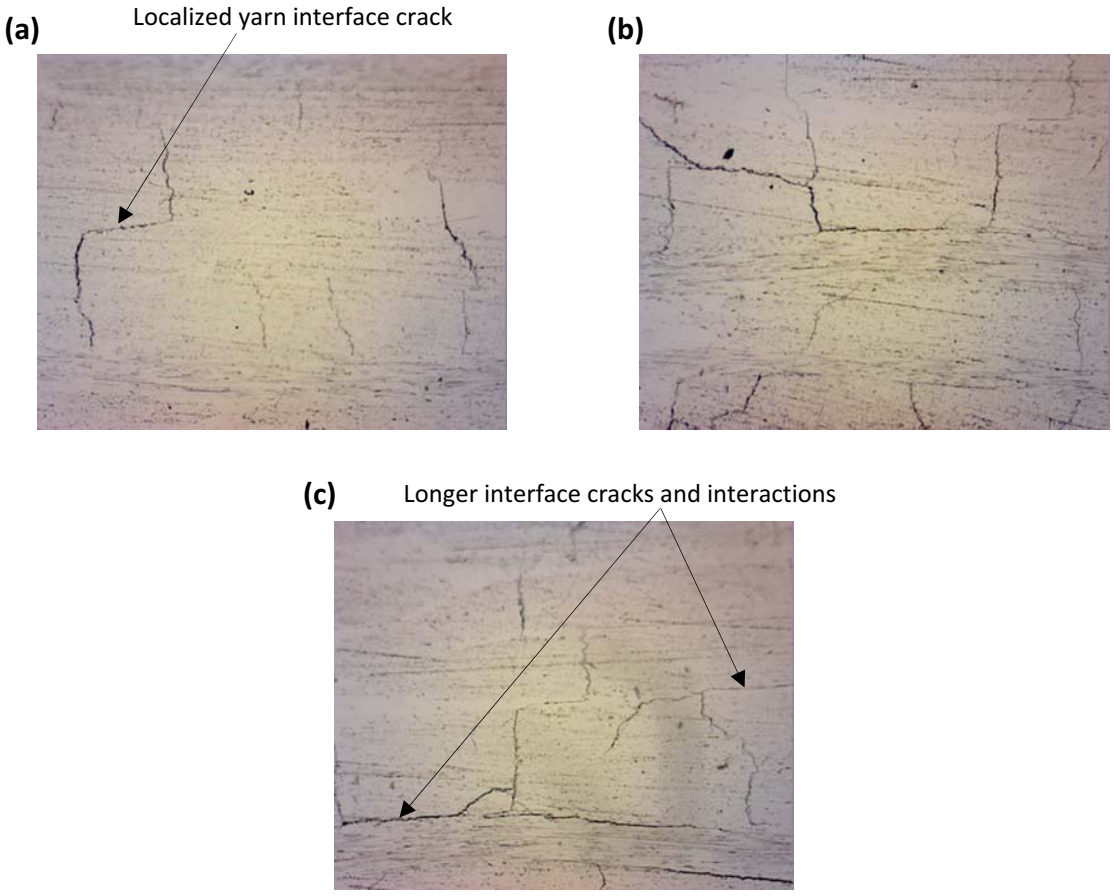

Figure 89. Images captured at 60x magnification using an optical microscope of edge replicas obtained for specimen B4-08 cycled at 258 MPa after (a) 1,000, (b) 15,000 and (c) 43,000 cycles.

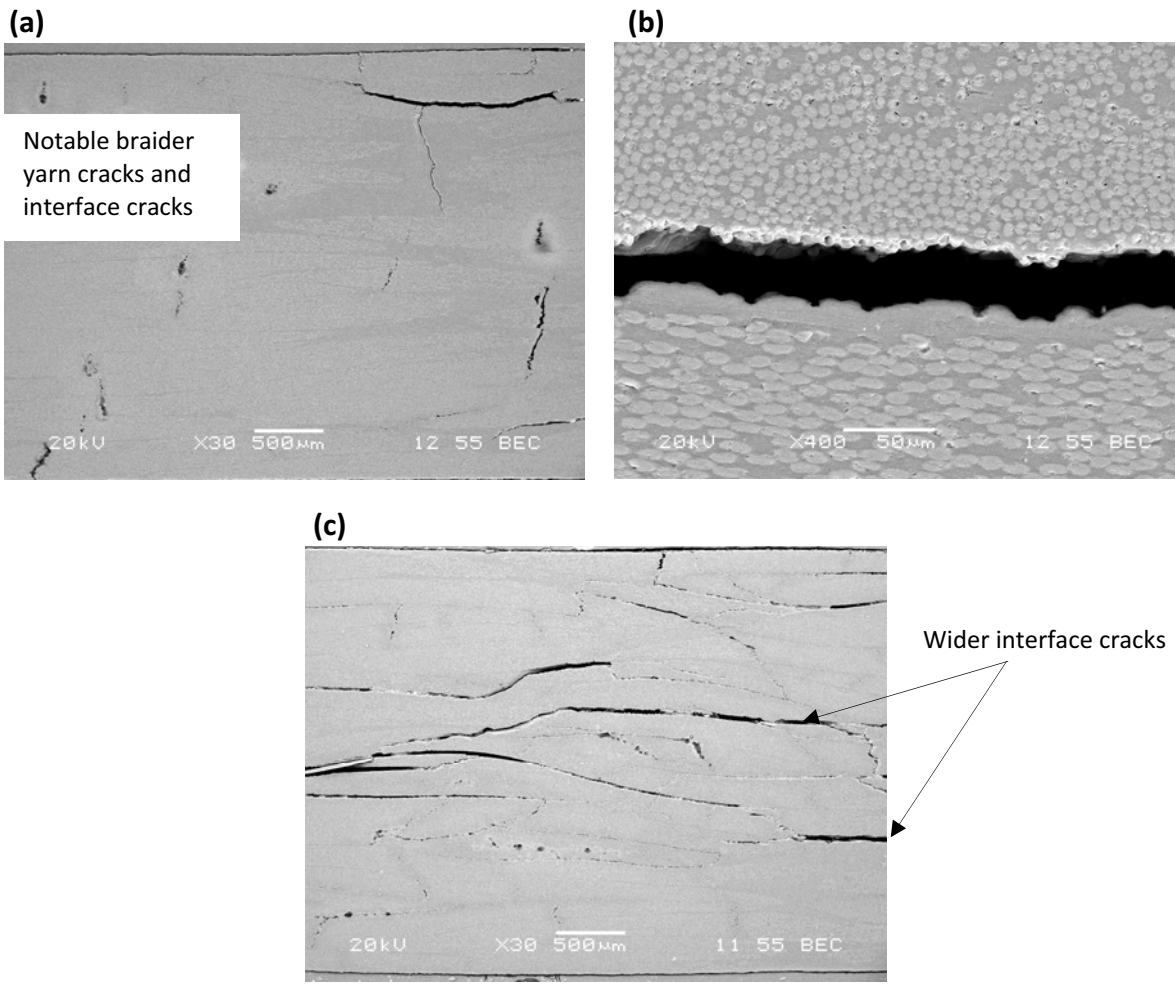

Figure 90. SEM cross-sectional photomicrographs for specimen cycled with 258 MPa: (a) 30X and (b) 400X magnifications, 75 mm from fracture surface; (c) 30X magnification, at fracture surface.

The obtained edge replicas were also used to plot the evolving crack density profiles for the three main observed damage modes: braider yarn cracks, interface cracks and matrix cracks. Two corresponding plots for specimens cycled with maximum applied stresses of 185 MPa and 258 MPa are shown in Figure 91. Three equivalent size zones along the length of the specimen edge were used to determine the average crack densities. For all maximum applied stress levels, the braider yarn crack density rate was gradual and the crack density was consistently rising for the duration of cycling. The crack density for each braider yarn was 2-3 cracks for all applied stress levels. The interface crack density rate was approximately constant for the duration of cycling, while the matrix crack density was relatively low and only slightly rising for all maximum applied stress levels. As mentioned, the number of braider yarn cracks

was notably higher than the number of interface or matrix cracks for all specimens regardless of the maximum applied stress level. The evolution of the braider yarn and yarn interface crack density rates were notably distinct from that observed for the room temperature specimens. Recall that for the room temperature specimens the braider yarn crack density rapidly increased initially up to a saturation state, after which the crack density increased with a more gradual rate. Combined plots of the braider yarn crack densities for specimens cycled with maximum stresses of 50% UTS and 70% UTS, at both room and elevated temperatures, are shown in Figure 92 (a) and (b), respectively. Recall that the 50% UTS specimens did not fail up to the run-off, while the 70% UTS specimens were cycled to failure. At the elevated test temperature the braider yarn crack development is more gradual during the early stages of cycling, but more consistent throughout cycling. The interface crack density also increases gradually, as does the interface crack length for the duration of cycling. Also, the crack density rate increases as the maximum applied stress increases.

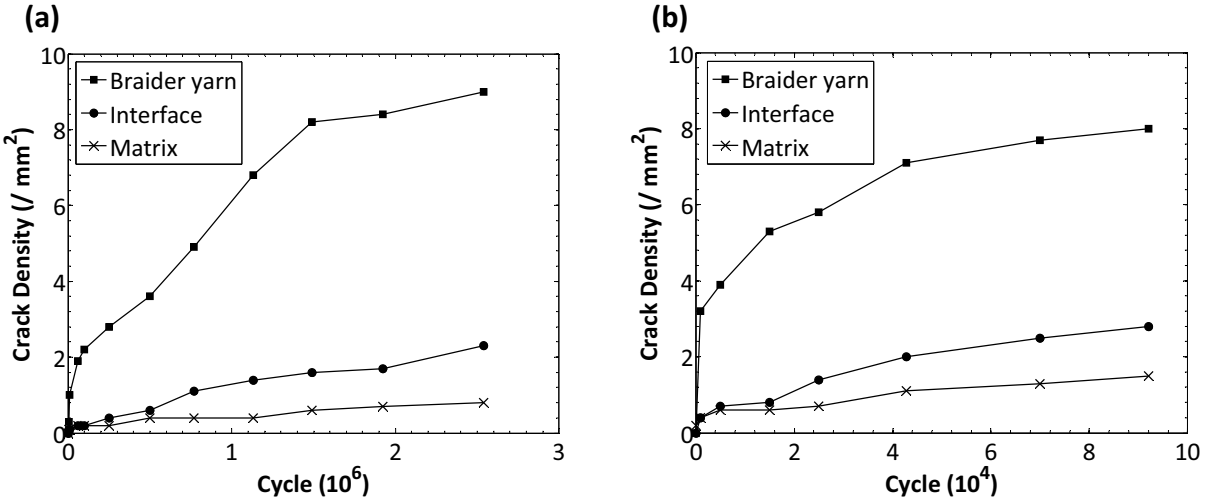

Figure 91. Elevated temperature crack density profiles for specimens cycled at (a) 185 MPa, (b) 258 MPa.

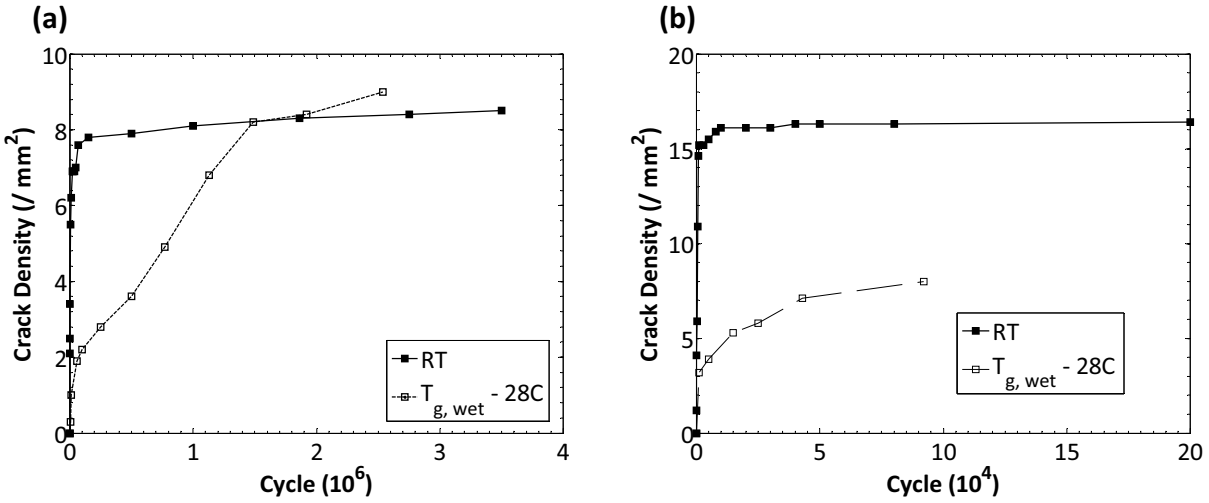

Figure 92. Combined braider yarn crack density profiles for specimens with σ_{max} of (a) 50% UTS, (b) 70% UTS.

IRT was also employed for some of the elevated temperature fatigue tests to monitor the surface temperature of the cyclically loaded test specimens and to visually capture thermal variations caused by cracking. To demonstrate the observations made using thermography, the results for a test specimen cycled at 221 MPa will be presented. A plot of the temperature profile for a location on the specimen surface within the central region of the gage section is shown in Figure 93; a data point was captured every cycle to generate the plot. The temperature profile follows a similar trend to that obtained for the room temperature specimens with a significantly lower temperature rise, which was found for all test specimens cycled at the elevated test temperature. This is a result of less damage development during the initial stage of cycling which limited the amount of heat dissipation from the specimen surfaces. This further suggests that the observed initial strain ratcheting caused by creep and viscous heating of the matrix due to mechanical cycling were the main contributors to the initial heat dissipation. In fact, the temperature profile reaches the secondary stage after approximately 20,000 loading cycles, which corresponds to the initiation of the plateau region in the energy dissipation profile. This further confirms that initial strain ratcheting behaviour is mainly due to creep and partially due to damage (albeit very little initial strain ratcheting was observed). During the secondary stage, the temperature profile slightly rises due to the development of damage.

The limitation of the heated environmental chamber prevented the IR camera from being too close to the specimen surface. Although the temperature rise during cycling was captured accurately, the thermograph resolution was limited to the pixel resolution of the camera, which at that distance from the specimen surface was not high. As a result, the resolution of the temperature variations between the braided fiber yarns and the matrix-rich zones on the thermographs was not always clear (recall that the thermographs obtained for the room temperature specimens were clear). A number of the specimens tested did however yield satisfactory thermographs, including those presented in Figure 94 for specimen B4-10. Note that the presented images are maps of the temperature rise and not the absolute temperature, which are analogous to the thermographs in Figure 64. During the early stages of cycling, the temperature is 'smeared' over the entire surface and the resolution of the braider yarns is not clear. As the number of loading cycles reach approximately 20,000, the hot zones correspond to the braider yarns as seen in Figure 94. As loading progressed, the hot spots associated with the braider yarn cracks were consistently clear. The point in cycling after which the braider yarns were associated with the hot zones in the thermographs corresponds to the secondary stage of the temperature profile shown in Figure 93. This illustrates that the heat dissipated due to braider yarn cracking occurs after approximately 20,000 loading cycles, which also corresponds to the point in cycling after which the stiffness began to drop (see Figure 77 (b)). This proves that the stiffness began to degrade when the braider yarn crack density reached a critical point during cycling.

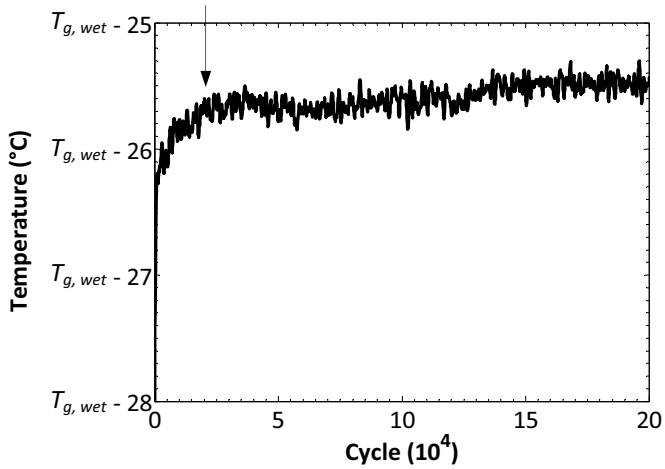

Figure 93. Surface temperature profile for specimen B4-10 (σ_{max} = 221 MPa, 60% UTS).

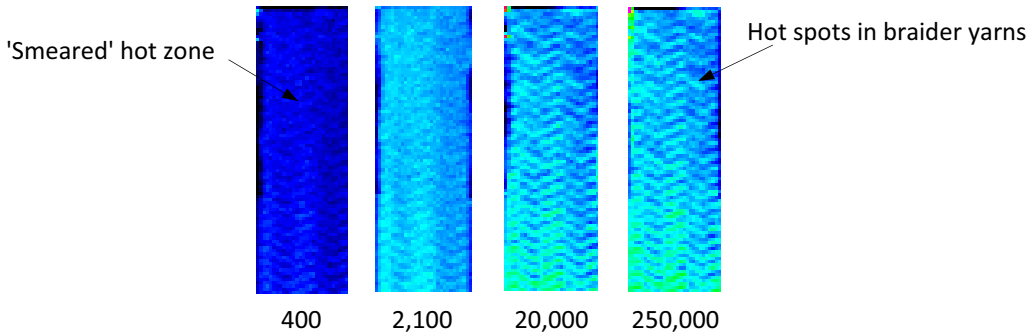

Figure 94. Captured IR thermographs during indicated cycles for specimen B4-10 (σ_{max} = 221 MPa).

The edge replicas, IR thermographs and SEM results for all maximum applied stress levels revealed that braider yarn cracking was the dominant damage mechanism. Braider yarn cracks were distributed throughout most braider yarns across the sample width and thickness, and along the length of the samples. Many braider yarns contained multiple cracks for all maximum applied stress levels. Although braider yarn cracks rapidly developed during the early stages of cycling up to a saturation state for the room temperature specimens, the development was more gradual initially and more consistent throughout cycling for the elevated temperature specimens. The interface crack development was also notable, however there were few interface cracks in comparison to the number of braider yarn cracks observed. The braider yarn and yarn interface crack density rates increased as σ_{max} increased. A number of localized interface cracks initiated later on during cycling and gradually developed between adjacent braider yarns and at the braider yarn and 0° yarn interfaces. As indicated, these cracks typically initiated at the tip of braider yarn cracks, which would be caused by the localized high stress fields at the braider yarn crack tips. Much later during cycling, these localized interface cracks began to propagate, becoming significantly longer and interacting with one another by the latter stages of cycling. This can be partially attributed to shear deformation which occurred at the braider yarn interlace locations and at the braider yarn crack tip locations, and possibly due to the straightening tendency of the 0° yarns, which would cause interface cracks to propagate under higher localized shear stress fields. Note that braider yarn crack growth, interface crack growth and crack interactions occurred earlier during cycling as the maximum applied stress increased. Although cracks propagated at the fiber-matrix interfaces, there was evidence of a

weakened or 'softened' matrix and/or fiber-matrix interface degradation as was evident in Figure 88, which have influenced the crack density and crack propagation rates. This is one of the main mechanisms that caused the variation in the crack development between the room and elevated temperature specimens.

For the specimens cycled with maximum applied stresses below the high cycle fatigue strength (i.e., 50% UTS), there were very few 0˚ yarn cracks after a run-out of $5x10^6$ cycles, suggesting the majority of these cracks occur prior to failure. Interactions between interface cracks were minimal initially, gradually increasing as loading progressed, and more significant after millions of loading cycles. Up to a run-out of $5x10^6$ cycles, the accumulation of interface damage and the corresponding interaction of damage modes was not sufficient to cause specimen failure. For the higher stress specimens, the propagation of interface cracks and their interactions occurred much sooner during cycling. During the latter stages of cycling the number of interface and matrix cracks reached a high density in the vicinity of the eventual fracture zone, which resulted in significantly more crack interactions. At this stage in cycling at the fracture zone vicinity, the braider yarns and the matrix lost their load carrying capacity and the load was redistributed to the 0˚ yarns causing some splitting type cracks in these yarns. After only a few more loading cycles, the 0˚ yarn fibers began to break which led to rapid fracture of the fiber yarns and ultimately specimen failure. Note that there were fewer splitting type cracks in the 0˚ yarns compared to the room temperature fatigue specimens cycled to failure. A photograph of the fracture surface for specimen B4-03 (295 MPa, 80% UTS) is shown in Figure 95 (a). The fracture surface has similar characteristics as the room temperature fatigue specimens. The fracture zone is localized but larger than that of the static test specimens, the fracture line has propagated along both the +60˚ and -60˚ braider yarn axes, and fracture is brittle in nature as shown in Figure 95 (a). An IR thermograph of the fracture surface was captured during the final loading cycle and is shown in Figure 95 (b). The heat spikes associated with the fracture line propagation along the +60˚ and -60˚ braider yarn axes is clear. The presence of some fiber pull-out is revealed by the brushy appearance of the fracture surface and confirmed by the observed bare fibers in the 0˚ yarns, which is also characteristic of brittle-natured fracture. Note that there was notably less fiber pull-out for the braider yarns, relative

to the room temperature specimens, as shown in Figure 95 (c). Furthermore, there was some indication of large-scale debonding and evidence of matrix fall-out in the fracture region; however, the affected zone was very localized. Out-of-plane deformation caused by large-scale debonding occurred during final fracture causing more interface and matrix cracking with a wider appearance in the cross-sectional plane (see Figure 90 (c)). Inspection of the internal damage state at locations further from the fracture surface revealed no large-scale debonding cracks, which confirms that large-scale debonding occurred only at fracture. This suggests that the fatigued specimens developed more extensive accumulation of localized matrix-dominated failures prior to fracture, which resulted in localized large-scale debonding. The observed damage development was notably distinct from the three-stage development for the room temperature specimens. Braider yarn and yarn interface cracks developed more gradually throughout cycling until prior to fracture, at which point the final crack interaction and accumulation instantly led to failure.

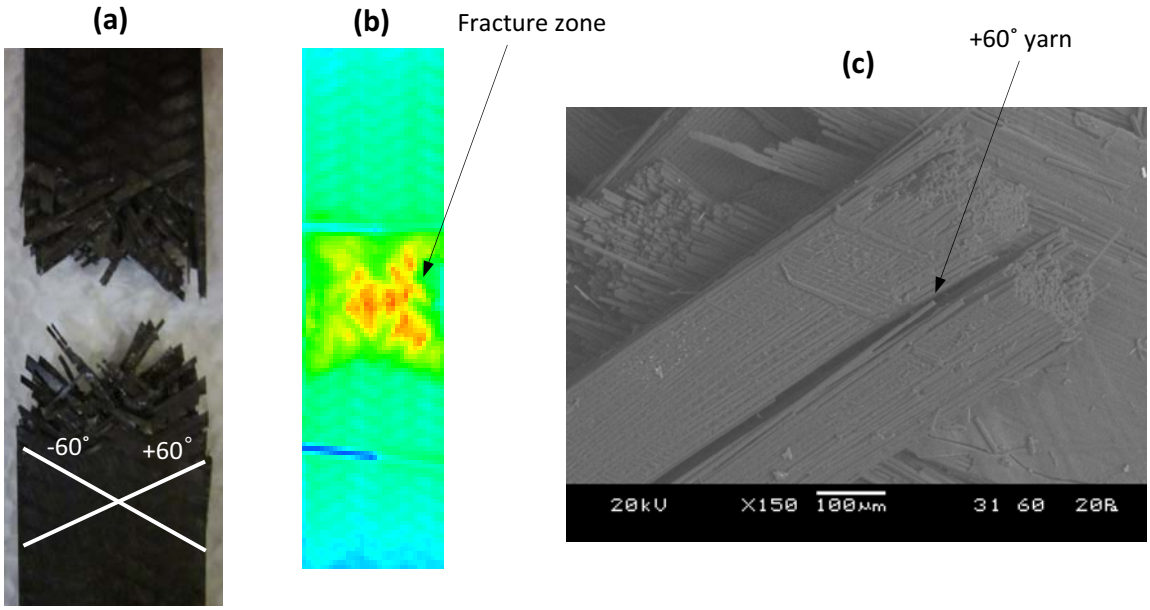

Figure 95. Failed fatigue test specimen (σ_{max} = 295 MPa): (a) image of the fracture surface, (b) IR thermograph of the fracture zone, (c) SEM photomicrograph of the fracture surface with 150X magnification.

5.2.3.4 General discussion: microscopic-macroscopic correlation

The results for the elevated temperature fatigue tests presented in Sections 5.2.3.2 and 5.2.3.3 provided a characterization of the braided material on both macroscopic and

microscopic scales, respectively. The following discussion will focus on the correlation between the microscopic damage characterization and the resulting material behaviour exhibited by the braided composite.

The stiffness degradation plots presented in Figure 77 illustrated that the stiffness degradation was more gradual and consistent throughout cycling. The corresponding microscopic damage characterization also revealed that damage progressed with a more gradual rate as shown in the braider yarn crack density profiles of Figure 91. Compared to the room temperature specimens, the initial damage development was significantly lower. This was confirmed by the specimen surface temperature profiles which resulted in a significantly lower temperature rise (or heat dissipation). However, the braider yarn cracks were found to be the dominant damage mechanisms throughout cycling. The evolving interface cracks and their interactions led to rapid specimen failure, but for the majority of cycling the braider yarn cracks were the main contributors to the exhibited stiffness degradation. The stiffness and crack density profiles in the plots of Figure 77 and Figure 91 evolved with similar rates and will now be analyzed. Figure 96 (a) and (b) show plots of the normalized stiffness as a function of the braider yarn crack density obtained from the edge replicas for specimens cycled with maximum applied stresses of 185 MPa (50% UTS) and 258 MPa (70% UTS), respectively. Unlike the room temperature specimens (see Figure 66), the braider yarn crack density is directly proportional to the stiffness degradation for the duration of cycling for all maximum applied stress levels. This shows that the braider yarn cracks are the main cause of stiffness degradation for the entire duration of cycling, which is another significant finding in this study. Recall that interface cracks will also contribute somewhat to stiffness degradation. Notice in the plots that initially the stiffness is approximately constant for a certain number of cycles; note that the number of cycles after which stiffness degradation begins decreases as σ_{max} increases. This shows that for the braided composite at elevated temperature, the braider yarn crack density must reach a particular threshold before stiffness degradation occurs. This threshold braider yarn crack density was approximately 2.0 cracks/mm^2 for all stress levels in this study, which occurred sooner during cycling at higher stresses due to the higher crack driving forces. This again is due to the increased resin toughness at elevated temperatures, which causes a reduction in the

crack density propagation rate due to local crack tip damping, causing more gradual stiffness degradation compared to the room temperature composite specimens. It should be noted that the observed cracks were consistently at the fiber-matrix interfaces and that the fracture surfaces were similar in appearance to the room temperature specimens (i.e., brittle natured). However, the crack growth rates were mitigated due to the elevated temperatures and caused by local crack tip effects. The softening of the resin may also be limiting the stress concentrations within the braider yarns due to the altered local deformation behaviour and a change in the load distribution between the fibers and the matrix. This may be another mechanism causing a slower braider yarn crack density propagation rate and less braider yarn damage compared to the room temperature specimens.

The interface crack density development was also gradual throughout the duration of cycling for the elevated temperature specimens. As shown in Figure 91, the interface crack density increases with approximately a constant rate, which is notably distinct from the room temperature specimens. In addition, the lengths of the interface cracks for the elevated temperature test specimens also increased with approximately a constant rate. Thus, the interface crack development rate consistently caused the same effect on the stiffness degradation rate of the specimen as already indicated. Consequently, the stiffness degradation was directly proportional to the braider yarn crack density in Figure 96 and not deviating from the main slope (as was shown for the room temperature specimens; see Figure 66). Since the interface crack density is significantly lower than the braider yarn crack density, it can be further assumed that the majority of the stiffness degradation was caused by the braider yarn cracks.

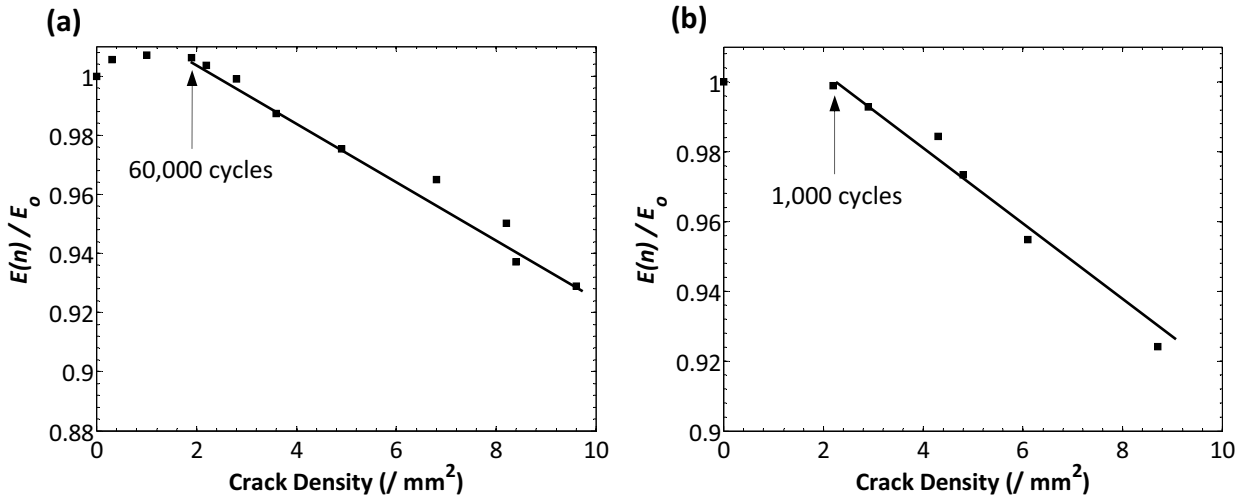

Figure 96. Stiffness as a function of braider yarn crack density for σ_{max} of (a) 185 MPa and (b) 258 MPa.

Regarding the exhibited energy dissipation behaviour, it was shown that regardless of the maximum applied stress level the energy dissipated per cycle (E_d) was highest during the first few loading cycles. The magnitude of E_d rapidly dropped and reached a plateau for the majority of cyclic loading, as was shown for the room temperature specimens. Note however that the initial drop in E_d was significantly lower compared to the room temperature specimens, which is a result of the limited quantity of damage that developed during the early stages of cycling at ($T_{g,\,wet}$ - 28)˚C. For the elevated temperature specimens, there was slight self-generated viscous heating which progressively decreased during the initial few cycles which contributed partially to the dissipated energy during that stage in cycling. Also, since the magnitude of the E_d plateau is higher for the elevated temperature specimens for all σ_{max}, damage develops with a higher rate during this stage of cycling, which was in fact the case (see Figure 92). Although the dissipated energy profiles are similar for both the room and elevated temperature specimens, there are notable microscopic behavioural differences that cause the analogous E_d behaviour.

Regarding the exhibited strain ratcheting behaviour, as was shown in Figure 83 slight strain ratcheting occurs during the first stage of loading for all applied stress levels. Since the crack development was gradually increasing during cycling, initial strain ratcheting was partially due to local viscous effects or creep. In fact, during the conducted tests that were paused to extract edge replicas for damage monitoring, there was virtually no recovery during the zero-

load dwell as was the case for the room temperature tests. This further confirms that the strain ratcheting due to creep was minimal throughout the duration of cycling, even at the elevated test temperature.

5.3 Creep and Aging Results

5.3.1 Completed Test and Analysis Overview

Although not the focus of this study, a series of creep tests and aging experiments were conducted in order to further establish whether or not there were any potential time-dependent or physical aging effects on the braided PMC material. These tests were conducted to provide some insight on the influence of the elevated temperature environment on the material behaviour; additional details on the creep behaviour of the braided composite can be found in [12]. One test specimen was aged for a duration of 48 hours at a constant ambient temperature of $(T_{g,\ wet} + 35)^{\circ}C$, then subsequently loaded statically to failure at room temperature. Four test specimens were utilized for creep testing at different applied stress levels at the constant ambient test temperature of $(T_{g,\ wet} - 28)^{\circ}C$. In addition, both untested (i.e., virgin) and tested material samples containing fatigue damage were aged for various durations at $(T_{g,\ wet} + 35)^{\circ}C$, and subsequently inspected using SEM. These results will now be presented in the subsequent sections.

5.3.2 Creep Results

A total of four creep tests, each at a different constant stress level, were conducted at the elevated test temperature of $(T_{g,\ wet} - 28)^{\circ}C$. The load-controlled tests consisted of instantaneously applying the desired stress and subsequently holding the stress constant for the test duration. Since a stress-controlled tension-tension fatigue test may exhibit creep deformation under the application of a positive mean stress, the mean stresses corresponding to the fatigue tests with σ_{max} of 50%, 60%, 70% and 80% UTS were employed as the constant creep stresses. The creep stresses used were therefore 27.5%, 33.0%, 38.5% and 44.0% UTS (102, 122, 142, 162 MPa). Recall that the stress ratio for all elevated temperature fatigue tests was set to 0.1. Plots of strain-time profiles for all four tests are shown collectively in Figure 97 for a time interval of 5 hours. Even at the highest constant stress, there is very little creep

strain. In fact, there is slight creep initially and no indication of creep after approximately 300 seconds. The creep strain is in fact only 0.01% in magnitude at the highest stress level. This confirms that the exhibited strain ratcheting observed during both the room temperature and elevated temperature fatigue tests was mainly due to fatigue damage accumulation, and that any creep effects can in fact be neglected.

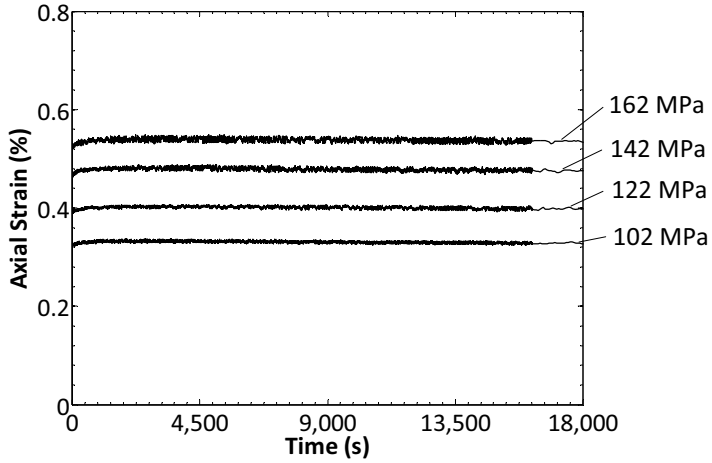

Figure 97. Elevated temperature creep test strain profiles.

5.3.3 Aging Results

The specimen that was aged for a duration of 48 hours at a constant ambient temperature of ($T_{g,\ wet}$ + 35)˚C was statically tested to failure at room temperature. Note that the aging temperature is notably higher than the elevated test temperature used for the static and fatigue tests that were presented in Section 5.2. This was done in order to provide an extreme ambient condition for observation of the potential effects of aging on the material behaviour. The stress-strain plots for the static test of the aged specimen (B2-05) and the non-aged specimen (B1-08) are shown in the plot of Figure 98. The stiffness of the composite increased slightly (0.8%), although it is within the scatter of the room temperature static data. The strength however decreased by 5%, which is likely due to the advanced crack propagation rate caused by the increased brittleness of the matrix due to aging [183]. The changes in the material properties caused by physical aging would have less of an impact at the temperature of ($T_{g,\ wet}$ - 28)˚C. Thus, the effects of physical aging can in fact be neglected.

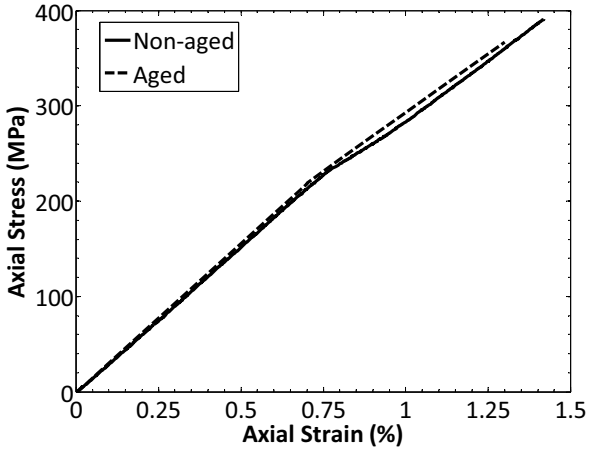

Figure 98. Aged and non-aged braided composite room temperature axial stress-strain plots.

To analyze the influence of aging on a material sample with and without damage, virgin material samples and samples containing fatigue damage were aged for 6 hours, 12 hours, 24 hours and 48 hours at ($T_{g,\ wet}$ + 35)˚C, and subsequently inspected using SEM and an optical microscope. The samples containing fatigue damage were cut from test specimens that were cycled at room temperature at a low stress (50% UTS) for $3x10^6$ cycles in order to generate a significant amount of damage. After aging, the sample edges and surfaces were inspected to determine whether there was any aging induced damage (or damage propagation). Also, some samples were sectioned in order to determine whether there was any aging induced damage within the sample interior. SEM photomicrographs of the surface of a non-aged virgin sample and a virgin sample aged for 48 hours are shown in Figure 99 (a) and (b), respectively. After 48 hours of aging, there was little aging induced damage, except for some local cracks along the fiber-matrix interfaces on the sample surfaces as shown in Figure 99 (b). No cracks were observed on the specimen edges or within the specimen interior for all the aged samples, regardless of the aging time. SEM photomicrographs of the interior cross-section of samples containing fatigue damage that were non-aged and aged for 48 hours are shown in Figure 99 (c) and (d), respectively. Existing cracks did not propagate and new cracks did not form under aging conditions for all samples examined. The cracks surfaces were not observed to be altered by aging. The effects of aging on existing damage within the samples was found to be minimal, can therefore be neglected at the lower test temperature of ($T_{g,\ wet}$ - 28)˚C.

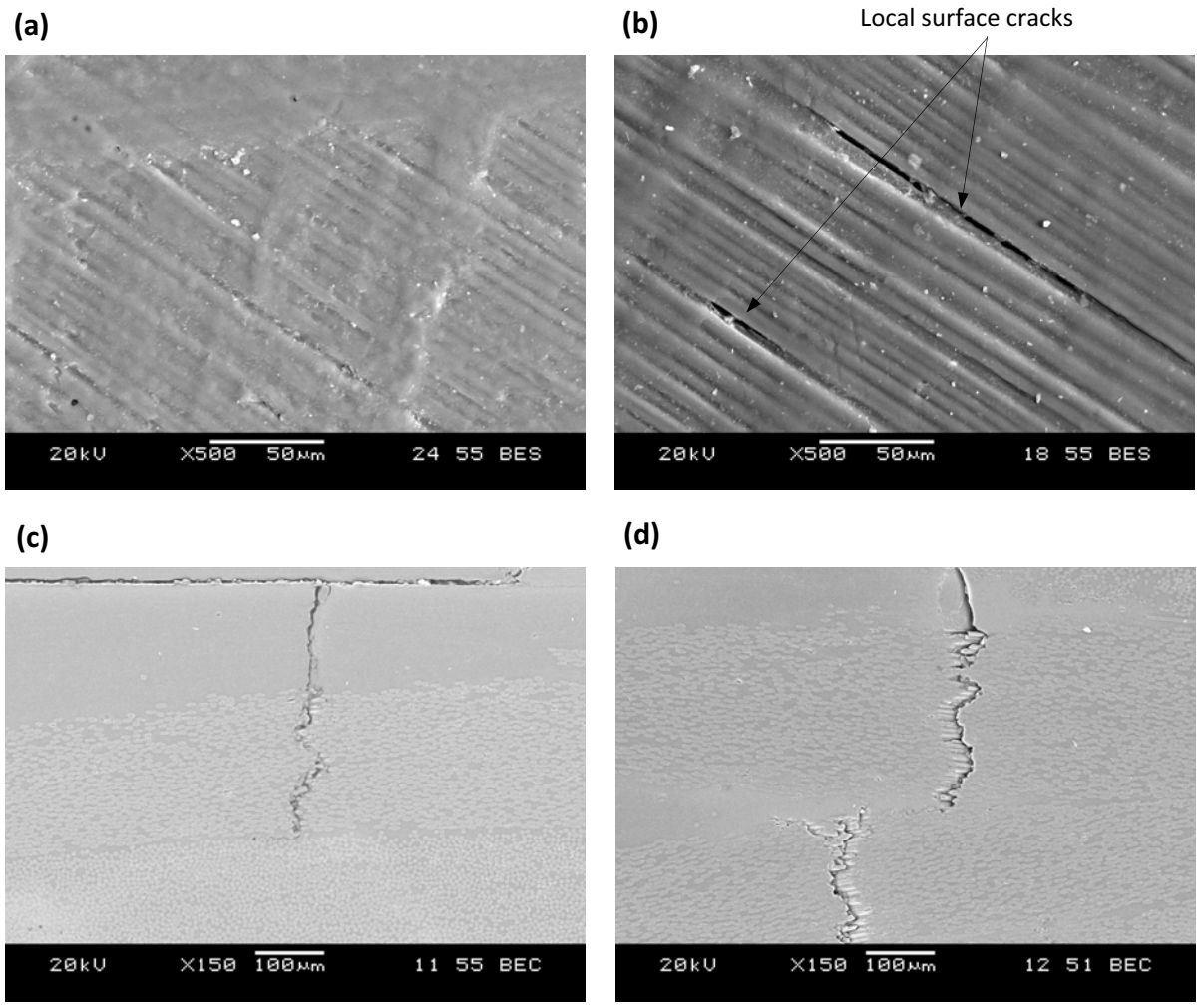

Figure 99. SEM photomicrographs (500X) of sample surface (a) virgin non-aged, (b) virgin aged 48 hours; SEM photomicrographs (150X) of damaged sample interior cross-section (c) non-aged, (d) aged 48 hours.

6 FATIGUE DAMAGE MODELING DETAILS

Details of the fatigue damage model development will be presented, along with an overview of the observed and measured damage mechanisms for the braided composite material. Comparisons of the model prediction results and the experimental data will also be shown. Some relevant test results for two on-axis woven laminate composites will also be analyzed in this chapter, with a relevant discussion pertaining to the applicability of the fatigue damage model. Finally, an overview focussed on the implementation of the developed fatigue damage model into a continuum damage mechanics (CDM) based constitutive model will be discussed.

6.1 Braided Composite Damage Development Discussion

The development of the fatigue damage model relied on quantitative measurements as well as qualitative observations from the experimental microscopic damage characterization of the braided composite material at both room and elevated temperatures. A relevant discussion regarding the damage observations for the room temperature fatigue tests will first be presented, followed by a similar discussion for the elevated temperature fatigue tests.

6.1.1 Room Temperature Fatigue Damage

Recall that the room temperature fatigue specimens exhibited a three-stage stiffness degradation profile, where there was an initial rapid drop in stiffness as shown in Figure 47. The

development of damage also followed a similar trend as was presented in Figure 62. The stiffness degradation during the initial stage of cycling was then directly correlated to the braider yarn crack density, as was shown in Figure 66. During the initial stage of cycling, stiffness degradation was dominated by braider yarn cracking, however interface cracking did contribute somewhat to the initial rapid stiffness degradation. During the second stage of cycling, interface cracks contributed to gradual stiffness degradation for all applied stress levels, but braider yarn cracking was more dominant as the maximum applied stress increased. The degree of cracking within the matrix-rich zones and within the 0˚ yarns was relatively minimal and considered negligible for the duration of cycling, and thus will be neglected in the model development.

It was observed that the braider yarn and interface crack densities followed an increasing logarithmic profile as the number of loading cycles increased. This was due to the more gradual increase in braider yarn and interface crack densities after the braider yarn crack 'saturation' state. A combined plot of the braider yarn crack densities, ρ_{by}, as functions of the logarithm of the number of cycles, log(n), for four maximum applied stress levels is shown in Figure 100. The linear regression fit line is also shown for each indicated maximum applied stress in the plot, where the R^2 correlation values are all between 0.91 - 0.96. A summary of the regression coefficients, a_1, corresponding to the plots in Figure 100 are included in Table 11. By inspecting the regression coefficients, a linear correlation can in fact be made with σ_{max}, which is illustrated in the plot of Figure 101 and defined by Equation (44). The braider yarn crack density can therefore be approximated by Equation (45) for any σ_{max}.

$$a_1 = 0.0145\,\sigma_{max} - 1.4783 \tag{44}$$

$$\rho_{by} = a_1 \log(n) \tag{45}$$

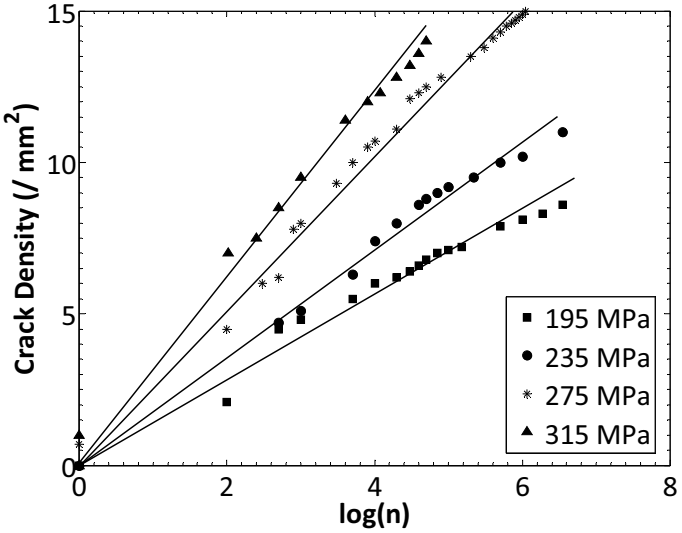

Figure 100. Braider yarn crack density as a function of log(*n*).

Table 11. Braider yarn and interface crack density regression coefficients.

Specimen No.	σ_{max} (MPa)	a_1	a_2
B2-01	195	1.4403	0.3455
B1-07	235	1.7550	0.3720
B1-03	275	2.5930	0.4044
B2-02	315	3.0952	0.4518

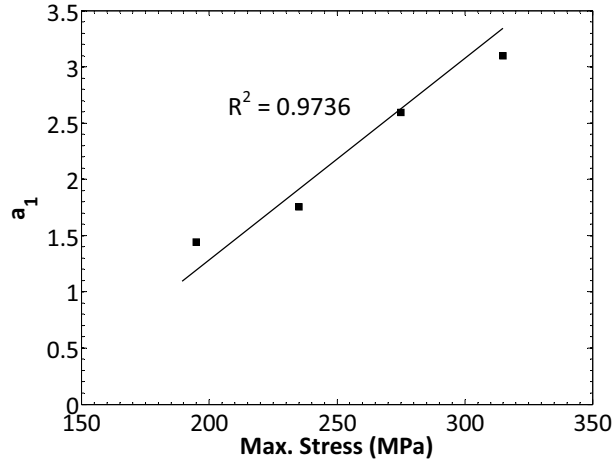

Figure 101. Braider yarn crack density regression coefficient, a_1, as a function of maximum stress.

Similarly for the interface crack density, a combined plot of the interface crack densities, ρ_{int}, as functions of the logarithm of the number of cycles, log(n), for the same four maximum applied stress levels is shown in Figure 102. The linear regression fit line is also shown for each indicated maximum applied stress in the plot, yielding R^2 correlation values between 0.85 - 0.95. A similar correlation between the regression coefficients, a_2, which are summarized in Table 11, and σ_{max} was made. This is illustrated in the plot of Figure 103, and defined by Equation (46). Thus, the interface yarn crack density can be approximated by Equation (47) for any σ_{max}.

$$a_2 = 0.0009\,\sigma_{max} + 0.1695 \tag{46}$$

$$\rho_{int} = a_2 \log(n) \tag{47}$$

Note that although the plots of the interface crack densities consider the number of cracks observed from the edge replicas, the increasing crack length is actually accounted for within the crack density measurements. Further details can be found within Appendix A.1.

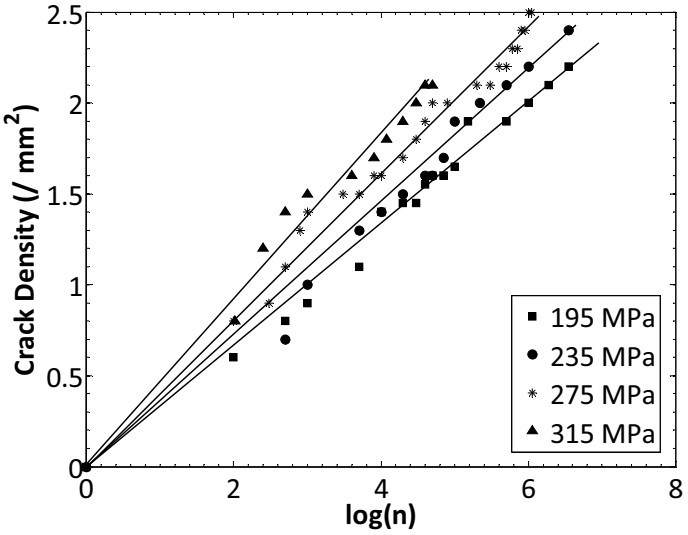

Figure 102. Interface crack density as a function of log(n).

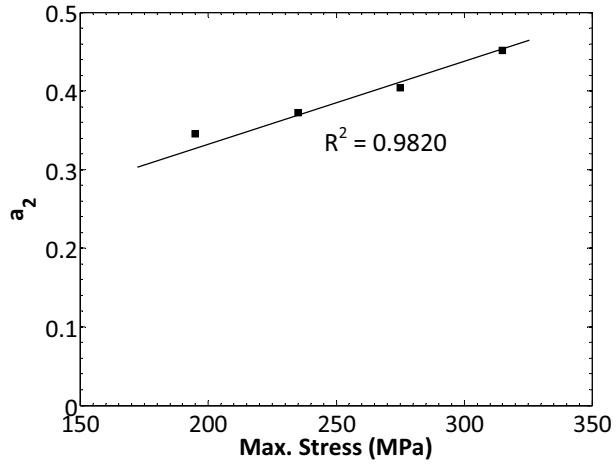

Figure 103. Interface crack density regression coefficient, a_2, as a function of maximum stress.

6.1.2 Elevated Temperature Fatigue Damage

The elevated temperature fatigue specimens exhibited a notably different stiffness degradation profile compared to the room temperature test specimens as was presented in Figure 77. As a result, a notably different crack density propagation rate was observed as was shown in Figure 91, which was due to the altered matrix properties at the elevated test temperature. The stiffness degradation rate was gradual for the duration of the tests, and was also directly correlated with the braider yarn crack density progression for the test duration (see Figure 96). The braider yarn crack development was the dominant cause of stiffness degradation for the duration of cycling. Interface crack development was also fairly gradual throughout cycling and notably contributed to stiffness degradation during the latter stages of cycling. Recall that there were few interface cracks during the early stages of cycling. Similar to the room temperature specimens, the degree of cracking within the matrix-rich zones and within the 0˚ yarns was relatively minimal and considered negligible, and thus will be neglected in the model development.

Due to the fact that the braided composite was loaded in the warp direction, the material exhibited a fiber-dominated stress-strain behaviour at the macroscopic level and was not significantly influenced by the elevated test temperature. However, the crack initiation and propagation rates were notably influenced by temperature due to local effects of the resin

material. This change in crack propagation or local damage development behaviour at elevated temperatures is manifested through the variation in the crack density profiles. It was observed that the braider yarn and interface crack density development was increasing such that a power law function could be used to represent the crack densities. This is not surprising due to the fact that the elevated temperature specimens exhibited a more gradual increase in crack density development compared to the room temperature specimens. A combined plot of the braider yarn crack densities, ρ_{by}, as functions of the number of loading cycles, n, for four maximum applied stress levels is shown in Figure 104. The power law function regression curves for each indicated maximum applied stress are also included with the plots, where the R^2 correlation values are all between 0.96 - 0.99. A summary of the regression coefficients, a_1 and a_2, corresponding to the plots in Figure 104 are included in Table 12. By inspecting the regression coefficients, correlations can in fact be made with the maximum applied stress, which is illustrated in the plots of Figure 105 and defined by Equations (48.a) and (48.b). The braider yarn crack density can therefore be approximated by Equation (49) for any σ_{max}.

$$a_1 = 0.00001499\,\sigma_{max}^{\,2} - 0.0034\,\sigma_{max} + 0.1218 \tag{48.a}$$

$$a_2 = 0.0000148\,\sigma_{max}^{\,2} - 0.00923\,\sigma_{max} + 1.6817 \tag{48.b}$$

$$\rho_{by} = a_1\, n^{a_2} \tag{49}$$

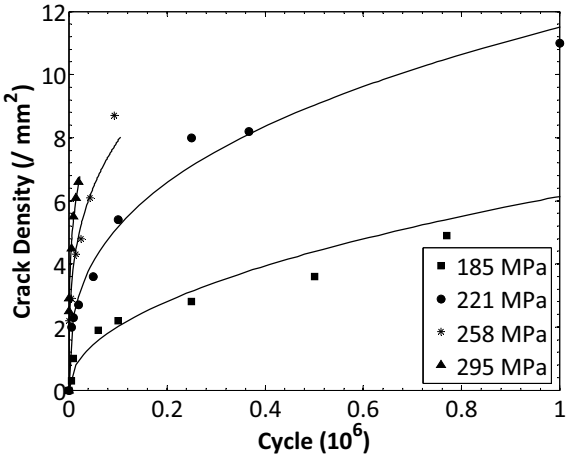

Figure 104. Braider yarn crack density as a function of cycles (n).

Table 12. Braider yarn and interface crack density regression coefficients.

Specimen No.	σ_{max} (MPa)	a_1	a_2	a_3	a_4
B4-07	185	0.0075	0.4855	0.0006722	0.5366
B5-09	221	0.0949	0.3472	0.003501	0.5062
B4-08	258	0.2482	0.3006	0.01786	0.4316
B4-06	295	0.4201	0.2402	0.032	0.3902

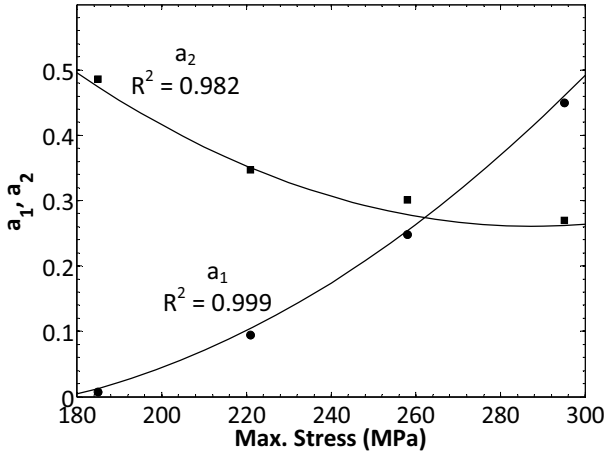

Figure 105. Braider yarn crack density regression coefficients, a_1 and a_2, as functions of maximum stress.

Similarly, a combined plot of the interface crack densities, ρ_{int}, as functions of the number of cycles, n, for the same four maximum applied stress levels is shown in Figure 106. The power law regression curves are also shown for each indicated σ_{max} in the plot, yielding R^2 correlation values between 0.94 - 0.97. A similar correlation between the regression coefficients, a_3 and a_4, which are summarized in Table 12, and σ_{max} was made. This is illustrated in the plot of Figure 107, and defined by Equation (50). Thus, the interface yarn crack density can be approximated by Equation (51) for σ_{max}.

$$a_3 = 2.04e-6\,\sigma_{max}^{\,2} - 0.000686\,\sigma_{max} + 0.05697 \tag{50.a}$$

$$a_4 = -1.77e-6\,\sigma_{max}^{\,2} - 0.000554\,\sigma_{max} + 0.7035 \tag{50.b}$$

$$\rho_{int} = a_3\, n^{a_4} \tag{51}$$

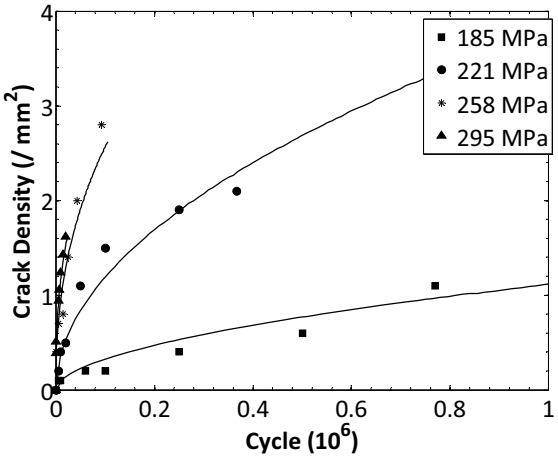

Figure 106. Interface crack density as a function of cycles (*n*).

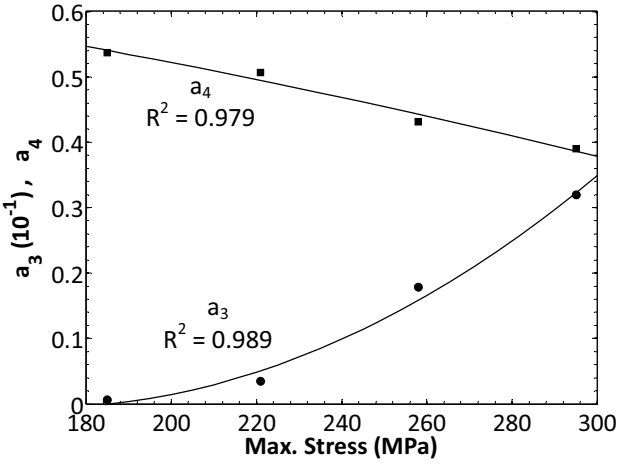

Figure 107. Interface crack density regression coefficients, a_3 and a_4, as functions of maximum stress.

6.2 Analytical Fatigue Damage Model Development

As indicated in Section 3.7, fatigue damage models can be classified in one of three categories: models that do not account for actual degradation mechanisms, but use S-N curves to define macroscopic strength criteria; residual strength/stiffness models; progressive damage models based on actual irreversible degradation mechanisms (e.g., matrix cracking, delamination, etc.). Analytical fatigue damage accumulation models are often based on residual stiffness measurements [139-141], but can alternately be based on actual damage mechanisms [59, 155]. The model developed in this study is an analytical fatigue damage accumulation

model that is based on measurements of actual observed crack modes, thus, is classified under the third category of fatigue damage models as a damage mechanics-based model. The data analysis on the crack density development presented in the previous section for the braided composite material will be employed within the definition of the analytical fatigue damage model.

Analytical fatigue damage accumulation models are often defined in terms of the number of loading cycles (or the normalized number of cycles - n/N_f), and are typically fitted to a specific experimental stiffness-based damage index [139]. These nonlinear damage models do not provide any consideration of the actual damage state of the material. Since many polymeric laminate composite materials exhibit a typical three-stage stiffness degradation evolution, and thus a three-stage damage degradation evolution (see Figure 17 in Section 3.5), these established damage accumulation models have been effectively employed for various unidirectional, cross-ply and quasi-isotropic laminates. With the presumption that the material under investigation exhibits this typical three-stage response, the damage accumulation models may be applicable. The braided material under investigation in this study did not exhibit a typical three-stage response at the elevated test temperature, as it did during room temperature fatigue loading, due to the local influence of temperature on the crack propagation behaviour. This was further illustrated in the damage analysis that was presented in Section 6.1. As a result, a nonlinear fatigue damage accumulation model may not be applicable for braided composite materials (and perhaps other textile fabric-reinforced polymeric composites). Since the development of different crack types was altered due to the elevated temperature environment, one modeling approach would be to break down the material degradation simulation into different material-degradation-causing damage components (i.e., braider yarn cracks and interface cracks). This would provide a sound physical connection between the damage model and the actual damage states exhibited by the braided material. This is an important step since the evolution of damage and the corresponding prediction of effective material properties for braided composite materials containing damage is not well established in the literature. Therefore, a damage mechanics-based analytical fatigue

damage accumulation model was developed in terms of braider yarn and interface crack density, which is applicable for the braided material at both room and elevated temperatures.

The damage model is defined as a function of the observed braider yarn and interface crack densities, and as a consequence as a function of the maximum applied stress. Since it was observed that damage was evenly widespread throughout the test specimens, using the crack densities in the damage model is in fact an accurate representation of the material damage state. The analytical fatigue damage model is given by Equation (52). The accumulated damage, D, is defined as the additive decomposition of the damage parameters d_1 and d_2, which represent damage due to braider yarn cracking and damage due to interface cracking, respectively.

$$D = d_1 + d_2 \tag{52}$$

The key is to define the damage parameters d_1 and d_2 in terms of the braider yarn (ρ_{by}) and interface (ρ_{int}) crack densities, respectively. Note that the model defined in Equation (52) can also include the effects of additional damage modes (i.e., d_3, d_4, etc.). The damage parameters in this study are defined by Equations (53.a) and (53.b).

$$d_1 = \alpha_1 \rho_{by}^{\beta_1} \tag{53.a}$$

$$d_2 = \alpha_2 \rho_{int}^{\beta_2} \tag{53.b}$$

The braider yarn and interface crack densities were defined by Equations (45) and (47) for room temperature fatigue, and Equations (49) and (51) for elevated temperature fatigue. The scalar coefficients α_1 and α_2 are simply scaling parameters that are independent of stress, and in fact equal (i.e., $\alpha_1 = \alpha_2 = \alpha$) for a particular test temperature. The scalar exponent coefficients β_1 and β_2 are functions of the maximum applied stress level, and vary with the test temperature. These coefficients do not greatly influence the magnitude of the accumulated damage, but slightly influence the rate of damage accumulation.

A summary of the damage model scalar coefficients are presented in Table 13 and Table 14 for both room temperature and elevated temperature fatigue, respectively. As shown, the

exponent coefficients, β_1 and β_2, are similar in magnitude for all stress levels and for both temperatures. Upon further inspection, β_1 and β_2 are in fact linear functions of the maximum applied stress for both temperatures. For the data in Table 13, combined plots of the exponent coefficients are shown in Figure 108, while the linear correlations in terms of stress are defined by Equations (54.a) and (54.b). For the data in Table 14, combined plots of the exponent coefficients are shown in Figure 109, while the linear correlations in terms of stress are defined by Equations (55.a) and (55.b).

$$\beta_1 = -0.0021\,\sigma_{max} + 2.4178 \tag{54.a}$$

$$\beta_2 = 0.0025\,\sigma_{max} + 2.3125 \tag{54.b}$$

$$\beta_1 = 0.0046\,\sigma_{max} + 0.5152 \tag{55.a}$$

$$\beta_2 = -0.0068\,\sigma_{max} + 3.7063 \tag{55.b}$$

Table 13. Fatigue damage model scalar coefficients - room temperature.

Max. Stress (MPa)	α_1	α_2	β_1	β_2
195	0.001	0.001	2.02	2.8
235	0.001	0.001	1.95	2.9
275	0.001	0.001	1.82	3.0
315	0.001	0.001	1.79	3.1

Table 14. Fatigue damage model scalar coefficients - elevated temperature.

Max. Stress (MPa)	α_1	α_2	β_1	β_2
185	0.002	0.002	1.35	2.50
221	0.002	0.002	1.60	2.10
258	0.002	0.002	1.65	2.01
295	0.002	0.002	1.90	1.71

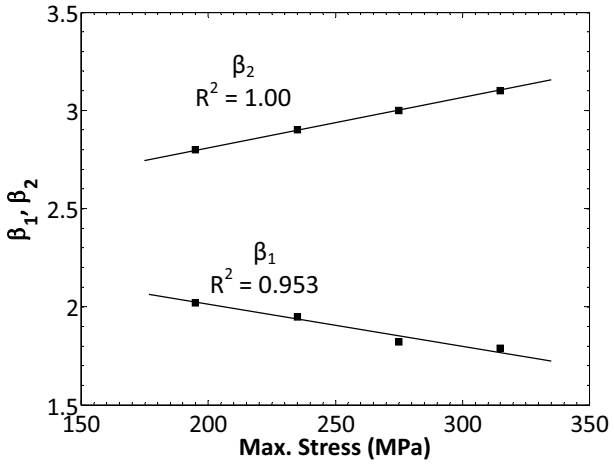

Figure 108. Fatigue damage model exponent coefficients, β_1 and β_2, as functions of maximum stress - room temperature.

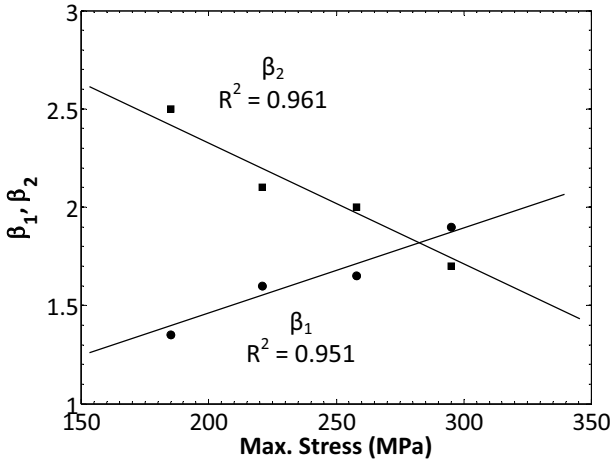

Figure 109. Fatigue damage model exponent coefficients, β_1 and β_2, as functions of maximum stress - elevated temperature.

Therefore, the application of the fatigue damage accumulation model for the braided composite material subjected to any particular maximum applied stress level requires the calculation of the corresponding braider yarn and interface crack densities, as defined by Equations (44)-(47) or Equations (48)-(51), for each loading cycle (n). Next, the damage model scalar parameters defined by Equation (54) or Equation (55) must be determined for the applicable σ_{max}. Finally, the damage accumulation for each loading cycle can be determined from Equation (52). Note that the fiber-dominated braided composite did not exhibit significant

macroscopic material property changes due to the elevated test temperature. However, the effects of temperature were observed through the crack development and are therefore present in the damage model by the different functions that are used to define the crack density rates. The different crack propagation rates, and thus different progressive damage states, at the elevated test temperature caused the difference in the observed macroscopic fatigue behaviour. The application of the damage model for the braided composite material with comparisons to experimental data will be presented in the subsequent section.

6.3 Comparison with Braided Composite Experimental Data

In order to validate the predictive capabilities of the presented fatigue damage model, an experimentally obtained macroscopic damage index must first be defined. Although it is difficult to quantitatively define 'fatigue damage', monitoring the stiffness evolution during cyclic loading is often conducted. If the fundamental concepts of damage mechanics are considered, damage may be defined as follows [159]:

$$D = \frac{A_D}{A_o} \tag{56}$$

where A_D is the effective damaged area, and A_o is the total area of a representative element. The concept of effective stress ($\bar{\sigma}$), as defined by Equation (57) [159], can be used to scale the actual nominal stress σ with the damage, D. Then, employing the principle of strain equivalence [61] yields a stiffness-based damage index which is defined by Equation (58). This is a suitable experimental damage index which will be used to correlate with the damage model predictions.

$$\bar{\sigma} = \frac{\sigma}{1 - D} \tag{57}$$

$$D = 1 - \frac{E}{E_o} \tag{58}$$

The experimental results show that the final stiffness when fracture occurs (E_f) is not zero, thus the damage index defined in Equation (58) ranges from 0 to $1-E_f/E_o$. It is sometimes convenient

to define an alternate form of the damage index, such that the accumulated damage ranges from 0 to 1. An example of a commonly employed damage index is defined by Equation (59).

$$D = \frac{E_o - E}{E_o - E_f} \tag{59}$$

In the following paragraphs, the predictions of the analytical damage model defined by Equation (52) will be compared to the experimental stiffness-based damage index defined in Equation (58) for validation. Combined plots of the predicted accumulated damage and the experimental damage index are shown in Figure 110 (a)-(d) for the braided composite material at room temperature subjected to the indicated σ_{max}. The model correlates very well with the experimental data for all maximum applied stresses. The model captures the aforementioned initial rapid increase in damage development due to braider yarn cracking and local interface crack initiation during the first stage of cycling. The gradual development of damage after braider yarn crack saturation during the second stage of cycling is also well captured by the model. This is further elaborated by considering plots of the individual damage model terms d_1 and d_2, for the 70% UTS fatigue damage prediction as is shown in Figure 111. It is clear that the first damage parameter, d_1, contributes to the majority of damage during the initial stage, while the second damage parameter, d_2, contributes less. During the second stage, both d_1 and d_2 contribute to the overall damage accumulation. Recall that the scaling parameters, α_1 and α_2, were the same, thus the damage model is capturing the accurate development of the two main crack mechanisms - braider yarn and interface cracks.

Similar plots for the braided composite at elevated temperature are shown in Figure 112 (a)-(d), also with excellent correlation between the model predictions and the experimental data. The model captures the distinct damage development observed at the elevated test temperature. A plot of the individual damage model terms d_1 and d_2, for the 60% UTS fatigue damage prediction is shown in Figure 113. The first damage parameter contributes entirely to the damage accumulation during the early stages, while the gradual increase of the second parameter begins to contribute to the overall damage accumulation during the latter stages of

cycling. Again, the damage model is capturing the accurate development of the two main crack mechanisms - braider yarn and interface cracks.

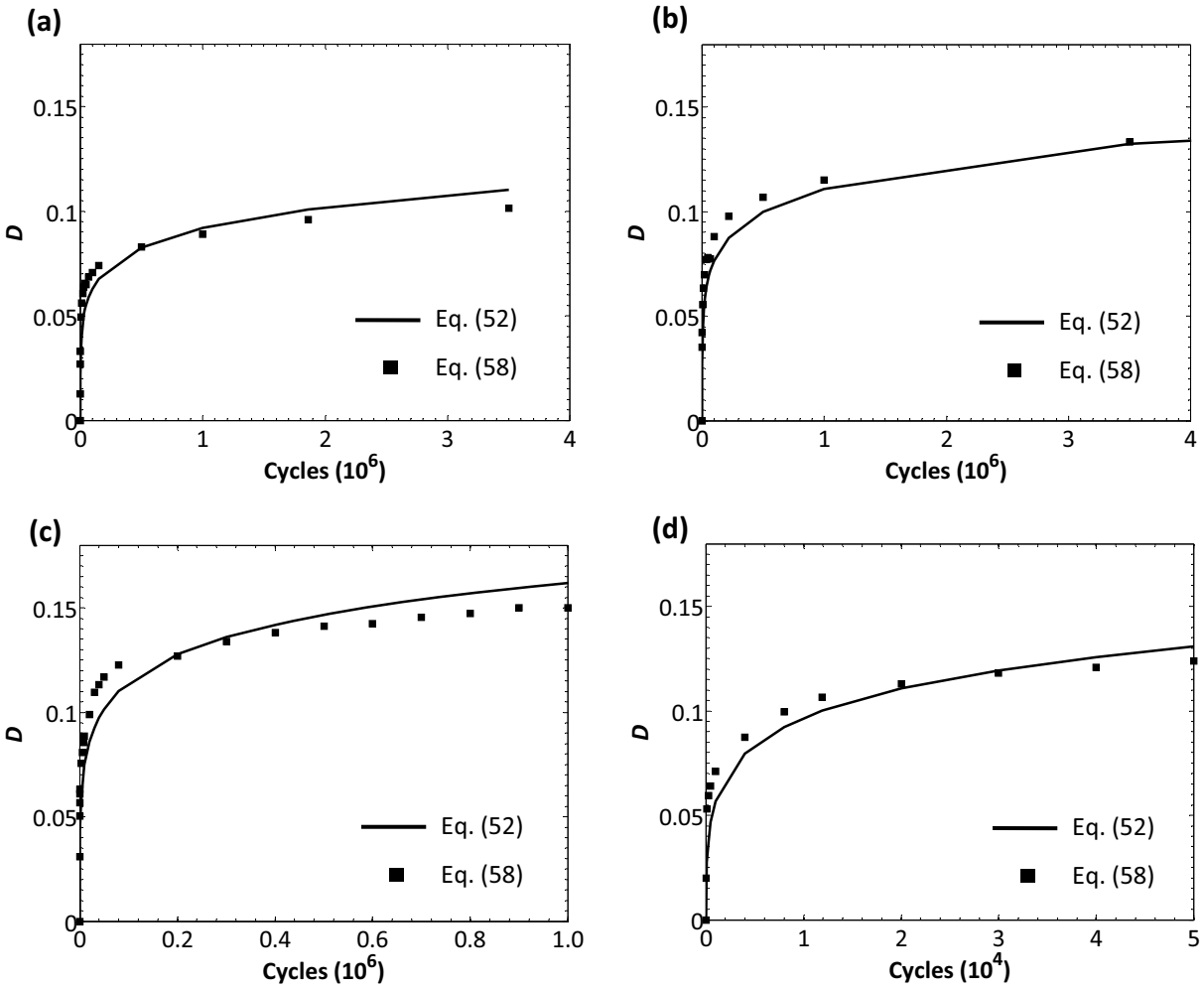

Figure 110. Damage model and experimental damage index plots for room temperature fatigue with maximum stress of (a) 50% UTS (195 MPa), (b) 60% UTS (235 MPa), (c) 70% UTS (275 MPa), (d) 80% UTS (315 MPa).

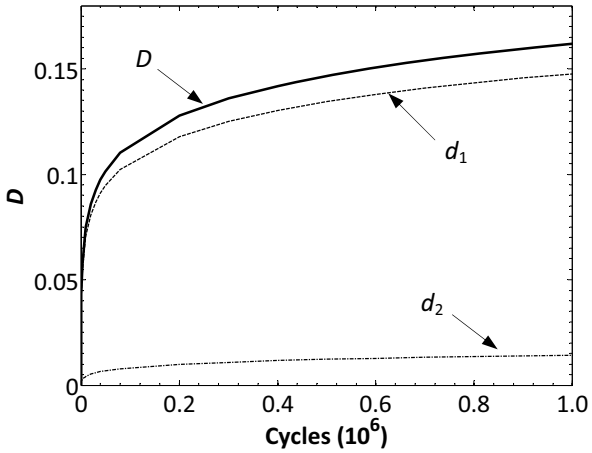

Figure 111. Damage model parameter and predicted damage accumulation plots - room temperature, 70% UTS.

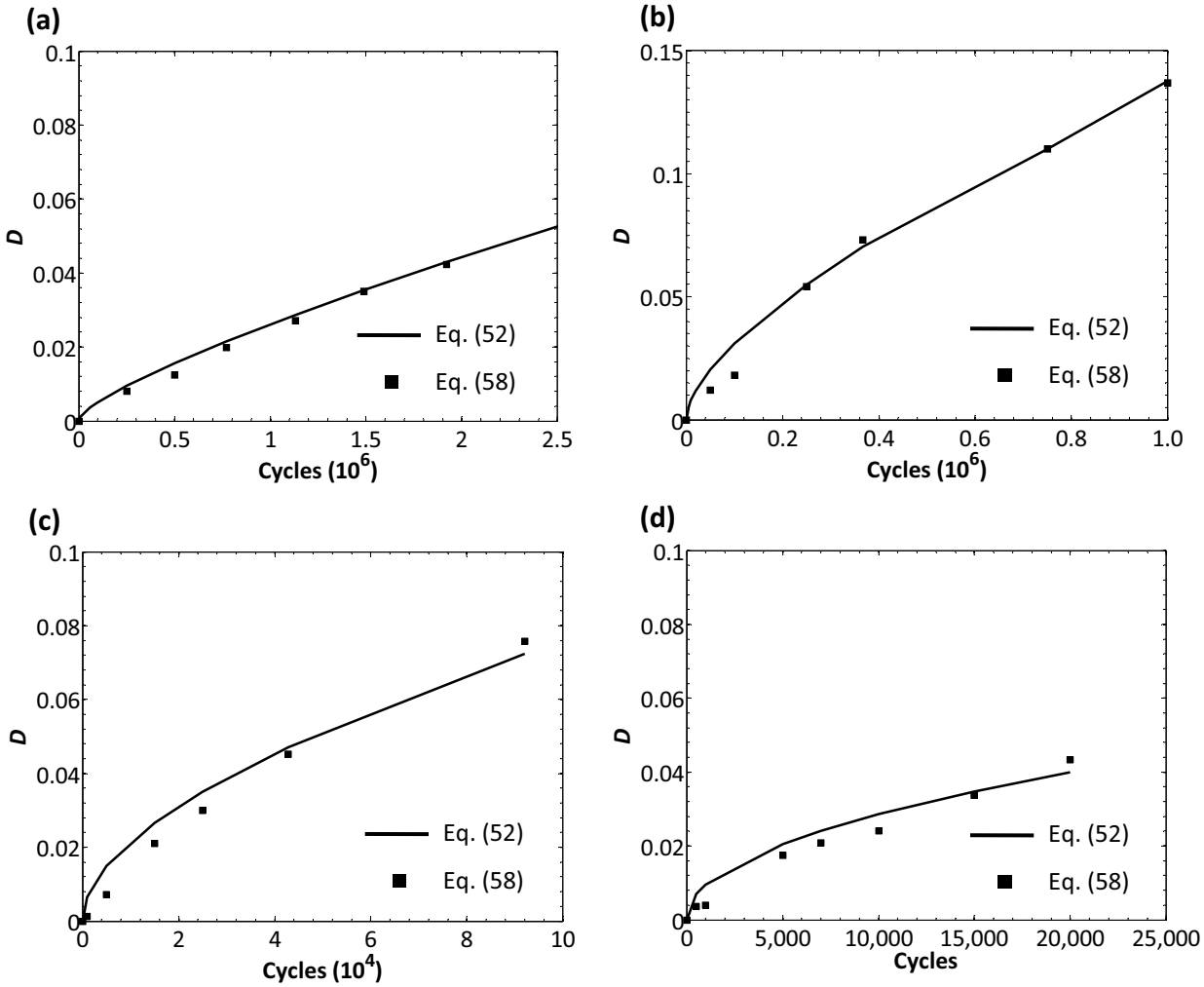

Figure 112. Damage model and experimental damage index plots for elevated temperature fatigue with maximum stress of (a) 50% UTS (185 MPa), (b) 60% UTS (221 MPa), (c) 70% UTS (258 MPa), (d) 80% UTS (295 MPa).

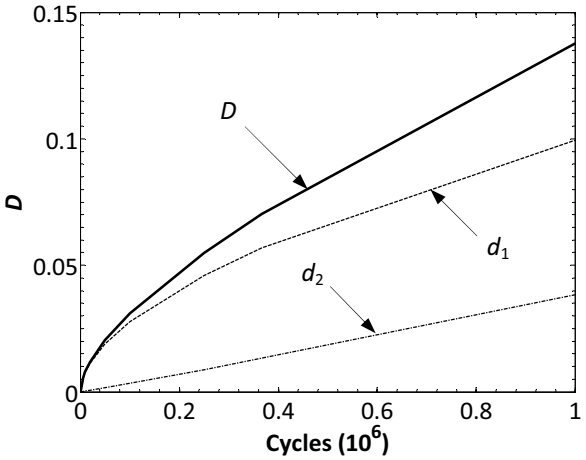

Figure 113. Damage model parameter and predicted damage accumulation plots - elevated temperature, 60% UTS.

The corresponding stiffness loss due to the observed damage was presented for both the room temperature and elevated temperature braided composite tests in Figure 47 and Figure 77, respectively. The stiffness degradation can be predicted by a number of analytical and numerical methods, including by defining a direct relationship between the crack density and the stiffness degradation [59]. The damage accumulation (*D*) predicted by the damage model can also be directly utilized to predict the stiffness degradation for the braided composite. One approach is to adopt the definition of Equation (58) and set the dynamic stiffness (*E*) equal to $(1\text{-}D)E_o$, then use the damage accumulation values, *D*, predicted by the damage model to determine the evolving stiffness. This approach was employed in this study and will now be presented. Plots of the predicted and experimental normalized stiffness degradation for the indicated stress levels are shown in Figure 114 and Figure 115, for the room temperature and elevated temperature tests respectively. As illustrated in the plots, the correlation between the predicted stiffness degradation and the experimentally obtained stiffness degradation are excellent for all stress levels, and at both test temperatures. Consider the plots in Figure 114 (a) after 500,000 loading cycles, where the predicted normalized stiffness is 0.9170 and the experimental is 0.9173, yielding an error of 0.03%. After 3,000,000 loading cycles, the predicted stiffness is 0.892 while the experimental value is 0.9008, yielding an error of 1.0%. For the plots in Figure 115 (b) after 20,000 loading cycles, the predicted stiffness is 0.969 and the

experimental is 0.9793, yielding an error of 1.1%. The error between the predicted values and the experimental values is consistently low at less than 2%, which is deemed acceptable. Note that the final stage of rapid damage increase, and thus rapid stiffness decrease, prior to failure is not captured by the presented results. The braider yarn crack densities during the final stages of cycling were not extracted since it was difficult to time the extraction intervals of the edge replicas prior to failure. The presented model would however capture this final stage of stiffness degradation if the crack densities prior to failure were known and defined. Since this stage of cycling was found to be relatively brief for both room temperature and elevated temperature tests, the presented prediction results are deemed to be acceptable for the triaxial braided composite.

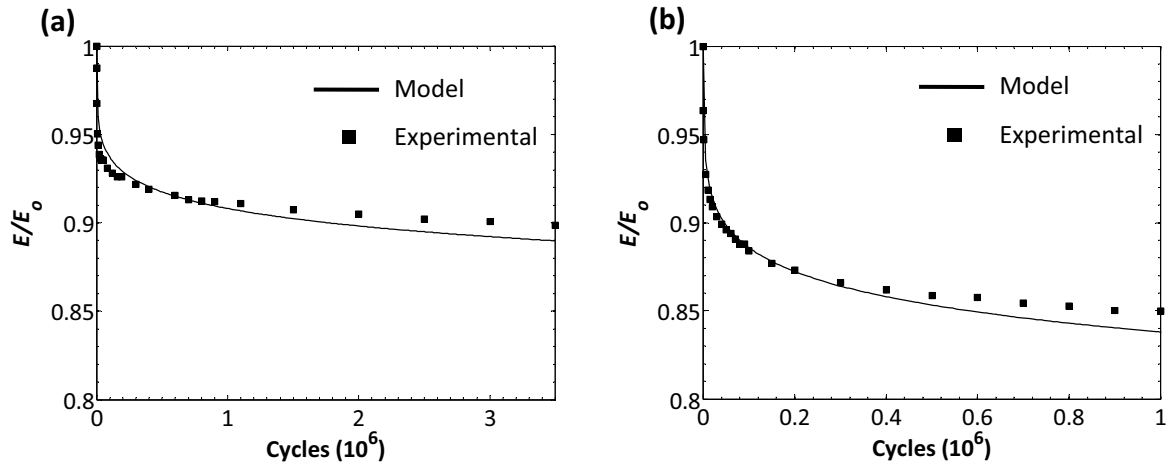

Figure 114. Room temperature predicted and experimental stiffness degradation (a) 50% UTS, (b) 70% UTS.

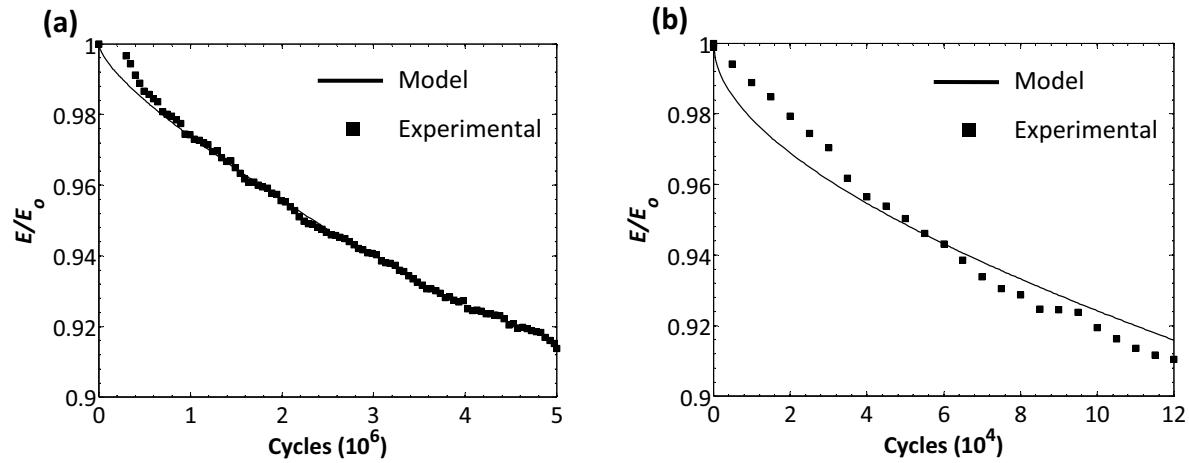

Figure 115. Elevated temperature predicted and experimental stiffness degradation (a) 50% UTS, (b) 70% UTS.

In addition to the presented analytical damage accumulation prediction model, a number of the aforementioned nonlinear analytical damage models based on stiffness degradation were also considered in this study. A model similar to that developed by Lemaitre and Plumtree [188] was modified and used for the braided composites. The damage accumulation parameter, D, is defined by Equation (60). The model material parameters, b_1 and b_2, were found to be functions of the maximum applied stress for the room temperature specimens, which was originally presented by Montesano *et al.* [189].

$$D = 1 - \left[1 - \left(\frac{n}{N_f} \right)^{b_1} \right]^{b_2} \tag{60}$$

The results were promising for the room temperature specimens, but the model was not sufficient for the elevated temperature tests as will be presented here. Consider the tests conducted at both room temperature and elevated temperature with a maximum applied stress level of 70% UTS. Plots of the experimental damage index and the predicted accumulated damage using Equation (60) are shown in Figure 116 (a) and (b) for the room temperature and elevated temperature tests, respectively. The damage index used in Figure 116 was defined in Equation (59), and the damage parameters are plotted as functions of the normalized number of cycles. The model predictions were excellent for all room temperature test specimens as shown in Figure 116 (a). Since for the room temperature test specimens the damage development occurred in a more conventional three-stage progression, the model faired well with similar accuracy to the damage accumulation model defined by Equation (52). For the elevated temperature test specimens, the model predictions were not as close to the experimental results as shown in Figure 116 (b). The errors were in access of 5% for some predictions points. Although the error is still quite low, the predictions of the damage model defined by Equation (52) were slightly better. In either case, the accuracy of the presented damage accumulation model in Equation (52) has been illustrated. Additional results for the damage model defined by Equation (60) can be found in [189].

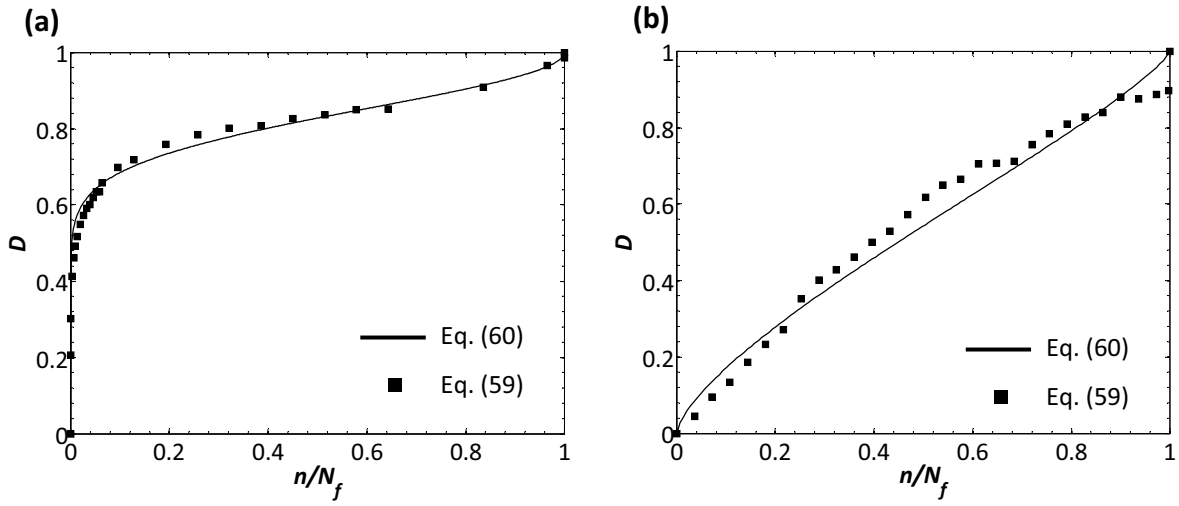

Figure 116. Fatigue damage model and experimental damage index plots with maximum stress of 70% UTS (a) room temperature, (b) elevated temperature.

6.4 Modeling Considerations for Woven Composites

Although the focus of this chapter is on the development and validation of the presented fatigue damage model for the braided composite, a discussion on the fatigue behaviour of two on-axis woven laminates will be presented. As was indicated, the braided composite did not exhibit notable viscoelastic behaviour at the macroscopic level, but local resin viscous behaviour was shown to influence the crack propagation rates. This may in fact be a characteristic of fiber-dominated composites. To this end, an investigation into the on-axis fatigue behaviour of two fiber-dominated composites will provide a relative comparison with the studied triaxial braided composite. This will facilitate the justification for the choice of the type of fatigue damage model developed, which may be suitable for other fiber-dominated PMC materials.

Two on-axis woven laminates were tested at both room temperature and elevated temperatures for relative comparison of the exhibited material behaviour and damage development with the braided composites. The first material studied was an 8HS woven carbon fiber reinforced bismaleimide laminate [14], while the second was a 4HS woven carbon fiber reinforced polyimide laminate [174]. A description of the respective composite laminate

constituents and the fiber geometries was presented in Section 4.1. Details of the exhibited fatigue behaviour of these woven laminates will be discussed here.

6.4.1 Eight-Harness Satin Woven/BMI Laminate

Results of the on-axis room temperature static and fatigue tests for the 8HS woven/BMI laminate were originally presented in [14]. Additional static and fatigue tests were conducted at elevated temperatures using the same experimental protocol described in Sections 4.3 and 4.4. The static and fatigue test procedures were similar to those presented in Section 4.5. The ultimate tensile static stress-strain plots for the two test temperatures are shown collectively in Figure 117. Like the braided composite, the stress-strain behaviour was linear at both test temperatures. The modulus reduced slightly from 70.2 GPa at room temperature to 69.1 GPa at 205˚C, which was only 1.6% lower. Also, the ultimate tensile strength only reduced by approximately 7% at the elevated test temperature. The fiber-dominated material behaviour is evident from the ultimate static test results. A similar observation was reported for an 8HS woven carbon fiber/AMB21 laminate tested at both room temperature and 255˚C [91].

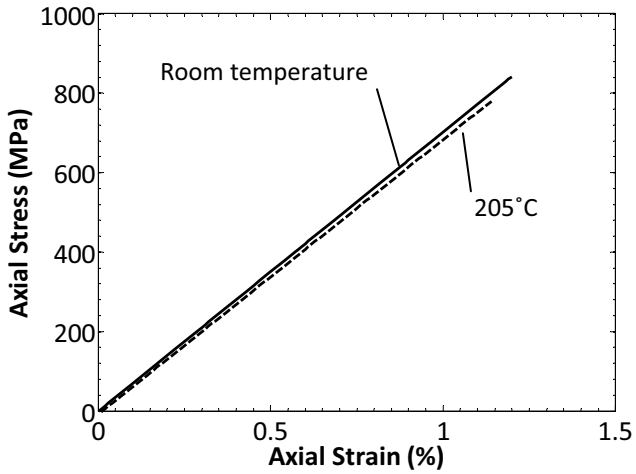

Figure 117. 8HS woven/BMI laminate static stress-strain curves.

The uniaxial tension-tension fatigue tests presented here were conducted with a σ_{max} of 65% UTS for both test temperatures. The stiffness results and damage observations for the conducted tests will now be presented and discussed. Both the room temperature and elevated temperature tests revealed that the material exhibited notable stiffness degradation, as is

shown in the normalized stiffness degradation plots of Figure 118. The room temperature specimens exhibited notably more stiffness degradation after a comparable number of cycles. For example, after 300,000 loading cycles the room temperature specimens showed a reduction in stiffness of 13.3%, while the stiffness reduction for the elevated temperature specimens was only 7.05%. The stiffness degradation rate was more gradual at elevated temperatures, which is evident by analyzing the plots in Figure 118. Similar to the braided composites, the 8HS woven/BMI laminates exhibit less stiffness degradation at elevated temperatures. It should be noted that for both room temperature and 205˚C specimens there was only minor strain ratcheting observed throughout the duration of each test. Moreover, the energy dissipated per unit volume (E_d) per cycle was fairly consistent throughout the duration of cycling regardless of the test temperature. This implies that damage accumulation is the main cause of energy dissipation, and that damage development is somewhat consistent throughout the duration of cycling. The main damage mechanisms observed for each test specimen via post-test SEM observations, regardless of test temperature, were through-the-yarn-thickness cracks in the weft yarns and intra-ply yarn debonds [14]. Some local matrix cracks were also observed in the resin-rich regions. Therefore, due to the differences in the stiffness degradation profiles, the crack propagation rates for the 8HS woven/BMI laminate are confirmed to be slower at 205˚C.

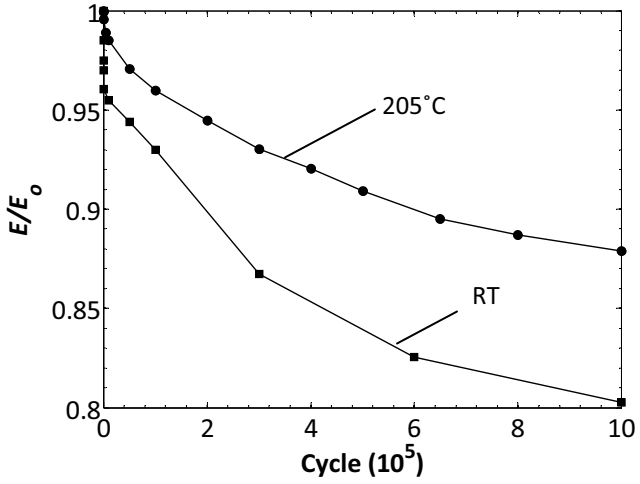

Figure 118. 8HS woven/BMI laminate stiffness degradation profiles (65% UTS).

6.4.2 Four-Harness Satin Woven/RP46 Laminate

Results of the on-axis room temperature and elevated temperature static tests for the 4HS woven/RP46 laminate were originally presented in [174]. Additional fatigue tests were subsequently conducted and those results will be presented here, along with the reproduced static test results. Static and fatigue tests were conducted at room temperature and at an elevated temperature of ($T_{g,\ wet}$ - 28)˚C using the same experimental protocol and procedures described in Sections 4.3 - 4.5. The ultimate tensile static test stress-strain plots for the two test temperatures are shown collectively in Figure 119. Like the braided composite and the 8HS woven/BMI laminate, the stress-strain behaviour was linear at both test temperatures. The modulus was approximately equal at both test temperatures (78.5 GPa), and the room temperature tests exhibited slightly higher ultimate stresses at fracture. The fiber-dominated material behaviour of the 4HS woven/RP46 laminate is evident from the ultimate static test results.

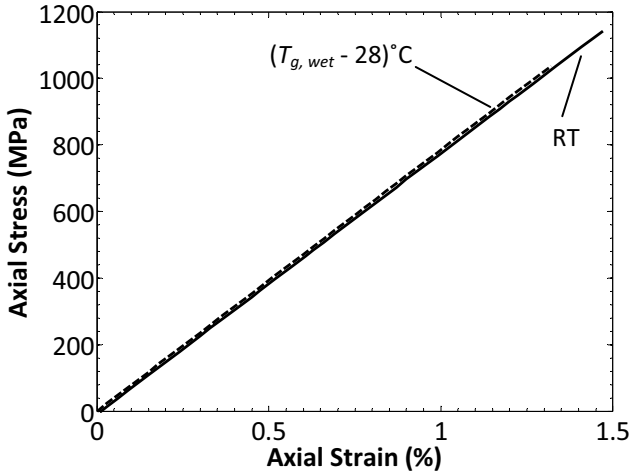

Figure 119. 4HS woven/RP46 laminate static stress-strain curves.

The uniaxial tension-tension fatigue tests presented here were conducted with a σ_{max} of 50% UTS for both test temperatures. The stiffness results and damage observations for the conducted tests will now be presented and discussed. Both the room temperature and elevated temperature tests revealed that the material exhibited very little stiffness degradation, as is shown by the normalized stiffness degradation plots of Figure 120. Note that this may be due to the lower maximum applied stress. Nevertheless, similar observations were made as with the

braided composites and the 8HS woven/BMI laminates, where the stiffness degradation is lower at the elevated test temperature. Little ratcheting was observed for both test temperatures. The energy dissipated per unit volume (E_d) per cycle for the elevated temperature tests was constant for the duration of cycling, while E_d was slightly higher initially and then constant for the duration of the room temperature fatigue tests. For the room temperature tests, the initial higher E_d was likely due to the initial rapid stiffness drop. This suggests that the energy dissipation was due primarily to the development of fatigue damage, which was consistent throughout cycling. The main damage mechanisms observed for each test specimen via post-test SEM observations, regardless of test temperature, were through-the-yarn-thickness cracks in the weft yarns and intra-ply yarn debonds [174]. Some cracking in the warp yarns (i.e., splitting) was also observed. Therefore, due to the differences in the stiffness degradation profiles, the crack propagation rates for the 4HS woven/RP46 laminate are confirmed to be slower at the elevated test temperature.

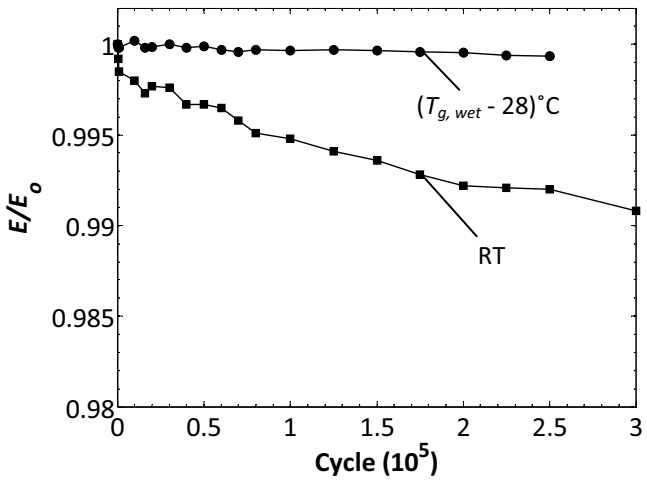

Figure 120. 4HS woven/RP46 laminate stiffness degradation profiles (50% UTS).

6.4.3 General Discussion

For both fiber-dominated woven laminates studied in this section, the relative material behaviour observed at room temperature and elevated temperature was analogous to the observations made with the braided composite. The stiffness degradation rate during cyclic loading was consistently lower at elevated temperatures, even though the material properties were only slightly influenced by the elevated temperature environment. This suggests that the

two fiber-dominated woven laminates undergo similar local resin deterioration at elevated temperatures, which effectively decreases the crack propagation rates. This provides additional support for the experimental results obtained for the braided composite material. This subsequently provides further support for the type of damage model developed in this study, and its relevance for predicting room temperature and elevated temperature fatigue damage development for fiber-dominated composites.

6.5 Implementation of Damage Model in a CDM Framework

Although the developed analytical fatigue damage model is suitable for predicting damage development and stiffness degradation of composite materials, the damage model can be subsequently implemented into a set of 'damaged' constitutive equations for fatigue damage simulations of composite components. Some details of the theory of CDM and the implementation of this procedure will be presented.

The premise of damage mechanics (or CDM) was introduced in Section 3.7 and is based on the concept of evolving microscopic changes in materials, which cause progressive deterioration of their bulk mechanical properties [159]. Consider for example damage accumulation during fatigue loading of composite materials, which causes stiffness and strength degradation as discussed in Section 3.2. CDM allows for the consideration of the microscopic damage state of the material in order to predict the macroscopic changes in the mechanical properties. The damage parameter defined by Equation (56) is introduced as a representation of the effective surface density of defects, assuming that the microscopic damage is uniform over the material component and small in size compared to the dimensions of the component. Thus, when the damaged component is loaded as shown in Figure 121, the concept of an effective stress can be introduced which was defined by Equation (57). In CDM, the effective stress is used to define the strain response of the damaged material [190]. Defining the damaged area, A_D, for a representative volume is of course difficult and likely impossible, thus the damage parameter, D, can be approximated by a suitable cumulative damage formulation. The damage accumulation models developed in this study, and defined by Equations (52) and (60), would be suitable choices for the braided composite material.

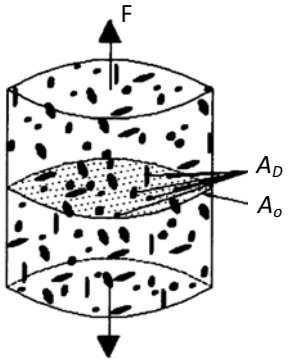

Figure 121. Representative volume element of material with microscopic damage [95].

The concepts outlined in the previous paragraph form the basis for developing damaged constitutive models within the framework of irreversible thermodynamics. The thermodynamics of irreversible processes is based on energy concepts and the evolving local states within a material. Within this framework, the constitutive equations for a mechanical system are effectively derived from the basic principles of thermodynamics. The thermodynamic state of a material that involves irreversible internal dissipation can be defined by external state variables which are measurable quantities (e.g., stress or strain, and temperature), and internal state variables which are non-measurable quantities (e.g., local damage). For mechanically loaded composite materials, the microscopic development of the various forms of damage are considered irreversible processes. The well known Clausius-Planck entropy inequality form of the second law of thermodynamics is employed to impose a restriction on the formulation of the internal dissipation terms [191]. Therefore to characterize a continuous media within the thermodynamic framework, a thermodynamic potential Ψ (which is analogous to a strain energy function) must be defined. The thermodynamic potential is a scalar function of the external and internal state variables of the thermodynamic system (i.e., Ψ(σ or ε, D) for isothermal conditions). An example of a thermodynamic potential developed by Ladeveze [166] for damaged elastic unidirectional-ply composite materials is shown in Equation (61).

$$\Psi = \frac{1}{2}\left[\frac{\sigma_{11}^2}{E_1^o} - \frac{2\nu_{12}^o}{E_1^o}\sigma_{11}\sigma_{22} + \frac{\langle\sigma_{22}\rangle_+^2}{E_2^o\left(1-d'\right)} + \frac{\langle\sigma_{22}\rangle_-^2}{E_2^o} + \frac{\sigma_{12}^2}{2G_{12}^o\left(1-d\right)}\right] \tag{61}$$

Note that Equation (61) is written in terms of the tensor terms and not the tensors themselves, and is for an orthotropic material subjected to a plane stress state. The thermodynamic potential, which is based on the previously defined effective stress concept, includes two scalar damage variables, d and d', which represent specific modes of damage. The cumulative damage models developed in this study (i.e., d_1 and d_2, or D) could be used as input within a similar thermodynamic potential. Note that the damage parameters presented in Equation (61) effectively scale the material stiffness terms (i.e., E_2, G_{12}).

The constitutive equations that govern the behaviour of a damaged material can then be defined from the thermodynamic potential function (Ψ) using the following expression.

$$\varepsilon_{ij} = \frac{\partial \Psi(\sigma, D)}{\partial \sigma_{ij}} \tag{62}$$

Note that Equation (62) is in fact a general set of equations for any type of material behaviour (e.g., linear elastic, plastic, viscoelastic) that includes the effects of irreversible damage. In other words, Equation (62) represents nonlinear material behaviour caused by irreversible damage, regardless of the bulk material constitutive behaviour. Note that for a constitutive model with many scalar damage parameters, it is often common to represent the scalar damage parameters in the form of a tensor [162, 163]. Specifically regarding fatigue of composites, the damage variable evolution laws must also be defined. This is where the evolution of the cumulative damage parameters (i.e., dD/dn) is incorporated within the CDM-based constitutive formulation. The framework for developing a CDM-based constitutive model for composite materials with evolving damage was presented, however the application of this technique is beyond the scope of this study and is left for a future study.

7 OVERALL DISCUSSION AND SUMMARY

The experimental results presented in Chapter 5 and the fatigue prediction model results presented in Chapter 6 will be the basis for the discussion in the subsequent paragraphs. First, a general discussion on the exhibited braided composite static properties will be presented, followed by a detailed discussion on the braided composite fatigue behaviour. Finally, a discussion on the developed fatigue damage prediction model will conclude the chapter.

7.1 Braided Composite Static Tests

The uniaxial tensile displacement-controlled quasi-static tests conducted on the triaxial braided composite material revealed that the elevated temperature environment did not significantly alter the measured macroscopic material properties (i.e., E_{11} and S_u). A similar observation was also made for the two woven-ply laminates studied. The braided composite did not exhibit any rate-dependent or time-dependent behaviour either. However, the local damage development was notably different for the room temperature and elevated temperature specimens. Recall that the room temperature braided specimens exhibited a bilinear stress-strain behaviour. This was the result of an instantaneous increase in the braider yarn crack density at the transition stress, which thereafter rendered the braider yarns ineffective in supporting additional applied load causing increased material compliance. This was observed through extracted edge replicas, FBG sensor chirping and IR thermographs. This is analogous to first-ply failure observed with some quasi-isotropic laminates. This type of damage

development was not observed with the elevated temperature test specimens. In fact, there was little damage up until ultimate failure, which was further confirmed by post *mortem* SEM observations. As a result of significantly reduced braider yarn crack development and the lack of a stress relieving mechanism in the braider yarns, the braider yarns were fully effective until specimen failure which resulted in the exhibited linear stress-strain behaviour. An additional investigation on neat resin test specimens revealed that the thermosetting resin modulus notably reduced at elevated temperatures, while a slight increase in the resin 'ductility' was also observed. The increased resin ductility combined with the constraint of the reinforcing braided fibers on the resin resulted in 'tougher' resin fracture behaviour at elevated temperatures, which acted to mitigate the onset and development of microcracks in the composite. In addition, the potential change in the local load distribution between the resin and the fibers, caused by the softening resin, may have further contributed to slowing crack development at elevated temperatures. These were the main mechanisms responsible for the notable change in the braided composite microscopic damage development. Although the composite material properties and fracture surface characteristics were similar at both test temperatures, the local influence of temperature on damage development was revealed. It should also be noted that there were few yarn interface and matrix cracks for the duration of all static tests.

7.2 Braided Composite Fatigue Tests

The uniaxial tension-tension stress-controlled fatigue tests conducted on the triaxial braided composite material also revealed that the elevated temperature environment had a notable influence on the development of microscopic fatigue damage. This resulted in a notable difference with the S-N data obtained at the two test temperatures, as was presented in Figure 74 (b). The S-N curves were both represented by a linear relationship between the maximum applied stress ratio (σ_{max}/S_u) and the logarithm of the number of cycles to failure ($\log N_f$). At higher applied stresses (i.e., LCF regime) the number of cycles to failure for both test temperatures were somewhat comparable, while at lower applied stresses (i.e., HCF regime) the number of cycles to failure were notably lower for the elevated temperature tests. In both

cases, a HCFS was established and confirmed using the thermographic technique (i.e., Risitano's method). At room temperatures, the HCFS represented a transition in the damage state of the material, where cycling with maximum applied stresses above the HCFS resulted in significant damage after just the first loading cycle. This is evident by considering the high energy dissipated during the initial few loading cycles that was caused by excessive crack development, which is evident by the plots in Figure 53 and Figure 55. This was not observed for the specimens cycled with maximum applied stresses below the HCFS. At the elevated test temperature, the HCFS also represented a transition from a slightly lower damage state to an advanced damage state at stresses above the HCFS (see Figure 84 and Figure 86). Also, the HCFS was lower in magnitude at the elevated test temperature.

In terms of the dynamic stiffness degradation, the room temperature specimens exhibited rapid degradation during the first stage of cycling, followed by gradual degradation during the second stage, and rapid degradation during the third stage prior to failure. The three-stage stiffness degradation profile is also commonly exhibited by many cross-ply and quasi-isotropic laminates. The elevated temperature specimens exhibited a more gradual stiffness degradation during the first stage of cycling, but a higher degradation rate during the second stage. In fact, the stiffness degradation for the elevated temperature specimens was more gradual for the entire duration of cycling. The notable difference in the stiffness degradation profiles was mainly due to the influence of temperature on the microscopic fatigue damage development, even though the macroscopic static material properties were only slightly altered by the elevated test temperature. For the room temperature specimens, damage developed in three distinct phases: (i) initial rapid development of braider yarn cracks up to a damage saturation state along with initiation of localized yarn interface cracks, followed by (ii) gradual development of braider yarn cracks and growth of yarn interface cracks, and finally (iii) severe interaction of different matrix-dominated damage modes leading to load redistribution and weakening of the warp yarns, fiber fracture and ultimately specimen failure. At the end of the first stage of cycling when the braider yarn crack saturation state was attained, the notable cracking within the braider yarns caused stress relief within these yarns and therefore less braider yarn crack development thereafter. The damage development was

confirmed by extracted edge replicas, obtained IR thermographs and post *mortem* SEM observations. For the elevated temperature tests, the damage development rate was significantly lower during the initial stages of cycling, but more consistent for the duration of cycling. This was confirmed from the extracted edge replicas and further confirmed by the infrared thermographs. Braider yarn crack development occurred during all stages of cycling, while yarn interface cracks only began to grow significantly during the latter stages of cycling. For both test temperatures, the braider yarn cracks were the dominant damage mechanisms observed due to the higher stresses within the braider yarns. The yarn interface cracks were also influential damage mechanisms, but there were fewer in quantity relative to the braider yarn cracks. Moreover, the development of the braider yarn and yarn interface cracks was directly correlated to the exhibited stiffness degradation for both test temperatures, as was presented in Figure 66 and Figure 96. These results demonstrated that braider yarn and interface cracks were the main contributors to stiffness degradation for the duration of cycling.

The main cause of the altered damage development (and associated stiffness degradation) exhibited by the braided specimens is the influence of temperature on the local resin behaviour. Softening of the resin at the elevated test temperature increased the resin toughness and likely reduced the stress concentration within the braider yarns due to a change in the local load distribution between the fibers and the matrix. This consequently slowed the development of microscopic crack development in the braided composite. This was particularly noticeable during the initial stage of cycling for the elevated temperature test specimens cycled at lower applied stresses; the crack development was slower and there was a delay in the stiffness degradation response. The reduced damage development rate during the elevated temperature fatigue tests was also evident by the temperature rise captured with the IR camera, which was significantly lower for the elevated temperature specimens. In addition, for both test temperatures the same braider yarn crack density caused the same stiffness degradation during the earlier stages of cycling (see Figure 66 and Figure 96). Recall that the braider yarn cracks were the main cause of stiffness degradation during this stage of cycling. Thus, this illustrates that the measured stiffness loss was only caused by damage accumulation at both test temperatures. Thus, the hypothesis that the elevated temperature environment

simply changes the crack propagation rate is in fact accurate. Similar observations were also presented for the two fiber-dominated woven-ply laminates studied.

It should be noted that for the same maximum applied stress, the room temperature specimens exhibited more stiffness degradation after a comparable number of cycles. This was a peculiar result considering that the elevated temperature specimens have notably lower fatigue lives for all applied stress levels. This can be explained by the fact that the mechanisms causing stiffness degradation for the major part of cycling differ from those that result in ultimate failure during the final stage of cycling. Although braider yarn and interface cracks result in stiffness degradation throughout the duration of cycling, the final failure event is initiated by additional local matrix cracks and yarn interface failures as was detected by inspection of the fracture surfaces and well as by the infrared camera. Once the saturation of these damage modes occurs, load is redistributed to the 0˚ yarns since the matrix and the braider yarns are less effective in supporting load. This causes the warp yarns to weaken due to developing splitting cracks, which subsequently leads to fiber fracture within the yarns as cycling progresses. This eventually results in fracture of the warp yarns, which ultimately leads to specimen failure. In addition, local damage observations revealed that although the braider yarn and yarn interface cracks developed along the fiber-matrix interfaces, at elevated temperatures these cracks were accompanied by additional damage in the resin due to the deterioration of the resin or the fiber-matrix interfaces. These modes of damage are matrix-dominated and the braided composite is more susceptible to these damage modes at elevated temperatures. Thus, although the damage state within the braider yarns under a particular applied stress is less advanced after a certain number of cycles at the elevated test temperature (which did not cause failure at room temperature), the failure event occurs due to the increased local matrix-induced damage which ultimately causes localized weakening of the 0˚ fiber yarns. This also explains the lower HCFS exhibited by the elevated temperature test specimens. In addition, consider that there were fewer interface cracks at failure for higher applied stresses, and that the fatigue lives in the LCF regime were comparable for both test temperatures. This illustrates that for the LCF regime, fewer interface cracks led to less matrix-induced damage development and therefore similar resulting fatigue lives at both

temperatures. This further supports the stated hypothesis regarding the fatigue lives. This also reveals that the failure-causing mechanisms were slightly different for LCF and HCF regimes, and that there were different exhibited residual strength developments. It should also be noted that the failure event for all fatigue tests conducted was rapid, which did not allow for significant stiffness degradation during the last stage of cycling (especially at elevated temperatures). This type of fracture behaviour was also found to occur with biaxial braided PMC test specimens [66].

It should also be noted that for both test temperatures, the exhibited ratcheting behaviour was mainly due to damage development (i.e., opening crack faces not fully closing upon unloading) since very little creep was observed. This was confirmed by a series of creep tests at the elevated test temperature, and by the fact that there was significantly less ratcheting during the elevated temperature tests. If the material exhibited creep deformation, this would have caused an increase in ratcheting deformation at elevated temperatures. The opposite was in fact observed, which was due to less damage development at elevated temperatures. This is a direct result of the fiber-dominated braided composite behaviour. Matrix-dominated PMC materials would tend to exhibit drastically different damage development and macroscopic material behaviour, with notable creep or time-dependent behaviour as well as potential fiber yarn reorientation phenomenon [72]. In fact, the characteristic local damage development for the braided composite and the associated macroscopic hysteretic behaviour may be typical of other fiber-dominated PMC materials. The fiber geometry seems to dictate the type of damage modes present, while the matrix material influences the rate of propagation of these damage modes. This is an important discovery that assists in better understanding the damage and deformation mechanics of other similar fiber reinforced PMC materials. This insight may lead to a generalized fatigue damage model for fiber-dominated PMC materials in the future. However, it should be noted that some studies on fiber-dominated unidirectional-ply PMCs [5, 82, 85, 87] have reported that the influence of elevated temperatures on the corresponding S-N data is less significant than that shown for the braided composite. It should also be noted that the tested 8HS woven/BMI and 4HS woven/RP46 laminates exhibited similar temperature influence as that presented for the

braided composite specimens. There is no doubt that the type of resin and the specific test temperature must be considered and analyzed in great detail in order to confirm this argument.

Another important finding of this study is that the average stiffness degradation rate (i.e., $\Delta E/N_f$) is a function of the maximum applied stress, at both test temperatures. This is due to the fact that the braider yarn and interface crack development rates are also functions of the maximum applied stress as shown in Figure 100 and Figure 104. As the maximum stress increases, the stiffness degradation rate increases and the crack development rates increase. This could be useful quantitative information for the design of components made from this braided composite material. Regardless of the applied stress magnitude (i.e., LCF or HCF regime), the stiffness degradation rate follows a power law function. In addition, a critical stiffness may be defined as a function of the maximum applied stress which can be used to predict the fatigue life. The correlation between the average stiffness degradation rate and the maximum applied stress can be used to facilitate the prediction of the fatigue life.

A final point is that the braided composite exhibited excellent fatigue performance at room temperature. For example, at a maximum stress of 70% UTS the fatigue life was $>10^6$ cycles. At elevated temperatures, the braided composites also exhibited excellent fatigue properties. Although there are few high temperature studies available in the literature, a comparison of room temperature S-N data from studies conducted on other carbon fiber/resin composites loaded in the fiber-dominated direction can be made. Some of these studies investigated quasi-isotropic, cross-ply or unidirectional laminates [27, 37, 41, 48, 85, 115], woven laminates [52], non-crimp fabric composites [62], and biaxial braided composites [66]. A comparison in terms of the fatigue lives corresponding to a maximum applied stress, which is defined as a fraction of the static UTS, suggests that the investigated triaxial braided composite of this study performs better, if not comparable, to other fiber-dominated carbon/resin composites when subjected to tension-tension fatigue loading with a stress ratio of R = 0.1. Also, the existence of a HCFS, which is not common for polymeric composites, further illustrates the excellent fatigue properties of the triaxial braided composite.

7.3 Fatigue Damage Model

The developed damage model presented in Chapter 6 was based on the experimentally obtained braider yarn and yarn interface crack densities. This provided a means to capture the influence of the elevated temperature environment on the crack propagation rate, and directly incorporate those effects into the analytical damage model. As indicated, the static material properties were only slightly influenced by the elevated test temperature, thus the effects of temperature were manifested through the slower crack propagation rates. Also, since the same damage mechanisms developed for the duration of cycling at both test temperatures, cumulative damage is governed by the same evolving crack densities at both test temperatures. Note that since the developed fatigue prediction model is based on actual damage mechanisms, it is classified in the third category of fatigue models (see Section 3.7). Few similar models based on crack density evolution have been developed in the open literature [59, 155], neither of which consider elevated temperature fatigue.

In terms of predictive capability, the developed fatigue damage model was able to accurately capture the damage development at both test temperatures when compared to a stiffness-based experimental damage index. The predicted stiffness degradation results for all stress levels, and both temperatures, showed excellent correlation with the experimental data. The accuracy of the prediction model in determining the residual stiffness was consistently within 2% of the corresponding experimental data. Also, since the damage model is based on crack density evolutions, its capability to predict damage accumulation (or residual stiffness) at both LCF and HCF regimes was demonstrated. This is one of the main advantages for a fatigue prediction model that is based on actual damage development parameters. In addition, the cumulative damage model allowed for the investigation of the two damage parameters, d_1 and d_2. The influence of each parameter on the damage development (and residual stiffness) can be isolated in order to define the corresponding affect on the material behaviour. This is an advantage for implementation of the damage model within a CDM-based constitutive model (see Equation (62)), where the individual damage parameters may be incorporated within the constitutive model separately.

8 CONCLUSIONS AND FUTURE WORK

An investigation focussed on the tensile static and fatigue behaviour of a triaxial braided carbon fiber reinforced thermosetting resin composite, at both room temperature and elevated temperature, was conducted in order to gain a better understanding of the intricate material behaviour. The exhibited material behaviour during both static and fatigue loading was correlated to the observed microscopic damage mechanisms. The corresponding analytical fatigue prediction model was subsequently developed, the results of which were compared to the experimental data. Two additional satin woven carbon fiber reinforced thermosetting resin composites were similarly investigated to provide a comparative analysis with the triaxial braided material. The subsequent sections list the notable conclusions of this study, the main contributions made through this research, and recommendations for future work.

8.1 Conclusions

The most notable conclusions that can be drawn from this study are summarized by the following points:

- The tensile static properties of the triaxial braided carbon fiber reinforced resin material, such as the axial modulus and ultimate strength, exhibited minimal temperature-dependence. It was also confirmed that there was virtually no time- or rate-dependent

stress-strain behaviour for both temperatures considered. This was due to the fact that the braided composite was loaded in a fiber-dominated direction.

- The development of microscopic damage during static testing was however significantly influenced by temperature. A bilinear stress-strain behaviour was clearly exhibited at room temperature, which was a result of extensive braider yarn matrix cracking at the transition point. Linear stress-strain behaviour was characteristic of the braided composite during elevated temperature tests, which revealed little damage development throughout loading. The 'softening' of the thermosetting resin matrix constituent at the elevated test temperature combined with a change in the local load distribution between the fibers and resin, resulted in reduced microscopic damage development.
- The elevated temperature environment had a notable influence on the tensile fatigue behaviour of the braided composite, particularly in terms of the exhibited residual stiffness. The stiffness degradation rate was notably lower at elevated temperatures, which was a result of slower crack propagation rates caused by softening of the matrix. The main observed damage mechanisms were braider yarn cracks and yarn interface cracks.
- The fatigue lives in the HCF regime were notably lower at elevated temperatures. This was attributed to different matrix-dominated mechanisms which caused failure to occur sooner at the elevated test temperature. This was a result of increased localized cracking at the fiber-matrix interfaces, within the matrix rich zones, and the associated matrix damage, which was more prominent at elevated test temperatures. These damage mechanisms caused the warp fiber yarns to weaken sooner, which resulted in shorter fatigue lives.
- By comparing the fatigue S-N data of the triaxial braided composite with other fiber-dominated carbon fiber/resin composites, the fatigue behaviour of the investigated braided composite is either superior or equivalent. The existence of a high cycle fatigue limit supports this claim.
- The developed damage mechanics-based analytical fatigue prediction model, which was defined using evolving damage parameters representative of actual damage mechanisms,

was able to predict damage development and stiffness degradation with an excellent correlation to the experimental data. The model is suitable for predicting damage development and the associated material property degradation.

- The investigated woven carbon fiber/resin laminates exhibited analogous static and fatigue microscopic damage behaviour and macroscopic material behaviour as the triaxial braided composite. This supports the claim that the exhibited elevated temperature behaviour may be characteristic of many fiber-dominated carbon fiber composites.

8.2 Contributions

The main contributions made through this study are summarized by the following points:

- An in-depth characterization of the static and fatigue behaviour of a braided composite, in terms of correlating microscopic damage mechanisms to the stiffness degradation, is a novel contribution to the open literature. The critical damage modes that caused stiffness degradation, and those that led to failure have been identified. A better understanding of the local damage development, the local deformation behaviour and the failure mechanisms of braided composite materials was achieved.
- The high temperature characterization of the braided polymeric composite is also unique and another significant contribution of this study. This study is the first of its kind in the open literature. A better understanding of braided composite fatigue behaviour and the effects of temperature on fiber-dominated thermosetting matrix composites was achieved.
- The development of the fatigue damage model for a braided composite at elevated temperatures is another novel contribution. The type of damage model, which was based on observed damage mechanisms, has never been developed for an elevated temperature study. In addition, the fatigue damage model may be applicable to other fiber-dominated composites.
- The combination of techniques employed to monitor damage development, using local damage detection techniques (fiber optic sensors, edge replication) coupled with a global

damage detection technique (thermography), is a novel contribution. This has never been achieved for an elevated temperature study, especially not the use of thermography and fiber optic sensors at elevated temperatures.

- This is one of only a few studies that used the thermographic approach (i.e., Risitano's method) to determine the high cycle fatigue strength for a polymeric composite material.
- This is the first fatigue study conducted on composite materials to capture actual damage development and to identify critical damage states using infrared thermography.
- A comprehensive review of reported elevated temperature fatigue studies conducted on polymeric composites in the open literature was presented, which has never been achieved.
- A list of publications and manuscripts currently in progress, as related to this research, is included in Appendix A.3.

8.3 Future Work

Although notable contributions were made in this study, additional work can be performed to further advance the knowledge base of this emerging research area. The following points are a summary of recommendations for future work:

- Obtain a proper crack count during the final stages of cycling prior to fracture in order to provide input for the fatigue damage model, which will allow for prediction of the entire fatigue life. An in-depth study of the failure events must be conducted to achieve this.
- Further verification of the crack development states and the crack propagation rates through use of another non-contact full-field real-time non-destructive evaluation technique that can clearly detect different damage modes - especially at elevated temperatures.
- Testing the capability of the developed damage prediction model with additional braided and woven composite materials for further validation. Additional tests with the two fiber-dominated woven laminates studied here can be conducted to this end. This would

provide further support for this class of fatigue damage model, which may eventually lead to wider acceptance in the aerospace industry.

- The implementation of the developed damage model into a damage mechanics-based constitutive model for finite element simulation of fatigue damage development in composite components can be done. This was in fact outlined in this study.
- A full experimental test program on the triaxial braided composite could be conducted at a few intermediate test temperatures. This will provide further comparison of the material properties and damage development at the intermediate temperatures. In terms of the fatigue damage prediction model, results from the elevated temperature tests can be used to relate the model parameters to not only the maximum applied stress, but to the test temperature as well.
- A similar experimental test program can be conducted on a material comprised of the same triaxial braided carbon fiber fabric with a different matrix material (e.g., RP46) to verify if the exhibited material behaviour and damage development is characteristic of braided materials, or the specific resin constituent.
- A similar experimental test program can be conducted on the same braided carbon fiber/resin composite material in a matrix-dominated loading configuration. A comparison of the matrix-dominated material response to the presented fiber-dominated braided composite material behaviour can be made, and would be valuable.

APPENDICES

A.1 Crack Density Evaluation Details

This appendix subsection will explain the approach used to count the number of braider yarn and interface cracks for establishing crack densities from the obtained edge replicas. Recall that the edge replicas were extracted at numerous cyclic intervals throughout a single test, and were utilized for various stress levels and for both room temperature and elevated temperature fatigue tests. The replicas were also extracted for the room temperature ultimate static tests.

To assist with the explanation of the braider yarn crack density counts, Figure A1 shows an edge replica extracted during a fatigue test. In the same figure a schematic representation of braider yarn and interface cracking is also shown. Two common crack patterns that were consistently observed are illustrated in Figure A1. The first crack pattern is the propagation of a single apparent crack through multiple adjacent braider yarns of the same orientation (i.e., all yarns +60˚, or -60˚) as indicated by the circle in the edge replica image. Although this may seem like a single crack, the crack actually propagated through two braider yarns, thus would be counted as two braider yarn cracks. This is the accurate approach because both cracked braider yarns would contribute approximately the same degree of stiffness degradation, thus both 'cracks' should be accounted for in the braider yarn crack density. The second crack pattern is the propagation of a long interface crack along the periphery of the 0˚ yarns, in the warp direction, as indicated by the ellipse in the edge replica image. These type of cracks were often observed to initiate between a 0˚ yarn and a braider yarn, and found to propagate along the 0˚ yarn direction through the interface of another braider yarn. Also, these cracks were often initiated as two separate cracks at the interfaces between a 0˚ yarn and two separate braider yarns, then combined to form one apparent crack as cyclic loading progressed. In either case, since the interface crack has propagated though the interfaces of two braider yarns as shown in the edge replica image, this would actually be considered as two cracks in the interface crack density count. Therefore, as the crack lengths increased during cycling due to propagation/interaction, this effect was actually accounted for within the interface crack density count.

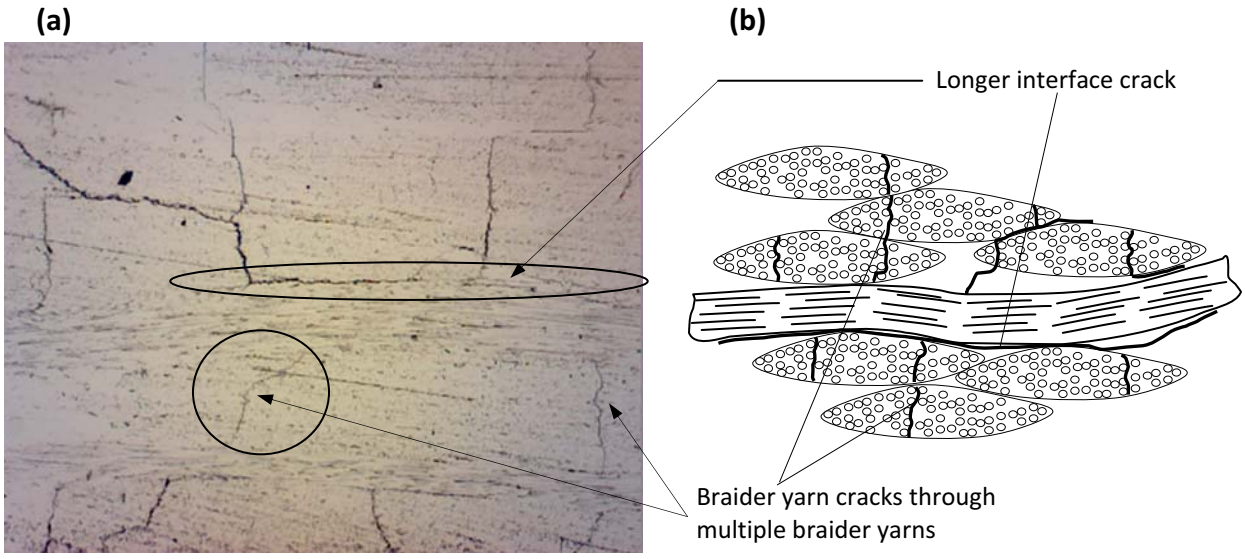

Figure A1. (a) Image of an obtained edge replica, (b) schematic of crack scenarios.

A.2 Risitano's Thermographic Method

The method assumes that the recorded temperature variation caused by cyclic loading of a test specimen is a measure of the heat dissipation due to intrinsic energy dissipative mechanisms (see Section 3.6). The test specimen is cycled for a limited number of cycles at a given maximum stress level in order to produce stabilization of the rising surface temperature caused by heat dissipation. This is repeated for many stress levels at a constant loading frequency, where the schematic of temperature variation versus cycles for various stress levels is shown in Figure A2 (a). For each stress level, the corresponding temperature increase from initial to stabilization (ΔT_{stab}) can be plotted at a function of the applied stress as shown schematically in Figure A2 (b). Then, from the plot it can be seen that when the threshold point is reached the temperature increase is greater and the fatigue limit or HCFS can be determined. The hypothesis is that when the fatigue limit is exceeded, the heat dissipation drastically increases because of the increase in the degree of intrinsic energy dissipation [178].

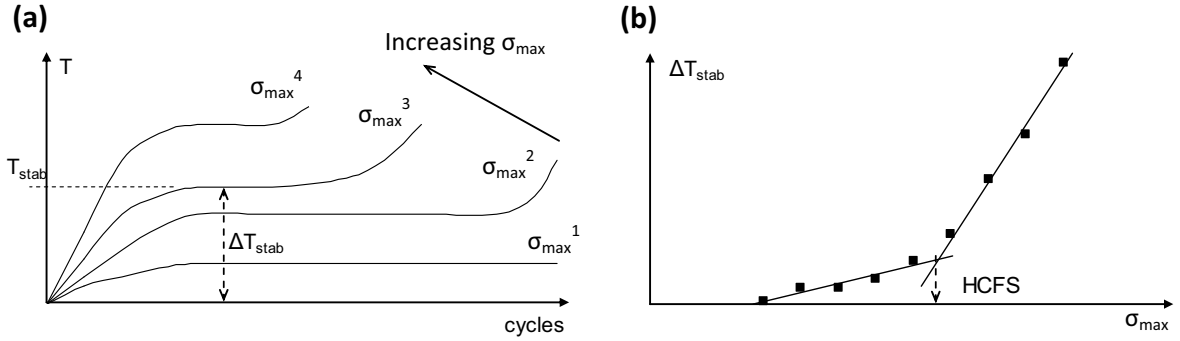

Figure A2. Schematic of Risitano's method (a) temperature profiles, (b) temperature rise-maximum stress plot.

A.3 List of Publications

Refereed Journal Papers

- **Montesano, J.**, Selezneva, M., Fawaz, Z., Poon, C., Behdinan, K.: Elevated Temperature Off-Axis Fatigue Behaviour of an Eight-Harness Satin Woven Carbon-Fiber/Bismaleimide Laminate. *Composites Part A* 43, 1454-1466 (2012).
- **Montesano, J.**, Fawaz, Z., Behdinan, K., Poon C.: Fatigue Damage in On-Axis and Off-Axis Woven-Fiber/Resin Composite. *Key Engineering Materials* 488/489, 230-233 (2012).
- Selezneva, M., **Montesano, J.**, Fawaz, Z., Behdinan, K., Poon, C.: Microscale Experimental Investigation of Failure Mechanisms in Off-Axis Woven Laminates at Elevated Temperatures. *Composites Part A* 42, 1756-1763 (2011).
- **Montesano, J.**, Selezneva, M., Poon, C., Fawaz, Z. and Behdinan, K.: Application of Fiber Optic Sensors for Elevated Temperature Testing of Polymer Matrix Composite Materials. *Science & Engineering of Composite Materials* 18, 109-116 (2011).
- **Montesano, J.**, Fawaz, Z., Behdinan, K., and Poon, C.: Fatigue of High Temperature Polymer Matrix Composites. *Materials Science Research Journal* 4, 381-406 (2010).

Conference Proceedings

- **Montesano, J.**, Fawaz, Z., Poon, C., Behdinan, K.: A Microscopic Experimental Investigation of Failure Mechanisms in a Triaxially Braided Polymer Composite. *Proceedings of the 9th Joint Canada-Japan Workshop on Composites*, Kyoto, Japan, July 30-Aug 1, 2012.
- **Montesano, J.**, Fawaz, Z., Poon, C., Behdinan, K.: Fatigue Damage Characterization of a Tri-axially Braided Polymer Matrix Composite Material. *Proceedings of the 15th European Conference on Composite Materials* (ECCM-15), Venice, Italy, June 24-28, 2012.
- **Montesano, J.**, Fawaz, Z., Poon, C., Behdinan, K.: Characterization of the Mechanical Properties and Fatigue Behaviour of a Three-Dimensional Braided Carbon-Fiber/Polyimide Composite. *Proceedings of the 2nd Joint US-Canada Conference on Composites*, Montreal, Canada, Sept 26-28, 2011.
- **Montesano, J.**, Selezneva, M., Poon, C., Fawaz, Z. and Behdinan, K.: Using Fiber Optic Strain Sensors for Elevated Temperature Fatigue Testing of Polymer Matrix Composites. *Proceedings of the 8th Joint Canada-Japan Workshop on Composites*, Montreal, Canada, July 26-29, 2010. In *Design, Manufacturing and Applications of Composites*; Eds. Ngo, A.D., Dennault, J., Nakai, A., Morii, T., Hoa, S.V., Hamada, H.; DEStech Publications Inc., Lancaster, PA, pp 229-240 (2010).
- **Montesano, J.**, Selezneva, M., Fawaz, Z., Behdinan, K., and Poon, C.: Strain and Damage Monitoring of Polymer Matrix Composite Materials at Elevated Temperatures Using Fiber Optic Sensors. *Proceedings of the SAMPE 2010 Spring Conference and Exhibition* (55th International SAMPE Symposium), Seattle, USA, May 17-20, 2010.
- Selezneva, M., **Montesano, J.**, Kulisek, V., Poon, C., Fawaz, Z. and Behdinan, K.: Application of FBG Sensors to Monitor Stiffness Degradation and Damage Progression in

Polymer Matrix Composites. *Proceedings of the SAMPE 2010 Spring Conference and Exhibition* (55th International SAMPE Symposium), Seattle, USA, May 17-20, 2010.

- **Montesano, J.**, Behdinan, K., Fawaz, Z., and Poon, C.: Considerations for Progressive Damage in Fibre-Reinforced Composite Materials Subjected to Fatigue. *Proceedings of the 23rd International Symposium - High Performance Computing Symposium 2009*, Kingston, Canada, June 14-17, 2009. In *High Performance Computing Systems and Applications*, LNCS 5976; Eds. Mewhort, D.J.K., Cann, N.M., Slater, G.W., Naughton, T.J.; Springer-Verlag, Berlin, pp 148-164 (2010).

Book Chapters

- **Montesano, J.**, Fawaz, Z., Behdinan, K., and Poon, C.: Fatigue of Polymer Matrix Composites at Elevated Temperatures - A Review. In *Composite Materials in Engineering Structures*; Ed. Davis, J.M.; Nova Science Publisher, Hauppauge, NY, pp 229-252 (2011).

Journal Papers Currently in Preparation

- A Microscopic Investigation of Failure Mechanisms in a Triaxial Braided Polymer Composite at Room and Elevated Temperatures. To be submitted to *Composites Part A* (2012).
- Fatigue Damage Characterization of a Triaxial Braided Polymer Matrix Composite at Elevated Temperatures. To be submitted to *Composite Structures* (2012).

REFERENCES

1. Hawk, J.: The Boeing 787 Dreamliner - More Than an Airplane. *Proceedings of the AIAA/AAAF Aircraft Noise and Emissions Reduction Symposium*, May 24-26, Monterey, USA (2005).

2. Mouritz, A.P., Bannister, M.K., Falzon, P.J., Leong, K.H.: Review of Applications for Advanced Three-Dimensional Fibre Textile Composites. *Compos. Part A* 30, 1445-1461 (1999).

3. Bannister, M.K.: Development and Application of Advanced Textile Composites. *Proc. Inst. Mech. Eng. Part L - J. Mater. Design and App.* 218, 253-260 (2004).

4. Vannucci R.D.: PMR Polyimide Compositions for Improved Performance at 371˚C. *Proceedings of the 32nd International SAMPE Symposium and Exhibition*, April 6-9, Anaheim, USA (1987).

5. Shimokawa, T., Kakuta, Y., Hamaguchi, Y., Aiyama, T.: Static and Fatigue Strengths of a G40-800/5260 Carbon Fiber/Bismaleimide Composite Material at Room Temperature and 150˚C. *J. Compos. Mater.* 42, 655-679 (2008).

6. Agarwal, B.D., Broutman, L.J., Chandrashekhara, K.: *Analysis and Performance of Fiber Composites - 3rd Edition*. John Wiley and Sons Inc., Hoboken, USA (2006).

7. Herakovich, C.T.: *Mechanics of Fibrous Composites*. John Wiley and Sons Inc., New York, USA (1998).

8. Mori, T., Tanaka, K.: Average Stress in Matrix and Average Elastic Energy of Materials with Misfitting Inclusions. *Acta Metal.* 21, 571-574 (1973).

9. Benveniste, Y.: A New Approach to the Application of Mori-Tanaka's Theory in Composite Materials. *Mech. Mater.* 6, 147-157 (1987).

10. Dvorak, G.J.: Plasticity Theories for Fibrous Composite Materials. In: *Metal Matrix Composites Vol. 2 - Mechanisms and Properties* (Everett, R.K., Arsenault, R.J. editors), Treatise on Materials Science and Technology (Vol. 33), Academic Press, Boston, pp 1-77 (1990).

11. Gommers, B., Verpoest, I., VanHoutte, P.: The Mori-Tanaka Method Applied to Textile Composite Materials. *Acta Mater.* 46, 2223-2235 (1998).

12. El Mourid, A., Ganesan, R., Levesque, M.: Modeling of the Linearly Viscoelastic Behaviour of a Braided Composite. *Proceedings of the 2nd Joint US-Canada Conference on Composites*, September 26-28, Montreal, Canada (2011).

13. Tate, J.S., Kelkar, A.D.: Stiffness Degradation Model for Biaxial Braided Composites Under Fatigue Loading. *Compos. Part B* 39, 548-555 (2008).

14. Montesano, J., Fawaz, Z., Behdinan, K., Poon, C.: Fatigue Damage in On-Axis and Off-Axis Woven-Fiber/Resin Composite. *Key Eng. Mater.* 488-489, 230-233 (2012).

15. Kawai, M., Taniguchi, T.: Off-Axis Fatigue Behaviour of Plain Weave Carbon/Epoxy Fabric Laminates at Room and High Temperatures and its Mechanical Modeling. *Compos. Part A* 37, 243-256 (2006).

16. Harris, B.: A historical review of the fatigue behaviour of fibre-reinforced plastics. In: *Fatigue in Composites - Science and Technology of the Fatigue Response of Fibre-Reinforced Plastics* (Harris B., editor), Woodhead Publishing Ltd, Cambridge, p. 3-35 (2003).

17. Dieter, G.E.: *Mechanical Metallurgy - 3rd Edition*. McGraw-Hill, Boston, USA (1986).

18. Rice, R.C., Jackson, J.L., Bakuckas, J., Thompson, S.: *Metallic Materials Properties Development and Standardization*. US Department of Transportation - Federal Aviation Administration (FAA). Report Number DOT/FAA/AR-MMPDS-01 (2003).

19. Suresh, S.: *Fatigue of Materials - 2nd Edition*. Cambridge University Press, Cambridge, UK (2003).

20. Hahn, H.T., Kim, R.Y.: Fatigue Behaviour of Composite Laminate. *J. Compos. Mater.* 10, 156-180 (1976).

21. O'Brien, T.K.: An Evaluation of Stiffness Reduction as a Damage Parameter and Criterion for Fatigue Failure in Composite Materials. PhD Dissertation, Engineering Science and Mechanics Department, Virginia Polytechnic Institute and State University (1978).

22. Hashin, Z., Rotem, A.: A Fatigue Criterion for Fibre Reinforced Composite Materials. *J. Compos. Mater.* 7, 448-464 (1973).

23. Broutman, L.J., Sahu, S.: A New Theory to Predict Cumulative Fatigue Damage in Fibreglass Reinforced Plastics. In: Composite Materials - Testing and Design, pp. 170-188. ASTM STP 497, Philadelphia (1972).

24. Hahn, H.T., Kim, R.Y.: Proof Testing of Composite Materials. *J. Compos. Mater.* 9, 297-311 (1975).

25. O'Brien, T.K., Reifsnider, K.L.: Fatigue Damage Evaluation Through Stiffness Measurements in Boron-Epoxy Laminates. *J. Compos. Mater.* 15, 55-77 (1981).

26. Highsmith, A.L., Reifsnider, K.L.: Stiffness-Reduction Mechanisms in Composite Laminates. In: Reifsnider, K.L. (ed.) Damage in Composite Materials, pp. 103-117. ASTM STP 775, Philadelphia (1982).

27. Rotem, A.: Fatigue and Residual Strength of Composite Laminates. *Eng. Fract. Mech.* 25, 819-827 (1986).

28. Hashin, Z.: Cumulative Damage Theory for Composite Materials: Residual Life and Residual Strength Methods. *Compos. Sci. Tech.* 23, 1-19 (1985).

29. Hashin, Z.: Analysis of Stiffness Reduction of Cracked Cross-Ply Laminates. *Eng. Fract. Mech.* 25, 771-778 (1986).

30. Hwang, W., Han, K.S.: Cumulative Damage Models and Multi-stress Fatigue Life Prediction. *J. Compos. Mater.* 20, 125-153 (1986).

31. Hwang, W., Han, K.S.: Fatigue of Composites - Fatigue Modulus Concept and Life Prediction. *J. Compos. Mater.* 20, 154-165 (1986).

32. Whitworth, H.A.: Modeling Stiffness Reduction of Graphite/Epoxy Composite Laminates. *J. Compos. Mater.* 21, 362-372 (1987).

33. Whitworth, H.A.: Cumulative Damage in Composites. *J. Eng. Mater. Technol.* 112, 358-361 (1990).

34. Yang, J.N., Jones, D.L., Yang, S.H., Meskini, A.: A Stiffness Degradation Model for Graphite/Epoxy Laminates. *J. Compos. Mater.* 24, 753-769 (1990).

35. Reifsnider, K.L., Gao, Z.: A Micromechanics Model for Composites Under Fatigue Loading. *Int. J. Fatigue* 13, 149-156 (1991).

36. Ellyin, F., El-Kadi, H.: A Fatigue Failure Criterion for Fiber Reinforced Composite Laminae. *Compos. Struct.* 15, 61-74 (1990).

37. Gathercole, N., Reiter, H., Adam, T., Harris, B.: Life Prediction for Fatigue of T800/5245 Carbon-Fibre Composites: I. Constant-Amplitude Loading. *Int. J. Fatigue* 16, 523-532 (1994).

38. El-Mahi, A., Berthelot, J.M., Brillaud, J.: Stiffness Reduction and Energy Release Rate of Cross-Ply Laminates During Fatigue Tests. *Comp. Struct.* 30, 123-130 (1995).

39. Hernaff-Gardin, C., Lafarie-Frenot, M.C., Goupillaud, I.: Prediction of Cracking Evolution Under Uniaxial Fatigue Loading in Crossply Composite Laminates. In: Degallaix, S., Bathias, C., Fougeres, R. (eds.) *Proceedings of the International Conference on Fatigue of Composites*, pp. 189 - 196. La Societe Francaise de Metallurgie et de Materiaux, Paris (1997).

40. Akshantala, N.V., Talreja, R.: A Mechanistic Model for Fatigue Damage Evolution in Composite Laminates. *Mech. Mater.* 29, 123-140 (1998).

41. Jen, M.R., Lee, C.H.: Strength and Life in Thermoplastic Composite Laminates Under Static and Fatigue Loads. Part I: Experimental. *Int. J. Fatigue* 20, 605-615 (1998).

42. Bond, I.P.: Fatigue Life Prediction for GRP Subjected to Variable Amplitude Loading. *Compos. Part A* 30, 961-970 (1999).

43. Whitworth, H.A.: A Stiffness Degradation Model for Composite Laminates Under Fatigue Loading. *Compos. Struct.* 40, 95-101 (1998).

44. Whitworth, H.A.: Evaluation of the Residual Strength Degradation in Composite Laminates Under Fatigue Loading. *Compos. Struct.* 48, 261-264 (2000).

45. Schon, J.: A Model of Fatigue Delamination in Composites. *Compos. Sci. Tech.* 60, 553-558 (2000).

46. Reifsnider, K., Case, S., Duthoit, J.: The Mechanics of Composite Strength Evolution. *Compos. Sci. Tech.* 60, 2539-2546 (2000).

47. Petermann, J., Schulte, K.: The Effects of Creep and Fatigue Stress Ratio on the Long-Term Behaviour of Angle-Ply CFRP. *Compos. Struct.* 57, 205-210 (2002).

48. Shokrieh, M.M., Taheri-Behrooz, F.: A Unified Fatigue Life Model Based on Energy Method. *Compos. Struct.* 75, 444-450 (2006).

49. Kang, G., Liu, Y., Wang, Y., Chen, Z., Xu, W.: Uniaxial Ratchetting of Polymer and Polymer Matrix Composites: Time-Dependent Experimental Observations. *Mater. Sci. Eng. A* 523, 13-20 (2009).

50. Giancane, S., Panella, F.W., Dattoma, V.: Characterization of Fatigue Damage in Long Fiber Epoxy Composite Laminates. *Int. J. Fatigue* 32, 46-53 (2010).

51. Pandita, S.D., Huysmans, G., Wevers, M., Verpoest, I.: Tensile Fatigue Behaviour of Glass Plain-Weave Fabric Composites in On- and Off-Axis Directions. *Compos. Part A* 32, 1533-1539 (2001).

52. Quaresimin, M.: Fatigue of Woven Composite Laminates under Tensile and Compressive Loading. *Proceedings of the 10th European Conference on Composite Materials (ECCM-10)*, 3-7 June, Brugge, Belgium (2002).

53. Tamuzs, V., Dzelzitis, K., Reifsnider, K.: Fatigue of Woven Composite Laminates in Off-Axis Loading I. The Mastercurves. *App. Compos. Mater.* 11, 259-279 (2004).

54. Post, N.L., Bausano, J., Case, S.W., Lesko, J.J.: Modeling the Remaining Strength of Structural Composite Materials Subjected to Fatigue. *Int. J. Fatigue* 28, 1100-1108 (2006).

55. Shivakumar, K., Chen, H., Abali, F., Le, D., Davis, C.: A Total Fatigue Life Model for Model I Delaminated Composite Laminates. *Int. J. Fatigue* 28, 33-42 (2006).

56. Steinberger, R., Valadas-Leitao, T.I., Ladstatter, E., Pinter, G., Billinger, W., Lang, R.W.: Infrared Thermographic Techniques for Non-destructive Damage Characterization of Carbon Fibre Reinforced Polymers During Tensile Fatigue Testing. *Int. J. Fatigue* 28, 1340-1347 (2006).

57. Pinter, G., Ladstatter, E., Billinger, W., Lang, R.W.: Characterization of the Tensile Fatigue Behaviour of RTM-Laminates by Isocyclic Stress-Strain Diagrams. *Int. J. Fatigue* 28, 1277-1283 (2006).

58. Bourchak, M., Farrow, I.R., Bond, I.P., Rowland, C.W., Menan, F.: Acoustic Emission Energy as a Fatigue Damage Parameter for CFRP Composites. *Int. J. Fatigue* 29, 457-470 (2007).

59. Gagel, A., Fiedler, B., Schulte, K.: On Modeling the Mechanical Degradation of Fatigue Loaded Glass-Fibre Non-Crimp Fabric Reinforced Epoxy Laminates. *Compos. Sci. Tech.* 66, 657-664 (2006).

60. Gagel, A., Lange, D., Schulte, K.: On the Relation Between Crack Densities, Stiffness Degradation, and Surface Temperature Distribution of Tensile Fatigue Loaded Glass-Fibre Non-Crimp-Fabric Reinforced Epoxy. *Compos. Part A* 37, 222-228 (2006).

61. Plumtree, A., Melo, M.: Cyclic Damage Evolution in a PMC Laminate. *Key Eng. Mater.* 348/349, 33-36 (2007).

62. Vallons, K., Lomov, S.V., Verpoest, I.: Fatigue and Post-Fatigue Behaviour of Carbon/Epoxy Non-Crimp Fabric Composites. *Compos. Part A* 40, 251-259 (2009).

63. Carvelli, V., Gramellini, G., Lomov, S.V., Bogdanovich, A.E., Mungalov, D.D., Verpoest, I.: Fatigue Behaviour of Non-Crimp 3D Orthogonal Weave and Multi-Layer Plain Weave E-Glass Reinforced Composites. *Compos. Sci. Tech.* 70, 2068-2076 (2010).

64. Burr, S.T., Morris, D.H.: Two-Dimensionally Braided Composites Subjected to Static and Fatigue Loading. *Proceedings of the Mechanics of Textile Composites Conference* (N96-25071 09-24, pp 33-53), Virginia Polytechnic Institute and State University, USA (1995).

65. Portanova, M.A., Deaton, J.W.: Impact and Fatigue Resistance of a [±30˚/0˚] 3-D Braided Carbon Epoxy Composite. In *Composite Materials: Fatigue and Fracture* (Martin, R.H. editor), ASTM International, Philadelphia, STP 1230, pp 368-388 (1995).

66. Kelkar, A.D., Whitcomb, J.D.: Characterization and Structural Behaviour of Braided Composites. US Department of Transportation Report DOT/FAA/AR-08/52, January 2009.

67. Tate, J.S., Kelkar, A.D., Whitcomb, J.D.: Effect of Braid Angle on Fatigue Performance of Biaxial Braided Composites. *Int. J. Fatigue* 28, 1239-1247 (2006).

68. Huang, Z.M., Teng, X.C., Ramakrishna, S.: Fatigue Behaviour of Multilayered Braided Fabric Reinforced Laminates. *Polymers Poly. Compos.* 13, 73-81 (2005).

69. Salkind, M.J.: Fatigue of Composites. In *Composite Materials: Testing and Design*. ASTM International, Philadelphia, STP 497, pp 143-169 (1972).

70. VanPaepegem, W., DeBaere, I., Lamkanfi, E., Degrieck, J.: Monitoring Quasi-Static and Cyclic Fatigue Damage in Fibre-Reinforced Plastics by Poisson's Ratio Evolution. *Int. J. Fatigue* 32, 184-196 (2010).

71. Wen, C., Yazdani, S.: Anisotropic Damage Model for Woven Fabric Composites During Tension-Tension Fatigue. *Compos. Struct.* 82, 127-131 (2008).

72. Montesano, J., Selezneva, M., Fawaz, Z., Poon, C., Behdinan, K.: Elevated Temperature Off-Axis Fatigue Behaviour of an Eight-Harness Satin Woven Carbon-Fiber/Bismaleimide Laminate. *Compos. Part A* 43, 1454-1466 (2012).

73. Lakes, R.S.: *Viscoelastic Materials*. Cambridge University Press, New York (2009).

74. Serafini, T.T., Vannucci, R.D.: Tailor Making High Performance Graphite Fiber Reinforced PMR Polyimides. NASA Technical Report, TM X-71616 (1975).

75. Tiano, T., Hurley, W., Roylance, M., Landrau, N., Kovar, R.F.: Reactive Plasticizers for Resin Transfer Molding of High Temperature PMR Composites. *Presented at the 32nd SAMPE ISTC*, November 5-9, Boston, USA (2000).

76. Xie, W., Pan, W., Chuang, K.C.: Thermal Characterization of PMR Polyimides. *Thermo. Acta* 367-368, 143-153 (2001).

77. Sacks, S., Johnson, W.S.: Effects of Aging on the Mechanical Behaviour of K3B Matrix Material. *J. of Thermoplastic Compos. Mater.* 11, 429-442 (1998).

78. Cytec Engineered Materials: 5250-4 RTM Technical Data (2002).

79. Montesano, J., Fawaz, Z., Behdinan, K., Poon, C.: Fatigue of High Temperature Polymer Matrix Composites. *Mater. Sci. Research J.* 4, 381-406 (2010).

80. Miyano, Y., McMurray, M.K., Kitade, N., Nakada, M., Mohri, M.: Loading Rate and Temperature Dependence of Flexural Behaviour of Unidirectional Pitch-Based CFRP Laminates. *Composites* 26, 713-717 (1995).

81. Lo, Y.J., Liu, C.H., Hwang, D.G., Chang, J.F., Chen, J.C., Chen, W.Y., Hsu, S.E.: High-Temperature Behaviours of an Innovative Polymeric Matrix Composite. In *High*

Temperature and Environmental Effects on Polymeric Composites (Harris, C.E., Gates, T.S. editors). ASTM International, Philadelphia, STP 1174, pp 66-77 (1993).

82. Branco, C.M., Eichler, K., Ferreira, J.M.: Fatigue Behaviour of E-glass Fiber Reinforced Phenolic Composites: Effect of Temperature, Mean Stress and Fiber Surface Treatment. *Theor. App. Fract. Mech.* 20, 75-84 (1994).

83. Uematsu, Y., Kitamura, T., Ohtani, R.: Delamination Behaviour of a Carbon-Fiber-Reinforced Thermoplastic Polymer at High Temperatures. *Compos. Sci. Tech.* 53, 333-341 (1995).

84. Case, S.W., Plunkett, R.B., Reifsnider, K.L.: Simulation Methods for Life and Remaining Strength Prediction of High-Temperature Polymeric Composites Subjected to Cyclic Loads. In *High Temperature and Environmental Effects on Polymeric Composites - 2nd Volume* (Gates, T.S., Zureick, A.H. editors). ASTM International, Philadelphia, STP 1302, pp 35-49 (1997).

85. Kawai, M., Yajima, S., Hachinohe, A., Kawase, Y.: High-Temperature Off-Axis Fatigue Behaviour of Unidirectional Carbon-Fibre-Reinforced Composites with Different Resin Matrices. *Compos. Sci. Tech.* 61, 1285-1302 (2001).

86. Sjogren, A., Asp, L.E.: Effects of Temperature on Delamination Growth in a Carbon/Epoxy Composite Under Fatigue Loading. *Int. J. Fatigue* 24, 179-184 (2002).

87. Sun, Z., Daniel, I.M., Luo, J.J.: Modeling of Fatigue Damage in a Polymer Matrix Composite. *Mater. Sci. Eng. A* 361, 302-311 (2003).

88. Gregory, J.R., Spearing, S.M.: Constituent and Composite Quasi-Static and Fatigue Fracture Experiments. *Compos. Part A* 36, 665-674 (2005).

89. Jen, M.H.R., Tseng, Y.C., Lin, W.H.: Thermo-mechanical Fatigue of Centrally Notched and Unnotched AS-4/PEEK APC-2 Composite Laminates. *Int. J. Fatigue* 28, 901-909 (2006).

90. Uematsu, Y., Kitamura, T., Ohtani, R.: Creep-Fatigue Interaction in Delamination Crack Propagation of Advanced CFRPs at High Temperatures. In *High Temperature and Environmental Effects on Polymeric Composites – Vol. 2* (Gates, T., Zureick, A.H. Editors). ASTM International, STP 1302, pp 110-132 (1997).

91. Gyekenyesi, A.L., Castelli, M.G., Ellis, J.R., Burke, C.S.: A Study of Elevated Temperature Testing Techniques for the Fatigue Behaviour of PMCS: Application to T650-35/AMB21. NASA Technical Report, TM-106927 (1995).

92. Miyano, Y., Nakada, M., Sekine, N.: Accelerated Testing for Long-Term Durability of GFRP Laminates for Marine Use. *Compos. Part B* 35, 497-502 (2004).

93. Shimokawa, T., Kakuta, Y., Saeki, D., Kogo, Y.: Carbon Plain-Weave Fabric Low-Temperature Vacuum Cure Epoxy Composite: Static and Fatigue Strength at Room and High Temperatures and Practicality Evaluation. *J. Comp. Mater.* 41, 2245-2265 (2007).

94. Reifsnider, K.L., Henneke, E.G., Stinchcomb, W.W., Duke, J.C.: Damage Mechanics and NDE of Composite Laminates. In *Mechanics of Composite Materials, Recent Advances* (Hashin, Z., Herakovich, C.T. editors), pp 399-420, Pergamon Press, New York, USA (1983).

95. Talreja, R.: Fatigue of Composites. Technomic Publishing Company Inc., Lancaster, USA (1987).

96. Cain, K.J.: Damage Characterization of a Unidirectional Off-Axis Graphite-Bismaleimide Laminate. PhD Dissertation, Mechanical Engineering, Waterloo (2002).

97. Selezneva, M., Montesano, J., Fawaz, Z., Behdinan, K., Poon, C.: Microscale Experimental Investigation of Failure Mechanisms in Off-axis Woven Laminates at Elevated Temperatures. *Compos. Part A* 42, 1756-1763 (2011).

98. Lomov, S.V., Ivanov, D.S., Truong, T.C., Verpoest, I., Baudry, F., Vanden Bosche, K., Xie, H.: Experimental Methodology of Study of Damage Initiation and Development in Textile Composites in Uniaxial Tensile Test. *Compos. Sci. Tech.* 68, 2340-2349 (2008).

99. Masters, J.E., Ifju, P.G.: A Phenomenological Study of Triaxially Braided Textile Composites Loaded in Tension. *Compos. Sci. Technol.* 56, 347-358 (1996).

100. Ivanov, D.S., Baudry, F., VanDenBroucke, B., Lomov, S.V., Xie, H., Verpoest, I.: Failure Analysis of Triaxial Braided Composite. *Compos. Sci. Tech.* 69, 1372-1380 (2009).

101. Reifsnider, K.L., Jamison, R.: Fracture of Fatigue-Loaded Composite Laminates. *Int. J. Fatigue* 4, 187-197 (1982).

102. Kellas, S., Morton, J., Curtis, P.T.: A Characteristic Fatigue Parameter for Notched Composites. *Int. J. Fatigue* 13, 35-43 (1991).

103. Jen, M.H.R., Kau, Y.S., Wu, I.C.: Fatigue Damage in a Centrally Notched Composite Laminate Due to Two-Step Loading. *Int. J. Fatigue* 16, 193-201 (1994).

104. Spearing, S.M., Beaumont, P.W.R.: Fatigue Damage Mechanics of Composite Materials - Part I: Experimental Measurement of Damage and Post-fatigue Properties. *Compos. Sci. Tech.* 44, 159-168 (1992).

105. Coats, T.W., Harris, C.E.: A Progressive Damage Methodology for Residual Strength Predictions of Notched Composite Panels. *J. Compos. Mater.* 33, 2193-2224 (1999).

106. Mouritz, A.P., Townsend, C., Shah Khan, M.Z.: Non-destructive Detection of Fatigue Damage in Thick Composites by Pulse-Echo Ultrasonics. *Compos. Sci. Tech.* 60, 23-32 (2000).

107. Scarponi, C., Briotti, G.: Ultrasonic Detection of Delaminations on Composite Materials. *J. Reinf. Plast. Compos.* 16, 768-790 (1997).

108. Beghini, M., Bertini, L., Vitale, E.: Analysis of Fatigue Delamination Growth in Carboresin Specimens with Central Hole. *Compos. Struct.* 17, 257-274 (1991).

109. Nayeb-Hashemi, H., Cohen, M.D., Zotos, J., Poormand, R.: Ultrasonic Characteristics of Graphite/Epoxy Composite Material Subject to Fatigue and Impacts. *J. Nondestr. Eval.* 5, 119-131 (1986).

110. Fujii, T., Shiina, T., Okubu, K.: Fatigue Notch Sensitivity of Glass Woven Fabric Composites Having a Circular Hole Under Tension/Torsion Biaxial Loading. *J. Compos. Mater.* 28, 234-251 (1994).

111. Hoover, J.W., Kujawski, D., Ellyin, F.: Transverse Cracking of Symmetric and Unsymmetric Glass-Fibre/Epoxy-Resin Laminates. *Compos. Sci. Tech.* 57, 1513-1526 (1997).

112. Li, C., Ellyin, F., Wharmby, A.: On Matrix Crack Saturation in Composite Laminates. *Compos. Part B* 34, 473-480 (2003).

113. Karger-Kocsis, J., Fejes-Kozma, Z.S.: Failure Mode and Damage Zone Development in a GMT-PP by Acoustic Emission and Thermography. *J. Reinf. Plast. Compos.* 13, 768-792 (1994).

114. Williams, R.S., Reifsnider, K.L.: Investigation of Acoustic Emission During Fatigue Loading of Composite Specimens. *J. Compos. Mater.* 8, 340-355 (1974).

115. Maier, G., Ott, H., Protzner, A., Protz, B.: Damage Development in Carbon Fibre-Reinforced Polyimides in Fatigue Loading as a Function of Stress Ratio. *Composites* 17, 111-120 (1986).

116. Whitcomb, J.D.: Thermographic Measurement of Fatigue Damage. In *Composite Materials: Testing and Design* (Tsai, S.W. editor), ASTM, STP 674, pp 502-516 (1979).

117. Hansen, U.: Damage Development in Woven Fabric Composites During Tension-Tension Fatigue. *J. Compos. Mater.* 33, 614-639 (1999).

118. Toubal, L., Karama, M., Lorrain, B.: Damage Evolution and Infrared Thermography in Woven Composite Laminates Under Fatigue Loading. *Int. J. Fatigue* 28, 1867-1872 (2006).

119. Chen, A.S., Harris, B.: Fatigue-Induced damage Mechanisms in Carbon Fibre-Reinforced Plastic Composites. *J. Mater. Sci.* 28, 2013-2027 (1993).

120. Takeda, N.: Characterization of Microscopic Damage in Composite Laminates and Real-Time Monitoring by Embedded Optical Fiber Sensors. *Int. J. Fatigue* 24, 281-289 (2002).

121. Takeda, S., Okabe, Y., Takeda, N.: Delamination Detection in CFRP Laminates with Embedded Small-Diameter Fiber Bragg Grating Sensors. *Compos. Part A* 33, 971-980 (2002).

122. Ussorio, M., Wang, H., Ogin, S.L., Thorne, A.M., Reed, G.T., Tjin, S.C., Suresh, R.: Modifications to FBG Sensor Spectra Due to Matrix Cracking in a CFRP Composite. *Constr. Build. Mater.* 20, 111-118 (2006).

123. Ling, H., Lau, K., Su, Z., Wong, E.T.: Monitoring Mode II Fracture Behaviour of Composite Laminates Using Embedded Fiber-Optic Sensors. *Compos. Part B* 38, 488-497 (2007).

124. Selezneva, M.: Application of FBG Sensors for Fatigue Monitoring of Advanced Polymer Matrix Composites. MASc Thesis, Aerospace Engineering, Ryerson University, Toronto (2010).

125. Montesano, J., Selezneva, M., Poon, C., Fawaz, Z., Behdinan, K.: Application of Fiber Optic Sensors for Elevated Temperature Testing of Polymer Matrix Composite Materials. *Sci. Eng. Compos. Mater.* 18, 109-116 (2011).

126. Sendeckyj, G.P.: Life Prediction for Resin-Matrix Composite Materials. In *Fatigue of Composite Materials* (Reifsnider, K.L. editor), pp 431 - 483. Composite Material Series 4, Elsevier, Amsterdam (1990).

127. Degrieck, J., VanPaepegem, W.: Fatigue Damage Modeling of Fibre-Reinforced Composite Materials: Review. *App. Mech. Review (ASME)* 54, 279-299 (2001).

128. Fawaz, Z., Ellyin, F.: Fatigue Failure Model for Fibre-Reinforced Materials Under General Loading Conditions. *J. Compos. Mater.* 28, 1432-1451 (1994).

129. Jen, M.R., Lee, C.H.: Strength and Life in Thermoplastic Composite Laminates Under Static and Fatigue Loads. Part II: Formulation. *Int. J. Fatigue* 20, 617-629 (1998).

130. Philippidis, T.P., Vassilopoulos, A.P.: Fatigue Strength Prediction Under Multiaxial Stress. *J. Compos. Mater.* 33, 1578-1599 (1999).

131. Sarfaraz, R., Vassilopoulos, A.P., Keller, T.: A Hybrid S-N Formulation for Fatigue Life Modeling of Composite Materials and Structures. *Compos. Part A* 43, 445-453 (2012).

132. Miner, M.A.: Cumulative Damage in Fatigue. *J. App. Mech. (ASME)* 12, A159-A164 (1945).

133. Marco, S.M., Starkey, W.L.: A Concept of Fatigue Damage. *Trans. ASME* 76, 627-632 (1954).

134. Henry, D.L.: A Theory of Fatigue Damage Accumulation in Steel. *Trans. ASME* 77, 913–918 (1955).

135. Howe, R.J., Owen, M.J.: Accumulation of Damage in a Glass-Reinforced Plastic Under Tensile and Fatigue Loading. In *Proceedings of the 8th International Reinforced Plastics Congress*, pp 137-148, British Plastics Federation, London (1972).

136. Hashin, Z., Rotem, A.: A Cumulative Damage Theory of Fatigue Failure. *Mater. Sci. Eng.* 34, 147-160 (1978).

137. Yang, J.N., Lee, L.J., Sheu, D.Y.: Modulus Reduction and Fatigue Damage of Matrix Dominated Composite Laminates. *Compos. Struct.* 21, 91-100 (1992).

138. VanPaepegem, W., Degrieck, J.: Experimental Set-up for and Numerical Modelling of Bending Fatigue Experiments on Plain Woven Glass/Epoxy Composites. *Compos. Struct.* 51, 1-8 (2001).

139. Mao, H., Mahadevan, S.: Fatigue Damage Modeling of Composite Materials. *Compos. Struct.* 58, 405-410 (2002).

140. Wu, F., Yao, W.: A Fatigue Damage Model of Composite Materials. *Int. J. Fatigue* 32, 134-138 (2010).

141. Mivehchi, H., Varvani-Farahani, A.: The Effect of Temperature on Fatigue Strength and Cumulative Fatigue Damage of FRP Composites. *Proc. Eng.* 2, 2011-2020 (2010).

142. Yang, J.N., Jones, D.L.: Load Sequence Effects on Graphite/Epoxy [±35]2S Laminates. In *Long-Term Behaviour of Composites*, pp 246-262. ASTM STP 813, Philadelphia (1983).

143. Caprino, G., D'Amore, A.: Flexural Fatigue Behaviour of Random Continuous-Fibre-Reinforced Thermoplastic Composites. *Compos. Sci. Tech.* 58, 957-965 (1998).

144. Bergmann, H.W., Prinz, R.: Fatigue Life Estimation of Graphite/Epoxy Laminates Under Consideration of Delamination Growth. *Int. J. Numer. Methods Eng.* 27, 323-341 (1989).

145. Feng, X., Gilchrist, M.D., Kinloch, A.J., Matthews, F.L.: Development of a Method for Predicting the Fatigue Life of CFRP Components. In *Proceedings of the International Conference on Fatigue of Composites* (Degallaix, S., Bathias, C., Fougeres, R. editors), pp 407-414. La Societe Francaise de Metallurgie et de Materiaux, Paris (1997).

146. Aboudi, J.: Micromechanical Analysis of Composites by the Method of Cells. *App. Mech. Rev. (ASME)* 42, 193-221 (1989).

147. Sun, C.T., Vaidya, R.S.: Prediction of Composite Properties from a Representative Volume Element. *Compos. Sci. Tech.* 56, 171-179 (1996).

148. Xia, Z., Chen, Y., Ellyin, F.: A Meso/Micro-mechanical Model for Damage Progression in Glass-Fiber/Epoxy Cross-Ply Laminates by Finite-Element Analysis. *Compos. Sci. Tech.* 60, 1171-1179 (2000).

149. Montesano, J., Behdinan, K., Fawaz, Z., Poon, C.: Considerations for Progressive Damage in Fibre-Reinforced Composite Materials Subjected to Fatigue. In *High Performance Computing Systems and Applications* (Mewhort, D.J.K., Cann, N.M., Slater, G.W., Naughton, T.J. Editors), LNCS 5976, Springer-Verlag, Berlin, Germany, pp 148-164 (2010).

150. Shi, Z., Zhang, R.: Fatigue Damage of Fiber Reinforced Composites: Simultaneous Growth of Interfacial Debonding and Matrix Annular Crack Surrounding Fiber. *J. Compos. Mater.* 42, 2247-2258 (2008).

151. Hashin, Z.: Analysis of Cracked Laminates: A Variational Approach. *Mech. Mater.* 4, 121-136 (1985).

152. Nairn, J.A.: Strain Energy Release Rate of Composite Microcracking: A Variational Approach. *J. Compos. Mater.* 23, 1106-1129 (1989).

153. Wang, S.S., Suemasu, H., Chim, E.S.M.: Analysis of Fatigue Damage Evolution and Associated Anisotropic Elastic Property Degradation in Random Short-Fiber Composite. *J. Compos. Mater.* 21, 1084-1105 (1987).

154. Poursartip, A., Ashby, M.F., Beaumont, P.W.R.: The Fatigue Damage Mechanics of a Carbon Fibre Composite Laminate: I - Development of the Model. *Compos. Sci. Tech.* 25, 193-218 (1986).

155. Bartley-Cho, J., Lim, S.G., Hahn, H.T., Shyprykevich, P.: Damage Accumulation in Quasi-Isotropic Graphite/Epoxy Laminates Under Constant-Amplitude Fatigue and Block Loading. *Compos. Sci. Tech.* 58, 1535-1547 (1998).

156. Reifsnider, K.L.: The Critical Element Model: A Modeling Philosophy. *Eng. Fract. Mech.* 25, 739-749 (1986).

157. Subramanian, S., Reifsnider, K.L., Stinchcomb, W.W.: A Cumulative Damage Model to Predict the Fatigue Life of Composite Laminates Including the Effect of a Fibre-Matrix Interphase. *Inter. J. Fatigue* 17, 343-351 (1995).

158. Laws, N., Dvorak, G.J., Hejazi, M.: Stiffness Changes in Unidirectional Composites Caused by Crack Systems. *Mech. Mater.* 2, 123-137 (1983).

159. Kachanov, M.: Continuum Theory of Media with Cracks. Izv. AN SSR, Mekhanika Tverdogo Tela, ASCE 7, 54 - 59 (1972).

160. Talreja, R.: Transverse Cracking and Stiffness Reduction in Composite Laminates. *J. Compos. Mater.* 19, 355-375 (1985).

161. Talreja, R.: Stiffness Properties of Composite Laminates with Matrix Cracking and Interior Delamination. *Eng. Fract. Mech.* 25, 751-762 (1986).

162. Talreja, R.: Internal Variable Damage Mechanics of Composite Materials. In *Yielding, Damage and Failure of Anisotropic Solids* (Boehler, J.P. editor). Mechanical Engineering Publications, London, pp 509-533 (1990).

163. Allen, D.H., Harris, C.E., Groves, S.E.: A Thermomechanical Constitutive Theory for Elastic Composites with Distributed Damage - I: Theoretical Development. *Int. J. Solids Struct.* 23, 1301-1318 (1987).

164. Allen, D.H., Harris, C.E., Groves, S.E.: A Thermomechanical Constitutive Theory for Elastic Composites with Distributed Damage - II: Application to Matrix Cracking in Laminated Composites. *Int. J. Solids Struct.* 23, 1319-1338 (1987).

165. Coats, T.W., Harris, C.E.: Experimental Verification of a Progressive Damage Model for IM7/5260 Laminates Subjected to Tension-Tension Fatigue. *J. Compos. Mater.* 29, 280-305 (1995).

166. Ladeveze, P., LeDantec, E.: Damage Modeling of the Elementary Ply for Laminated Composites. *Compos. Sci. Tech.* 43, 257-267 (1992).

167. Ladeveze, P.: A Damage Computational Method for Composite Structures. *Comput. Struct.* 44, 79-87 (1992).

168. Ladeveze, P.: A Damage Computational Approach for Composites: Basic Aspects and Micromechanical Relations. *Comput. Mech.* 17, 142-150 (1995).

169. Ladeveze, P., Allix, O., Deu, J.F., Leveque, D.: A Mesomodel for Localisation and Damage Computation in Laminates. *Comp. Meth. App. Mech. Eng.* 183, 105-122 (2000).

170. Shokrieh, M.M., Lessard, L.B.: Multiaxial Fatigue Behaviour of Unidirectional Plies Based on Uniaxial Fatigue Experiments - Part I: Modeling. *Int. J. Fatigue* 19, 201-207 (1997).

171. Shokrieh, M.M., Lessard, L.B.: Multiaxial Fatigue Behaviour of Unidirectional Plies Based on Uniaxial Fatigue Experiments - Part II: Experimental Validation. *Int. J. Fatigue* 19, 209-217 (1997).

172. Shokrieh, M.M., Lessard, L.B.: Progressive Fatigue Damage Modeling of Composite Materials, Part I: Modeling. *J. Compos. Mater.* 34, 1056-1080 (2000).

173. Shokrieh, M.M., Lessard, L.B.: Progressive Fatigue Damage Modeling of Composite Materials, Part II: Material Characterization and Model Verification. *J. Compos. Mater.* 34, 1081-1116 (2000).

174. Thamilselvan, G.: Methodology for Fabricating High Temperature Composite Panel and Evaluation. MASc Thesis, Aerospace Engineering, Ryerson University, Toronto (2011).

175. ASTM Standard D6856-03: Standard Guide for Testing Fabric-Reinforced Textile Composite Materials. ASTM International, USA (2008).

176. ASTM Standard D3039-08: Standard Test Method for Tensile Properties of Polymer Matrix Composite Materials. ASTM International, USA (2008).

177. ASTM Standard D3479-96: Standard Test Method for Tension-Tension Fatigue of Polymer Matrix Composites Materials. ASTM International, USA (2007).

178. LaRosa, G., Risitano, A.: Thermographic Methodology for Rapid Determination of the Fatigue Limit of Materials and Mechanical Components. *Int. J. Fatigue* 22, 65-73 (2000).

179. Bremond, P.: Lock-in Thermography: A Tool to Measure Stress and to Detect Defects in Aircraft Industry. *Proceedings of the 9th Australian International Aerospace Congress*, Canberra, Australia (2001).

180. Montesano, J., Fawaz, Z., Poon, C., Behdinan, K.: A Microscopic Experimental Investigation of Failure Mechanisms in a Triaxially Braided Polymer Composite. *Proceedings of the 9th Joint Canada-Japan Workshop on Composites*, July 30 - Aug 1, Kyoto, Japan (2012).

181. Colombo, C., Libonati, F., Pezzani, F., Salerno, A., Vergani, L.: Fatigue Behaviour of a GFRP Laminate by Thermographic Measurements. *Eng Procedia* 10, 3518-3527 (2011).

182. Kang, G.: Ratchetting: Recent Progresses in Phenomenon Observation, Constitutive Modeling and Application. *Int. J. Fatigue* 30, 1448-1472 (2008).

183. Crochon, T. PhD Dissertation, Ecole Polytechnique, Montreal (2013).

184. Kobayashi, S., Takeda, N.: Experimental Characterization of Microscopic Damage Behaviour in Carbon/Bismaleimide Composite - Effects of Temperature and Laminate Configuration. *Compos. Part A* 33, 1529-1538 (2002).

185. Sue, H.J., Garcia-Meitin, E.I.: Crazing in High-Performance Thermoset Resins. *J. Mater. Sci. Letters* 12, 1463-1466 (1993).

186. Cain, K.J., Glinka, G., Plumtree, A.: Damage Evolution on Off-Axis Unidirectional Graphite Bismaleimide Composite Loaded in Tension. *Compos. Part A* 34, 987-993 (2003).

187. Koyanagi, J., Yoneyama, S., Nemoto, A., Melo, J.D.D.: Time and Temperature Dependence of Carbon/Epoxy Interface Strength. *Compos. Sci. Tech.* 70, 1395-1400 (2010).

188. Lemaitre, J., Plumtree, A.: Application of Damage Concepts to Predict Creep-Fatigue Failures. *J. Eng. Mater. Tech.* 101, 284-292 (1979).

189. Montesano, J., Fawaz, Z., Poon, C., Behdinan, K.: Fatigue Damage Characterization of a Tri-axially Braided Polymer Matrix Composite Material. *Proceedings of the 15th European Conference on Composite Materials* (ECCM15), 24-28 June, Venice, Italy (2012).

190. Lemaitre, J.: A Continuous Damage Mechanics Model for Ductile Fracture. J. Eng. Mater. Tech. 107, 83-89 (1985).

191. Holzapfel, G.A.: *Nonlinear Solid Mechanics - A Continuum Approach for Engineering*. John Wiley and Sons, West Sussex, England (2000).